Imperial College London

Studies of Liquid-Liquid Two-Phase Flows Using Laser-Based Methods

Rhys Gareth Morgan

March 2012

Department of Chemical Engineering and Chemical Technology

Imperial College London

South Kensington Campus

London SW7 2AZ

A thesis submitted to Imperial College London in partial fulfilment of the requirements of the degree of Doctor of Philosophy and for the Diploma of Membership of the Imperial College

“Nothing is so dangerous to the progress of the human mind than to assume that our views of science are ultimate, that there are no mysteries in nature, that our triumphs are complete, and that there are no new worlds to conquer.”

Humphry Davy

Declaration

This thesis is a description of the work carried out in the Department of Chemical Engineering, Imperial College London, between October 2007 and March 2012, under the supervision of Emeritus Professor Geoffrey F. Hewitt and Dr Christos Markides. Except where acknowledged, the material is the original work of the author and no part of it has been submitted for a degree at any other university.

Abstract

The research described in this thesis has been focused on the detailed investigation of horizontal co-current liquid-liquid two-phase flows. The experiments were carried out in channels of square and circular cross section and involved the use of two immiscible liquids of matched refractive index; namely an oil (Exxol^{TM}D80) and a 81.7 wt% glycerol-water solution. The experiments were carried out in a refurbished liquid-liquid flow facility (TOWER) and the focus was on examining the flows using high-speed laser-based visualisation methods which allowed both qualitative evaluation of the nature of the flows (i.e. the flow patterns) and quantitative measurements of parameters such as drop size and velocity distribution. The laser-based techniques used included Planar Laser Induced Fluorescence (PLIF), Particle Tracking Velocimetry (PTV) and Particle Image Velocimetry (PIV). Using these techniques, it was possible to obtain high spatial and temporal resolution measurements of velocity and phase distribution of liquid-liquid flows which enabled the detailed diagnostic inspection to an extent that has not been previously possible. 144 experiments were carried out in three experimental campaigns. In the first campaign, a square cross section channel was used in order to avoid image distortion by the channel walls. In the second and third campaigns, a circular tube was employed and a graticule correction method was used to correct the distortion to the PLIF and PTV/PIV images which occurs when the circular cross-section visualisation cell is used. In the two circular tube experiments, two methods of injection of the phases were used: (1) the heavier (glycerol solution) phase was injected in its natural location at the bottom of the channel, and (2) in the second case the heavier phase was injected at the top of the channel.

The PLIF images gave a clear indication of the distribution of the phases at the channel centre line and have been used qualitatively in obtaining information about the flow patterns occurring.

The PLIF images have also been used quantitatively in generating data on phase distribution, in-situ phase fraction, interface level and drop size distribution. Much of the data on in-situ phase fraction and interface level fits well with a simple laminar-laminar stratified flow model. The PTV/PIV method provided extensive data on velocity profiles; in the lower (aqueous glycerol solution) phase, the profile usually showed the curved shape characteristic of laminar flow and in the upper (Exxol^{TM}D80) phase, the velocity profile often showed the flattened form characteristic of turbulent flow.

Acknowledgements

I feel extremely fortunate to have been surrounded by some truly great people while I have undertaken this PhD. The following attempts to articulate the gratitude and thanks I have for their involvement in this work, whether it be of an academic nature or otherwise. Firstly, I would like to thank my supervisors, Professor Geoffrey F. Hewitt and Dr Christos Markides. It's difficult to concisely convey the appreciation I have for all the guidance, encouragement and teaching that I have had from them. I would like to express my thanks and appreciation for the help I have had from Dr Ivan Zadrazil and Dr Colin Hale. Also, I would like to thank the Chemical Engineering Workshop for the help in refurbishing the TOWER facility to enable my experimental work to be conducted. There are a few friends that I would like to thanks, these being Patrick Wray, Kat Fu and Henry Morris. Finally, I would like to extend a massive thank you to my mother, father and the rest of my family for their love, support and encouragement during not just this PhD but all of my educational endeavours that led to this point.

Table of Contents

List of Figures

List of Tables

CHAPTER 1

Introduction

1.1 Background

The research activities presented in this thesis focused on the detailed investigation of horizontal co-current flows of two immiscible liquids. The co-current flow of two immiscible liquids is encountered in a host of different settings and industrial processes, such as in continuous-flow chemical processing (CFCP) on microchips (Toskeshi et al., 2000), microchannel tubular reactors for continuous production in the pharmaceutical industry (Wegmann and von Rohr, 2006), as well as in the fine chemicals industry where liquid-liquid slug flow capillary microreactors are used to improve heat and mass transfer (Kashid and Agar, 2007). However, most notable and pertinent to the current investigation is the transportation of hydrocarbons in subsea pipelines from petroleum production facilities, where the production flowlines from the wellhead contain water which can either occur naturally in the reservoir ("connate water") or result from water injection into the reservoir to increase pressure and in turn oil recovery.

Though a more detailed review of relevant literature is given in Chapter 2, it is important, in this Introduction, to place the present work in the context of the history of development of this subject area. Investigation into liquid-liquid flows began with the injection of water into oil flows with the aim of improving the pumping requirements when transporting viscous heavy oils (Russell and Charles, 1959). This is still a pertinent issue but the scope of the work has

significantly developed in the intervening 50 years. Multiphase pumping for subsea boosting from oil wells enables the cost-efficient development of marginal and previously inaccessible fields. Enhanced oil recovery from ultra-deep wells, such as those in the oil fields of the Santos Basin, Brazil and the Gulf of Mexico, has benefited from the development of multiphase pumping, as has the recovery from more remote oil reservoirs (Bell et al., 2005). However, in these applications, it is often necessary to pass the multiphase mixtures along long distance subsea flowlines to a central processing facility. The design of the subsea infrastructure, such as flowline sizing, hinges on being able to predict the hydrodynamic behaviour of the flows they contain. An improved understanding of the rheological behaviour and flow dynamics of such multiphase flows can lead to significant advancements in empirical and phenomenological models capable of the accurate prediction of these flows, and in turn to better designs and operation of related industrial facilities. Obtaining a comprehensive mechanistic understanding and being able to develop such models hinges crucially on being able to visualise the flows and to provide detailed and high-quality experimental data. Since Russell et al. (1959) embarked on investigating oil-water flows, considerable effort has been focused on the characterisation of liquid-liquid flows (Charles et al., 1961; Hasson et al., 1970; Guzhov et al., 1973; Arirachakaran et al., 1989; Hussain, 2004; Liu, 2005). However, in contrast to the case of gas-liquid flows (see for instance Taitel and Dukler, 1976), only limited work has been done on developing predictive tools for the transition between liquid-liquid flow regimes. Modelling endeavours for liquid-liquid flows have focused on the transition from oil-continuous flows to water-continuous flows ("phase inversion") (Arirachakaran et al., 1989; Chen, 2001; Yeo et al., 2002) and pressure gradient prediction (Malinowsky, 1975).

Most horizontal liquid-liquid flow visualisation studies have employed high-speed photography (Soleimani 1999) or high-speed photography coupled with an endoscopic technique (Angeli and Hewitt, 2000a,b). However, one of the most powerful tools for the study of fluid flow and mixing is laser-induced fluorescence (LIF). Liu (2005) used LIF to visualise co-current vertical

downwards liquid-liquid flows and produced images with a strong and clear distinction between the two phases. The studies by Liu (2005) provided encouragement to the project described here, namely the application of LIF and related techniques to the study of co-current horizontal liquid-liquid flows.

1.2 Objectives

The two main objectives for the work contained in this thesis were: (1) the development of a visualisation technique to yield high spatial and temporal resolution images of liquid-liquid flows, and; (2) to enhance understanding of the flows of two immiscible liquids through the application of the developed technique. Specifically, the work aimed to develop understanding of the behaviour of: (i) liquid-liquid flow regimes; (ii) the vertical phase distribution; (iii) the in-situ phase fraction; (iv) the interface level; (v) the droplet size distribution; (vi) interface wave velocity, and; (vii) velocity profiles.

1.3 Research Overview

This thesis presents what is believed to be the first application of high-speed planar laser-induced fluorescence (PLIF) and particle tracking and image velocimetry (PTV/PIV) for the detailed spatiotemporally resolved measurement and characterisation of horizontal liquid-liquid flows. The primary undertakings of this work were focused on: (1) the development of the experimental facility; (2) developing the optical system for the laser-induced fluorescence measurements, and; (3) the PLIF and PTV/PIV image processing methodology (for the latter, existing correlation algorithms were employed).

The liquid-liquid flow experimental rig used was based on an existing facility (TOWER) but it was necessary to carry out extensive refurbishment of the facility in order to acquire accurate and control and measurement of the independent variables of the rig. An important development here was the introduction of electronic measurement systems whose output could be logged with time. Development of the laser-induced fluorescence technique was focused on three areas: (1) test fluid selection, based upon establishing a pair of refractive index matched liquids of suitable physical properties with one test fluid seeded with a fluorescent dyestuff, the peak in the excitation spectrum of which is over the same wavelength band as the laser output spectrum peak; (2) the optical system, i.e., the laser (and associated optics) and the high speed camera (including the necessary filters) and their synchronisation, and; (3) the design of the optical visualisation sections and a graticule (printed grid) technique to correct for the distortion to the PLIF and PTV/PIV images. Finally and although multifaceted, the image processing techniques developed can be divided into two main categories: (1) a computational code written to binarise the PLIF images, from which, several forms of analysis have been performed, and: (2) a technique that combines both PIV and PTV to calculate the velocity profile of the flow.

In total three experimental campaigns were undertaken, which collectively comprise of 144 independent experimental runs using the high spatiotemporal resolution optical measurement technique.

1.4 Thesis Structure

In what follows in this thesis, Chapter 2, provides an overview of the liquid – liquid flow research that has been conducted by previous investigators. Specifically, attention is given to literature pertaining to: (1) flow phenomenology and regime maps; (2) the phase inversion phenomena, and; (3) the emulsion viscosity of liquid – liquid systems. Chapter 3 provides

details of the experimental facility and methods that have been used, to firstly, acquire images of flows containing two immiscible liquids using the LIF technique, and secondly, to process these images to generate quantitative results. Chapter 3 begins by providing details of the Two-Phase Oil–Water Experimental Rig (TOWER); TOWER is a multiphase flow facility at Imperial College London, designed for the investigation of liquid-liquid flows. Considerable improvement and development of this facility was necessary to carry out the work described here. Chapter 3 continues by presenting information pertaining to the pulsed laser system, the, high-speed camera system and the methods used to synchronise these two systems. Synchronisation of the laser produced pulses with camera exposures allowed capturing of successive laser-induced fluorescence images. Chapter 3 also provides details on the test fluids, including their physical properties and the basis for their selection, i.e., refractive index matching. Information is also provided on the design of the two visualisation cells (one with a square cross-section, the other with a circular cross-section) that that have been used in the PLIF experimental campaigns. It is necessary to correct the distortion to the PLIF and PTV/PIV images which occurs when the circular cross-section visualisation cell is used and details of the graticule correction methodology are presented (together with the image binarisation technique and the methods used to generate results) are also provided in Chapter 3.

The results of the experimental campaigns are presented in Chapters 4, 5 and 6. Chapter 4 presents LIF results acquired using a square cross-section visualisation cell placed in a square cross section horizontal duct; the use of this duct geometry avoided the image distortion which occurs with circular channel geometry. Though the results obtained using the square section duct were very interesting, it is clear that a duct of circular cross-section would be more representative of industrial pipe systems. In order to obtain results with circular cross section ducts, a method employing photography of a graticule within the duct was developed. Knowing the positions of locations on the graticule, it was possible to correct the images obtained for the circular tube cross section. In the studies on circular tubes, the experiments were extended to

include velocity measurements using PTV/PIV (Particle Tracking Velocimetry / Particle Image Velocimetry). Chapters 5 presents the results of the PLIF and PTV/PIV study performed when using the circular cross-section visualisation cell; in this study, the (heavier) aqueous phase was injected *below* the lighter (oil) phase at the test section entrance (i.e. in its natural location). Chapter 6 presents the results of a second PLIF and PTV/PIV study performed using the circular cross-section visualisation section. In this second study, the fluids were introduced to the test section such that the denser fluid is *above* the lighter fluid at the inlet. This was done to investigate the influence that entrance effects have on liquid-liquid flows.

Each of the studies presented in Chapters 4, 5 and 6 consist of two parts. Firstly, the observed flows are described qualitatively and classified into flow regimes and a flow regime map is presented. Secondly, the quantitative measurements are presented; for all the studies, these measurements included phase distribution, in-situ phase fraction, interface level and droplet size distribution. For the circular tube experiments (Chapters 5 and 6) interface wave velocity and velocity profile measurements were also made and are reported.

Finally, the conclusions of the investigations and recommendations for future work are summarised in Chapter 7.

CHAPTER 2

Literature Review

2.1 Introduction

This Chapter reviews the research and significant developments in the study of liquid-liquid flows in horizontal pipelines. Section 2.2 reviews the flow regimes (i.e., the geometric configuration of the flowing fluids) in liquid-liquid flows and the associated regime maps. An important transition in dispersed liquid-liquid flows is *phase inversion* in which the continuous phase changes from one fluid to the other and the literature in this transition is reviewed in Section 2.3. Though a considerable proportion of the research into the phase inversion phenomenon has been focused on agitated vessels, the work presented herein is exclusively that pertaining to pipe flows. A key parameter needed for the closure of phase inversion predictions is the emulsion viscosity; an overview of liquid-liquid emulsion viscosity correlations and models is presented in Section 2.4.

2.2 Flow Regimes and Maps

One of the first studies into two-phase liquid-liquid flows was conducted by Russell et al. (1959) who investigated flow patterns of oil-water flows in a smooth transparent 8.0 m long horizontal pipe of 25.4 mm internal diameter. Russell *et al*. (1959) investigated the effects of superficial water velocity (U_{w}) and the ratio of inlet oil and water velocities ($U_{\mathrm{o}}/U_{\mathrm{w}}$) on the

flow pattern and the nature of the liquid-liquid interface (see Figure 2-1). Thirteen different U_{w} values (ranging from 0.116 ft/sec to 3.55 ft/sec) were used with oil-water inlet velocity ratios ($\mathrm{U_o/U_w}$) ranging from 0.1 to 10. The oil used in the research had a viscosity of 18 $\mathrm{mPa.s}$ and a density of 834 $\mathrm{kg.m^{-3}}$. Russell et al. (1959) observed three main flow patterns which are categorised as:

1. Stratified flow – oil and water travel along the pipe in two separate layers.

2. Mixed flow – oil and water phases are completely mixed; this occurred at high flow rates.

3. Bubble flow – oil drops (called "bubbles" in this investigation) travel along the top of the pipe.

The flow was found to be *stratified* (1 from the above list) for low flowrates. For stratified flow, the experimental results of Russell et al. (1959) conform to the findings of a theoretical analysis which shows that for laminar flow the hold-up (i.e., interface level) was independent of the superficial water velocity and is only a function of viscosity and the phase input ratio. Phase break-up and droplet formation were observed at higher flowrates i.e., this regime was termed *mixed flow* (pattern 2 from the above list). The third flow regime, "bubble flow" occurred at the lowest oil-water velocity ratios investigated, typically $U_{\mathrm{o}}/U_{\mathrm{w}} = 1.4$ to 1.5. In summary, the Russell et al. (1959) observations reveal that increasing the mixture flowrate leads to an increase in the turbulence in the flow resulting in fingering and ligament formation that in turn results in droplet formation and ultimately a droplet layer i.e., *mixed flow*.

Charles et al. (1961) investigated flow patterns in horizontal two-phase oil-water flows in a 8.78 m long pipe with a 25.4 mm internal diameter using oil phases of three different viscosities, namely: $\mu_{\mathrm{oil}} = 6.29$, 16.8 and 65.0 $\mathrm{mPa.s}$. The densities of the oil phases were adjusted to values close to that of the water ($\rho_{\mathrm{oil}} \approx 988\ \mathrm{kg.m^{-3}}$) by the addition of carbon

tetrachloride (Liu, 2004). Experimental runs were performed for a decreasing oil phase flowrate at a constant water flowrate for each of the three oil phases. The range of oil phase-water velocity ratio and the ranges of superficial velocity for each of the test liquids were similar to those studies by Russell et al. (1959). Charles et al. (1961) observed the following flow patterns as the input oil phase-water ratio was decreased;

1. concentric oil-in-water
2. oil-slugs-in-water
3. oil-bubbles-in-water
4. oil-drops-in-water

Here, a distinction was made between "drops" and "bubbles" of the oil phase in that the "bubbles" were much larger that the "drops". The results obtained by Charles et al. (1961) are shown in Figure 2-2 and are somewhat similar to the observations by Russell et al. (1959), though Charles et al. (1961) did not observe stratified flow. Though (in terms of superficial mixture velocity and flowrate ratios) Charles et al. (1961) did operate in the regime in which Russell et al. (1959) observed stratified flow, it has to be recalled that the phase densities were made nearly equal in the Charles et al. (1961) study. The degree of stratification of two immiscible liquids when flowing in a pipeline will depend on the density ratio (R) between the oil and water phases. In the Charles et al. (1961) study, $R \approx 0.99$ and stratified flows were not observed. On the other hand, Russell et al. (1959) used phases for which $R \approx 0.83$ and the density difference was sufficient to promote stratified flow. The corresponding flow pattern terminologies adopted by Russell et al. (1959) and Charles et al. (1961) are tabulated in Table 2-1.

Charles et al. (1961) concluded the oil-water flow pattern is "*largely independent*" of the oil viscosity. The flow patterns observed for the different viscosity oils are the same apart for the most viscous oil (65.0 mPa. s), which at high oil-water input ratios yielded different results, as seen by comparing Figures 2-2(a) and 2-2(b) with Figure 2-2(c). Charles et al. (1961) attributed the difference in behaviour to surface forces which may become significant enough for the higher viscosity fluids to affect the flow pattern. It was also postulated by Charles et al. (1961) that the more viscous oil wetted the pipe wall more than the other oils. From the findings presented pictorially in Figure 2.2, Charles et al (1961) constructed two flow regime maps, one for the lower viscosity oils ($\mu_{\text{oil}} = 6.29$ mPa. s and 16.8 mPa. s) and another for the higher viscosity oil ($\mu_{\text{oil}} = 65.0$ mPa. s). From this, Charles et al. (1961) identified the conditions under which an oil-continuous flow pattern inverts to a water-continuous flow pattern. This is represented by the line PQ in Figure 2-3(b). This phenomenon has subsequently been termed phase inversion and is discussed in Section 2.3.

Table 2-1: Corresponding flow classifications for Russell et al. (1959) and Charles et al. (1961)

Corresponding flow pattern terminologies	
Russell et al (1959) classification	**Charles et al (1961) classification**
Bubble flow	Oil-drops-in-water Oil-bubbles-in-water Oil-slugs-in-water
Mixed flow	Water-drops-in-oil
Stratified flow	Not observed
Not observed	Concentric oil-in-water

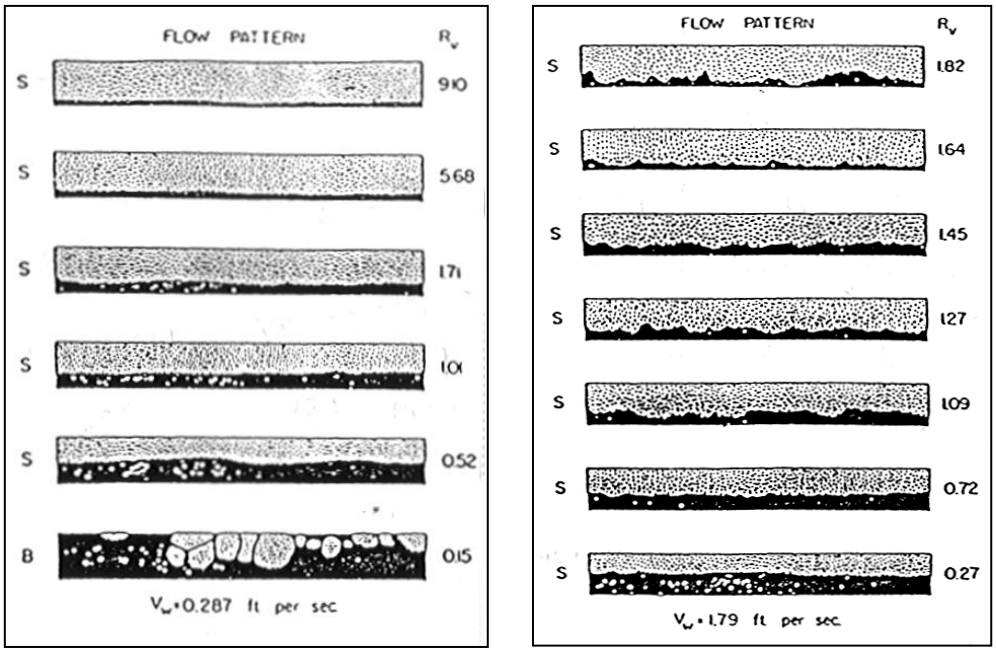

(a) (b)

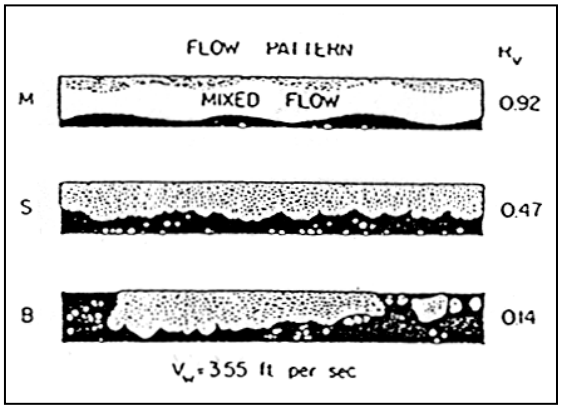

(c)

Figure 2-1: Flow patterns in oil-water pipe flow for superficial water velocities, U_{m} of: (a) 0.287 ft/sec; (b) 1.79 ft/sec, and; (c) 3.55 ft/sec at different inlet oil-water ratios, Rv (where, $Rv = U_{\mathrm{o}}/U_{\mathrm{w}}$), Russell et al. (1959)

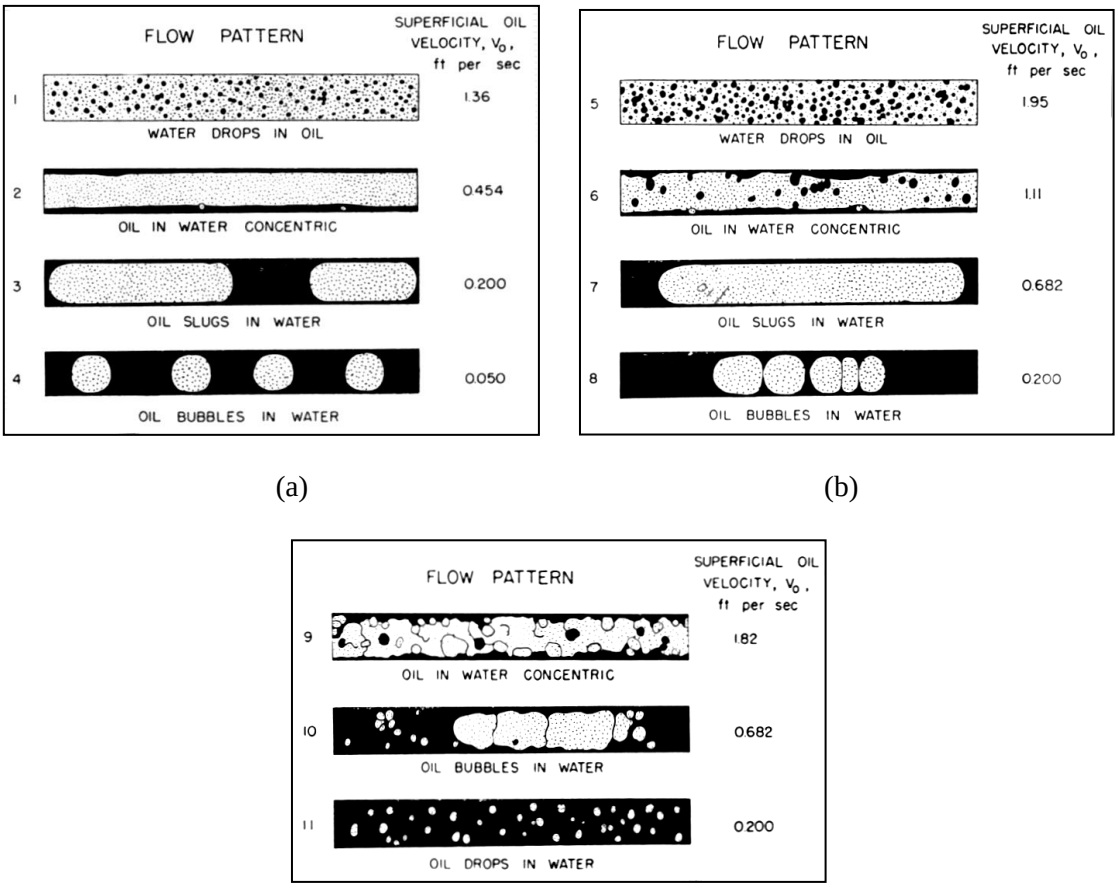

Figure 2-2: Flow patterns observed for the $\mu_{\text{oil}} = 16.8$ mPa.s oil flowing in the presence of water at water superficial velocities of U_{m} of: (a) 0.10 ft/sec; (b) 0.682 ft/sec, and; (c) 2.04 ft/sec, Charles et al. (1961)

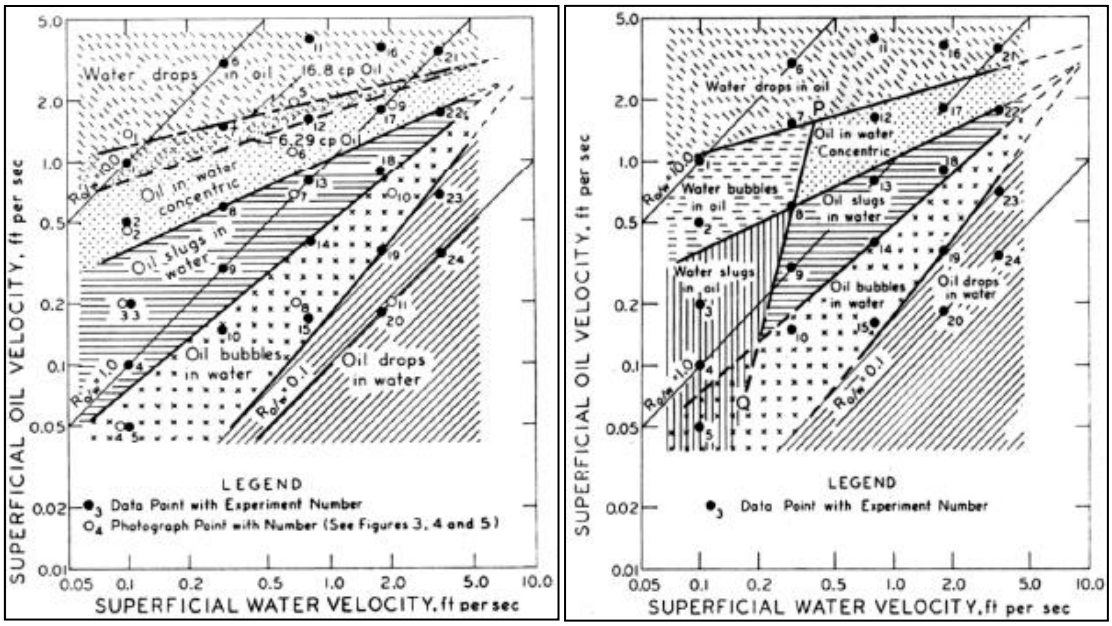

(a) (b)

Figure 2-3: Flow regime maps for two-phase oil-water flows for oil viscosities of (a) $\mu_{\text{oil}} = 6.29$ and 16.8 mPa. s (b) $\mu_{\text{oil}} = 65$ mPa. s (where, $\rho_{\text{oil}} = 988$ kg. m^{-3}), Charles et al. (1961)

An important regime in two-phase liquid-liquid flows is *core-annular flow* in which the less viscous (water) phase flows as a film at the tube wall with the more viscous phase (oil) flowing in the core of the pipe. Using high speed cine photography (at 1250 to 2300 fps, frames-per-second), Hasson et al. (1970) studied core-annular flow mechanisms of two immiscible liquids, the break-up mechanisms of core-annular flow and the resultant flow patterns. Flows of distilled water ($\mu_{\text{w}} = 0.82$ mPa. s) and an oil phase (a kerosene-perchlorethylene solution, with $\mu_{\text{oil}} = 1.0$ mPa. s) were studied in a 2.7 m long pipeline with an internal diameter of 12.6 mm. The two phases had equal densities of 1020 kg. m^{-3}. At lower flow rates, Hasson et al. (1970) identified four flow patterns which were similar to those observed by Russell et al. (1959) and Charles et al. (1961). These are listed below and are shown in Figure 2-4.

1. Dispersions – oil-in-water and water-in-oil dispersions; this corresponds to the flow regimes termed *water-drops-in-oil* and *oil-drops-in-water*
2. Slugs – water slugs in oil and oil slugs in water
3. Stratified layers
4. Annular flow

Hasson et al. (1970) found that the flow patterns that follow annular flow as the velocity is increased depend on three main factors:

1. The break-up mechanism of the annulus core
2. The liquid flow rates
3. The wetting properties of the pipe wall (as was observed by Charles et al., 1961)

Hasson et al. (1970) experimented with hydrophobic and hydrophilic pipelines and found that the different wetting properties of the wall can affect the break-up mechanism of the annular core and the flow pattern that it develops into. It was found that in hydrophobic pipes the flow pattern tends to be water-continuous and the wall film break-up mechanism did not occur. In contrast, in a hydrophilic pipeline both water-continuous and oil-continuous flow regimes were identified after annular flow break-up. Annular core break-up was found to be a high flowrate phenomenon, caused when the amplitude of interfacial waves reached the centre of the core, which give rise to slug flow. Conversely, wall film rupture is a low flowrate phenomenon. Hasson et al. (1970) constructed flow pattern maps of oil flowrate against water flowate for: (1) hydrophobic; (2) hydrophilic, and; (3) an intermediate pipeline at 200 cm from the pipe inlet. These flow regime maps can be seen in Figure 2-5 below.

The annular flow break-up mechanisms that Hasson et al. (1970) observed can be categorised into two groups: (1) wall film rupture, and; (2) annular core break-up due to interfacial waves.

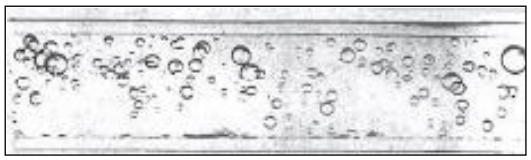

(a)

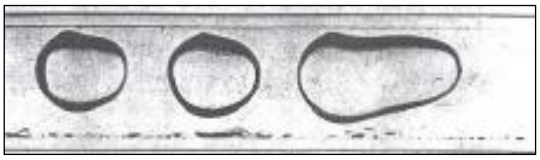

(b)

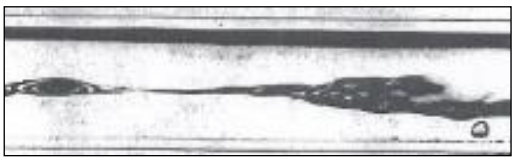

(c)

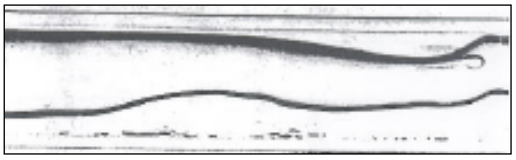

(d)

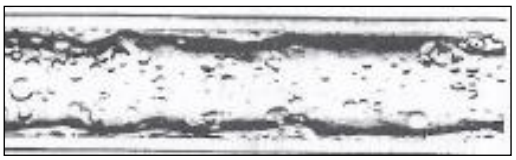

(e)

Figure 2-4: Flow patterns observed for equal density two-phase distilled water ($\mu_{\text{oil}} = 0.82$ mPa. s) and kerosene-perchloroethylene solution ($\mu_{\text{oil}} = 1.0$ mPa. s) flows: (a) dispersions; (b) slugs; (c) stratified layers; (d) annular flow, and; (e) mixed. Hasson et al. (1970)

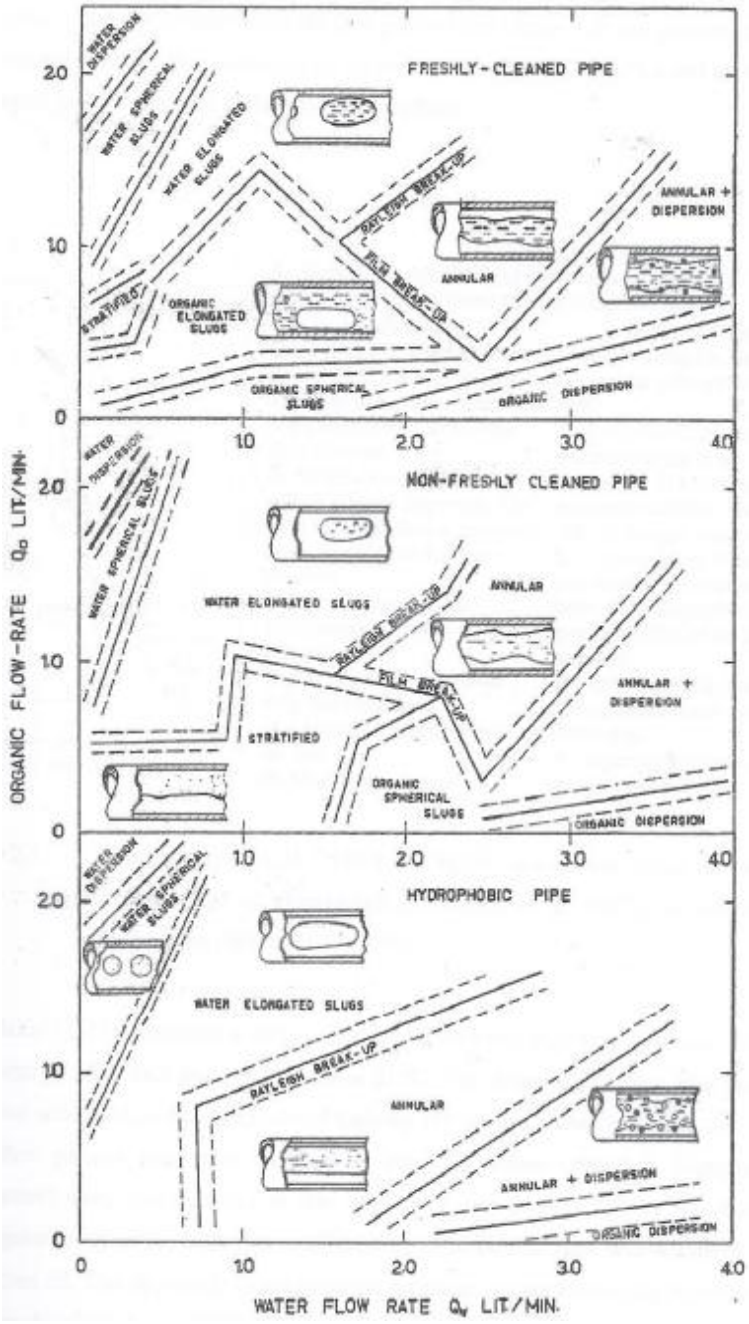

Figure 2-5: Flow patterns observed for a two-phase kerosene-perchlorethylene and distilled water system, Hasson et al. (1970)

Guzhov et al. (1973) investigated horizontal two-phase liquid-liquid flow patterns for oil and water system (where, $\mu_{\text{oil}} = 21.7$ mPa. s and $\rho_{\text{oil}} = 896$ kg. m^{-3} at 20°C) in a pipeline of 39.4 mm internal diameter. Guzhov et al. (1973) constructed a flow pattern map of their results,

plotting superficial mixture velocity U_{m} against input water fraction $\varphi_{\mathrm{in,w}}$; this is shown in Figure 2-6. The flow pattern classification terminology adopted by Guzhov et al. (1973) was similar to that used by Arirachakaran et al. (1989) (see Figure 2-7). However, unlike Arirachakaran et al. (1989), Guzhov et al. (1973) did not observe annular flow. Oglesby et al. (1979) produced a revised version of the Guzhov et al. (1973) flow pattern map for two-phase oil ($\mu_{\mathrm{oil}} = 21.7$ mPa.s, $\rho_{\mathrm{oil}} = 896$ kg.m^{-3}) and water flows in a 39.4 mm internal diameter pipeline.

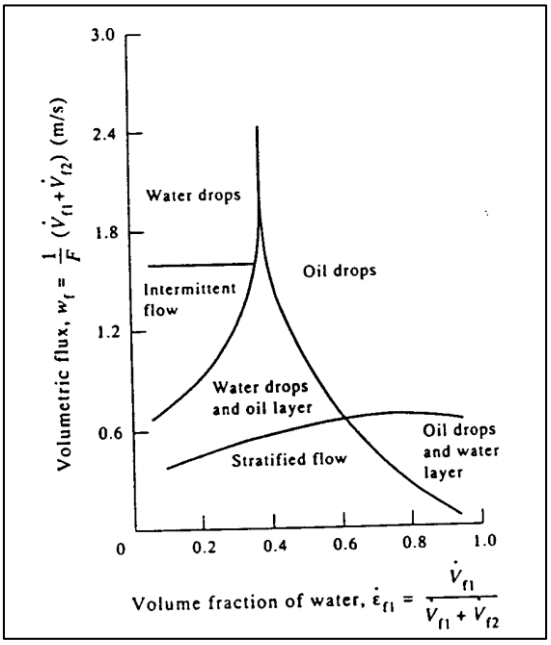

Figure 2-6: Flow pattern map for the flow of oil (where $\mu_{\mathrm{oil}} = 21.7$ mPa.s) and water in a 39.4 mm ID pipe (Guzhov et al., 1973)

Oglesby et al. (1979) also investigated the effect of viscosity on horizontal oil-water flow patterns using oils of viscosity $\mu_{\mathrm{oil}} = 58.0$, 84.0 and 115.0 mPa.s at 20°C. The observed flow patterns were generally similar to those observed by previous researchers and included stratified, dispersed and intermittent flow. However, in addition, Oglesby et al. (1979) observed annular flow with a water core and oil annulus. The observation of this flow regime seemingly

contradicts the *minimum viscous dissipation principle* adopted in the work of MacLean (1973) and Joseph et al. (1984), which has been described by Liu (2005) as:

'In a pipe flow of two liquids with different viscosities under an applied pressure drop, the low-viscosity liquid would tend to encapsulate the high viscosity liquid."

Liu (2005, p.38)

If it is postulated that the water core exhibits turbulent flow (which has a high turbulent viscosity) and the oil annulus flow is laminar, analysis of the apparent viscosities shows that the integrity of the principle still holds (Liu, 2005).

Oglesby et al. (1979) identified a phase inversion region (discussed in Section 2.3) which can be seen in their flow pattern map (Figure 2-7) as a narrow vertical band.

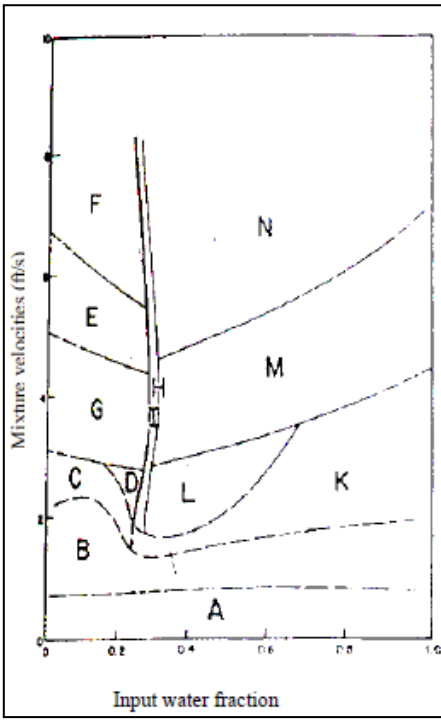

A- Segregated: (no mixing at the interface)
B- Semi-segregated: (some mixing at the interface)

Oil dominant	*Water dominant*
C- semi-mixed: layers of free oil and oil in water dispersion. The layer of the dispersion occupies less than 50% of the pipe diameter.	**I**- Slug: oil slugs in water
D- Mixed: layers of free oil and oil in water dispersion. The layer of the dispersion occupies more than 50% of the pipe diameter.	**J**- Annular: oil core and water film
E- Semi-dispersed: Non-homogeneous water in oil dispersion.	**K**- Semi-mixed: layers of free water and water in oil dispersion. The layer of the dispersion occupies less than 50% of the pipe diameter.
F- Dispersed: Homogeneous fully dispersed flow	**L** – Mixed: layers of free water and water in oil dispersion. The layer of the dispersion occupies more than 50% of the pipe diameter.
G – Annular: water core and oil film	**M**- semi-dispersed: Non-homogeneous water in oil dispersion.
H- Slug: Water slugs in oil.	**N**- dispersed: homogeneous fully dispersed flow.

Figure 2-7: Flow pattern map for two-phase oil-water flow in a 41mm internal diameter pipe, with oil viscosity $\mu_{\text{oil}} = 84.0$ mPa. s, Oglesby et al. (1979)

Arirachakaran et al. (1989) studied two-phase oil-water flow patterns (using four different oils of viscosities $\mu_{oil} = 4.7$, 58.0, 84.0 and 115.0 mPa.s) in horizontal pipelines of 25.4 and 38.1 mm internal diameter. Superficial mixture velocities and input water fraction were varied from $U_m = 0.45$ to 3.6 m.s^{-1} and $\varphi_{in,w} = 0.05$ to 0.90, respectively. However, unlike Hasson et al. (1970), Arirachakaran et al. (1989) did not observe water-annulus annular flow. This was explained by suggesting that the oils used in the study were not viscous and heavy enough to sustain an oil-core for this flow regime. Thus the flow patterns observed were predominantly water-continuous. It was concluded by Arirachakaran et al. (1989) that the range of conditions over which oil-annulus annular flow is observed diminishes as the oil viscosity is decreased. Oil-annulus annular was not observed for the 4.7 mPa.s (lowest viscosity) oil.

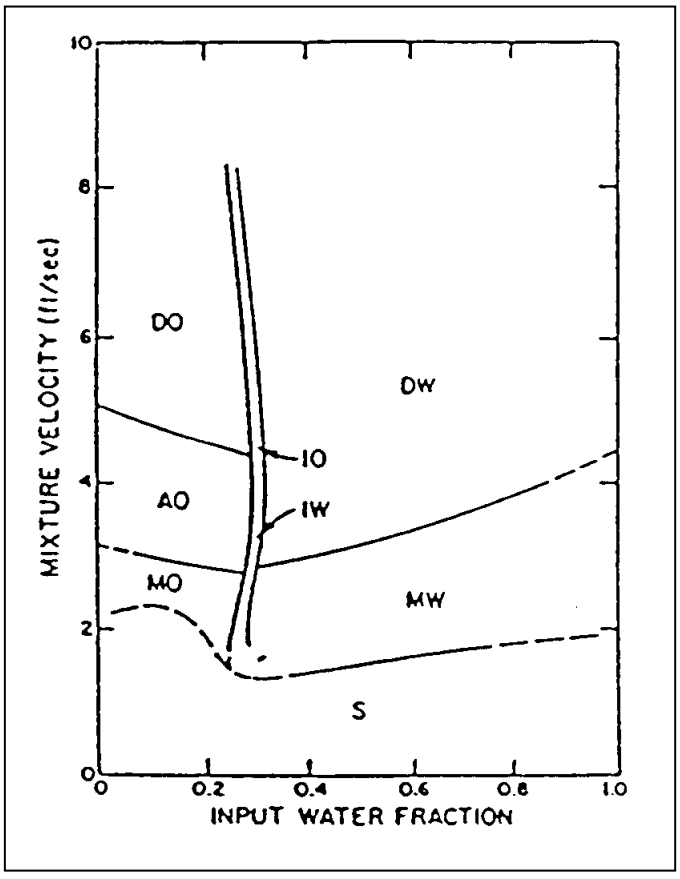

Figure 2-8: Flow pattern map, Arirachakaran et al. (1989)

Arirachakaran et al. (1989) found that when water is the continuous phase the oil viscosity has little effect on the flow pattern. This is in agreement with the observations made by Charles et al. (1961). Arirachakaran et al. (1989) revised the flow pattern map of Guzhov et al. (1973) using earlier flow pattern classifications and found good agreement with their own map. The definitions used in Figure 2-8 are as follows: Stratified flow (S); Mixture flow (MO, MW; Annular Flow (AO); Intermittent flow (IO, IW), and; Dispersed flow (DO, DW).

Nädler & Mewes (1995) used conductivity probes to investigate two-phase oil-water flow patterns in a horizontal Perspex pipeline with a 59 mm internal diameter. In this work, $\mu_{\text{oil}} = 20$ mPa. s and $\rho_{\text{oil}} = 841$ kg. m^{-3}. Nädler & Mewes (1995) observed 7 flow patterns and constructed flow regime maps of their findings; these are shown in Figures 2-9 and 2-10, respectively. It should be noted that they did not observe annular flow. Nädler & Mewes (1995) identified regions between oil and water continuous dispersed flow (regions II and V respectively in Figure 2-10) where oil and water occurred in continuous layers simultaneously, regions IIIa and IIIb in Figure 2-10.

One key development they made was to distinguish between dispersions and emulsions. Nadler and Mewes (1995) identified a flow as an emulsion when one phase is uniformly dispersed in nearly equal sized droplets in the other, continuous, phase. Conversely, they identified a flow as a dispersion when:

"Layers of one continuous phase in which the other phase is nonuniformly dispersed."

Nädler & Mewes (1995)

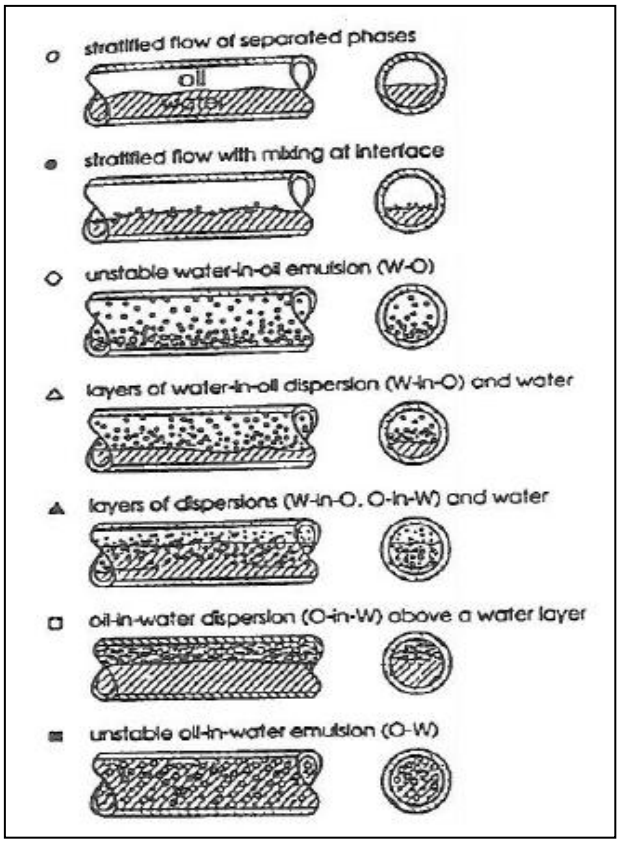

Figure 2-9: Two phase flow patterns observed by Nädler & Mewes (1995).

Trallero (1995) reclassified two-phase oil-water flow patterns into three categories. These are listed below and illustrated in Figure 2-11.

- Segregated flow: -
    a. Stratified flow (ST)
    b. Stratified flow with mixing at the interface (ST&MI)

- Dispersed flow: - Water dominated: -
    a. Dispersion of oil in water and water (Do/w&w)
    b. Oil in water dispersions (o/w)

  Oil dominated: -
    a. Dispersions of water in oil and oil in water (Dw/o&Do/w)
    b. Water in oil dispersion (w/o)

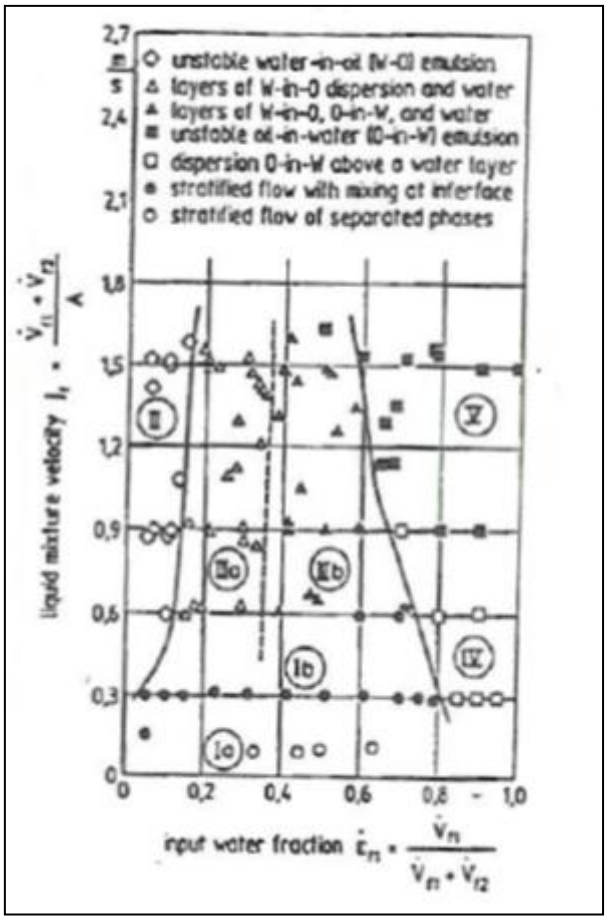

Figure 2-10: Oil-water flow regime map for a horizontal pipeline of 59mm ID as identified by Nädler & Mewes (1995)

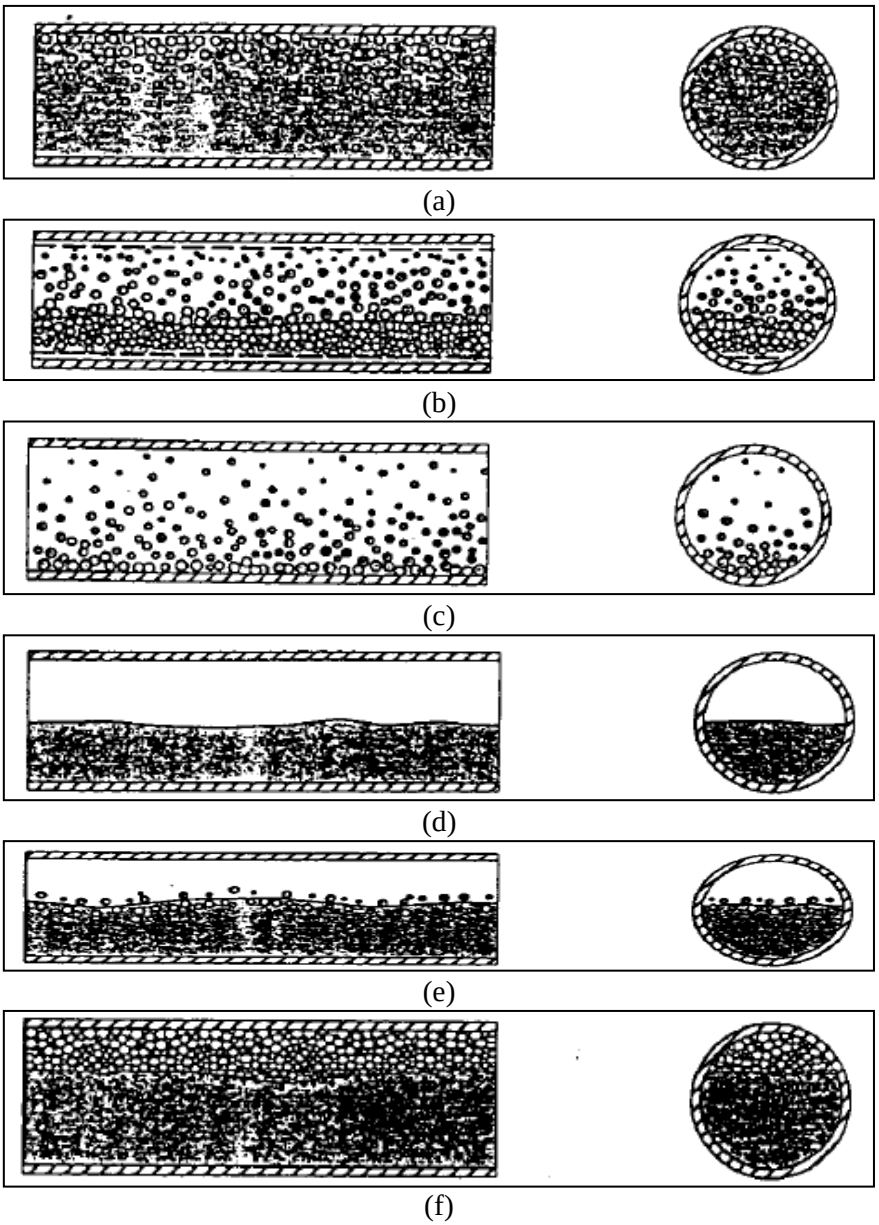

Figure 2-11: Two-phase oil-water flow pattern classifications: (a) oil in water emulsion (o/w); (b) dispersion of water in oil and oil in water (Dw/o & Do/w); (c) water in oil emulsion (w/o); (d) stratified flow (ST); (e) stratified flow with mixing at the interface (ST & MI), and; (f) dispersion of oil in water and water (Do/w & w), Trallero (1995)

Angeli (1996) and Angeli & Hewitt (2000a) investigated two-phase oil-water co-current flows (where, $\mu_{\text{oil}} = 1.6$ mPa. s and $\rho_{\text{oil}} = 801$ kg. m^{-3}) using the TOWER (Two-Phase Oil-Water Experimental Rig) facility at Imperial College London (which is detailed in Section 3.2)

focusing on droplet size distribution. Angeli (1996) used two test sections (where ID = 25.4 mm), one of stainless steel, the other of acrylic resin to investigate the effect of wall roughness and wetting properties on the flow pattern. To visualise the flow and in turn determine the flow pattern Angeli (1996) used high speed photography and high frequency impedance probes were used to establish the local phase fraction, $\langle\varphi\rangle_{y,t}$. To determine the continuous phase in dispersed flows a conductivity needle probe was used. Observations of flow patterns were made for mixture velocities, ranging from $U_{\mathrm{m}} = 0.2$ to 3.9 m.s^{-1} and for oil input volume fractions $\varphi_{\mathrm{in,w}} = 0.14$ to 0.96. The flow regime maps for the stainless steel and acrylic resin test sections constructed by Angeli & Hewitt (2000a) are shown in Figure 2-12(a) and 2.14(b) respectively. Comparing the maps for the respective test section materials it is seen that mixed flow patterns appear at lower mixture velocities in the stainless steel pipe than in the acrylic resin pipe, where oil remains the continuous phase for a wider range of operating conditions. Angeli (1996) found that the flow pattern was largely independent of the pipe roughness but the wetting properties of the pipe could affect the flow pattern when oil was the continuous phase. On comparison with the flow regime map by Arirachakaran et al. (1989) it is noted that Arirachakaran et al. (1989) did not observe three-layer flow.

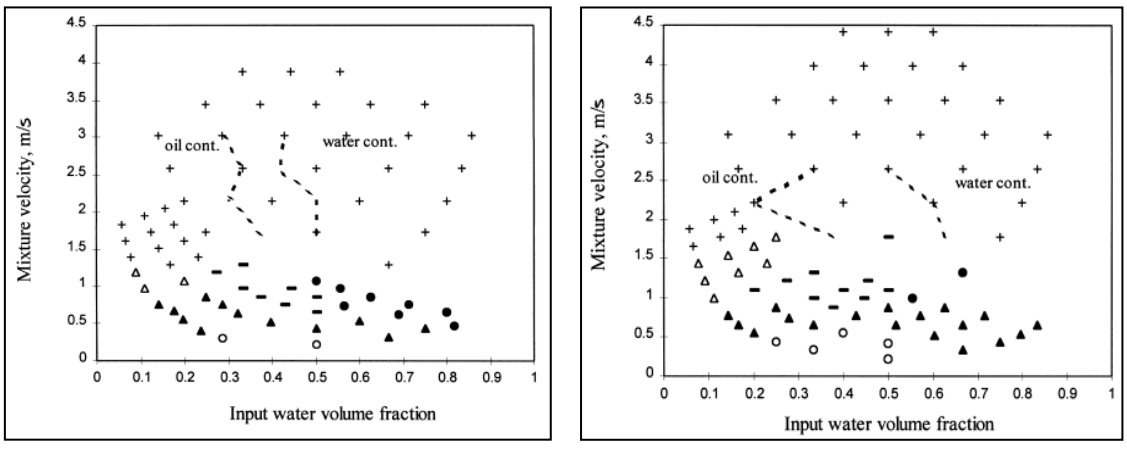

(a) (b)

Figure 2-12: Flow patterns by Angeli & Hewitt (2000a) in the (a) stainless steel test section, (b) acrylic resin test section. ○, stratified wavy (SW); ▬, three layers (3L); Δ, stratified mixed/oil

(SM/oil); - - - , phase continuity boundaries; ▲, stratified wavy/drops (SWD); ●, stratified mixed/water (SM/water); +, mixed (M)

Nadler & Mewes (1997) continued their multiphase flow research by investigating the effects of emulsification and phase inversion on pressure drop for different flow regimes of oil-water mixtures, in a 48m long horizontal test section with a 59mm internal diameter. The study was performed using oil viscosities of $\mu_{\text{oil}} = 22$, 27 and 35 mPa.s; the different viscosities were achieved by changing the liquid temperature. Nadler & Mewes (1997) constructed a flow regime map from their results which is presented in Figure 2-13 and observed phase inversion occurring within the dispersion layer. In Figure 2-13 this is represented by the boundary line between regions IIIa (water-in-oil dispersion above a water layer) and IIIb (water-in-oil dispersion above an oil-in-water dispersion, above water).

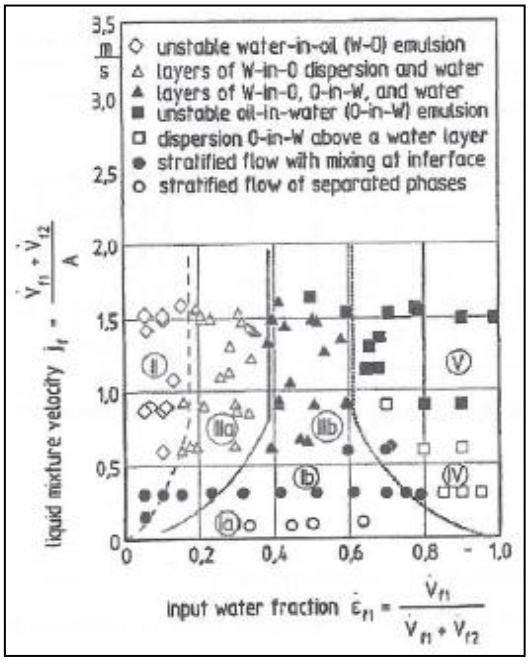

Figure 2-13: Flow regime map constructed by Nadler & Mewes (1997) for two-phase oil-water flow based on input water fraction.

Soleimani (1999) continued the research conducted by Angeli (1996) using the same experimental facility (TOWER) and fluids. A high speed camera and high frequency impedance probes were again used to visualise the flow and to establish the local phase fractions respectively. Soleimani (1999) studied the effects that helical static mixers immediately downstream of the inlet had on the two-phase flow patterns. The effect of cross-shaped and honeycomb flow straighteners [used to reduce swirl] placed downstream of the mixers was also investigated. Soleimani (1999) constructed a flow regime map (see Figure 2-14) based on observation made when an entrance mixer and/or straightener was not used. The results are in good agreement with the findings of previous researchers (Guzhov et al., 1973, Arirachakaran et al., 1989, Nadler & Mewes, 1995 and Angeli, 1996). When re-evaluating the $U_m = 1.25$ m.s^{-1} region in which Angeli (1996) observed 3-layer flow, Soleimani (1999) concluded that stratified flow of oil and water dispersions occur and no 3-layer flows were observed.

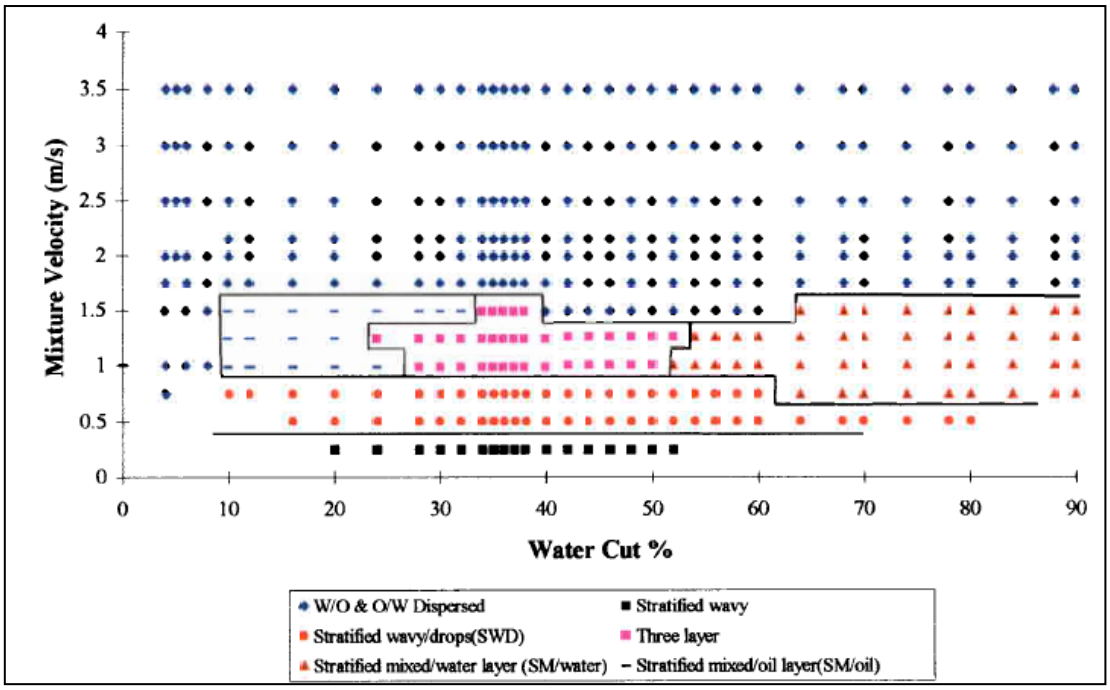

Figure 2-14: Flow pattern map for the stainless steel test section of the TOWER facility, Soleimani (1999)

Hussain (2004) extended the research by Angeli (1996) and Soleimani (1999) using the same experimental facility and fluids which have been detailed earlier in this section of this report. Hussain (2004) conducted two different experimental campaigns; a case with a 5-element Kenic™ element kinetic mixer placed immediately downstream of the tube inlet and another without a mixer at the inlet. Flow regime maps for each of these cases were constructed and are presented in Figures 2-15 and 2-16. The results obtained are consistent with findings of Angeli (1996) and Soleimani (1999). There is a noticeable difference between the flow patterns Hussain (2004) observed with and without a mixer present. Without a mixer present Hussain observed 6 flow regimes:

1. Stratified wavy [SW]
2. Stratified wavy / drops [SWD]
3. Stratified mixed / oil layer [SM/O layer]
4. Three-layer [3L]
5. Stratified mixer / water layer [SM/W layer]
6. Dispersed-flow [DF]

When the mixer was in used Hussain (2004) only observed 4 flow regimes;

1. Wavy-flow
2. Dispersed oil-in-water
3. Dispersed water-in-oil
4. Fully dispersed flow

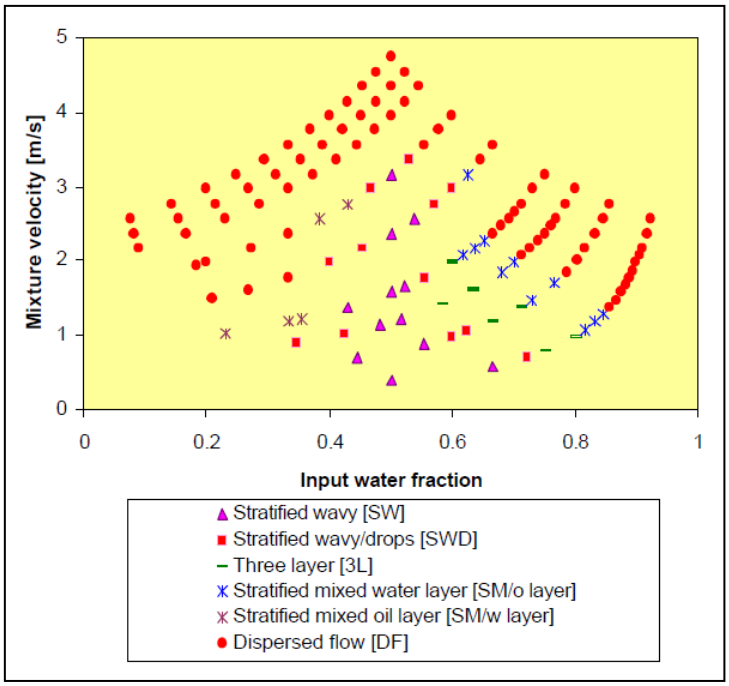

Figure 2-15: Flow patterns map without mixer at the tube inlet, Hussain (2004)

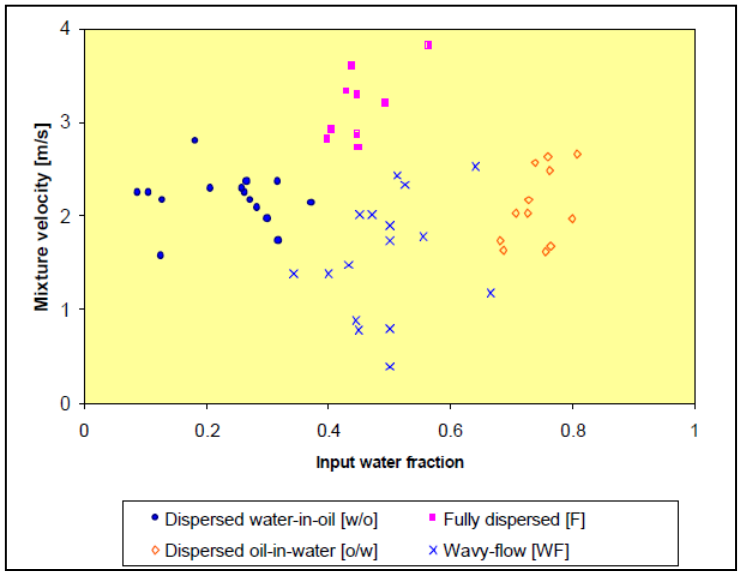

Figure 2-16: Flow patterns map with a 5-element Kenics™ mixer at the tube inlet, Hussain (2004)

Brauner (2001) proposed a unified approach for prediction the transition to dispersed flow patterns in liquid-liquid systems. She revised the Kolmogorov (1949) – Hinze (1955)

phenomenological model for droplet break-up in turbulent flow and proposed that energy considerations can be employed to help determine the maximal drop size in a dense dispersion. Brauner (2001) employed the Hughmark (1971) – Kubie & Gardner (1977) model for drop or bubble size larger than 0.1D due to the limitation imposed by the turbulence model used by Hinze (1955). The flow pattern transition predictions by Brauner (2001) are shown in Figure 2-17 and Figure 2-18 in comparison with the flow pattern data of Guzhov et al. (1973) and Trallero (1995) respectively, where good agreement is observed.

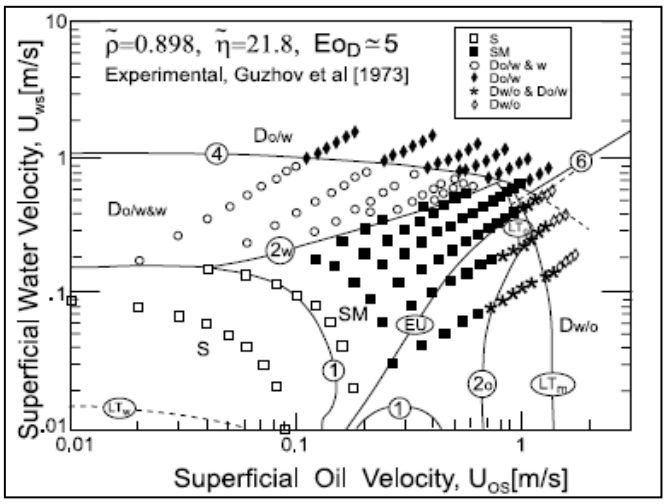

Figure 2-17: Flow pattern maps prediction for transitions to dispersed oil in water and transition to dispersed water in oil and comparison with experimental data of Guzhov et al (1973) in horizontal oil-water system, Brauner (2001)

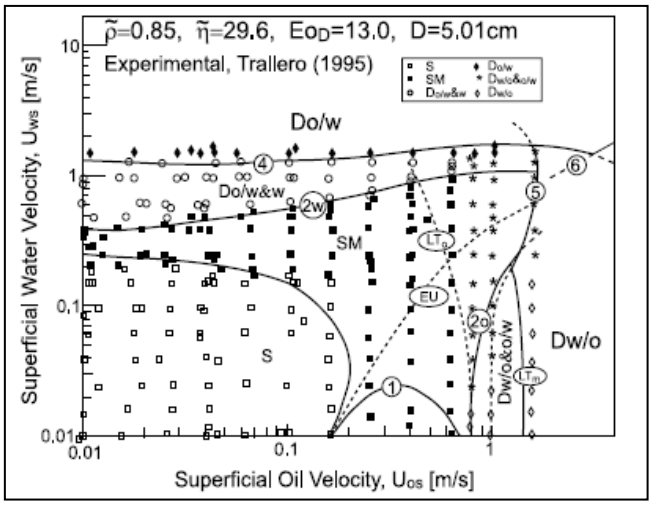

Figure 2-18: The Brauner (2001) predictions for transitions to Do/w (boundary 4) and transition to Dw/o (boundary 5) in a horizontal oil-water system (Trallero (1995))

Sotgia and Tartarini (2001) conducted experimental and theoretical two-phase oil-water flow research. They used an experimental rig with numerous horizontal ducts that range in diameter from 3 to 28mm and a range of oils to achieve viscosity ratios from $m = 10$ to 1300, and density ratios from 0.8 to 0.9. Sotgia and Tartarini (2001) observed 4 flow patterns for a 21 mm duct, which are in good agreement with previous research:

1) smooth-interface stratified flow
2) wavy-interface stratified flow – type 1
3) wavy-interface stratified flow – type 2
4) core-annular flow

Lovick (2003) investigated oil-water flows in the dual continuous flow regime using an experimental rig with a 38.8mm internal diameter stainless steel, test section, using an oil with a viscosity of $\mu_{\text{oil}} = 6$ mPa. s and a density of $\rho_{\text{oil}} = 828$ kg. m^{-3}. A mixture velocity range of $U_{\text{m}} = 0.8$ to 3 m.s^{-1} and an oil input volume fraction range of 0.1 to 0.9 were used. Lovick (2003) observed 3 flow patterns, namely:

1) stratified wavy – at low lower velocities
2) dual continuous flow – up to a mixture velocity of 1.5 $m.s^{-1}$
3) dispersed flow – at higher mixture velocities

Experimental research into *dual continuous* flow patterns in oil-water flows was continued by Lovick & Angeli (2004), who classified a regime as *dual continuous* flow when both phases retain their continuity at the top and bottom of the pipe while each phase is dispersed, at various degrees, into the continuum of the other. The dual *continuous flow* regime is illustrated in Figure 2-19.

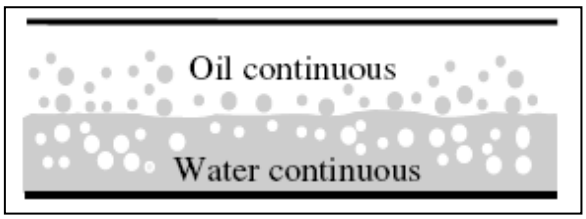

Figure 2-19: Schematic diagram of dual continuous flow, Lock & Angeli (2004)

Using the same fluids, ranges of conditions and equipment as Lovick (2003) they identified the dual continuous flow pattern boundaries. Lovick & Angeli (2004) constructed a flow regime map of mixture velocity against oil input volume fraction (see Figure 2-20) and established the onset of dual continuous flow occurs at a mixture velocity of $U_m = 0.8$ $m.s^{-1}$ and occurs at intermediate mixture velocities between stratified and dispersed flow patterns for a range of oil input volume fractions.

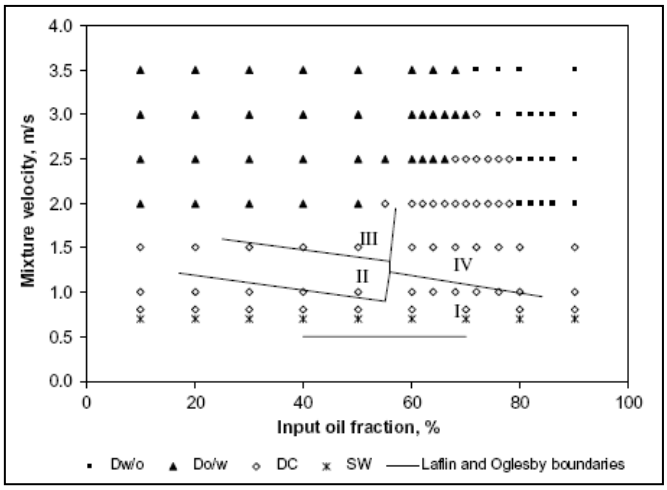

Figure 2-20: Flow pattern map (Lovick & Angeli (2004)) with the results from Laflin & Oglesby (1976) (solid lines. (I) dual continuous flow; (II) dispersion of oil in water and water; (III) dispersion of oil in water; (IV) dispersion of water in oil

As has be seen from the above discussion, a wide variety of flow patterns have been observed in liquid-liquid flows. The flow pattern depends not only on the flow rates and physical properties of the phases but also on the wetting properties of the flow channel. The roles of interfacial tension and wetting angle have not so far been systematically investigated. The use of Laser Induced Fluorescence (LIF) in the present work has allowed much more objective observations of flow structure but it is clear that a much wider range of conditions remains to be investigated in the future.

2.3 Phase Inversion

Phase inversion is a phenomenon that occurs in dispersions of two immiscible liquids and is defined as a transition in which one of the phases changes from being the dispersed (discontinuous) phase to being the continuous phase, for example the transition from an oil-in-water dispersion to a water-in-oil dispersion.

Sound understanding and prediction of this phenomenon is imperative due to the significant effect it has on properties such as viscosity, pressure drop, heat transfer and phase distribution, especially near the pipe wall (Lang and Auracher, 1996). Phase inversion is an important consideration in the process industries where fluid transport and heating or cooling are required. Most phase inversion literature relates to liquid-liquid dispersions in agitated vessels. However, the will be on phase inversion in two-phase liquid-liquid channel flows.

Central to developing a comprehensive understanding of the phase inversion phenomenon are the concepts of inversion point and the ambivalent range (range of ambivalence). The inversion point is defined as the critical phase composition (volume per cent of the dispersed phase) at which phase inversion occurs (Yeh et al., 1964). Associated with the inversion point is a hysteresis effect which is manifested by a range of conditions (volume fractions) over which either of the two immiscible liquid components can be the dispersed phase (Figure 2-21); this is called the ambivalent range (Yeo et al., 2002).

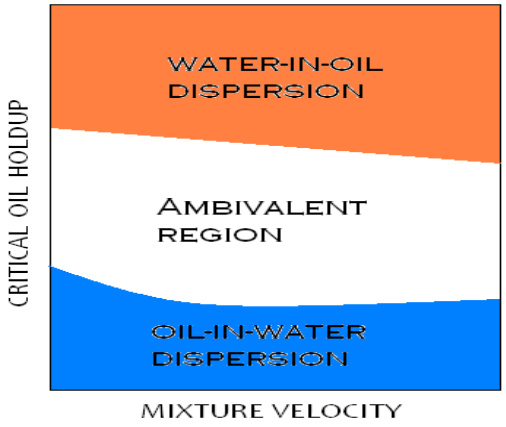

Figure 2-21: Graphical representation of the ambivalent range, Yeo et al. (2002)

From Figure 2-21 it can be seen that the critical dispersed phase holdups for inversion from oil-in-water dispersions to water-in-oil dispersions are much higher than for the reverse inversion.

Yeh et al. (1964) developed an equation to predict the phase inversion point of two immiscible liquids based upon the viscosities of the two components:

$$\frac{\varphi_{\mathrm{Disp}}}{1-\varphi_{\mathrm{Disp}}} = \left(\frac{\mu_{\mathrm{Disp}}}{\mu_{\mathrm{Cont}}}\right)^{1/2} \qquad 2.1$$

Where φ_{Disp} is the volume fraction of the dispersed phase at the inversion point, μ_{Disp} is the dynamic viscosity of the dispersed phase and μ_{Cont} is the dynamic viscosity of the continuous phase.

Yeh et al. (1964) found that phase inversion predictions from Equation 2.1 were poor for some experimental systems, including water–cyclohexanol, water–oleic acid, water–n-octyl alcohol and also for most of the ternary systems they investigated. Yeh et al. (1964) found agreement with experimental results was greatly improved when the bulk-phase viscosity (viscosity of the continuous phase, μ_{Cont}) is replaced with the interfacial viscosity (μ_{γ}). Thus equation 2.1 becomes;

$$\frac{\varphi_{\mathrm{Disp}}}{1-\varphi_{\mathrm{Disp}}} = \left(\frac{\mu_{\mathrm{Disp}}}{\mu_{\gamma}}\right)^{1/2} \qquad 2.2$$

Clayton (1935) calculated that the volume fraction of the dispersed phase could not exceed 74.02%. This maximum value represents the point as which uniform spheres touch each other and coalescence occurs (Yeh et al., 1964). This value represents the Ostwald Ratio for the maximum packing efficiency of a rhombohedral face centred cubic structure. The volume fraction of the dispersed phase can exceed this value because the dispersed phase is not limited to uniform spheres i.e., the dispersed phase drops need not be spherical or uniform in size.

Arashmid & Jeffreys (1980) established that the collision frequency and coalescence frequency of agitated dispersions can be combined to accurately predict the ambivalent range and the phase inversion concentration. They found that the volume percentage of the dispersed phase can range from 20% to 90% and the extent of the ambivalent range depends on how the dispersion was produced. A series of other factors have been identified that affect phase inversion including the physical properties of the liquids, the process conditions, wettability characteristics, the pipe materials and the associated geometry and orientation (McClarey & Mansoori, 1978). An alternative theory for the occurrence of phase inversion was presented by Efthimiadu and Moore (1993) who proposed that it is a form of instability with regard to the type of dispersion and it can occur whenever the equilibrium between coalescence and re-dispersion shifts towards coalescence.

Arirachakaran et al. (1989) investigated the phase inversion phenomenon in an oil-water system, researching the effects of input water fraction, oil viscosity, mixture viscosity and laminar flow regime on the process. Although they did not investigate the effects of droplet size, droplet size distribution and flow regime on phase inversion they did identify them as influential factors. Arirachakaran et al. (1989) presented a mechanism for the phase inversion process in an oil-water system, which is shown in Figure 2-22. Their mechanism shows there is a range of volume fractions over which either component can form the dispersed phase; the ambivalent range.

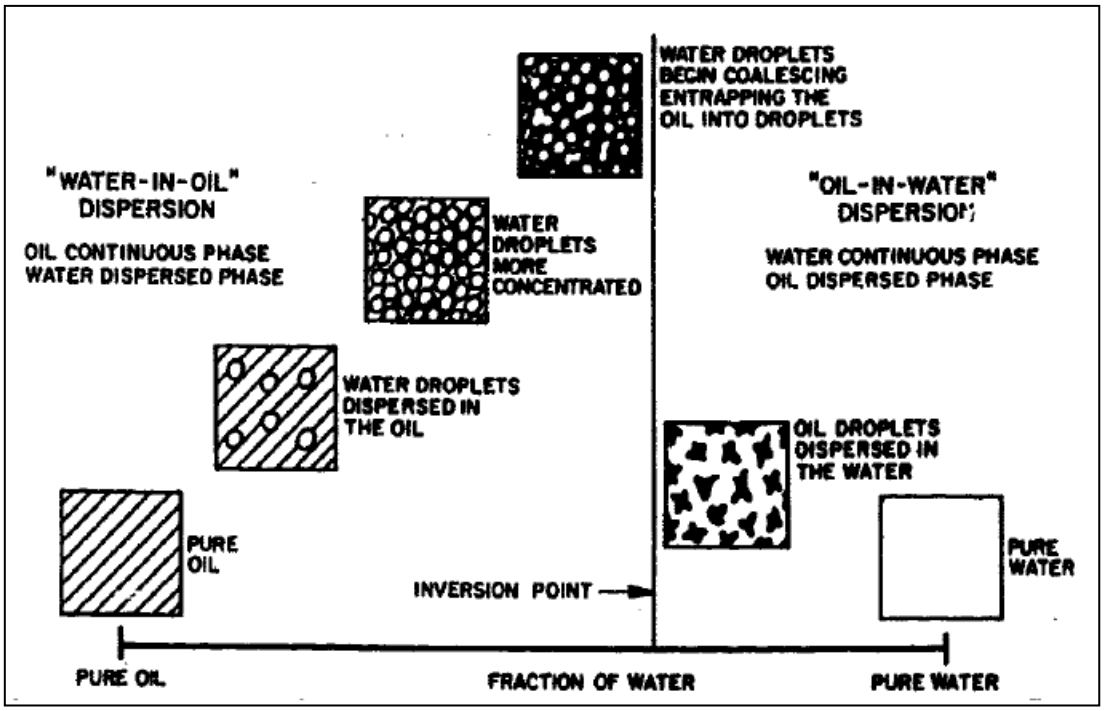

Figure 2-22: Phase inversion process for an oil-water dispersion system, Arirachakaran et al (1989)

Arirachakaran et al. (1989) combined their phase inversion data with those of other researchers (Guzhov et al., 1973; Russell et al., 1959; Charles et al., 1964 and Oglesby et al., 1969) and assumed that there exists a logarithmic relationship in the fully laminar oil phase region between oil viscosity and the input water fraction required to invert the system. Figure 2-23 shows the relationship that Arirachakaran et al. (1989) identified, with the correlation they developed shown below:

$$\varphi_{\mathrm{in,w}} = 0.500 - 0.1108 \log(10^3 \mu_{\mathrm{oil}}) \qquad 2.3$$

where $\varphi_{\mathrm{in,w}}$ is input water fraction required to invert the system and μ_{oil} is the oil viscosity. Brocks and Richmond (1994) reported a constant value of $\varphi_{\mathrm{in,w}} = 0.15$ for oil viscosities above $\mu_{\mathrm{oil}} = 0.2$ mPa. s. However, the experiments of Brocks and Richmond (1994) incorporated

some cases with surfactants and, in this case, the mechanism of phase inversion is found to be different from that in a system with pure liquids. (Xu et al., 2007).

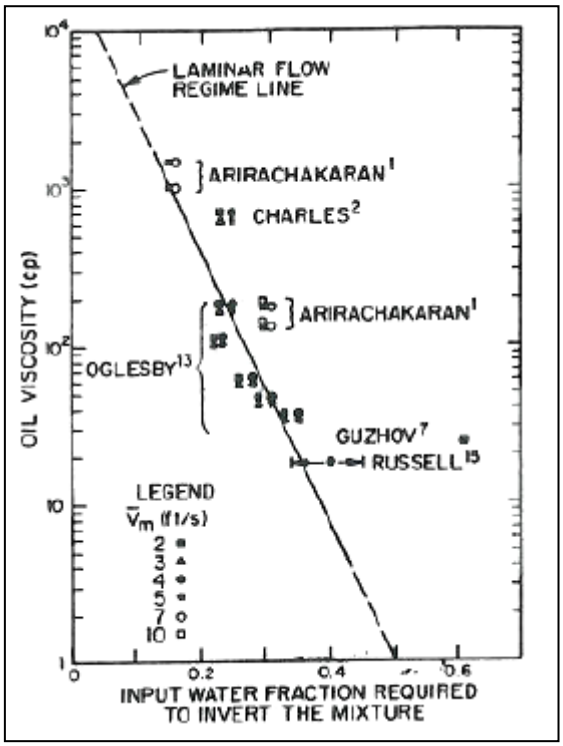

Figure 2-23: Phase inversion point correlation, Arirachakaran et al. (1989)

Since Arirachakaran et al. (1989) did not consider the effect of interfacial tension on phase inversion. They made an assumption that for an oil with a viscosity $\mu_{\text{oil}} = 1$ mPa. s, the system should invert at an input water fraction of 0.5, which is based on the concept that phase inversion occurs to reduce interfacial energy by reducing interfacial area, and as a result, phase inversion should occur at an input water fraction of 0.5. Selker & Sleicher (1965) however argued that the magnitude of the interfacial tension cannot affect phase inversion. Their reason being that if the converse were the case, it would infer interfacial tension between two liquids is a function of the curvature of the interface. Both of these proposals have been discounted by Luhning & Sawistowski (1971) and are not supported by experimental data. Yeh et al. (1964) and McClarey & Mansoori (1978) affirmed that, if no other forces are present, interfacial

tension would cause phase inversion to occur at 50%. However, other factors need to be taken into account. Yeo et al. (2002) presented a simple equation (based on the criterion of interfacial energy minimisation) to predict the limits of the ambivalence region:

$$\frac{\varphi_{o,i}}{1-\varphi_{o,i}} = \frac{d_{32_{o/w}}}{d_{32_{w/o}}} \qquad 2.4$$

where $\varphi_{o,i}$ is the holdup of the organic phase at phase inversion and d_{32} is the Sauter mean diameter which is defined as the diameter of a sphere that has the same volume to surface area ratio as the object of interest. The subscripts o/w and w/o denote oil-in-water and water-in-oil dispersions respectively. The predictions of this equation were in good agreement with experimental results obtained by Selker and Sleicher (1965).

The Yeo et al (2002) model does not, however, account for wetting effects which further accentuate the hysteresis effect (ambivalent range). The wetting effects (interfacial energy associated with the solid surface) only become significant when the surface area to volume ratio is large enough or when the drops are large which is the case with pipe flow but is not the case with agitated vessels hence its omission from the model in this case (Tidhar et al., 1986).

One of the key observations from the experimental work by Arirachakaran et al. (1989) is that the mixture viscosity exhibits a peak at the phase inversion point, shown in Figure 2-24; here, the viscosity is calculated from the pressure gradient which also shows a peak at the phase inversion location. Arirachakaran et al. (1989) conclude that the magnitude of this peak depends predominantly on the flow regime of the mixture when inversion takes place. Martinez et al. (1988) and Pal (1993) also observed that for an oil-water system the viscosity increases as water fraction is increased until it reaches a maximum at the phase inversion point, and then begins to drop. In earlier studies, Falco et al. (1974) also observed a peak in viscosity for a water-in-oil

emulsion at the inversion point. They attributed this peak to a change in the structure of the dispersed water phase from a lamellae structure to a continuous phase.

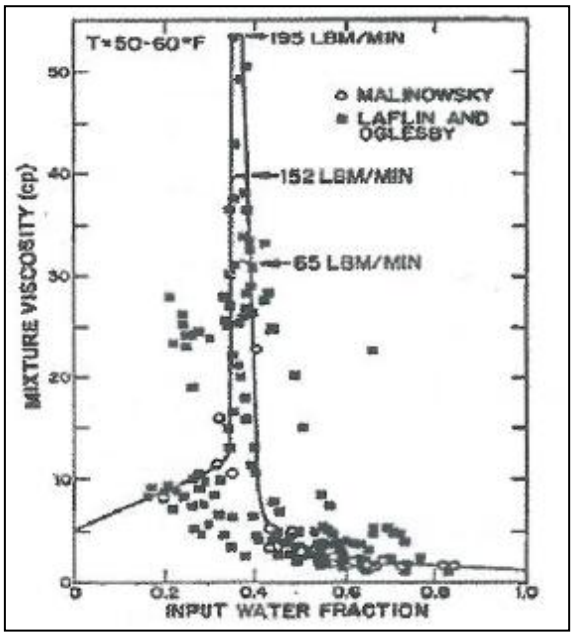

Figure 2-24: Mixture viscosity against input water fraction for low viscosity oil, Arirachakaran et al. (1989)

Oglesby (1979) observed a significant change in pressure drop at the phase inversion point. An increasing mixture velocity and oil viscosity increased the magnitude of the change in pressure drop. Oglesby (1979) also observed that the input water fraction at the phase inversion point decreased as the oil viscosity increased.

Soleimani (1999) observed a peak in pressure gradient between 34% and 37% input water volume percentage caused by phase inversion, as shown in Figure 2-25 below. Soleimani (1999) found that phase inversion occurs at lower water-cuts for higher mixture velocities. This can be explained by the fact that at higher mixture velocities the degree of mixing is higher and the two liquids are more homogeneously mixed.

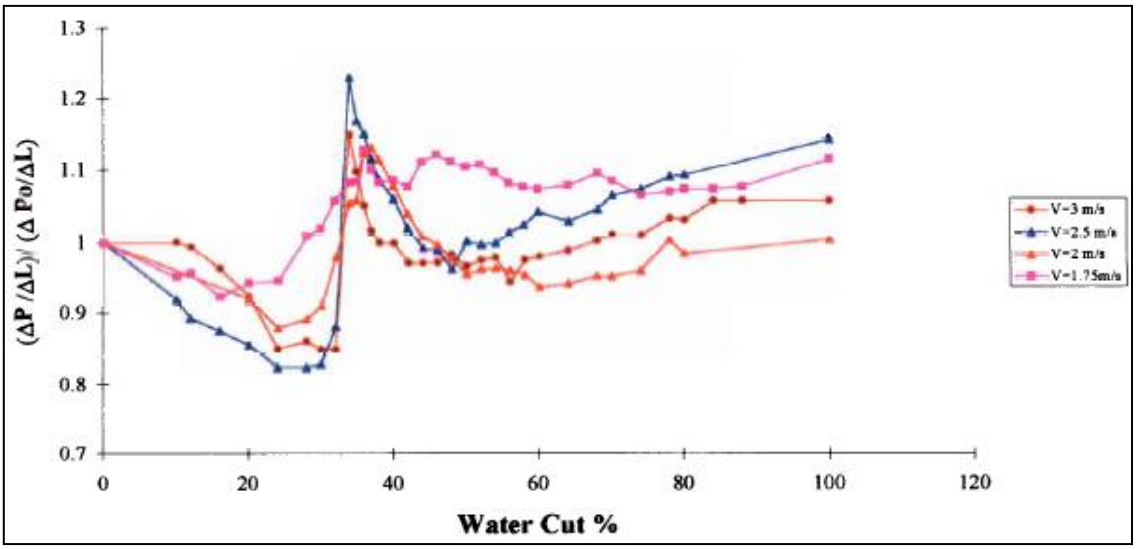

Figure 2-25: Pressure gradient in two-phase liquid-liquid flows, Soleimani (1999)

Nadler & Mewes (1995) observed two pressure gradient peaks for oil-water pipeline flow; this is shown in Figure 2-26. They associated the first peak to the transition from a water-in-oil dispersion to a region of stratified/dispersed flow and the second peak being the transition from that flow regime to an oil-in-water dispersion.

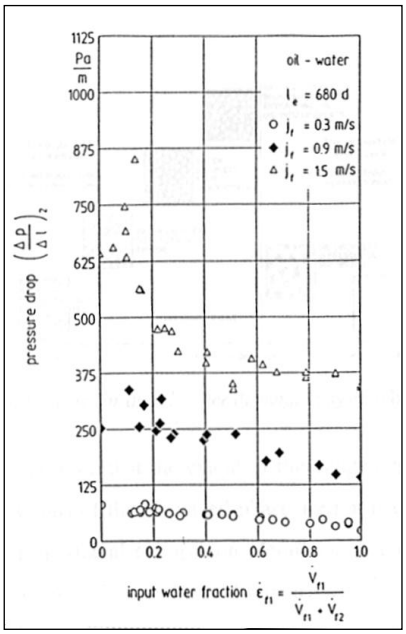

Figure 2-26: Pressure drop for oil-water flow (Nadler and Mewes, 1995)

Nadler and Mewes (1997) developed a simplified phase inversion model based upon the momentum equations for two-phase liquid-liquid stratified flow. They modelled phase inversion in terms of the critical water cut (φ_{C}) at which phase inversion occurs (Equation 2.5).

$$\varphi_{\mathrm{C}} = \frac{1}{1 + k\left[\frac{C'_{\mathrm{o}}}{C'_{\mathrm{w}}}\frac{\rho_{\mathrm{o}}^{(1-n_{\mathrm{o}})}}{\rho_{\mathrm{w}}^{(1-n_{\mathrm{w}})}}\frac{\mu_{\mathrm{o}}^{n_{\mathrm{o}}}}{\mu_{\mathrm{w}}^{n_{\mathrm{w}}}}\frac{1}{[dv_{\mathrm{m}}]^{(n_{\mathrm{o}}-n_{\mathrm{w}})}}\right]^{\frac{1}{k_2}}} \qquad 2.5$$

In Equation 2.5, ρ_{o} and ρ_{w} are the oil and water density respectively, μ_{o} and μ_{w} are the oil and water viscosity respectively, d and v_{m} are the pipe diameter and the total liquid velocity respectively and C'_{w}, C'_{o}, n_{o} and n_{w} are the parameters of the Blasius friction factor equation which is given as;

$$f = C'\mathrm{Re}^{-n} \qquad 2.6$$

where Re is the Reynolds number.

Nadler & Mewes (1995a) reported that for a well-mixed two-phase liquid-liquid flow where both layers are in the same flow regime – for example in slug flow, n_{o} is equivalent to n_{w}, inferring that the liquid velocity does not affect the critical water cut.

Decarre and Fabre (1997) proposed the following correlation to predict the dispersed phase concentration (φ_{Disp}) at the phase inversion point based on the dispersed and continuous phase properties:

$$\varphi_{\mathrm{Disp}} = \left[1 + \left(\frac{\mu_{\mathrm{Cont}}}{\mu_{\mathrm{Disp}}}\right)^{1/6}\left(\frac{\rho_{\mathrm{Cont}}}{\rho_{\mathrm{Disp}}}\right)^{5/6}\right]^{-1} \qquad 2.7$$

Chen (2001) proposed the following correlation to predict the critical water fraction based on the Arirachakaran et al. (1989) model.

$$\varphi_w = 0.3788 - 0.1108 \log_{10} \frac{\eta_o}{\eta_w} - 9.6533 \left(\frac{\rho_w - \rho_o}{\rho_w} \right) + 2.4841 \left(\frac{\rho_w - \rho_o}{\rho_w} \right) \qquad 2.8$$

Although Chen (2001) accounted for the oil-water density ratio the correlation did not take into account the mixture velocity (Xu et al., 2007). The scope of the Chen correlation is limited because it was developed with reference to a configuration of laminar flow in stratified layers.

Brauner and Ullmann (2002) developed a model for phase inversion based on the free energy of the dispersion; the dispersion (oil-in –water or water-in-oil, say) showing the minimum free energy was the stable one. This model is reviewed in detail by Xu et al. (2007). To develop a correlation for the critical water fraction, Brauner and Ullmann (2002) made the following assumptions:

1) The composition of the oil phase and water phase and the system temperature are invariant with phase inversion.
2) Wall-liquid wettability effects can be neglected.
3) The free energy of the oil phase and water phase remains the same.
4) Only the free energies of the interfaces have to be considered.

$$\varphi_w = \frac{\tilde{\rho}\,\tilde{\upsilon}^{0.4}}{1 + \tilde{\rho}\,\tilde{\upsilon}^{0.4}} \qquad 2.9$$

Where $\tilde{\rho} = \rho_o / \rho_w$ (density ratio) and $\tilde{\upsilon} = \upsilon_o / \upsilon_w$ (kinematic viscosity ratio). Xu et al. (2007) reported that the Brauner and Ullmann (2002) correlation performed well when compared with available data on the critical holdup for phase inversion. Although phase inversion in stirred

tanks is not the focus of this report the research conducted in this field is of interest. For example, the effect of an electric field on phase inversion in stirred tanks was investigated by Tsouris & Dong (2000). They observed that when a sudden voltage increase was imposed on the system the system would invert from a water-in-oil dispersion to an oil-in-water dispersion.

2.4 Emulsion Viscosity

It is evident from the work on phase inversion described in Section 2.3 that the viscosity of dispersions behaves in an anomalous manner near the phase inversion point. In this present Section, the literature on dispersion viscosity is reviewed. A number of simple approaches to calculating the viscosity of a liquid-liquid mixture have been discussed in the literature. One obvious approach is to use, to calculate mixture viscosity μ_{m}, a linear interpolation between the viscosities of the pure components:

$$\mu_{\mathrm{M}} = \varphi_{\mathrm{A}}.\mu_{\mathrm{A}} + (1 - \varphi_{\mathrm{A}}).\mu_{\mathrm{B}} \qquad 2.10$$

An alternative approach is to use reciprocal interpolation as suggested by Bingham (1916) as follows:

$$\mu_{\mathrm{M}} = \left[\frac{\varphi_{\mathrm{A}}}{\mu_{\mathrm{A}}} + \frac{(1 - \varphi_{\mathrm{A}})}{\mu_{\mathrm{B}}}\right]^{-1} \qquad 2.11$$

However, adopting linear or reciprocal interpolation is not appropriate since neither approach predicts a viscosity maximum as a function of volume fraction i.e., the fail to account for the phase inversion phenomena (discussed in Section 2.3).

The principle factors affecting the viscosity of an emulsion μ_E are: (i) the volume fraction of the dispersed phase φ_{Disp}, and; (ii) the temperature T . Farah et al (2005) listed nine other minor factors that influence the effective viscosity of a water-in-oil emulsion, these being the:

1. viscosity of the continuous phase, μ_{Cont}
2. viscosity of the dispersed phase, μ_{Disp}
3. shear rate, γ
4. average droplet size, μ_{Drop}
5. droplet size distribution
6. density of the continuous phase, ρ_{Cont}
7. density of the dispersed phase, ρ_{Disp}
8. nature and concentration of emulsifying agents
9. presence of solids

There are essentially two groupings of emulsion viscosity models (i) those at constant temperature, and; (ii) those that account for the influence of temperature changes on effective viscosity. Following an investigation in to the effect of temperature on the test fluids used in the experimental campaigns detailed in Chapters 4, 5 and 6 (i.e., Exxsol D80 and a water-glycerol-dyestuff solution) which is presented in Section 3.8, a thermocouple was inserted directly upstream of the test section inlet (see Figure 3.5) to monitor the temperature of the fluids. Many of the existing models define the relative emulsion viscosity μ_R as a ratio of the emulsion viscosity μ_E to that of the continuous phase μ_{Cont}:

$$\mu_R = \frac{\mu_E}{\mu_{Cont}} \qquad 2.12$$

Einstein (1906) developed a viscosity prediction model for infinitely dilute suspension systems in which the volume fraction of the dispersed phase φ_{Disp} is less than 2% in a solid-liquid dispersion. The model is limited to rigid spheres and owing to the diluteness of the suspension

there is no appreciable interaction between the dispersed spheres. The model proposed is as follows:

$$\mu_{\mathrm{R}} = 1 + k.C \qquad 2.13$$

where k is 2.5 and C is the volume fraction of the dispersed phase, or more precisely it is the volume of dispersed phase spheres in unit volume of suspension.

Numerous researchers have used the work by Einstein (1906) as a basis from which to develop models for concentrated emulsions, non-spherical and polydisperse liquid-liquid systems. Taylor (1932) presented a model for the relative emulsion viscosity μ_{R} that accounts for the influence of the dispersed phase viscosity μ_{Disp} as well the continuous phase viscosity μ_{Cont}. The model, which is valid for emulsions with a low concentration of dispersed spherical drops, is given as:

$$\mu_{\mathrm{R}} = 1 + 2.5\varphi_{\mathrm{Disp}}\left[\frac{K + 0.4}{K + 1}\right] \qquad 2.14$$

where K is the ratio of the dispersed phase viscosity μ_{Disp} to that of the continuous phase μ_{Cont}:

$$K = \frac{\mu_{\mathrm{Disp}}}{\mu_{\mathrm{Cont}}} \qquad 2.15$$

For dispersions of spherical solid particles K tends to infinity and Equation 2.14 reduced the Einstein viscosity model (Equation 2.13) i.e., the Taylor (1932) equation is a modified form of the Einstein (1906) viscosity model for emulsions where K is given as:

$$K = 2.5\left(\frac{\mu_{\text{Disp}} + 0.4\mu_{\text{Cont}}}{\mu_{\text{Disp}} + \mu_{\text{Cont}}}\right) \quad 2.16$$

Eiler (1943) presented a relative emulsion viscosity μ_R correlation for Newtonian systems using bitumen emulsions. This is given as:

$$\mu_{\text{R}} = \left[1 + \left(\frac{1.25\varphi_{\text{Disp}}}{1 - \alpha_E\varphi_{\text{Disp}}}\right)\right] \quad 2.17$$

where, $1.28 < \alpha_E < 1.30$.

Hatschek (1928) obtained the following relationship:

$$\mu_{\text{R}} = \frac{1}{1 - \sqrt[3]{\varphi_{\text{Disp}}}} \quad 2.18$$

Mooney (1950) extended Einstein's viscosity model to predict the relative emulsion viscosity μ_R of finite concentration monodisperse systems i.e., systems in which the dispersed particles having the same shape, size and mass. In order to do so the interaction between the dispersed spheres must be taken into account. Mooney (1950) described this interaction as a crowding effect. The equation is given as:

$$\mu_{\text{R}} = exp\left(\frac{2.5\varphi_{\text{disp}}}{1 - k.\varphi_{\text{disp}}}\right) \quad 2.19$$

where 2.5 was selected to give correspondence with the Einstein (1906) viscosity model for very dilute suspensions when the volume fraction approaches zero. The constant k is a self-crowding factor.

Mooney (1950) also presented a model com for polydisperse systems, those being systems wherein the dispersed phase particles have a broad range of size, shape and mass characteristics. These systems involve a variable factor, λ_{ij}, which measures the crowding of spheres of radius r_j by spheres of radius r_i. For a suspension comprised of n groups of spheres of different diameters Mooney (1950) presented the following equation:

$$\ln \mu_R = 2.5 \sum_{i=1}^{n} \frac{\varphi_i}{1 \sum_{i=1}^{n} \lambda_{ij} \varphi_j} \qquad 2.20$$

Based on a geometric argument, Mooney presented the following limits for the crowding factor: $1.35 < \lambda_{ij} < 1.91$. On comparison with data obtained by Vand (1950) 1.43 was presented as a suitable value for λ_{ij}.

Brinkman (1952) considered the impact to the relative emulsion viscosity μ_R of adding a single dispersed particle to a system already containing n dispersed particles. It was assumed that the relative emulsion viscosity μ_R would increase by the factor given by the Einstein (1906) viscosity equation. Brinkman (1952) derived the following expression for the relative emulsion viscosity μ_R:

$$\mu_R = \frac{1}{\left(1 - \varphi_{Disp}\right)^{2.5}} \qquad 2.21$$

Roscoe (1952) investigated the effect of the of the size distribution of the dispersed droplets on the relative emulsion viscosity μ_R and found that when the spherical droplets have a wide spectrum of sizes, the Brinkman (1952) viscosity model works well for all dispersed phase fraction φ_{Disp} values. However, when the dispersed phase is comprised of uniform sized

spheres, Roscoe (1952) found the Einstein (1906) model is limited to dispersed phase fractions $\varphi_{\mathrm{Disp}} < 0.05$. For medium and high dispersed phase fractions φ_{Disp} Roscoe (1952) proposed a modified form of the Brinkman (1952) model in which the phase fraction of the dispersed phase is multiplied by 1.35, i.e.:

$$\mu_{\mathrm{R}} = \frac{1}{\left(1 - 1.35\varphi_{\mathrm{Disp}}\right)^{2.5}} \qquad 2.22$$

Pal and Rhodes (1989) developed the correlation presented by Brinkman (1952) into model for both Newtonian and non-Newtonian emulsions which accounts for hydrate effects and the flocculation of dispersed droplets:

$$\mu_{\mathrm{R}} = \frac{1}{\left(1 - K_O K_f(\gamma)\varphi_{\mathrm{Disp}}\right)^{2.5}} \qquad 2.23$$

Where, K_O is a hydration factor that depends on the nature of any emulsifying agents that may be present and, $K_f(\gamma)$ accounts for flocculation and only used in non-Newtonian emulsions.

Phan-Thein & Pham (1997) presented a different equation for the effective viscosity for a droplet suspension model for which they used the model by Taylor (1932) as a starting point. The model, in which the particles are of a size where Brownian motion is unimportant, is given as:

$$(\mu_{\mathrm{R}})^{2/5}.\left(\frac{2\mu_{\mathrm{R}} + 5K}{2 + 5K}\right)^{3/5} = \left(1 - \varphi_{\mathrm{Disp}}\right)^{-1} \qquad 2.24$$

For rigid droplets ($\mu_{\mathrm{Disp}} \to \infty$) the effective viscosity reduces to:

$$(\mu_{\mathrm{R}}) = \left(1 - \varphi_{\mathrm{Disp}}\right)^{-2.5} \qquad 2.25$$

Equation 2.25 reduces to the Einstein (1906) model (Equation 2.13) in the limit of small volume fractions of the dispersed phase.

Pal (2000) reviewed the model proposed by Phan-Thein & Pham (1997) and found that it under predicts the relative viscosity for concentrated emulsions by a large amount and fails to account for the presence of surfactants. Pal (2000) presented a modified form of Equation 2.26 to describe the viscosity-concentration relationship of emulsions of nearly spherical droplets. This model showed good predictive ability when compared to experimental data. The correlation is given as:

$$(\mu_{\mathrm{R}}).\left(\frac{2\mu_{\mathrm{R}} + 5K}{2 + 5K}\right)^{3/5} = \left(1 - K_O.\varphi_{\mathrm{Disp}}\right)^{-5/2} \qquad 2.26$$

where, K_O is a constant that factors for the presence of absorbed surfactants on the surface of droplets. It is a constant for a given emulsion, but varies between systems.

Krieger – Dougherty (1959) presented an equation for concentrated solid-in-liquid suspensions which is given as:

$$\mu_{\mathrm{R}} = \left[1 - \frac{\varphi_{\mathrm{Disp}}}{\varphi_{\mathrm{Max}}}\right]^{-[\mu_{\mathrm{int}}]\varphi_{\mathrm{Max}}} \qquad 2.27$$

where, $[\mu_{\mathrm{int}}]$ is the intrinsic viscosity and has a theoretical value of 2.4 for rigid spheres, φ_{Max} is the maximum packing concentration and represents an effective fluidity limit at which the system loses liquid characteristics and becomes an elastic solid. A difficulty arises when calculating emulsion viscosity due to problems associated with measuring φ_{Max} for emulsions.

Chong et al. (1971) presented a graphical extrapolation technique to determine φ_{Max} for solid-in-liquid suspensions. Unlike soild-in-liquid suspensions, emulsion viscosities μ_{E} do not tend to infinity as φ_{Disp} approaches φ_{Max}. Furthermore, for emulsions φ_{Disp} can exceed φ_{Max}, when $\varphi_{\mathrm{Disp}} > \mu_{\mathrm{Max}}$ the droplets of the dispersed phases can no longer remain spherical and undergo deformation. Due to these reasons extrapolation methods to determine μ_{Max} are unsuitable.

A limitation of the Krieger-Doughtery (1959) model is that it is confined to Newtonian systems. However, Barnes (1994) postulated that the system could be adopted for use with non-Newtonian fluids by making μ_{m} dependent on shear-rate.

Aoamari et al. (1998) presented shear viscosity data for water-in-oil systems using a Crude Arabian Light (CAL) which, showed the existence of not only φ_{Max} but also φ_{Crit}, the critical water volume fraction which represents the onset of physical contact between water droplets.

Ronningsen (1995) presented a model for predicting the viscosity of water-in-crude oil (w/o) emulsions based on experimental results from eight different North Sea crude oils. The model is a development of the exponential model proposed by Richardson (1933). The exponential relationship between viscosity and the volume fraction of the dispersed phase represents the fact that the emulsion becomes increasingly more non-Newtonian and that such emulsions exhibit a non-linear relationship. The model is given as:

$$\mu_{\mathrm{R}} = e^{K.\varphi_{\mathrm{Disp}}} \qquad 2.28$$

where K is a constant.

A modified form of this model was presented by Broughton & Squires (1938) as follows:

$$\mu_{\mathrm{R}} = Ae^{K.\varphi_{\mathrm{Disp}}} \qquad 2.29$$

Equation 2.29 was the basis for the Ronningsen (1995) model who postulated that A and K could be expressed as linear function of temperature such that:

$$A = k_1 + k_2.T \qquad 2.30$$

$$K = k_3 + k_4.T \qquad 2.31$$

which can be substituted into Equation 2.29 to give:

$$\ln \mu_{\mathrm{R}} = k_1 + k_2.T + k_3.\varphi_{\mathrm{Disp}} + k_4.\varphi_{\mathrm{Disp}}.T \qquad 2.32$$

where k_1, k_2, k_3 and k_4 are constants.

Pal (1998) correlated emulsion viscosity μ_{E} data using experimental data for mineral oil-in-water and kerosene-in-water emulsions. In the correlation presented emulsion viscosity is a function of particle Reynolds number $\mathrm{Re_p}$, the volume fraction of the dispersed phase φ_{Disp}, the maximum packing concentration of the dispersed phase φ_{Max} and intrinsic viscosity $[\mu_{\mathrm{int}}]$. The model assumes that the emulsion droplets are large enough to neglect the influence of Brownian

motion and therefore the Peclet number is disregarded. The model assumes that the capillary number (Ca) small. The correlation is given as:

$$\varphi_{\mathrm{Max}}^{1/2}\left[1-\mu_{\mathrm{R}}^{-\frac{1}{[\mu_{\mathrm{int}}]}/\varphi_{\mathrm{Max}}}\right]=A_o+A_1.\log_{10}\left(\mathrm{Re_p}\right)+A_2\left[\log_{10}\left(\mathrm{Re_p}\right)\right]^2 \qquad 2.34$$

2.5 Concluding remarks

In the above discussion, attention has been focussed on flow regimes in liquid-liquid flows (Section 2.2), on phase inversion phenomena (Section 2.3) and on mixture viscosity (Section 2.4). Though it is convenient to divide the material under these headings, it should be stressed that the topics covered are closely connected. Thus, there is a close relationship between phase inversion and flow regimes and between apparent viscosity and phase inversion. A major topic area not dealt with in this chapter is that of modelling methods for liquid-liquid flows. Such modelling methods will be introduced and described in the context of interpretation of the experimental results presented in Chapters 4, 5 and 6.

CHAPTER 3

Experimental Apparatus and Methods for Liquid-Liquid Flow Studies

3.1 Introduction

The experimental facility and procedure, as well as the visualisation equipment and the image processing methodology used to conduct the studies of co-current horizontal liquid-liquid flows using the PLIF and PTV/PIV technique are described below. This Chapter begins (in Section 3.2) with a description of the generic liquid-liquid flow facility (TOWER) used for the experiments carried out in the work described in this thesis. The main focus of the work on liquid-liquid flows has been on the application of PLIF and PTV/PIV to the study of flow patterns and phase distribution in a liquid-liquid flow in which the refractive index of the two liquids has been carefully matched and the remaining Sections in this Chapter describe the experimental background to these studies. Sections 3.3 and 3.4 give descriptions of the laser equipment, and camera systems respectively and the synchronisation of the laser and camera systems is described in Section 3.5. The bases of the fluorescence phenomenon are described in Section 3.6 and the principles of the laser-induced fluorescence (LIF) method are outlined in in Section 3.7. The selection of the test fluids (including refractive index matching) and their physical properties are detailed in Sections 3.8 and 3.9, respectively. Section 3.10 describes the visualisation sections for use in the LIF experiments and, finally, the image processing methodology and the means of obtaining quantitative data are discussed in Section 3.11.

3.2 The TOWER Facility

The experiments were carried out in the **T**wo-Phase **O**il-**W**ater **E**xperimental **R**ig (TOWER), which is a multiphase flow facility at Imperial College London designed for the investigation of phenomena occurring in co-current horizontal liquid-liquid flows. Though the TOWER facility was originally built around 20 years ago, it has been necessary to conduct a major refurbishment of the facility for the present work and the details of this refurbishment are outlined in Section 3.2.1 below. A schematic diagram of the facility is shown in Figure 3-1. Basically, each of the two liquid phases is pumped from the respective storage tanks and through flow meters before separately entering the test section where they flow in contact; the mixture is passed back from the end of the test section to the separator vessel from which the two fluids are passed to the respective storage tanks.

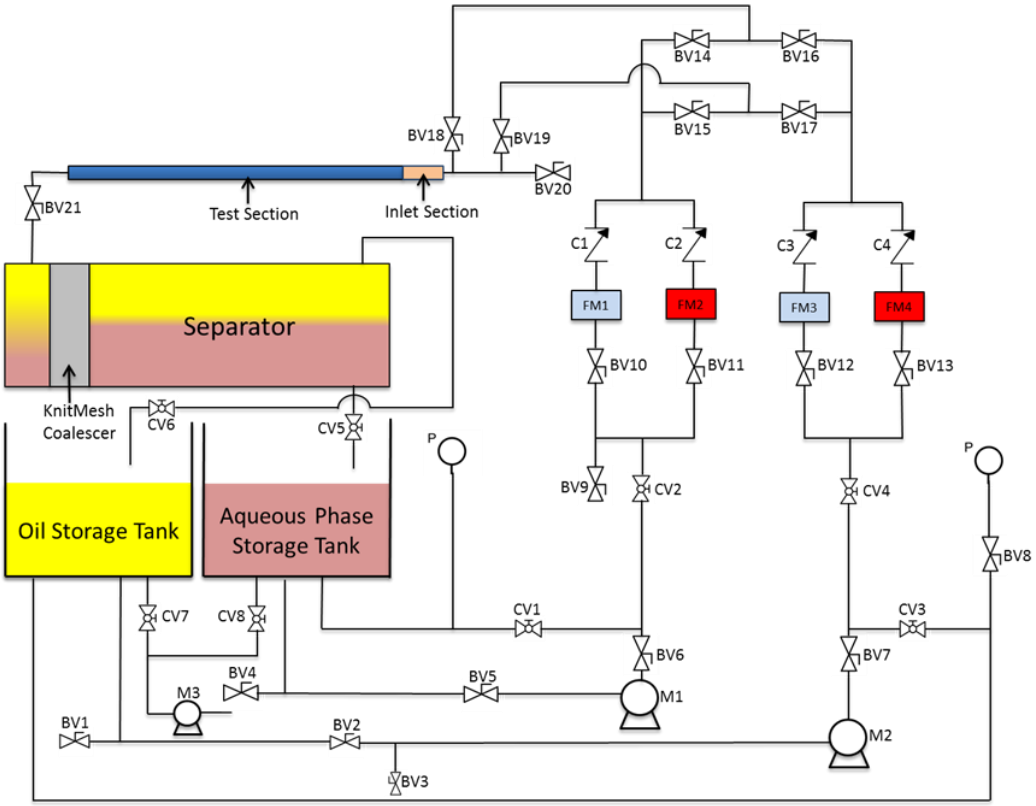

Figure 3-1: Schematic Diagram of the TOWER facility

3.2.1 Components of the TOWER Facility

3.2.1.1 Separator

The liquid – liquid separator is a vessel constructed from PVC reinforced with steel and is positioned above the storage tanks. The vessel is 1.94 m long and 0.54 m ID and contains a 0.5 m diameter, 0.3 m long KnitMesh™ coalescer. The KnitMesh™ coalescer is included to improve separation efficiency of the test fluids and enable a smaller vessel size to be used compared with conventional separators. The KnitMesh™ coalescer consists of a mesh pad of strands of two materials (metal and plastic) with highly different surface free energies knitted together. These two materials, metal and plastic have different wetting properties and can therefore collect either fluid in a continuum of the other.

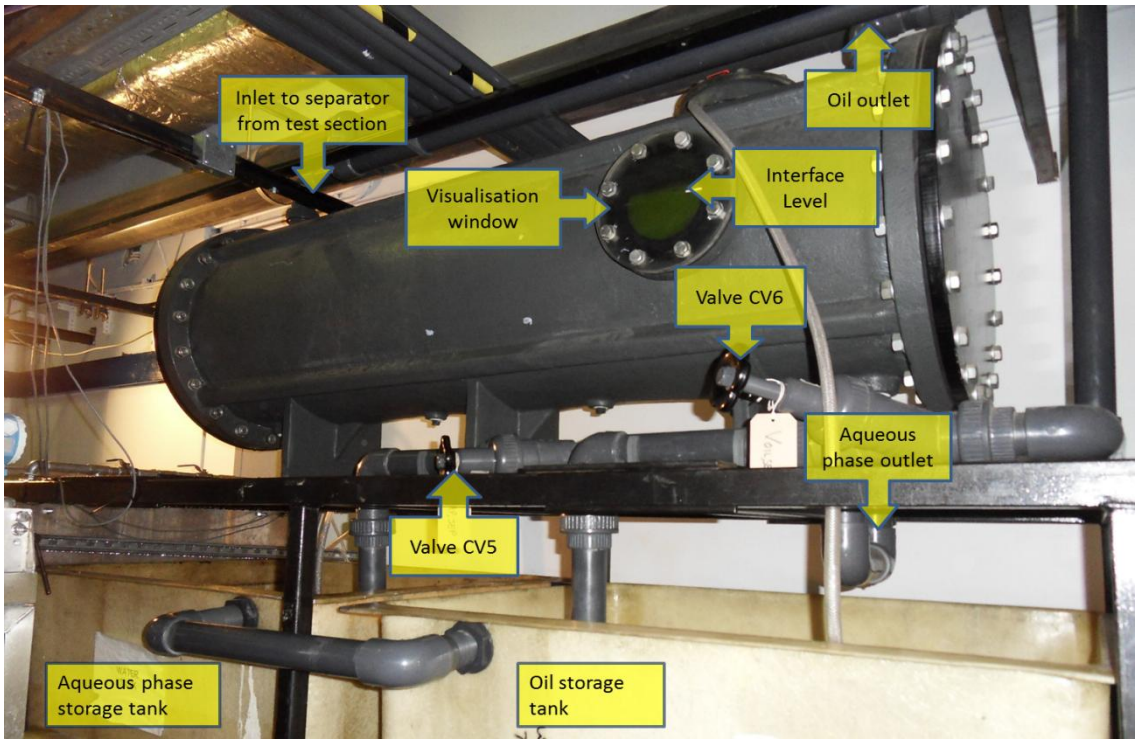

Figure 3-2: Photograph showing the arrangement of the separator and the storage tanks

3.2.1.2 Flow Metering

The flow rates are measured by means of four NB Liquid Turbine Flow Meters, fitted with a Fluid Well FllQ-X LCD digital display; these new flow meters were fitted on the present work as part of the refurbishment of the facility. The flow rates can be time-logged on a computer by means of a 4-20 mA linear current output. Each fluid can be directed through one of two turbine flow meters. The orientation of this arrangement is illustrated in Figures 3-1 and 3-3. In Figures 3-1 & 3-3, FM1 and FM3 are the low range (2-20 $L.min^{-1}$) flowmeters for the aqueous phase and the oil phase respectively and FM2 & FM4 are the high range (14-140 $L.min^{-1}$) flowmeters for the aqueous phase and the oil phase respectively. To direct the aqueous phase flow through the low range flowmeter FM1 valve BV10 is opened and BV11 is closed, whereas to direct flow through FM2 BV10 is closed and BV11 is open. To orientate the oil flow through the low range flowmeter (FM3) valve BV12 is opened and BV13 is closed whereas to direct the oil through FM4 valve BV12 is to be open and BV12 closed. The reason for providing two flow meters for each phase was to allow experimental runs to be conducted over a broader range of flow rates and phase fractions, whilst minimising the overall uncertainty in the setting and measurement of the flow rates. The accuracy of the NB Liquid Flow Turbines is ±0.5% of the full scale value, while their repeatability is ±0.1% of full scale.

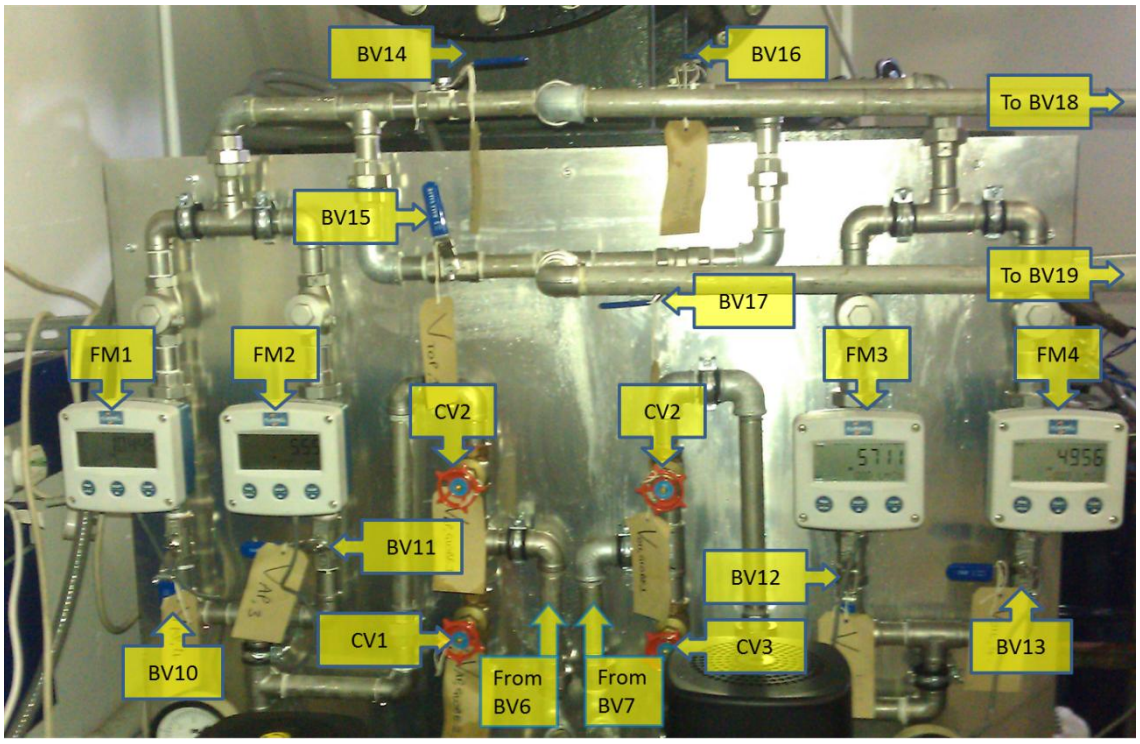

Figure 3-3: Photograph of the flow control panel

3.2.1.3 Pumps

Two Grundfos CRN 10-5 pumps with three phase supplies were used, one for each fluid; again, these pumps were fitted to the facility as part of the refurbishment conducted in the present work. The pump for the oil phase is fitted with double back to back shaft seals. The pumps each have a rated flowrate of 2.788 $L.s^{-1}$ and a rated head of 361 kPa. The pumps are shown in Figure 3-4 below:

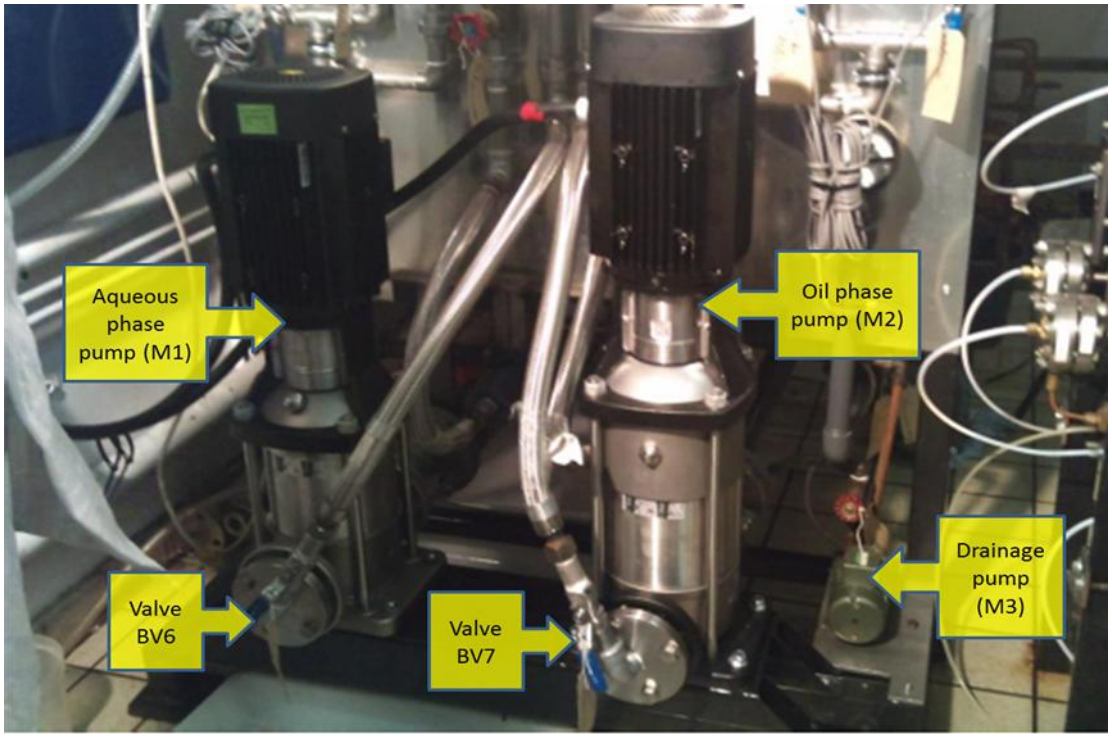

Figure 3-4: Photograph illustrating the flow control panel of the TOWER facility

3.2.1.4 Tanks

Each of the test fluids is stored in a 0.681 m^3 tank constructed from fibreglass and resin by Wilford Plastics Ltd. Each tank has two inlet and two outlet streams as shown in Figure 3-1. The inlet streams are from the separator and the recycle stream from the corresponding pump. Of the outlet streams from each tank one leads to the pump and the other is a drainage line.

3.2.1.5 Inlet Section

The inlet to the test section is configured so that either test fluid can be injected at the top or bottom of the test section, see Figure 3-5. In the LIF experiments, the two liquids used were, a kerosene-like oil (EXXOL D80) and an aqueous glycerol solution. To introduce oil on top of the glycerol solution valves BV15 and BV16 are opened whereas valves BV14 and BV17 are

closed. Conversely, to introduce the aqueous phase on top of the oil phase valves BV15 and BV16 are closed and valves BV14 and BV17 are open. For both cases valves BV18 and BV19 are open.

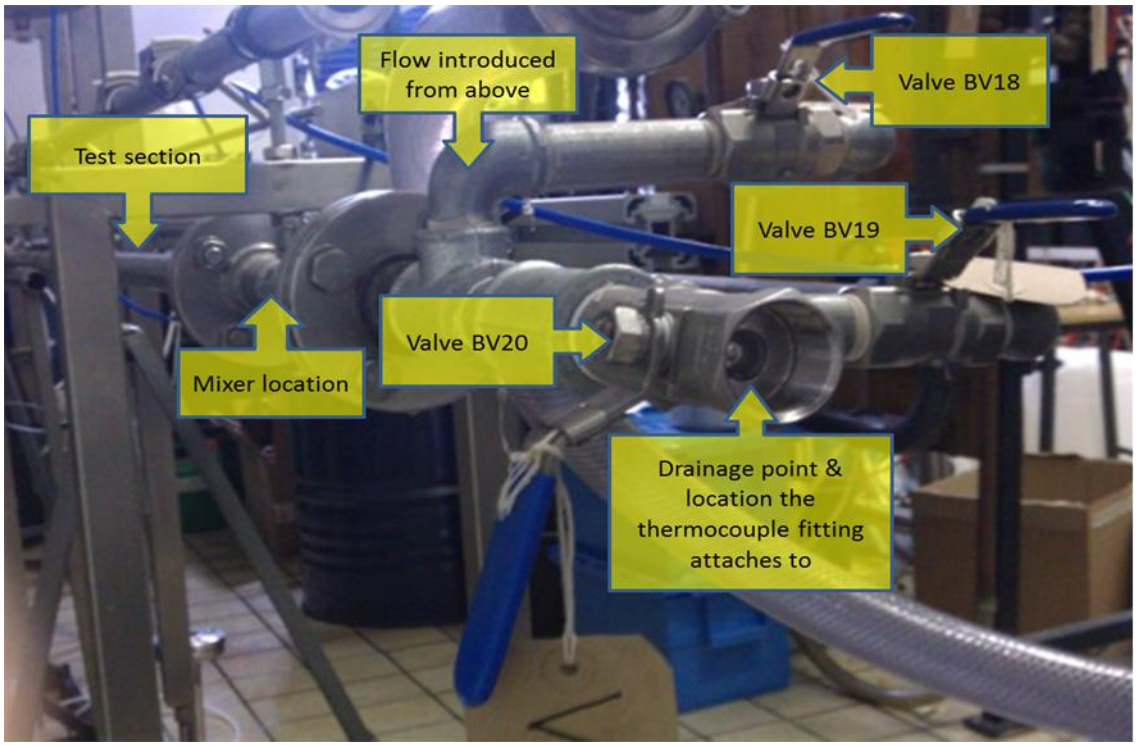

Figure 3-5: Photograph showing the orientation at the pipe test section inlet

3.2.1.6 Test Section

The rig has a 7.30 m long, 1-inch (D = 25.4 mm) nominal bore stainless steel test section constructed from stainless steel (SCH 80) and mounted in a precisely horizontal orientation. The test section is 7.30 m long, with the visualisation sections positioned 6.20 m from the test section inlet. The visualisation sections are discussed in Section 3.10.

3.2.1.7 Pressure Gauges

There are two pressure gauges; one for water pressure measurement and the other for the oil pressure measurement. The pressure gauges are connected to the pump outlet pipe as shown in Figure 3-1.

3.2.1.8 Thermocouple

A 1.5 mm type K thermocouple (Figure 3.6) can be fitted to the TOWER facility to monitor the temperature during experimental runs. When being used, it is located upstream of the test section inlet, fitting into the exposed thread of drainage value BV20. The positioning can be seen in Figure 3-5.

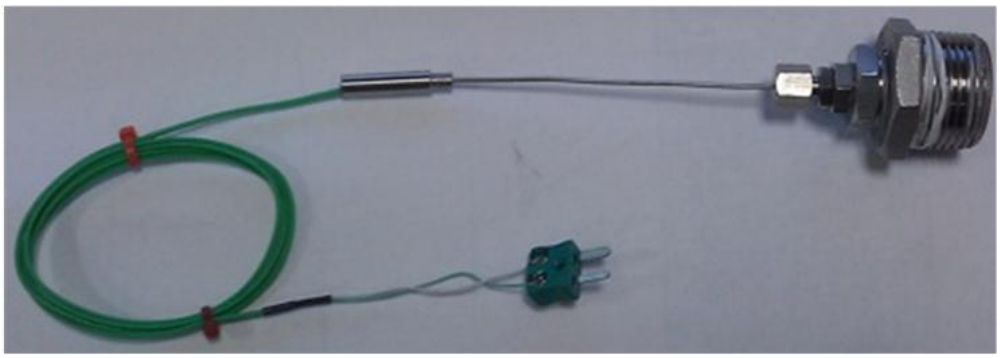

Figure 3-6: 1.5 mm type K thermocouple

3.3 Laser Equipment

In the Laser Induced Fluorescence (LIF) technique, as applied in the current experimental work, a sheet of light derived from a laser is passed through the test section through which the liquid-liquid two phase flow is passing. Since the refractive index of the two fluids is matched, the laser sheet passes through the test section without distortion at the fluid-fluid interfaces. By

adding a fluorescent dyestuff to the aqueous phase it is possible to visualise that phase and to determine the position of the oil-aqueous phase interfaces in the plane through which the laser sheet is passing. This Planar Laser Induced Fluorescence (PLIF) system was used to study flows in a square cross section channel (see Chapter 4) and also in a round cross section channel (Chapters 5 and 6); in the latter case it was necessary to correct the images for the distortion caused by the circular channel wall.

3.3.1 Copper Vapour Laser

An Oxford Lasers LS20-10 20 W nominal output pulsed copper vapour laser was used as a green light source for the laser-induced fluorescence (LIF) experiments. The output spectrum is peaked at 510.6 nm and the laser has a pulse energy of approximately 2 mJ/pulse with an internal clock frequency of 10 kHz. Other Pulse Repetition Frequencies (PRFs) can be achieved by use of an external frequency source and setting the frequency switch to "auto" (see Figure 3-8) which overrides the internal clock frequency when the external source is within the operable range of the laser. The ability is utilised in synchronising the laser and camera systems. This is explained in section 3-5.

3.3.2 Laser Sheet Generator

A Fibre Optic Light Sheet Generator produced by Oxford Lasers is used to generate the laser sheet and is connected to the copper vapour laser by means of a fibre optic cable. The laser sheet has a thickness of less than 1 mm and a throw distance (the distance between the main output lens and the position of the minimum thickness of the laser sheet) of 155 mm. The orientation of the laser sheet and test section visualisation section is illustrated in Figure 3-7.

3.4 High Speed Imagers

For the LIF experimental campaigns detailed in this thesis, two high speed cameras were used. The specifications of these cameras are detailed below in sections 3.4.1 and 3.4.2. The synchronisation of the cameras with the copper vapour laser (Section 3.3) is explained in Section 3.5. The orientation of the camera relative to the visualisation section and the laser sheet is illustrated in Figure 3-7.

3.4.1 Olympus iSPEED 3 System

The i-SPEED 3 monochromatic system produced by Olympus has a maximum resolution of 1,280 × 1024 pixels at which the highest attainable frame rate is 2,000 frames per second (fps). This camera system was used to record the laser illumination of the test section in the PLIF experimental studies using the circular cross-section visualisation cell; these are presented in Chapter 5 and Chapter 6.

3.4.2 Phantom V710 Monochromatic System

A Phantom V710 Monochromatic System produced by Vision Research was used to record the laser illumination of the test section in the PLIF experimental study using the square cross-section visualisation cell; this is presented in Chapter 4. The camera has a maximum resolution of 1,280 × 800 at which the frame rate is 7,530 fps. The camera was borrowed from the EPSRC Instrument Loan Pool.

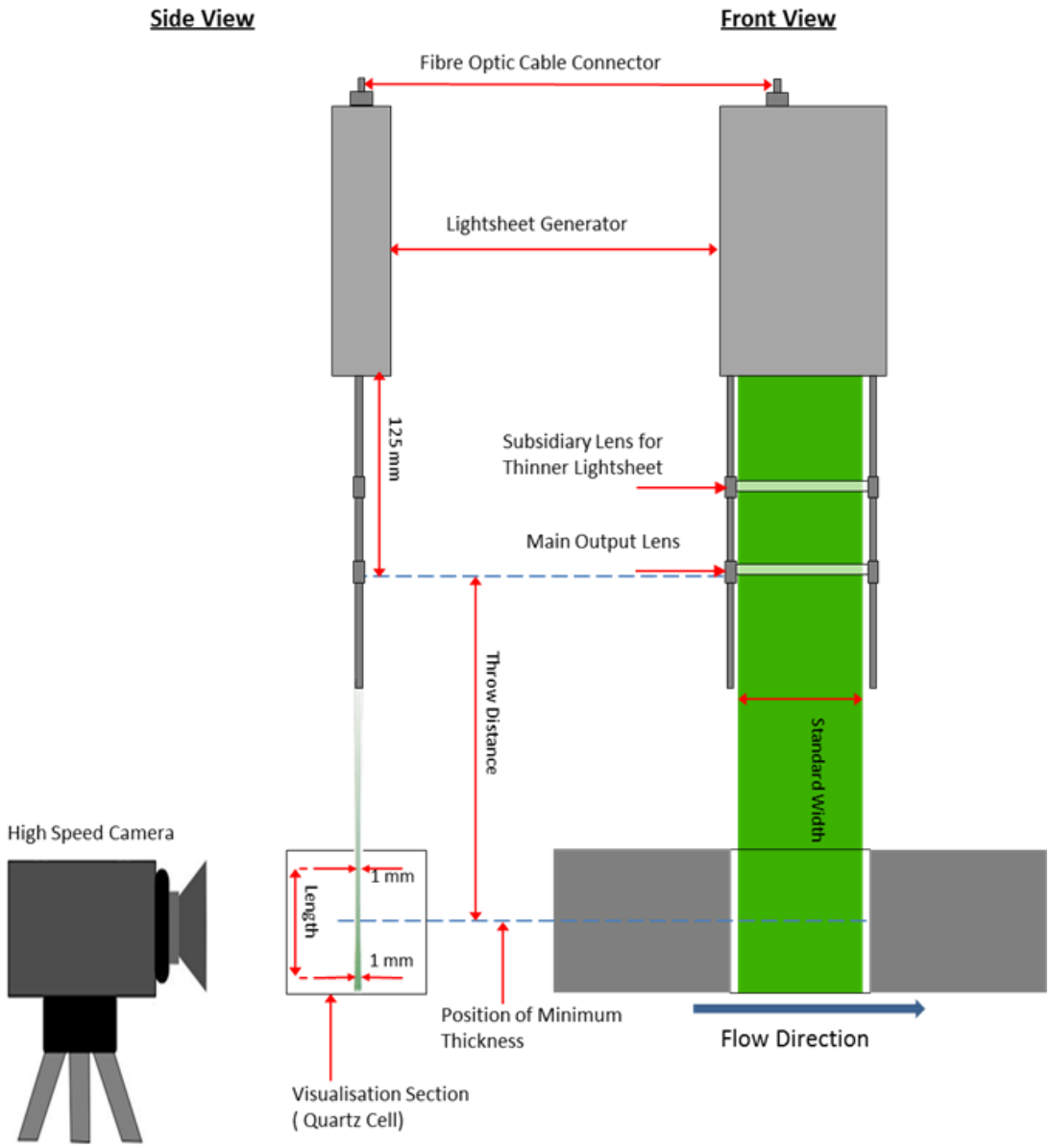

Figure 3-7: Illustration of the laser sheet, square cross-section visualisation cell and camera orientation

3.4.3 Cameras Len and Filter

A Macro 105mm F2.8 EX DG medium telephoto lens produced by Sigma Imaging Ltd was used in the LIF experimental campaigns. The suitability of the lens was confirmed from evaluation of its MTF (Modulation Transfer Function) against Image Height chart, which relates

the lens' ability to distinguish and resolve fine details between light and dark areas as a function of the distance from the centre of the image. The aperture was optimised to setting of *f*/8 (where *f* is the focal length of the camera) to maximise image sharpness. The resulting spatial pixel resolution was 42 μm per pixel. However, a large aperture size and close focal distance results in a shallow depth of field, hence considerable care was taken in configuring the apparatus arrangement to generate well focused images. Finally, in order to eliminate the contamination of the acquired PLIF signals by the laser excitation light, a 525 nm longpass optical filter of diameter 50 mm was placed in front of the lens during the PLIF measurements.

3.5 Laser-Camera Synchronisation

As the copper vapour laser delivers a pulsed output it is necessary to synchronise it with the camera system to ensure the laser pulses during an exposure of the camera so that the camera captures the laser-induced fluorescence effect. This is demonstrated pictorially in Figure 3-8 below. A trigger box is used to synchronise the laser with the camera such that a single laser pulse falls within a single exposure of the camera.

The importance of camera – laser synchronisation is recognised when one considers the implications of not having such synchronisation. Even if the laser and camera are set to operate at the same frequency the signals could be out of phase resulting in the laser pulses falling outside the camera exposures and a consequent failure to illuminate the target field during the camera exposures. Thus, without synchronisation, one could not see, let alone distinguish between the liquid phases.

When the camera is triggered it sends a TTL (transistor-transistor logic) signal via its "Exposure Out" output to the trigger box. The TTL output is a binary electrical signal which has a "low"

voltage level and a "high" voltage level which become "high" at the start of each frame for the duration of the exposure, at the end of which the signal returns to the "low" level, returning "high" at the start of the next frame and so on. This signal is sent to the trigger box at the frame rate at which the camera is set to. From the trigger box the signal is sent to the laser in phase with the camera signal albeit it via a frequency reader. The signal reduces the pulse repetition frequency of the laser from its internal clock frequency of 10 kHz to the frequency the camera is set to until the camera stops capturing images.

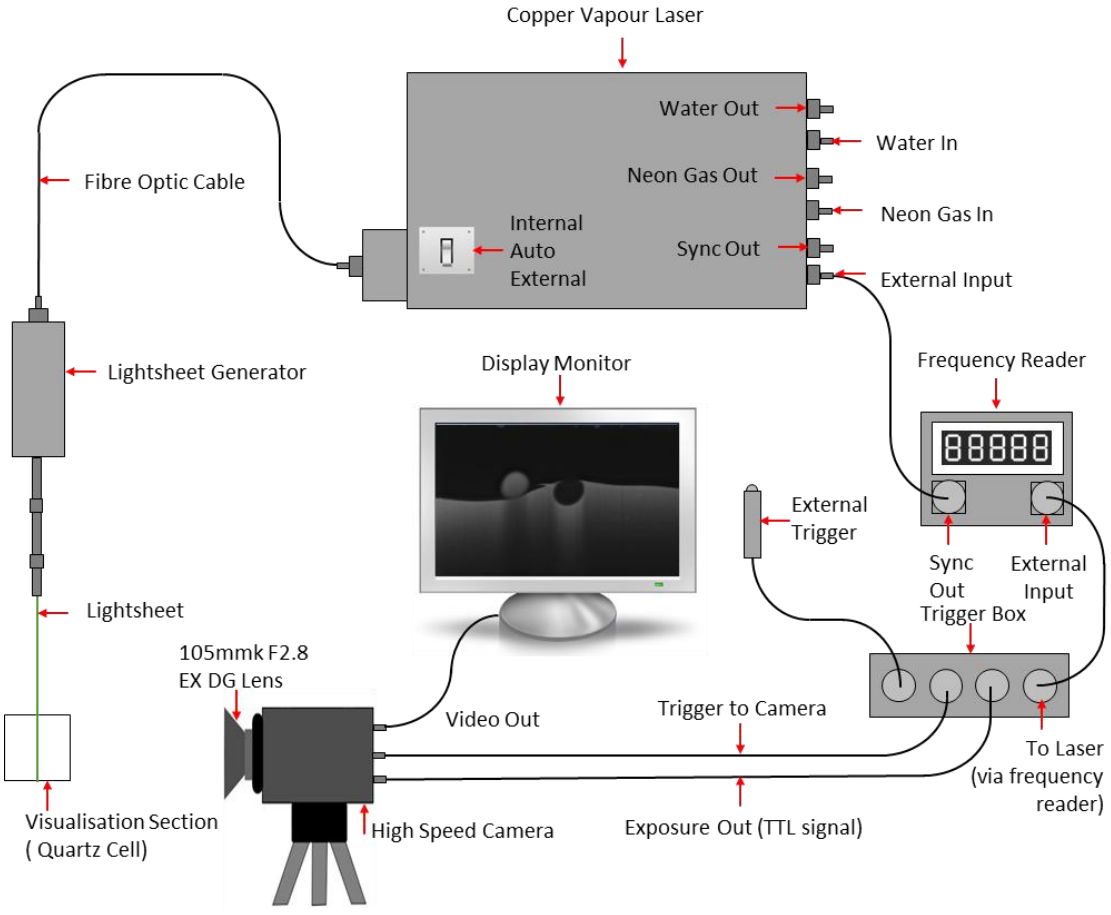

Figure 3-8: Laser-camera synchronisation equipment

3.6 Fluorescence

The LIF technique is based upon photoluminescence, in which a substance absorbs electromagnetic radiation, which in turn results in the emission of photons. There are two main forms of photoluminescence, fluorescence (on which LIF is based) and phosphorescence. Phosphorescence is characterised by the delayed emission of photons whereas fluorescence is characterised by the rapid emission of photons of lower energy (i.e. longer wavelength) than those absorbed. In fluorescence, electromagnetic radiation (a photon) is absorbed in approximately 10^{-15} seconds, which causes the excitation of an electron to a higher energy level, which lasts for approximately 10^{-4} seconds. When the electron relaxes to its ground state, the energy is emitted as a photon of light. However, when when the electron is excited some energy in excess of the lower vibration energy is dissipated and the the emitted photon will be of lower energy, i.e. there is a Stokes shift. This process is illustrated in Figure 3-9. Thus, each fluorescent material has two characteristic spectra, its absorption spectrum, which shows the relative effectiveness of different wavelengths of electromagnetic radiation to cause the material to fluoresce and secondly, its emission spectrum which shows the relative intensities of the wavelengths of electromagnetic radiation emitted. This is an important factor when establishing a suitable fluorescent dyestuff; this is discussed in Section 3.8. Another parameter to consider is the quantum yield which denotes the efficiency of the fluorescence, or rather, the ratio of photons emitted to the number of photons absorbed. This is given below:

$$\Phi = \frac{Number\ of\ Quanta\ Emitted}{Number\ of\ Quanta\ Absorbed} = Quantum\ Yield \tag{3.1}$$

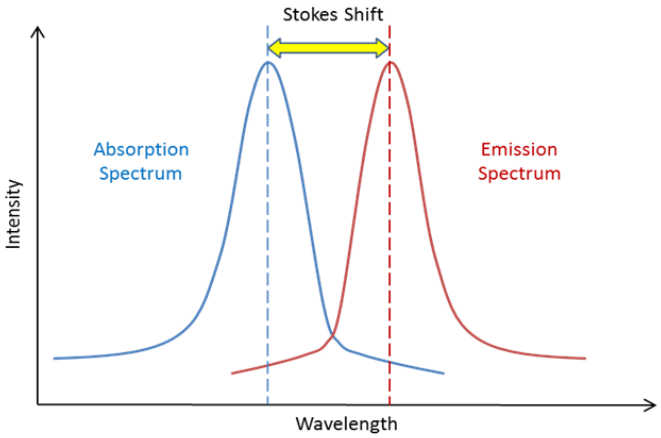

Figure 3-9: Diagram illustrating Stokes shift

3.7 Principles of Laser-Induced Fluorescence

There are a multitude of flow visualisation techniques that can be adopted for studying multiphase flows (Hewitt et al., 1990; Barbosa et al., 2001; Liu, 2005). Of these, there are two main categories, tracer and optical methods, of which planar LIF (PLIF) falls into the latter category. PLIF is a spectroscopic technique that has been applied in the work described in this thesis because it can be used to visualise the complex interfacial configurations which occur in the flow of two immiscible liquids. One fluid, the aqueous phase contains a fluorescent dyestuff; when the laser sheet passes through this phase, this dyestuff fluoresces and this fluorescent emission can be captured by the camera. LIF has the advantages of being a very sensitive visualisation technique; it can detect substances in concentrations as low as one part per ten billion, and has very good specificity. Furthermore, it is a non-intrusive technique, whereas tracer methods that involve the injection of a solid tracer into the flow (such as is used with Particle Image Velocimetry, PIV) can result in changes to the flow patterns. However, there is a caveat to the effectiveness of LIF; to achieve clear distinction between the fluids there are a multitude of factors that have to be accounted for such as the attenuation mechanisms of

light, which largely pertain to the liquids used. The effects of such attenuation mechanisms can be mitigated through careful selection of the test fluids and the fluorescent dyestuff. The selection of the fluids and dyestuffs is discussed in Section 3.8.

3.8 Fluid Selection & Refractive Index Matching

When a parallel beam of light strikes a dispersed system its intensity can be attenuated by four means, namely: absorption, diffraction, refraction and reflection. Attenuation via the last three mechanisms, which can collectively be termed scattering, can be eliminated by matching the refractive indices of the two liquid phases. This allows the plane of illumination to be viewed without distortions arising from changes in refractive index in the flow field and through the walls of the containing duct. To prevent attenuation via absorption the test fluids must be transparent to both the activating light (the laser sheet) and the generated light (the light emitted from the fluorescence process). However, the LIF process hinges on the fluorescent dyestuff absorbing photons from the activating laser sheet so intensity of the fluorescence decreases with distance along the laser sheet. Thus optical transparency and matched refractive indices are imperative; the full extent of the fluid selection criteria is discussed in Section 3.8.1.

3.8.1 Selection Criteria

For the experiments described here, proper selection of the test fluids and fluorescent dyestuff was of prime importance. The criteria applying are listed below for the fluids and dyestuff respectively.

1 Selection Criteria for the Test Fluids

A	Transparent (colourless or pale) liquids.
B	Matched Refractive Indices
C	One phase (the organic phase) to be able to dissolve the fluorescent dyestuff (Eosin Y).
D	Suitable physical properties - importance of density and viscosity with regards to pumping.
A	Transparent (colourless or pale) liquids.
B	Matched Refractive Indices
C	One phase (the organic phase) to be able to dissolve the fluorescent dyestuff (Eosin Y).
D	Suitable physical properties - importance of density and viscosity with regards to pumping.
E	Low toxicity
F	Low flammability
G	Low corrosiveness
H	Economic considerations require the fluid to be of low cost

2 Selection Criteria for the Fluorescent Dyestuff

A	Soluble in either the oil phase (Exxsol 080) or the aqueous solution (water-glycerol solution).
B	The absorption spectrum of the dye should be between wavelengths 500-520nm and the emission spectrum should be in the range of visible light.
C	The interfacial surface behaviour is not changed by the addition of the dye.
D	The disturbances to the flow due to localised heating due to the LIF process should be minimal.
E	The dye should have a minimal effect on the refractive index of the test fluids.
F	Stable i.e., does not form a precipitation.

3.8.2 Fluorescent Dyestuff Selection

Eosin Y ($C_{20}H_8Br_4O_5$) has been selected as the fluorescent dyestuff for the LIF experimental campaigns included in this thesis after evaluating its performance against the aforementioned criteria, see Section 3.8.1. The suitability of Eosin Y against the main criterion upon which selection was based, the absorption spectrum of the dyestuff having a high excitation coefficient at the laser output spectrum peak wavelength (510.6nm), is illustrated in Figure 3-11. The molar extinction coefficient is a measure of how strongly light is absorbed by a substance for a given wavelength. The concentration of the dyestuff used is discussed in Section 3.8.4. Additionally, Eosin Y has a quantum yield, Φ, of 0.67.

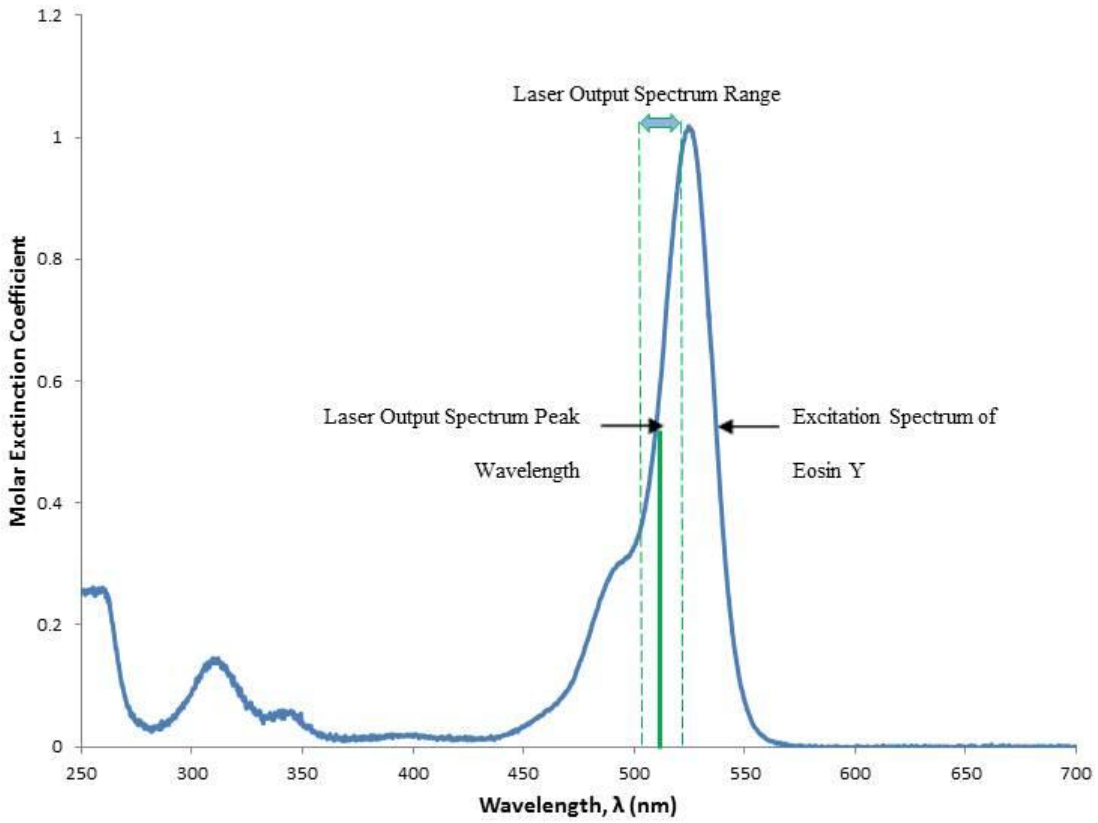

Figure 3-10: Comparison of the excitation spectrum of Eosin Y with the output spectrum of the Copper Vapour Laser

3.8.3 Test Fluid Selection Methodology

The methodology used to establish a refractive index matched pair of test fluids began with preliminarily selecting a water - glycerol solution as one phase, but without specifying the composition. The basis for this is that glycerol is soluble in water in all proportions and there are a large selection of oils with refractive indices between the refractive indices of water (1.333) and glycerol (1.473). A mixture of water and glycerol will have a refractive index in the range 1.333 to 1.473, with the value depending on the proportions of each component of the mixture. The criteria for this selection of the oil centred on the physical properties and that it has a refractive index between that of water and glycerol. Exxsol D80 was found to satisfy both the refractive index and physical properties requirements. Following the identification of these potential fluids the refractive indices of Exxsol D80 and water - glycerol solutions of different compositions were measured at different temperatures. Considering refractive index values for water-glycerol solutions published by Dow Chemicals, the range 75 to 85 wt% glycerol was preliminarily identified for investigation and the refractometer measurements were focused in this range.

An Abbe 60 Refractometer manufactured by Bellingham & Stanley was used to measure the refractive indices of the liquid samples, with Bellingham & Stanley Part No. 10-43, i.e., 1-bromonaphthalene, 98% ($C_{10}H_7Br$) used to calibrate the equipment and the test cell was mounted in a temperature-controlled water bath. These refractive index measurements are presented in Figure 3-11(a).

No literature could be found that detailed how closely the refractive indices of the fluids need to be to each other to ensure LIF images of sufficiently high clarity are produced. However, it was noted that Liu (2005) had matched the refractive indices to three decimal places in her LIF

experiments. This was taken a preliminary guide to how closely matched the refractive indices needed to be. Prior to loading the matched fluids into the TOWER facility offline LIF tests were performed to establish whether the fluids identified were sufficiently well matched to produce images of an acceptable clarity.

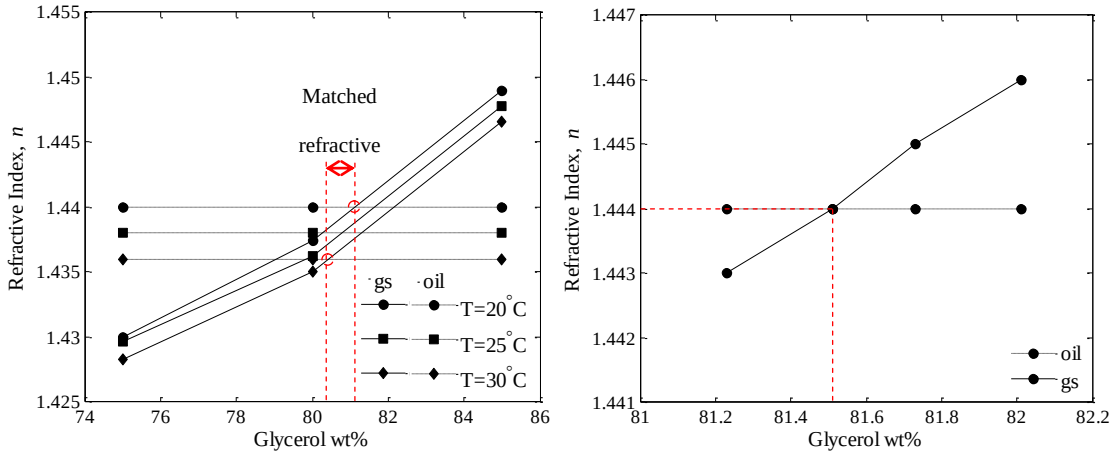

Figure 3-11: Refractive indices of (a) Exxsol D80 and water-glycerol solutions as a function of a temperature and composition and (b) Exxsol D80 and water-glycerol-dye (0.2mL/L of Eosin Y) at 20°C

Once a narrower band of glycerol-water solutions had been identified (79 to 81wt%), the refractive indices of water-glycerol solutions with Eosin Y were measured to establish the effect of adding the dyestuff and a composition that matched with the refractive index of Exxsol D80. These results are shown in Figure 3-11(b) above. From Figure 3-11(b) it can be seen that the refractive index of Exxsol D80 matches that of a 81.5 wt.% glycerol solution with 0.2 ml per litre of a 5 wt.% solution of Eosin Y.

3.8.4 Fluorescent Dye Concentration Optimisation

Initially, 0.2 ml of a 5 wt% solution of Eosin Y per litre of water-glycerol solution was used. This concentration was adopted as a starting point as it was the one used by Liu (2005). However, it was found that this did not provide an adequate level of brightness and contrast between the phases. An investigation was conducted to establish the optimum concentration of dyestuff. Water-glycerol solutions (81.5 wt%) with differing concentrations of Eosin Y were prepared and offline tests were conducted to analyse the image clarity that results from them. The Phantom V710 camera system used in this preliminary study is an 8-bit monochromatic high speed camera, which means it allows 256 different intensities of light (i.e., 256 shades of grey) to be recorded. The images obtained were analysed by measuring the intensity of light in pixels corresponding to the water-glycerol-Eosin Y solution and the Exxsol D80 regions respectively. The effect of increasing the Eosin Y concentration in the water-glycerol solution was monitored to ensure that the refractive indices of the test fluids remain sufficiently well matched. It was found that 0.4 ml of a 5% wt. Solution of Eosin Y per litre of water-glycerol solution was the optimum concentration. The resulting mass fraction of dye in the glycerol-water-dye mixture was 1.7×10^{-5} and the corresponding molar fraction is 1.4×10^{-5}, to 2 significant figures.

Although the selected concentration is well below the level at which the pixels for the water-glycerol solution become saturated with light, if the concentration is higher the opaque nature of Eosin Y starts to colour the aqueous phase resulting in it no longer being optically transparent; an essential requirement for being able to visualise the plane at which the dyestuff is activated.

Following the installation of the thermocouple detailed in Section 3.2.1.9, it was used to establish the temperature of the fluids in the rig during operation. This information was used to

establish whether the fluids still have a close refractive index match at the operating temperature.

It was found that the continued operation of the pumps can results in the test fluids heating up by over 20°C. The rate of temperature increase is significantly higher at higher flowrates. One should avoid prolonged operation of the pumps to prevent the fluids heating and hence changes in the refractive indices and physical properties (i.e., viscosity) of the fluids. The effect of temperature on viscosity and density of the test fluids is presented in Section 3.9.

3.9 Physical Properties of the Test Fluids

A comprehensive analysis of the physical properties of the test fluids has been performed. Firstly, the temperature dependence of the densities of the test fluids is presented in Figure 3-12 below. The densities were measured using a DMA 5000M densitometer manufactured by Anton Paar. For both the density and viscosity measurements temperature was controlled using a Minichiller produced by Buber.

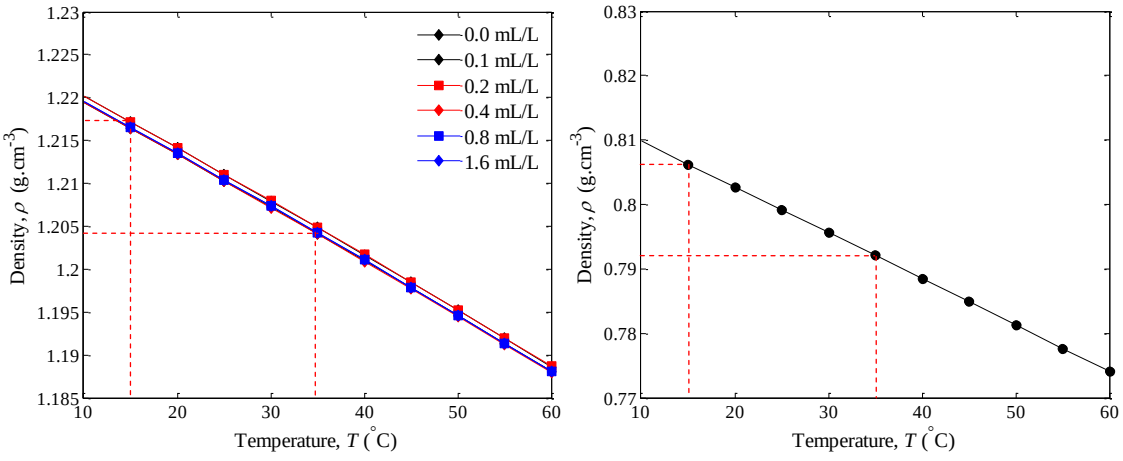

(a) (b)

Figure 3-12: Density as a function of temperature for (a) 81.7wt% water-glycerol solution with different concentrations of Eosin Y and (b) Exxsol D80 oil

From Figure 3-12(a) it is seen that the concentration of Eosin Y has little effect on the density of the glycerol solution. Attention has been drawn to the densities at 15°C and 35°C because these temperatures were found to be the upper and lower limits encountered during operation of the TOWER facility. Hence, these are the upper and lower density limits of the test fluids encountered during experimental operation. An 81.7wt% glycerol-solution with 0.4mL/L of Eosin Y has a density of 1204.1 $\mathrm{kg.m^{-3}}$ to 1216.4 $\mathrm{kg.m^{-3}}$, whereas that of Exxsol D80 is 792.1 $\mathrm{kg.m^{-3}}$ to 806 $\mathrm{kg.m^{-3}}$ across this temperature range.

It should be noted that the samples used to construct Figures 3-12(a) and 3-13(a) have a glycerol weight percentage of 81.7wt% opposed to 81.5wt% as identified in Figure 3-11(b). This is because upon completion of loading the glycerol-solution into the storage tank (see Section 3.2.1.4) – due to the batch nature of the loading process – was 81.7wt%. Upon measuring the refractive index of this glycerol-solution it was found to still be matched (to three decimal places) to Exxsol D80 so was not altered.

Viscosity values were measured using a Physica MCR301 viscometer produced by Anton Paar. The temperature dependence of the viscosities of the test fluids are presented graphically in Figure 3-13 below. The values at 15°C and 35°C have been highlighted for the aforementioned reason.

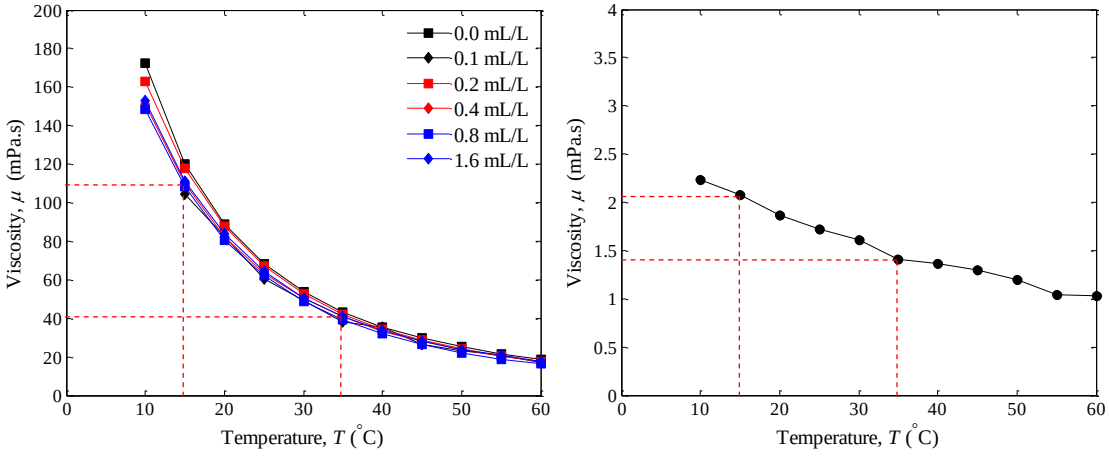

(a) (b)

Figure 3-13: Viscosity as a function of temperature for (a) 81.7wt% water-glycerol solution with different concentrations of Eosin Y and (b) Exxsol D80 oil

An 81.7wt% glycerol-solution with 0.4mL/L of Eosin Y has a viscosity of 109.8 mPa. s at 15°C, which reduces to 40.8 mPa. s at 35°C; a range of almost 70 mPa. s. Whereas, Exxsol D80 has a viscosity from 2.1 mPa. s to 1.4 mPa. s across this temperature range, which, although much more stable than the glycerol-solution, still represents a reduction of over 30%. Hence, the importance of temperature monitoring (and ideally, regulation) during experimental runs is evident.

Figure 3-14 demonstrates that shear stress versus strain rate graph is linear and passes through the origin, where the constant of proportionality is viscosity, i.e., the tests fluids obey Newtonian fluid behaviour as defined in Equation 3.1 below.

$$\tau = \mu . \frac{du}{dy} = \mu . \dot{\gamma} \qquad (3.1)$$

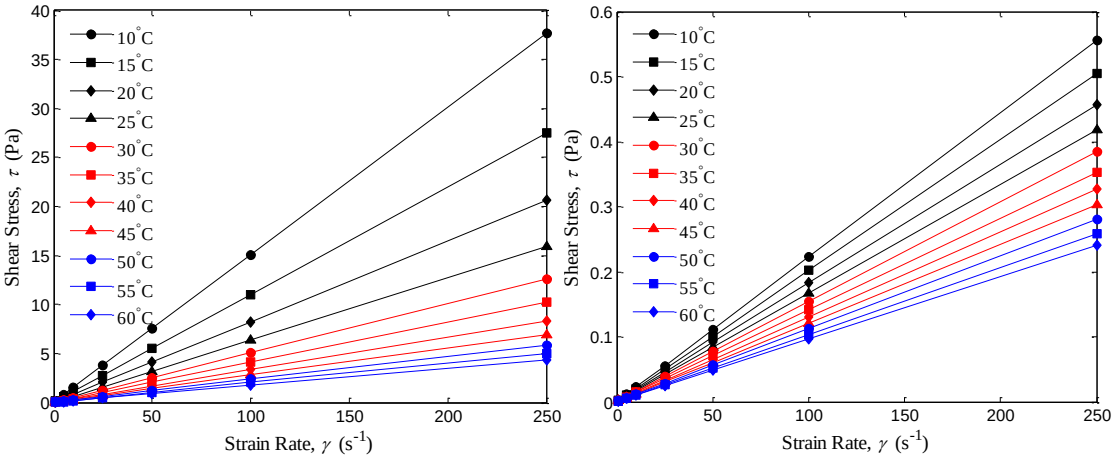

Figure 3-14: Shear stress, τ, against strain rate, γ, for (a) 81.7wt% water-glycerol solution with 0.4 mL/L of Eosin Y and (b) Exxsol D80 oil

Furthermore, direct measurements were made of the interfacial tension between the glycerol solution and oil phases at varying concentrations of Eosin Y dye in the glycerol solution phase. This was done in order to ascertain whether, and if so to what degree, the addition of the Eosin Y dye (whose addition was necessary for the fluorescence measurements) affected this important property of the two-phase system. A significant modification of the interfacial tension could lead to altered observations of interfacial phenomena and, consequently, for the system to be non-representative of normal liquid-liquid flows. Figure 3-15 shows the results from these measurements. The abscissa shows the concentration of Eosin Y in mL of 5% wt. aqueous solution per litre of glycerol solution. Error bars signify the total relative experimental uncertainty in the measurements at a 95% confidence level (2 standard deviations), which was estimated by showing that the repeatability of the measurements was ±4%. The result implies that, within our ability to measure interfacial tension to this stated accuracy and certainly within the variability in this fluid property over a range of water-oil combinations (typically oil-water interfacial tension is from 10 to 50 $mN.m^{-1}$, with most values around 17 – 30 $mN.m^{-1}$), the interfacial tension is not altered significantly from its value at zero dye concentration, giving

confidence that the results shown here are representative of a liquid-liquid flow in the absence of the fluorescent dyestuff.

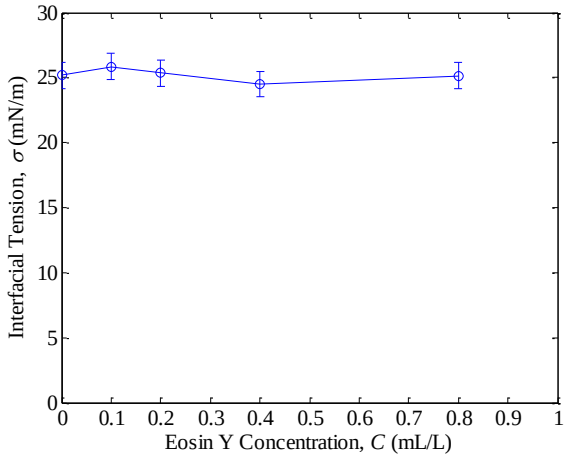

Figure 3-15: Variation in glycerol solution-oil interfacial tension as a function of Eosin Y concentration

The properties of the fluids are summarised in Table 3-1 below:

Table 3-1: Physical properties of the selected test fluids at 20°C

	Oil Phase	Aqueous Phase
Composition	Exxsol D80	81.7wt% w/ 0.4 mL/L Eosin Y
Density ($kg.m^{-3}$)	802.7	1213.3
Viscosity ($mPa.s$)	1.9	82.3
Refractive Index	1.444	1.444

It is interesting to compare the physical properties of the fluids used in the present tests to those employed in previous liquid-liquid flow studies. The oil has identical physical properties to those of the oils used by Soleimani (1999), Hussain (2004) and Liu (2005) and has similar property values to those of the oils used by Angeli (1996) and Angeli and Hewitt (2000). The density ratio of the test fluids (glycerol solution to oil) is 1.5 and is comparable to the density ratio (1 to 1.5) applicable in many previous studies (Russell et al., 1959; Charles and Lilleleht,

1966; Simmons and Azzopardi, 2001; Ioannou et al., 2005). In the present work, the fluids have a viscosity ratio (glycerol solution to oil) of approximately 20. Though this viscosity ratio is comparable to that in some of the earlier work (Charles and Lilleleht, 1966 and Guzhov et al., 1973) it should be noted that, in contrast to the earlier work (where the oil is the less dense and more viscous fluid), in the current study the oil is the less dense and also the less viscous fluid. This interesting difference to the previous studies needs to be recognised clearly in considering the present results.

It is emphasised at this point that the two liquids under investigation are immiscible and that there is no diffusion of one phase into the other. As such, the purpose here is not the recovery of instantaneous concentration information that would be necessary in diffusive flows (as done elsewhere, for example, by Markides and Mastorakos (2006)). Indeed, in the flows presented in Chapters 4, 5 and 6 the normalised concentration of the two phases is at all times either locally zero or unity. Instead, the key measurement of interest relates to the correct identification of the interface between the two phases, where this exists in the flow. Towards this end, the PLIF measurement methodology employed is purely concerned with the presence or absence of fluorescent dye, which (given that the dye is only soluble in the glycerol/water phase and insoluble in oil) signifies the local, unique presence of glycerol solution. This is dissimilar to PLIF-based concentration measurements (e.g., those by Markides and Mastorakos, 2006), where the local concentration of dye and light intensity are crucial in recovering concentration information from the emitted fluorescent light. As long as adequate laser light is present in the entire measurement plane our ability to determine the presence of dye does not depend on a uniform light illumination, or if this is not possible, on corrections for light intensity variations. Details of the procedure used to determine the local on/off presence of glycerol solution are given below in Section 3.11.

3.10 Visualisation Section Design

Two designs of visualisation section have been employed in the experiments described in this thesis, namely a square cross section visualisation section (see Section 3.10.1) and a circular cross section visualisation section (see Section 3.10.2).

3.10.1 Square Cross Section Visualisation Section

Adopting a square cross section cell eliminates the necessity to match the refractive index of the wall material with that of the test fluids, provided the laser sheet strikes the square section perpendicular to its surface, i.e. the laser light travels along the normal. This is explained by Snell's law and Figure 3-16.

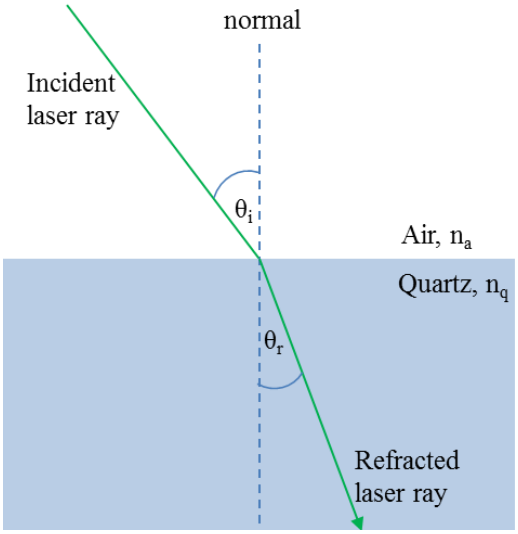

Figure 3-16: Diagram illustrating the refraction of light at the interface between two media

Thus, when a light sheet travels along the normal (i.e. $\theta_i = 0°$) from Snell's law (Equation 3.2) it can be seen that the light does not get refracted, .i.e. angle $\theta_r = 0°$, thus the light sheet continues to travel along the normal.

$$\frac{\sin\theta_i}{\sin\theta_r} = \frac{n_q}{n_a} \qquad (3.2)$$

A square cross section duct was used in the vertical flow LIF experiments of Liu (2005) and the use of a similar duct was a natural starting point in the current horizontal flow studies. The use of a square cross section duct does, of course, compromise the geometric similarity of the duct with subsea pipelines. However, as a means to mitigate the hydrodynamic disparity, visualisation is focused in the centre line of the cell. An important consideration that needs to be factored into the design of the visualisation cell is the optical clarity of the build material. Selection of the wall material was based on analysis of the transmittance spectra of potential materials. On this basis a square cross section quartz cuvette with the ends cut off was selected.

The quartz cell has the following dimensions; 18 mm internal length sides, 2 mm wall thickness and 48 mm long. The quartz cell is housed in a brass casing which has windows cut out of it to allow one to view the quartz cell (see Figure 3-17). In these experiments, the aqueous glycerol solution and the Exxsol-D80 were introduced into the normal inlet zone of the 25.4 mm diameter circular stainless steel horizontal test line with the Exxsol-D80 being fed in at the top of the tube. The mixture then flowed for 6.20 m along the circular test line before reaching a circular-to-square smooth transition piece. Following this transition piece, the fluid flowed through a 360 mm long, 18x18 mm square cross section brass duct before reaching the quartz cell (of the same cross section) where the LIF measurements were made. Following the quartz cell, the mixture passed through a further 200 mm length of square cross section duct before reaching a square-to-circular transition piece and passing into the normal outlet line for transmission to the separator. The orientation of the square visualisation section relative to the laser sheet and the camera is shown in Figure 3-7. The square geometry reduces laser light intensity non-uniformity in the measurement plane and image distortion due to the effects of reflection, refraction and absorption.

Figure 3-17: Square cross section visualisation section

3.10.2 Round Cross Section Visualisation Section

Though, as will be seen, the results obtained with the square cross section duct were very interesting, it is obvious that a duct of circular cross section would be more representative of industrial pipeline systems. The problem is that of image distortion by the (normally circular) walls of the flow tube. If a solid transparent material could be identified which had a refractive index identical to the (matched) refractive indices of the fluids, then an observation cell could be made from this material with the cell having a circular hole at its centre to carry the flow and planar outer walls to minimise image distortion. Considerable effort was placed on establishing a triply refractive index matched system, i.e. one in which both test fluids and the pipeline wall material have the same refractive indices. However, this task is particularly challenging due to the added constraint of establishing a wall material of suitable characteristics i.e., transparent to both the laser light and the fluorescence light, sufficient strength and rigidity and unreactive with the test fluids. It was found that the material most closely matching these requirements was borosilicate glass; however, the refractive index of this material is 1.474 which is not a close enough match to that of the fluids used in the square cross section duct studies (1.444). Furthermore, it was not found possible to find another refractive index matched fluid pair which had a refractive index close enough to that of borosilicate glass to allow use of this material. Another material considered was ECTFE (Ethylene Chlorotrifluorotheylene) but this was

dismissed due its milky translucent appearance meaning it is not sufficiently transparent to the laser and fluorescence light. Though it is still possible that a suitable triply matched refractive index system could ultimately be found, efforts to do so in the present study were abandoned and an alternative approach to using LIF in circular tube geometries was pursued.

The alternative approach to using LIF in circular tubes was to accept that the images initially produced would be distorted due to lack of refractive index matching between the fluids and the flow tube walls and to correct for this distortion using an image processing technique. Basically, a short length of circular cross section transparent tube was inserted concentrically into the main (circular) test section. As a precursor to the experiments, a graticule was mounted in the short transparent tube such that its surface was in the same position as that traversed by the planar laser sheet. Points on the graticule were in a known position and these could be related to their apparent position in the (distorted) image. This allowed the image to be corrected for the distortion effect.

The circular cross-section visualisation cell design adopted is shown in Figure 3-18 and comprises of an $L_S = 100$ mm long (or, 3.6 equivalent diameters, $L_S/H_T = 3.6$) length of borosilicate glass pipe with an internal diameter of $H_T = 27.6$ mm housed in a Perspex box. The void between the pipe section and the internal walls of the box are filled with the test fluid that is not seeded with fluorescent dye (i.e., Exxsol D80). The cell is located $L_E = 6.20$ m downstream of the inlet of the 25.4 mm diameter test section pipe (such that $L_E/D = 244$) which was used to set up the flows. The borosilicate glass tube had a slightly larger diameter than the test section pipe but the effect of this is expected to be small. As was stated above, the difference in refractive index between the wall material and the fluids causes a distortion of the image; this distortion was minimised by the choice of wall material and the use of a planar

fluid-filled box outside the tube, Details of the image correction method are given in Section 3.11.1.

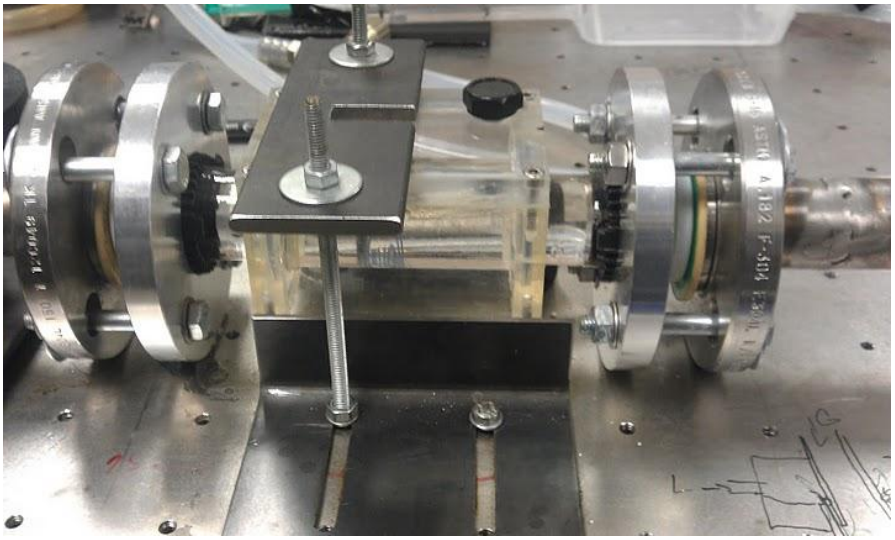

Figure 3-18: Circular cross section visualisation section

3.11 Image Processing Methodology and Results Generation

This section outlines the processing that is performed on the raw generated PLIF images for both the square and circular cross section visualisation section experimental campaigns. The results of this analysis are presented in Chapters 4 and Chapters 5 & 6 for the square and round cross sectional test pieces, respectively. However, for the PLIF studies involving the use of the circular cross-section visualisation cell (see Section 3.10.2), prior to performing any of the results-generating processes (detailed in Sections 3.11.2 to 3.11.7), the raw PLIF images underwent a correction process to correct for the distortion arising from the curvature of the visualisation cell. This correction process is described in Section 3.11.1 below.

3.11.1 Graticule Correction Technique

The graticule calibration piece (see Figure 3-19) contains a flat planar surface on to which crosses of known size and spacing are printed. During the calibration this surface is orientated so that it aligns with the central vertical plane of the visualisation cell; i.e. the same plane as to which the laser light sheet penetrates the visualisation cell during PLIF operation, see Figure 3-7. It should be noted that during the calibration no laser light was used; only ambient light was used to illuminate the visualisation cell. Prior to, and after each set of PLIF experimental runs the graticule calibration piece was inserted into the visualisation section. This was done by detaching the downstream connection between the visualisation cell and the main pipeline. Once the graticule had been inserted, the test section was filled with Exxsol D80. As the size and spacing of the crosses on the graticule are known, one can use the values to measure the displacement and distortion of them when it is viewed through the visualisation section, Figure 3-20(a) shows a raw image of the graticule when viewed through the visualisation section. Thus, one can determine the manipulation that needs to be performed on the image of the graticule to restore the crosses to their actual size and spacing, Figure 3-20(b) shows Figure 3-20(a) after it has undergone correction. This operation is performed using the DaVis software produced by LaVision. The resulting correction was based upon the average of 500 instantaneous images. Since the images of the liquid – liquid flows obtained using the PLIF technique undergo the same distortion the same manipulation as that used for the graticule images can be applied to the flow images to remove the distortion. Figure 3-20(c) shows a raw liquid – liquid flow image and Figure 3-20(d) shows the corrected image corresponding to that in Figure 3-20(c) after the manipulation has been undertaken. Though the correction is a necessary one, it should be noted that the distortion is small in the case illustrated; this reflects the choice of the wall material in the visualisation section (i.e. borosilicate glass) and the use of a planar walled cell filled with Exxsol-D80 to surround the visualisation section. As the

correction is only applicable to liquid – liquid flow images if the cell has not moved, considerable care was taken to immobilise the test section and adjoining visualisation section. A permissibility limit of 1 pixel was imposed on the movement of the visualisation cell when compared with the calibration images.

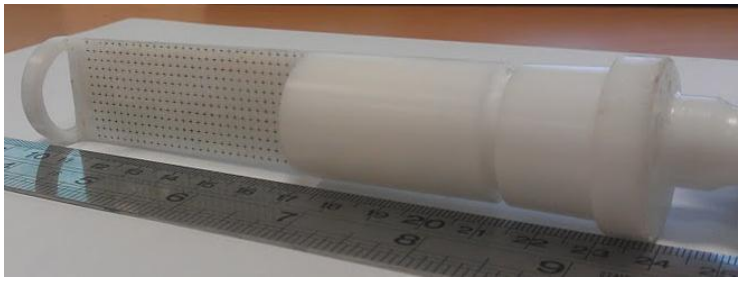

Figure 3-19: Graticule calibration piece

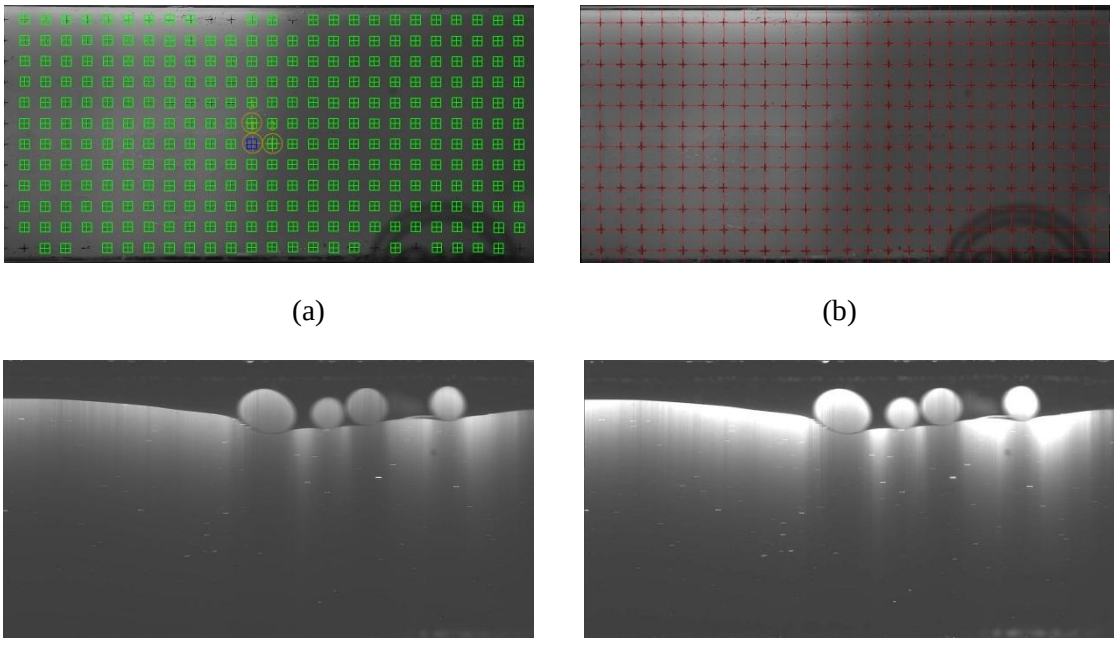

(a) (b)

(c) (d)

Figure 3-20: Demonstration of the graticule image correction technique.

3.11.2 Binarisation and Phase Distribution Profile

The phase distribution (specifically, vertical profile) analysis, the results of which are presented in Sections 4.4, 5.4 and 6.4, has been performed by converting the flow images into binarised black and white equivalents by using a thresholding approach and processing the pixel information of the resulting image using MATLAB. An example of the thresholding procedure is presented in Figure 3-21 in which the black regions represent the oil phase and the white regions represent the glycerol solution phase (which contains the fluorescent dye).

In the image shown in Figure 3-21(a), two droplets of glycerol solution in oil are seen at the interface. Below these droplets, we note two 'shadow' regions in the continuous glycerol solution region that appears at the bottom of the channel. It should be noted also that the intensity of the fluorescence decreases with distance down into the glycerol solution layer. It may be concluded, therefore, that both the "shadowing" effect and the fall in intensity with depth are due to absorption of the incident laser light sheet in the glycerol solution. The droplets in Figure 3-21(a) give a local increase in the penetration depth of the laser sheet in the glycerol solution and this gives rise to the shadowing effect. Obviously, if the absorption of the laser sheet within glycerol solution layer was excessive then it may have become difficult to always distinguish between the (non-fluorescing) oil zones and the (fluorescing) glycerol solution zones. However, as long as the spatial decay of the fluorescent signal into the image due to this attenuation is low enough to ensure that the signal remains high relative to the dark signal that signifies the complete absence of dye and therefore the presence of the oil phase, then successful binarisation of the signal can be achieved. The dark signal in Figure 3-21(a) can be seen clearly at the top of the image, indicating unambiguously that only oil is present.

The post-processing procedure involved, firstly, the identification of a typical decay profile into the fluorescent glycerol solution phase, which was found to be well approximated by a first order decay. A normalised correction profile was then defined as the inverse of this decay. Each vertical instantaneous image was then corrected by multiplying all vertical (y-direction) intensity profiles, i.e., at each horizontal position x, by the correction profile. This was done from the location of the interface into the regions of presence of fluorescent signal, based on the intensity value at the interface location.

In a second stage, following this correction, the image was binarised by applying an adaptive threshold that was selected to be at the 5% rise height between the minimum (dark) single in the image and maximum (bright) signal, corresponding to the pure oil and pure glycerol solution phases respectively. Figure 3-21(b) demonstrates the ability of the correction and thresholding procedures to eliminate the attenuation of the incident light and then to convert this image into black and white, corresponding to the instantaneous presence of pure oil and pure glycerol solution respectively. The threshold value was chosen as a compromise between smaller values that were more sensitive in identifying the exact location of the interface and larger values which were more robust to noise.

Figure 3-22 demonstrates the effect of varying levels of thresholding. Here, the thresholding parameter α is the rise height from the dark background, as a % relative to the image maximum. Specifically, Figure 3-22(a) shows the effect of α on the identification of the interface shown in Figure 3-21, while Figure 3-22(b) shows the effect of α on the calculation of the instantaneous image-averaged in-situ phase fraction $\langle\varphi\rangle_y(t)$ from the image in Figure 3-21 (this variable is defined below, in Equation 3-3). The resulting relative uncertainty that is introduced by the choice of the threshold value α in the result for the interface locations and consequently the *instantaneous* vertical phase fraction profiles, as in Figure 3-21(c), has been estimated from

measurements to be about ±10% at a 95% confidence level, with a corresponding (systematic) uncertainty in the result for the instantaneous phase fraction of ±4%.

Figure 3-21(c) shows an example (from Figure 3-21(b)) of instantaneous phase fraction (horizontal axis) $\varphi(y,t) \equiv \varphi(y)_i$ against the height inside the visualisation cell y for the processed image, zero being the bottom of the channel/cell (vertical axis). The vertical phase profiles $\bar{\varphi}(y)$ reported in Chapters 4, 5 and 6 refer to aggregated (i.e., time-averaged) phase profiles over a number of instantaneous profiles n (such as that in Figure 3-21(c)) for a given flow condition:

$$\bar{\varphi}(y) = \frac{1}{n}\sum_{i=1}^{n} \varphi(y)_i \qquad (3.3)$$

At least 1,000 frames were used to evaluate the time-averaged vertical profile of (oil) phase fraction from Equation 3.3 for each condition. As with all other flow parameters calculated from the raw images, the number of pixels was converted to a length by using the known dimensions of the height of visualisation cell. The relative experimental uncertainty in the estimation of the time-averaged profiles amounts to less than ±1% at a 95% confidence level.

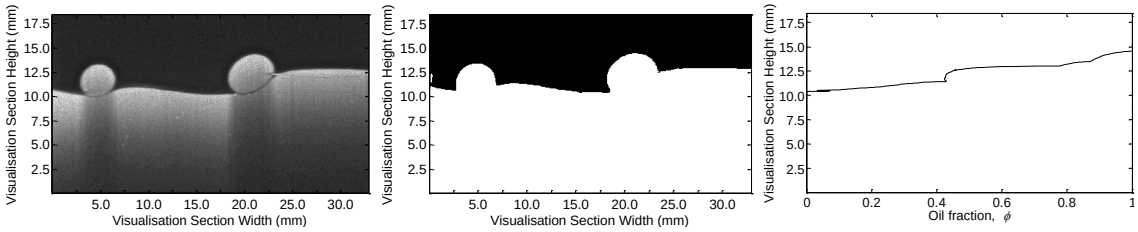

(a) Raw PLIF image (b) Binarised image, from (a) (c) Instantaneous vertical phase fraction profile, from (b)

Figure 3-21: Diagram to show MATLAB image processing technique to generate phase distribution data

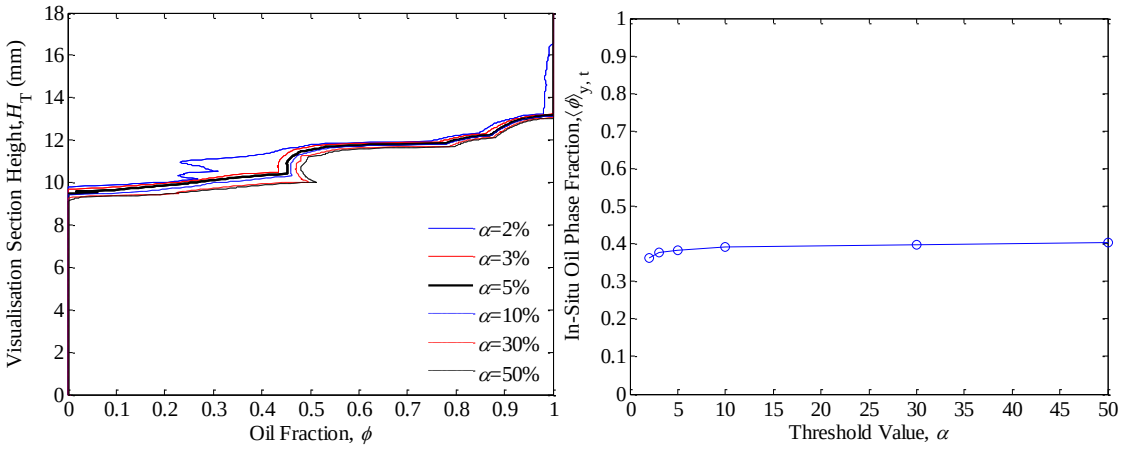

(a) (b)

Figure 3-22: Investigation of the effect of thresholding and binarisation on the instantaneous image presented in Figure 3-23: (a) Variations in the identification of the interface location, and (b) variations in the image-averaged instantaneous in-situ oil fraction $\langle\varphi\rangle_{y,t}$ (as defined in Equation 2), in both cases due to the use of different thresholding parameters α, from 2% to 50%. Our selected value was $\alpha = 5\%$

3.11.3 In-Situ Phase Fraction

The instantaneous in-situ oil phase fraction $\langle\varphi\rangle_y(t) \equiv \langle\varphi\rangle_{y_i}$ in a single image is defined as the measured instantaneous volumetric ratio of oil, which is equal to the fraction of dark area in a single image. The in-situ phase fraction data $\langle\varphi\rangle_{y,t}$ has been acquired by employing the same initial steps as those detailed for the phase distribution analysis, and then by time-averaging the resulting vertical phase profiles to obtain a mean oil content in the measurement section for each flow condition, such that from *n* images:

$$\langle\varphi\rangle_y(t) = \frac{1}{H_T}\int_{y=0}^{y=H_T} \varphi(y,t)\, dy \qquad (3.4)$$

$$\langle\varphi\rangle_{y,t} = \frac{1}{n}\sum_{i=1}^{n}\langle\varphi\rangle_{y_i} \qquad (3.5)$$

The uncertainty in the instantaneous in-situ oil phase fraction amounts to ±4%. The in-situ phase fraction data $\langle\varphi\rangle_{y,t}$ is presented in Section 4.5, 5.5 and 6.5.

3.11.4 Interface Level

The instantaneous interface level $H(x,t)$ is defined as the height of the oil-glycerol interface from the bottom of the channel. The interface level analysis has been performed by selecting thirty images of maximum temporal spacing (by 100 frames) to ensure sample independence and by recording height H at five points (x positions) in each image, as shown pictorially in Figure 3-23 below. Thus, for each flow condition 150 interface height values were generated. The experimental uncertainty in the instantaneous interface level $H(x,t)$ is the same as that for the instantaneous interface location, i.e. ±10%.

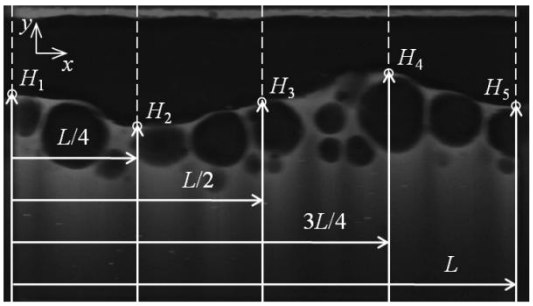

Figure 3-23: Interface level image processing, showing important definitions

The mean μ_H (Equation 3.6) and the standard deviation σ_H (Equation 3.7) of this data has been determined for each run (i.e., set of conditions):

$$\mu_H = \frac{1}{n}\sum_{i=1}^{n} H_i \tag{3.6}$$

$$\sigma_H = \sqrt{\frac{1}{n-1}\sum_{i=1}^{n}(H_i - \mu_H)^2} \tag{3.7}$$

In the interface level results that follow (see Section 4.6, 5.6 and 6.6) the $\mu + 2\sigma$ and $\mu - 2\sigma$ values are plotted. Assuming a normal distribution, these values represent the upper and lower limits of the 95 % confidence interval. The resulting relative uncertainties in the statistical estimation of the mean and standard deviation of the height H are both less than ±1% (0.8% and 0.6%, respectively).

3.11.5 Droplet Size Distribution

Finally, the droplet size analysis (see Section 4.7, 5.7 and 6.7) has been performed by measuring the area A_d of a number of droplets, after converting the PLIF images to black and white binarised images. For each set of conditions approximately 20 images and 100 droplets were selected and averaged. Equations (3.8) and (3.9) were used then to evaluate a mean effective droplet diameter μ_d:

$$d = 2\sqrt{A_d/\pi} \tag{3.8}$$

$$\mu_d = \frac{1}{n}\sum_{i=1}^{n} d_i \tag{3.9}$$

The relative uncertainty in the statistical estimation of the mean of the droplet size d is ±1%.

3.11.6 Interface Wave Velocity

The interface wave velocity has been calculated using an algorithm that has been developed in Matlab. The steps to the procedure as outlined in what follows. The first task is identifying the location of the glycerol solution – oil interface, this has been performed using the binarisation technique outlined in Section 3.11.2 and then calculating the verticle height of the interface from the bottom surface of the cell. This was done for every axial position in a frame and for every frame in a given run, i.e., for a fixed superficial mixture velocity U_{m} and input oil fraction φ_{in} combination. It should be noted that runs containing droplets above the interface were not analysed. Following identification of the interface level for an instantaneous image (this is shown for two successive images in Figure 3-24(a), where the abscissa is the axial direction of the flow and the interface level is on the ordinate axis) the image undergoes pre-processing. Firstly, the average interface level for a given instantaneous image is subtracted and then, secondly, the profile is scaled so that the interface level at the entrance and exit of the visualisation cell for a given a given instantaneous image occupy the same vertical plain. This is done by subtracting the linear profile between the ends from the actual profile. The result of this profile is shown for two successive instantaneous images in Figure 3-24(b). The aforementioned pre-processing was necessary for the cross-correlation process in MatLab to be performed. The cross correlation process between two successive images was then performed using Matlab. Figure 3-24(c) shows a plot of the correlation between the two images that have been used to construct Figures 3-24(a) and 3-24(b), where the abscissa is the axial displacement of the interface profile. A threshold was imposed on the correlation between two successive images, this being $C = 0.99$, if the correlation peak was below this level the correlation was deemed to be poor and the interface wave velocity between those two successive images was discarded. The point on the abscissa that corresponds to the correlation peak is the horizontal displacement of the interface wave (see Figure 3-24(d)). This, coupled with the time duration Δt

between the images (which is known though the frame rate), enables the interface velocity between two successive images to be calculated via Equation 3.10. It should be noted that for a given run the sampled images were selected such that the time interval between them was sufficient to provide an interface wave displacement of at least 15 pixels.

$$U_{\mathrm{int}} = \frac{D_{\mathrm{int}}}{\Delta t} \tag{3.10}$$

For a give run (i.e., a fixed mixture velocity U_{m} and input oil fraction φ_{in} combination) a series of U_{int} values are generated for successive images. From these, a time-average interface wave velocity $\langle U_{\mathrm{int}} \rangle_t$ and corresponding standard deviation can be computed. These are shown in Equations 3.11 and 3.12.

$$\langle U_{\mathrm{int}} \rangle_t = \frac{1}{n} \sum_{i=1}^{n} U_{\mathrm{int}} \tag{3.11}$$

$$\sigma_{U_{\mathrm{int}}} = \sqrt{\frac{1}{n-1} \sum_{i=1}^{n} \left(U_{\mathrm{int},i} - \mu_{U_{\mathrm{int}}} \right)^2} \tag{3.12}$$

For a given run, the interface wave velocity U_{int} between two successive images that lie outside the range $\langle U_{\mathrm{int}} \rangle_t \pm 4\sigma_{U_{\mathrm{int}}}$ are discarded. From the data set that remains, new values for the average interface wave velocity $\langle U_{\mathrm{int}} \rangle_t$ and associated standard deviation $\sigma_{U_{\mathrm{int}}}$ are calculated and the interface wave velocity U_{int} values that lie outside the 95% confidence interval (i.e., $\langle U_{\mathrm{int}} \rangle_t \pm 2\sigma_{U_{\mathrm{int}}}$) are discarded. It is the data set that remains that has been used to compute the average interface wave velocity $\langle U_{\mathrm{int}} \rangle_t$ for a given run.

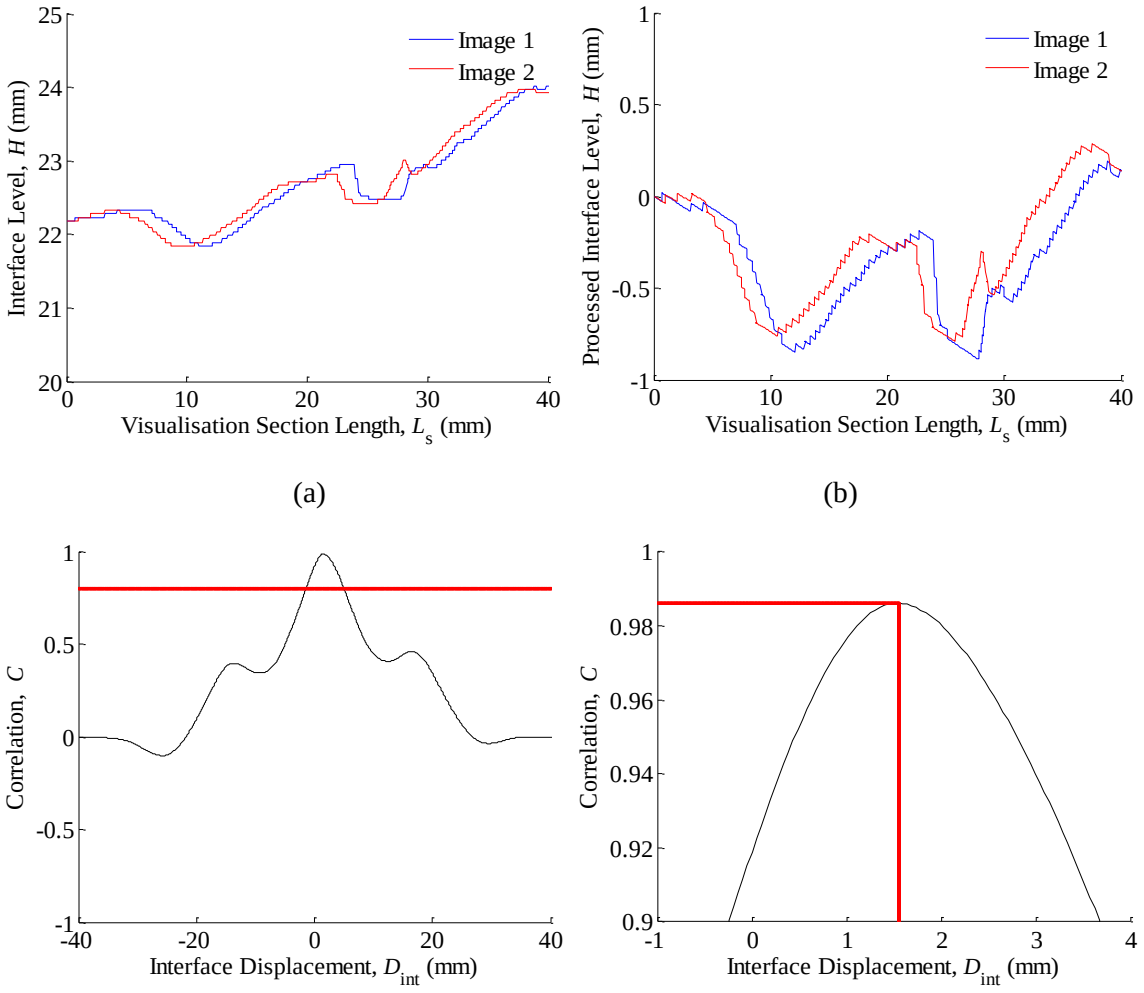

Figure 3-24: Process for determining the velocity of the waves at the liquid – liquid interface, specifically: (a) interface level profiles for two successive images; (b) the two successive images shown in Figure 3-26(a) after having undergone pre-processing; (c) the correlation between the pre-processed interface levels shown in Figure 3-26(b), including a C =0.99 acceptability threshold, and; (d) illustration that the peak C value corresponds to the interface displacement between the two successive images

3.11.7 Velocity Profiles

The velocity profiles of the glycerol-solution phase have been calculated using the DaVis software produced by LaVision. The process is conducted using a technique involving both Particle Image Velocimetry (PIV) and Particle Tracking Velocimetry (PTV). Although these processes ordinarily require the presence of seeded particles – which were not utilised in the studies presented in Chapters 4, 5 and 6 – determining the velocity profiles via this approach was possible from the presence of micro-bubbles of the oil in the glycerol-solution. The procedure first involves pre-processing the distortion-corrected images (see Section 3.11.1 for details of the graticule correction method), see Figure 3-27(a) for an example. It should be stated here that the velocity profile analysis was only performed on the flow images obtained with the use of the circular cross-section visualisation cell. The pre-processing involves subtracting a sliding minimum over time, i.e., for any pixel in a given image, its intensity is compared with the intensity of the corresponding pixel in both the image before and after in the time series and the minimum value of the three is subtracted. This improves the image quality by improving the signal-to-noise ratio, i.e., the contrast between the micro-bubbles and the background. A pre-processed image is shown in Figure 3-25(b). On completion of the pre-processing the velocity vectors are initially calculated via a multi-pass PIV algorithm. The PIV-PTV process is performed between successive images and the resultant velocity vectors relate to the movement of the fluid between them. Initially, the vectors of 128×128 interrogation windows within the whole image were established, these vectors were refined in a second pass using the same pixel size interrogation windows. The subsequent pass was performed using 64×64 interrogation windows; in which the vectors of the four 64×64 interrogation windows summate to the value of the 128×128 interrogation windows into which they fit. An example of the output from the PIV step of the overall procedure for determining the velocity profiles is presented in Figure 3-25(c); note that the velocity vectors that it contains are based on

interrogation windows of 64×64 pixels. The final velocity vectors are calculated using a PTV approach in which individual micro-bubbles are tracked. The 64×64 interrogation windows are split into sixty four 8×8 interrogation windows. A size restriction on the micro-bubbles was imposed, a range of 3 to 5 pixels. This was in order to prevent over sampling of individual micro-bubbles. Figure 3-27(d) presents an example of the velocity vectors that are generated between two successive images.

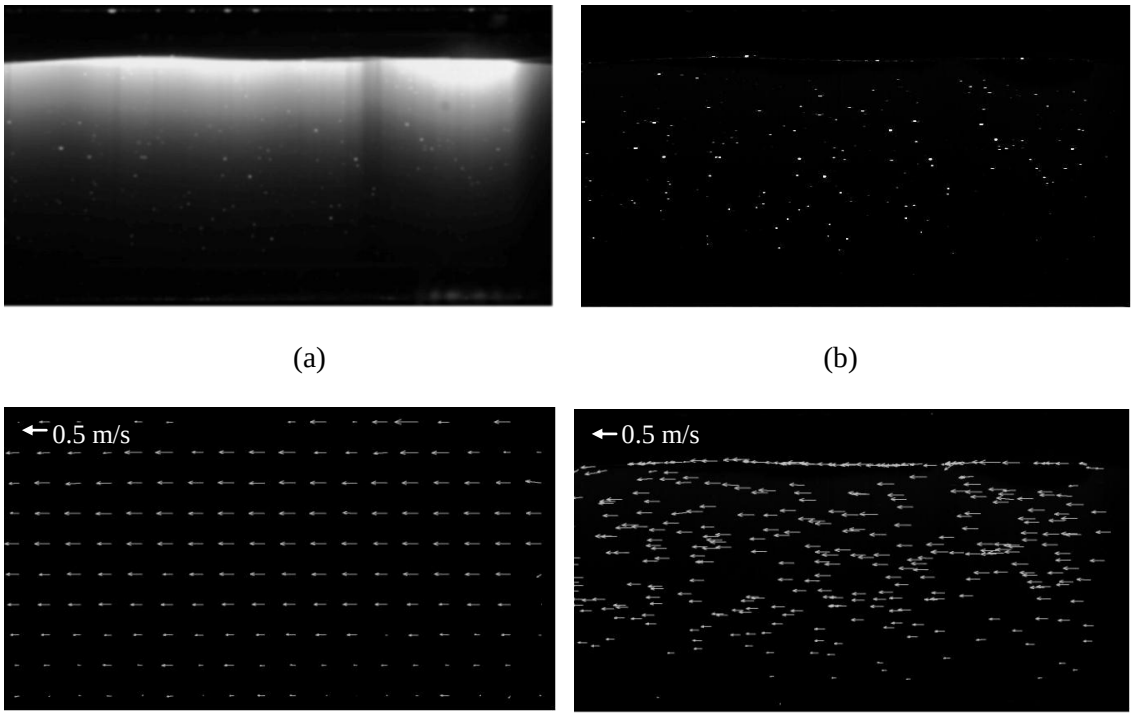

(a) (b)

(c) (d)

Figure 3-25: The PIV-PTV process for acquiring velocity vectors between two images separated by a known time interval: (a) a distortion-corrected LIF image; (b) shows the image in Figure 3-25(a) after it has undergone pre-processing (i.e., subtraction of sliding minimum pixel intensity); (c) a velocity vector map calculated using the PIV technique between two successive images, and; (d) a PTV vector map which is calculated from the PIV vector map shown in Figure 3-25(c). In (c) and (d) the size of the vectors (arrows) refers to the velocity

For a given run, i.e., time series of images, the vectors can be aggregated into a single image (shown in Figure 3-26). Such an image (i.e., time-averaged PTV velocity vector map) may contain spurious velocity vectors due to the fact no filter was applied on the instantaneous PTV velocity vector maps (see Figure 3-25(d)) due to the low vector density in those maps. However, this constraint does not apply to the time-averaged PTV maps (Figure 3-26) and filtering can be applied at this stage to remove the spurious vectors. This was done by employing a permissibility range on the velocity vectors in both the abscissa and ordinate directions. Vectors outside the ranges $V_x = 10 \pm 10$ m.s^{-1} and $V_y = 10 \pm 10$ m.s^{-1} were removed. As a next step, a median filter was used. In this step, velocity vectors in the time-average PTV vector map were removed if they were larger than 1.8 times the RMS (root mean square) of their neighbouring velocity vectors. An individual velocity vector is based upon the correlation peak between corresponding interrogation windows in successive images. If a velocity vector is removed due to the aforementioned criterion, it is replaced by another vector, that relates to the next highest peak in the correlation, if, it is less than 2.2 times the RMS of the neighbouring velocity vectors. If the second highest peak does not fit the third highest peak is tested and so on. From the aggregated PTV velocity vector map (Figure 3-26), a velocity profile can be generated (see Figure 3-27). The velocity profiles presented in Chapter 5 and Chapter 6 have been curve-fitted using the TableCurve 2D software package produced by Systat Software.

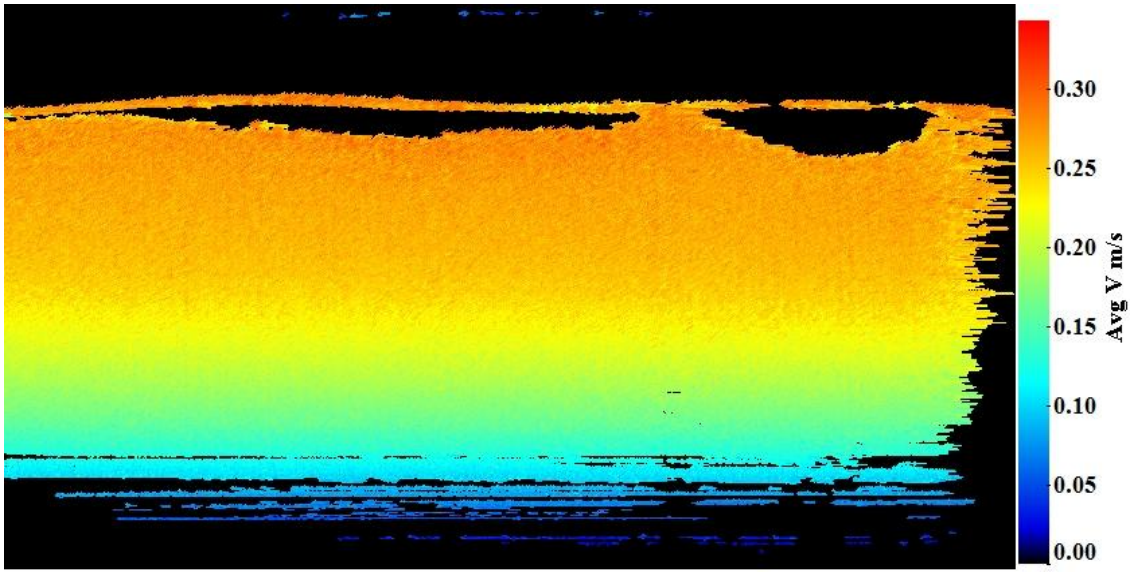

Figure 3-26: Aggregated PTV vectors for a given time series of LIF images at a fixed superficial velocity U_{m} and input oil fraction φ_{in} combination

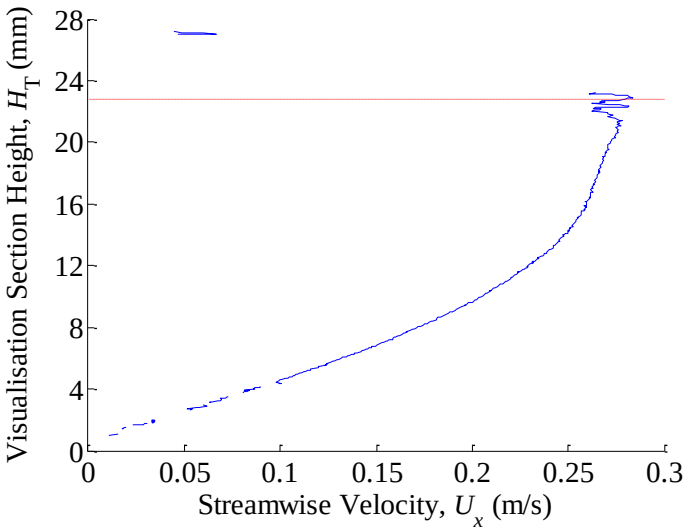

Figure 3-27: Flow velocity profile. The dotted red line indicates the average interface level μ_H for the particular flow run (superficial velocity U_{m} and input oil fraction φ_{in} combination) analysed

CHAPTER 4

Laser-Induced Fluorescence Studies of Horizontal Liquid-Liquid Flows in a Square Cross Section Duct

4.1 Introduction

The Planar Laser Induced Fluorescence (PLIF) technique was described in detail in Chapter 3. This technique yields high spatial and temporal resolution measurements, thus allowing the detailed diagnostic inspection of co-current liquid-liquid flows. In the current work, this technique was first applied to flow in a square cross section duct. Though square cross section ducts are clearly less typical of applications than are ducts of circular cross section, the use of the square cross section test section geometry avoids the distortion of the images which occurs with circular tubes. Work was pursued also with channels of circular cross section; in that case, it was necessary to correct the images for distortion. This latter work is described in Chapters 5 and 6.

In what follows, Section 4.2 describes the experimental bases for the square cross section duct experiments. Qualitative analysis of the results, including images of the flow regimes observed are presented in Section 4.3, which also includes a flow regime map constructed from the flow regime observations. In the succeeding sections the quantitative analysis of the images is

presented. In Section 4.4 the vertical phase distribution profiles results are presented, followed by results for in-situ phase fraction (Section 4.5), interface level (Section 4.6) and droplet size distribution (Section 4.7). Application of predictive methods to the results obtained is discussed in Section 4.8 and the conclusions of the work are presented in Section 4.9.

4.2 Experimental Operation

The experiments on the square cross section duct were carried out on the TOWER facility (Section 3.2) using a square cross section quartz visualisation section (Section 3.10.1). In these experiments, the PLIF system was synchronised with a Phantom V710 Monochromatic high speed video System (see Section 3.4.2). The test fluids were introduced into the test section such that the oil phase was injected at the top and the glycerol solution at the bottom (see Figure 3.5). Specific details on the operation of the TOWER facility from which these results have been obtained are outlined in Appendix 1.

Flow conditions are defined via two independent parameters that were varied independently in 48 runs: (i) the superficial mixture velocity U_m, defined as the sum of the volumetric flow rates of the two liquids (oil and glycerol solution) in the pipe section $Q_T = Q_{oil} + Q_{gs}$ divided by the cross-sectional area of the pipe $A = \pi D^2/4$; and (ii) the inlet volumetric phase fraction of oil in the pipe φ_{in}, defined as the volumetric flow rate of oil Q_{oil} divided by the total volumetric flow Q_T at the inlet of the pipe section. The two impendent inlet flow variables U_m and φ_{in} were kept constant during each run (i.e., each set of conditions) and were set by controlling the volumetric flow rates of each phase (i.e., the oil $Q_{oil}$and glycerol Q_{gs}) by means of globe valves, The experimental conditions spanned a range of U_m from 0.07 to 1.46 $m.s^{-1}$, though the main quantitative results in this chapter focus on the regimes observed in the lower U_m range (0.07 to 0.30 $m.s^{-1}$). In addition, φ_{in} was varied between 0.1 and 0.9. The matrix of experimental

conditions was selected based upon consultation of previous flow regime maps, most notably those by Soleimani (1999) and Hussain (2004), see Chapter 2.

4.3 Flow Regimes and Flow Regime Maps

In the co-current flow of two liquids, the accurate prediction of flow regimes and the characteristics that define them is desirable. Such flow regime predictions can allow more rigorous two-phase phenomenological models to be created that in turn can provide more accurate quantitative predictions of the flow. Of particular importance are predictions of the pressure drop across a multiphase oil production pipeline and the local in-situ phase fraction, the latter being a primary consideration (when coupled with the thermodynamic operating conditions of the pipeline) for evaluating whether hydrates will form in the pipelines.

Eight distinct flow regimes have been observed in the present PLIF study; the classification philosophy is akin to that of previous researchers (Russell et al. 1959; Charles et al. 1961; Nadler and Mewes 1995; Angelia and Hewitt, 2000; Solemani, 1999; Hussain, 2004). Examples of each of these 8 flow regimes are provided by instantaneous flow images in Figure 4-1 below. These can be grouped into four, more general flow types, which are: (1) stratified flow; (2) mixed flow, which is characterised by two distinct continuous phase regions with droplets in each; (3) two-layer flow, which comprised of a dispersed region and a continuous, unmixed region; and (4) dispersed flows. The categorisation of the eight flow regimes into these four groups is presented in Table 4-1. This categorisation of the flow phenomena is based on two important flow parameters: the input oil fraction φ_{in}; and the superficial mixture velocity U_m. A flow regime map corresponding to this flow characterisation, in which these parameters are indicated explicitly, is presented in Fig. 4-2.

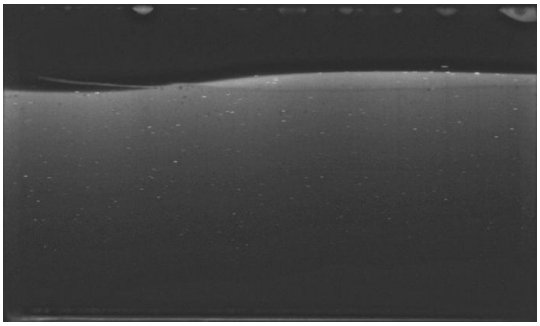

(a) Stratified flow

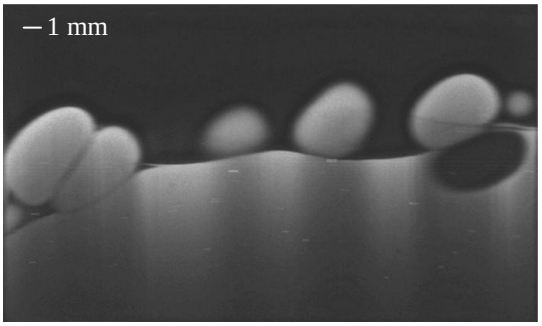

(b) Stratified flow with droplets

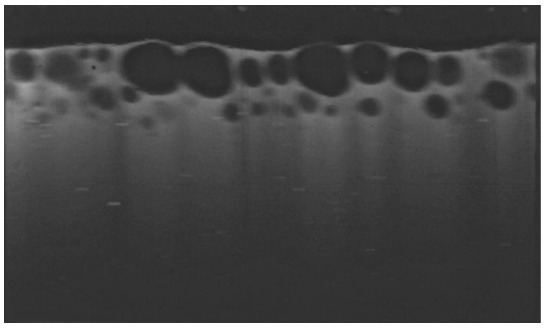

(c) Oil droplet layer

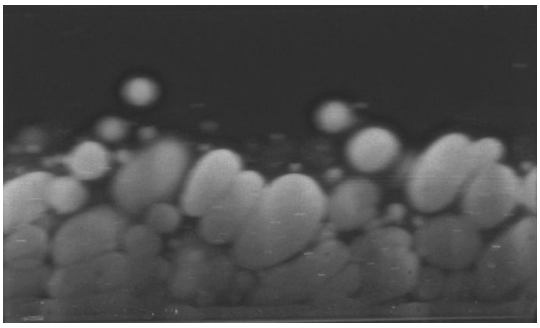

(d) Glycerol solution droplet layer

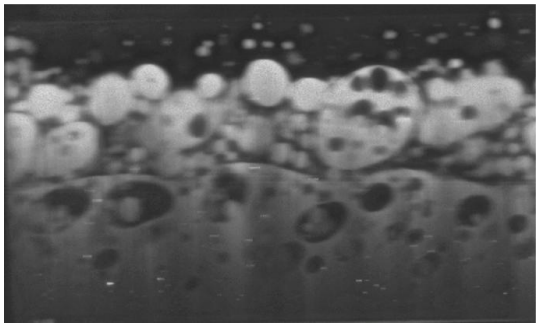

(e) Three layer flow

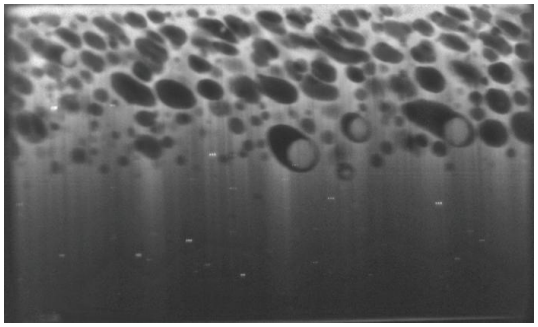

(f) Oil dispersion over glycerol solution

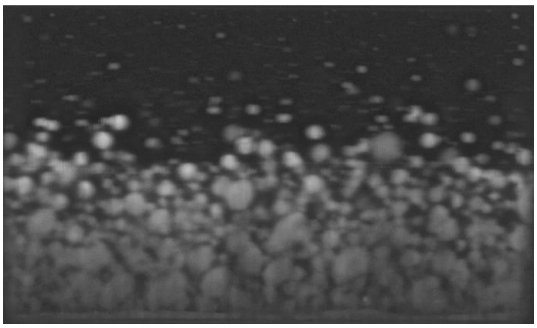

(g) Oil flow over glycerol solution dispersion with glycerol solution film

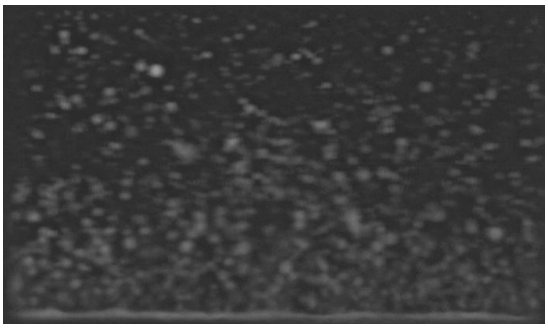

(h) Glycerol solution dispersion with glycerol solution film

Figure 4-1: Images of the 8 distinct flow regimes observed in the square cross section campaign

Table 4-1: Categorisation of observed flow regimes

Flow Regime Categories	Flow Regimes
Stratified Flow	Stratified flow
	Stratified flow with droplets
Mixed Flow	Oil droplet layer
	Glycerol solution droplet layer
	Three-layer flow
Two-Layer, Dispersed Over/Under Continuous Flow	Oil dispersion over glycerol solution flow
	Oil flow over glycerol solution dispersion
Dispersed Flow	Oil continuous dispersed flow
	Glycerol solution continuous dispersed flow

The observed flow regimes are in good general agreement with previous observations (Soleimani, 1999; Lovick and Angeli, 2003; Hussain, 2004). However, some regimes observed in previous investigations were not seen in the current study. Some investigators reported the establishment of oil-annulus annular flows (Russell et al. 1959; Charles et al. 1961; Hasson et al. 1970; Arirachakaran et al. 1989). In addition, Charles et al. (1961) and Hasson et al. (1970) reported the presence of water-annulus annular flow and oil-slugs-in-water. Neither annular or slug flow were observed in the current experimental campaign.

The absence of oil-annulus annular flow in the current campaign aligns with the findings and conclusions of Arirachakaran et al. (1989) who attributed the presence of annular flow to the physical properties of the oil phase. Specifically, that as the oil viscosity decreases the range of conditions (the input oil phase fraction φ_{in} and the superficial mixture velocity U_m) over which oil-annulus flow is observed diminishes, i.e., the oil is not dense and viscous enough to sustain a water core. Arirachakaran et al. (1989) reached this conclusion following an experimental campaign involving four different oils, each with a different viscosity; for the lowest viscosity

oil ($\mu_{\text{oil}} = 4.7$ mPa. s) oil-annulus annular flow was not observed. Angeli (1995), Nadler and Mewes (1995), Soleimani (1999) and Hussain (2004) did not observe the existence of annular flows but their results are consistent with those of Arirachakaran et al. (1989) as they all used oils with viscosity values below the oil viscosity value ($\mu_{\text{oil}} = 4.7$ mPa.s) for which Arirachakaran et al. (1989) did not observe annular flow.

However, several investigators observed annular flow when using oils with viscosities $\mu_{\text{oil}} > 4.7$ mPa. s. For example, Hasson et al. (1970) used an oil viscosity $\mu_{\text{oil}} = 21.7$ mPa. s; Charles et al. (1961) used oils of viscosity $\mu_{\text{oil}} = 6.27$ mPa. s and $\mu_{\text{oil}} = 65$ mPa. s, and; Oglesby et al. (1979) used an oil of viscosity $\mu_{\text{oil}} = 84$ mPa. s. Hasson et al. (1970) attributed the presence of water-annulus annular flow to the preferential wetting properties of water. The absence of annular flows has also been attributed to the effect of relative densities of the two test fluids. Those who observed the regime (Hasson et al. 1970; Charles et al. 1961) employed fluids of similar densities, i.e., $\rho_{\text{oil}}/\rho_{\text{aq}} \approx 1$. Investigators who used fluids with density ratios dissimilar to unity, e.g. $\rho_{\text{oil}}/\rho_{\text{aq}} \approx 0.8$ (Kurban 1997, Angeli,1996, Soleimani, 1999 and Hussain,2004) did not observe annular flow. The density ratio of the fluids used in the present study is $\rho_{\text{oil}}/\rho_{\text{gs}} \approx 0.66$.

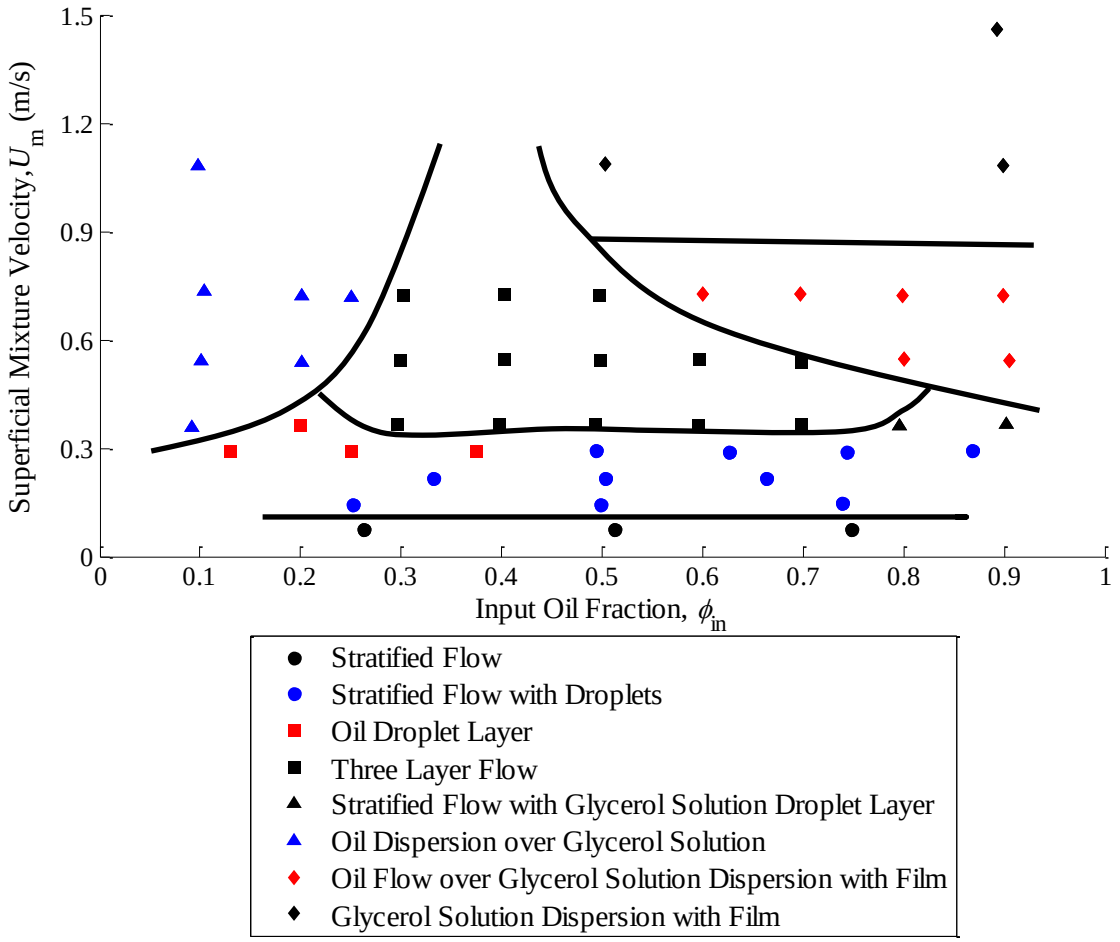

Figure 4-2: Flow regime map

The locations of the flow patterns observed in the present experiments are shown in Figure 4-2 as a function of total mixture superficial velocity and input oil fraction. From the flow regime map (Figure 4-2) it can be seen that the smooth stratified flow regime is observed for all investigated oil input phase fractions (φ_{in} = 0.25 to 0.75) at superficial mixture velocities of U_m = 0.07 m.s^{-1}. As the total superficial velocity increases, different arrangements of stratified flow with droplets were observed up to the onset of *three-layer* flow at a superficial mixture velocity of U_m = 0.36 m.s^{-1}. As the superficial mixture velocity increases further, the range of oil input phase fractions over which three-layer flow is observed diminishes and dispersed flows are seen to cover a boarder range of oil input phase fractions. Oil dispersions are found at

increasingly higher oil input phase fractions and glycerol solution dispersions at increasingly lower oil input phase fractions as the superficial mixture velocity increases.

A notable finding in the present work has been the positive identification of three-layer flows (e.g., see Figure 4.1(e)). Three-layer flow is characterised by distinct continuous oil and glycerol solution phase regions at the top and bottom of the pipe respectively with a highly mixed zone between them. There have been some reports of such flows (Angeli and Hewitt, 2000a,b; Soleimani, 1999; Hussain, 2004), but the present investigation sheds further light onto their nature. Lovick and Angeli (2004) reported a *dual continuous flow* regime that is characterised by both phases retaining their continuity at the top and bottom of the pipe while each phase is dispersed, at various degrees, into the continuum of the other (see Figure 2-18). This description has a large degree of commonality with three layer flow. The flow regime map constructed from the PLIF images is presented in Figure 4-2.

An earlier version of the experimental facility employed in this study was used in the liquid-liquid flow studies by Soleimani (1999) and Hussain (2004). Hence, one can make direct comparisons with the flow regime maps of these investigators. The fundamental modification has involved the replacement of the water phase used in the previous investigations with a glycerol solution containing a small concentration of a fluorescent dye. The use of the glycerol solution allows matching of the refractive indices of the two fluids; an essential requirement for the generation of PLIF images free of distortion arising from refraction. In the present experiments, the heavier (glycerol solution) had a density somewhat higher than water ($1213.3\,\mathrm{kg.m^{-3}}$) and a viscosity much higher than water ($82.3\ \mathrm{mPa.s}$). It is interesting to observe the effect of these changes in physical properties on the resulting flow regimes. Hussain (2004) reported stratified wavy flow at higher superficial mixture velocities (up to $U_m = 3\ \mathrm{m.s^{-1}}$), whereas in the current campaign the limit for stratified flow is $U_m = 0.3\ \mathrm{m.s^{-1}}$. Furthermore, Hussain (2004) reported three layer flow in the oil fraction range $\varphi_{in} = 0.2$ to 0.5

which is different to the range observed in the current experiments, namely $\varphi_{in} = 0.3$ to 0.7. Soleimani (1999) found the onset of stratified wavy flow with droplets and the onset of three layer flows occur at lower superficial mixture velocities than found in the present experiments. There is a significant overlap in the superficial mixture velocity and oil fraction combinations between the three layer flow regime observed in the present study with the *dual continuous flow* regime reported by Lovick and Angeli (2004). Lovick and Angeli (2004) reported the onset of dual continuous at $U_m = 0.80$ m.s^{-1} and that, as the superficial mixture velocity increases, the range of oil input fractions over with the regime is observed diminishes; this behaviour is similar to that for three layer flows in the present experiments.

Another pertinent finding of the present campaign has been the positive identification of secondary and multiple dispersions. Such dispersions have been widely reported in agitated vessels (Luhning and Sawistowski, 1971; Pacek and Nienow, 1995 and Liu et al, 2005). However, their presence in two-phase dispersed flows has been reported less widely. Pal (1993) observed secondary dispersions in pipeline flow exclusively around the transition from water-in-oil (w/o) to oil-in-water (o/w) dispersions. However, in the current campaign secondary dispersions were not limited to the ambivalent range (see Section 2.3 for details). This is illustrated in Figures 4-3(a) and 4-3(b) in which oil-in-glycerol solution-in-oil (i.e. o/w/o) and glycerol solution-in-oil-in-glycerol solution droplets (i.e. w/o/w) are observed at $\varphi_{in} = 0.13$ and $\varphi_{in} = 0.87$, respectively.

The results are in agreement with the findings of Liu (2005) who found that both water-in-oil-in-water (w/o/w) and oil-in-water-in-oil (o/w/o) droplets could appear under the same experimental conditions. This is shown in Figures 4.3(b) and 4.4(a) in which both oil-in-glycerol solution-in-oil (i.e. o/w/o) and glycerol solution-in-oil-in-glycerol solution (i.e. w/o/w) droplets can be seen. Multiple dispersions were also observed, Figure 4.4(b) shows a ternary dispersion of glycerol solution-in-oil-in-glycerol solution-in-oil (w/o/w/o).

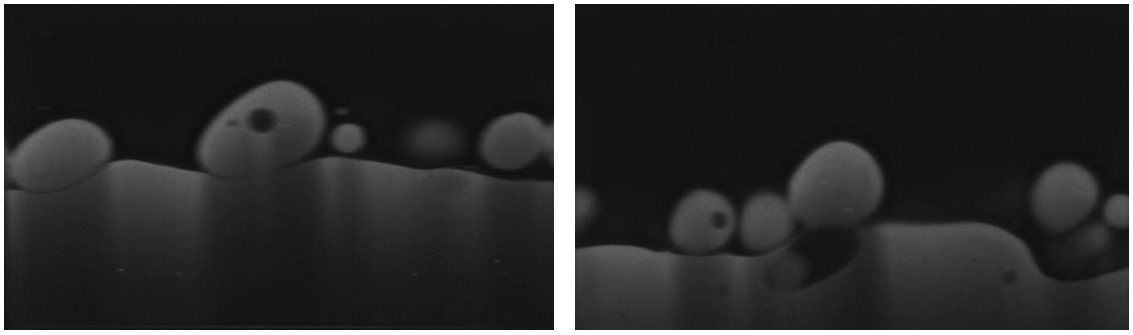

(a) (b)

Figure 4-3: Secondary dispersions of (a) oil-in-glycerol solution-in oil droplets at an oil input fraction of φ_{in} = 0.13, and (b) oil-in-glycerol solution-in oil and glycerol solution-in-oil-in-glycerol solution droplets at an oil input fraction of φ_{in} = 0.87, both at a superficial mixture velocity U_m of 0.29 m.s^{-1}

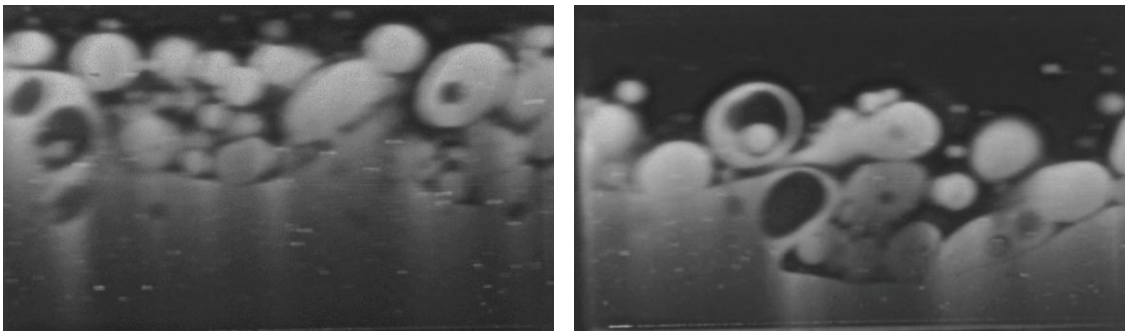

(a) (b)

Figure 4-4: (a) Secondary dispersions oil-in-glycerol solution-in oil droplets at an oil input fraction of φ_{in} = 0.13, and (b) secondary and ternary dispersions of oil-in-glycerol solution-in oil and glycerol solution-in-oil-in-glycerol solution droplets at an oil input fraction of φ_{in} = 0.87, both at a superficial mixture velocity $U_m$of 0.29 m.s^{-1}

4.4 Vertical Phase Distribution Profiles

The vertical distribution of the phases in the PLIF pictures has been determined using the technique detailed in Section 3.11.2. An additional quantifiable output of the work detailed in

this section is the phase fraction of the dispersed phase φ_{disp} above and below the interface i.e., the glycerol solution phase fraction entrained in the oil above the interface and the oil entrained in the glycerol solution below the interface. This has been achieved by coupling the phase distribution profiles with the respective interface level H measurements as detailed in Section 4.6. Measurements of the entrained fraction can be used to determine effective viscosity of each layer (aqueous phase continuous and oil phase continuous) by accounting for the presence of droplets in the respective layers. This in turn yields a revised viscosity ratio (of the fluid above the interface to that of the fluid below the interface), which is a key input required for the closure of predictive techniques to predict the in-situ phase fraction (Section 4.5).

Figure 4-5 shows vertical oil phase fraction profiles $\bar{\varphi}(y)$ (defined in Equation 3.3) for the full range of oil fractions φ_{in} and with selected superficial mixture velocities U_m of: (a) 0.07 m.s^{-1}, (b) 0.14 m.s^{-1}, (c) 0.21 m.s^{-1} and (d) 0.29 m.s^{-1}. Figure 4.6 shows vertical phase profiles $\bar{\varphi}(y)$ for the full range of superficial mixture velocities U_m and selected input oil fractions φ_{in} of: (a) 0.25, (b) 0.50 and (c) 0.75.

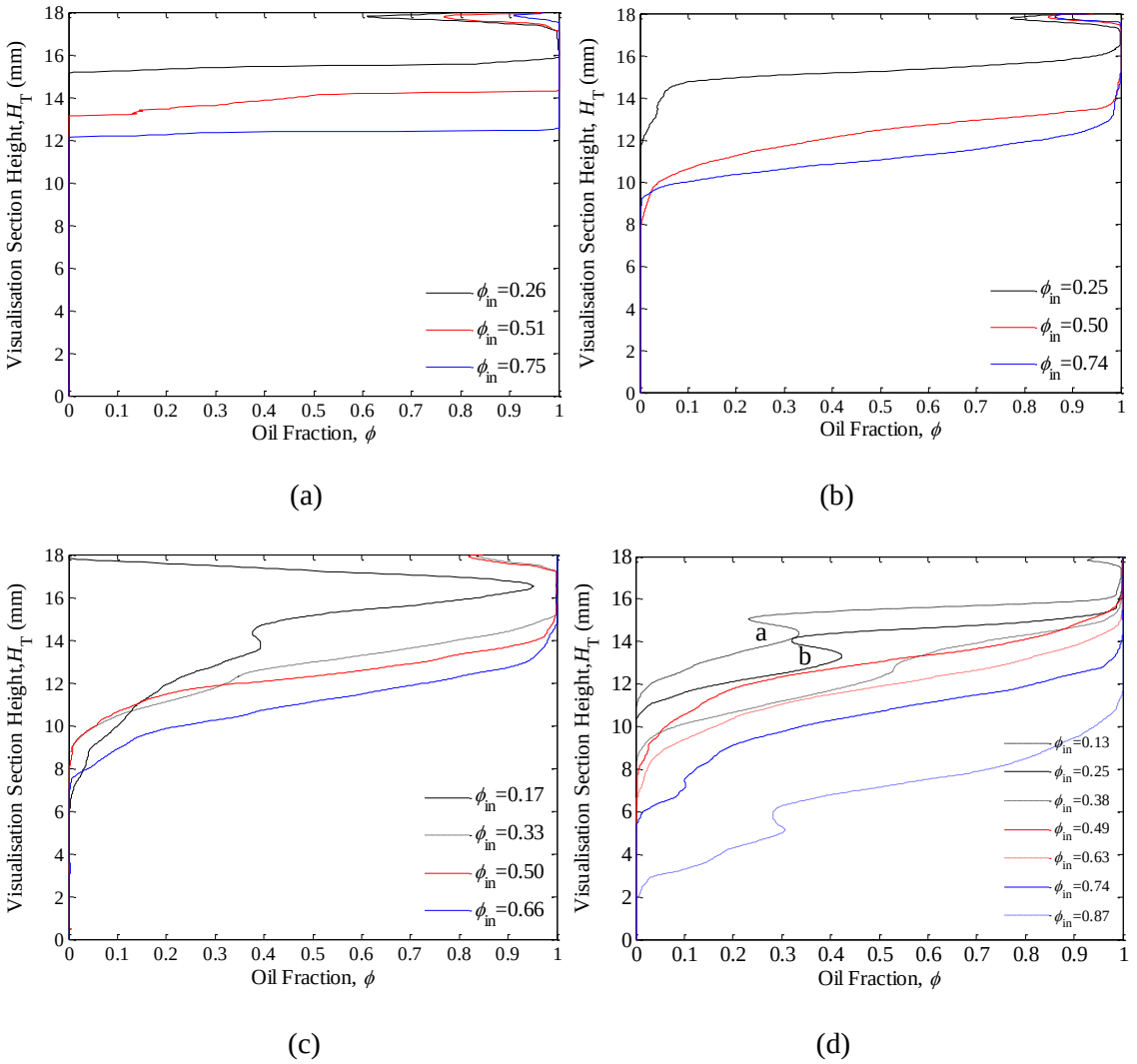

Figure 4-5: Vertical oil phase fraction profiles $\bar{\varphi}(y)$ at different input oil fractions φ_{in} for a superficial mixture velocity U_m of: (a) 0.07 m.s^{-1}; (b) 0.14 m.s^{-1}; (c) 0.21 m.s^{-1}, and; (d) 0.29 m.s^{-1}

From inspection of Figures 4-5 and 4-6 one can infer that there are three distinct regions in the flow; an oil zone at the top of the channel, an aqueous phase zone at the bottom of the channel and a mixed region between them. This zone categorisation of the flow is illustrated in Figure 4-7.

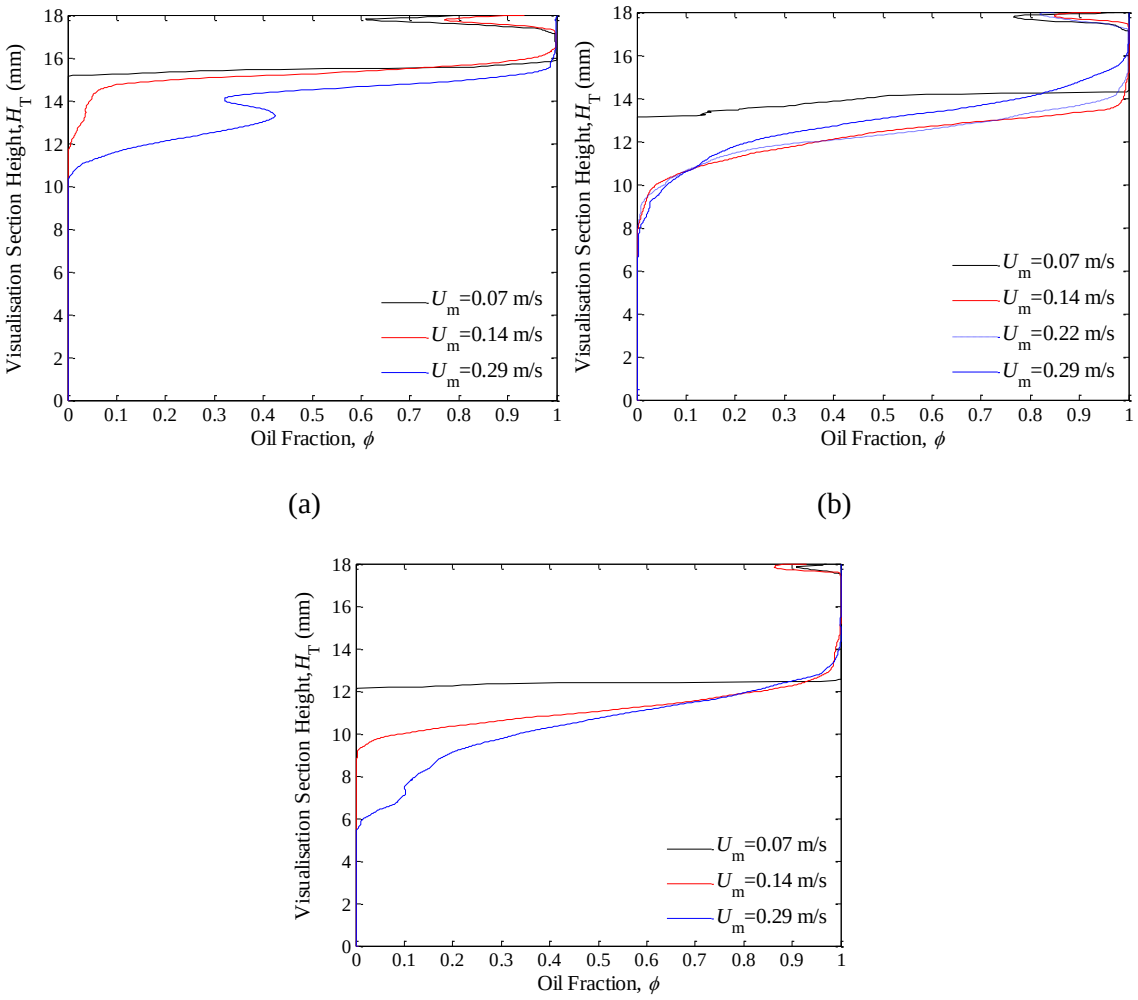

Figure 4-6: Vertical oil phase fraction profiles $\bar{\varphi}(y)$ for different superficial mixture velocities U_m at an input oil fraction φ_{in} of: (a) 0.25, (b) 0.50, and (c) 0.75

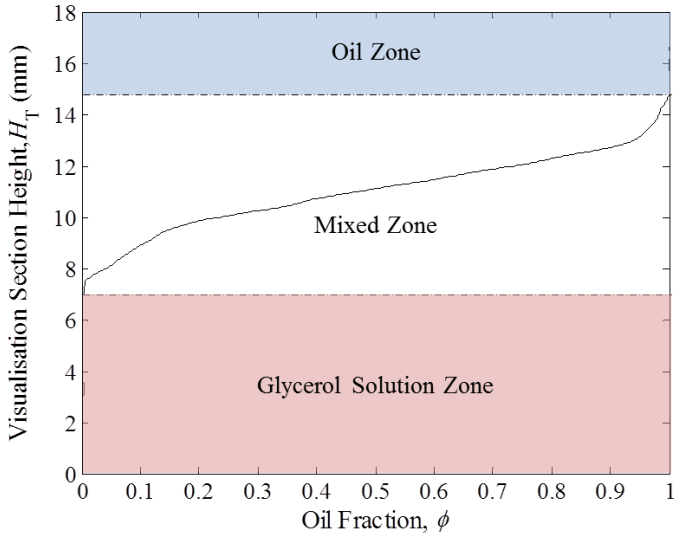

Figure 4-7: Schematic zone categorisation of liquid-liquid flows based upon phase distribution

At lower superficial flow velocities, the mixed zone covers a narrow vertical range and hence the transition from the glycerol zone to the oil zone (i.e. $\varphi = 0$ to $\varphi = 1$) occurs over a small vertical distance and the interface is nearly horizontal, as exemplified by the results shown in Figure 4-5(a) for $\varphi_{in} = 0.26$ and $U_m = 0.07$ m.s^{-1}. In this case, the flow is in the stratified smooth flow regime and the fluctuations in the interface height with time are minimal, i.e., the flow is not significantly wavy. This is supported by Figure 4-8 which shows instantaneous images of the flow taken at different times for these low superficial flow velocity conditions.

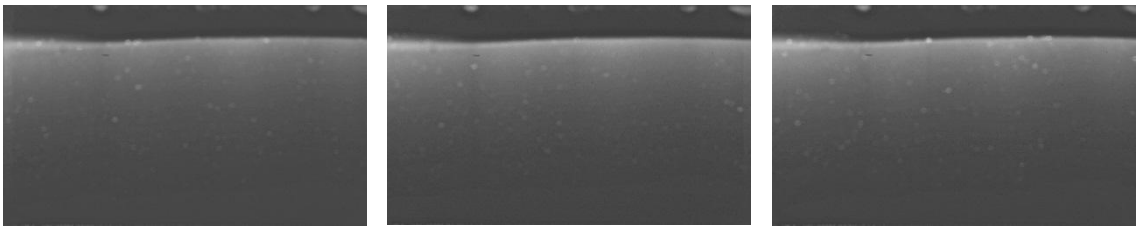

(a) (b) (c)

Figure 4-8: Instantaneous flow images for an oil input phase fraction $\varphi_{in} = 0.26$ and superficial mixture velocity $U_m = 0.07$ m.s^{-1} at: (a) $t = 0$ seconds; (b) $t = 1$ s, and; $t = 2$ s

A constant gradient transition from the glycerol zone to the oil zone (i.e. $\varphi = 0$ to $\varphi = 1$), such as that for $\varphi_{in} = 0.74$ and $U_m = 0.14$ m.s^{-1} shown in Figure 4-5(b), can be explained by the presence of waves at the interface of regular frequency f and constant amplitude A, such as the case of a sine wave at the interface, see Figure 4-9(a). When time-averaged, results for such an interface configuration have the form shown in Figure 4-9(b).

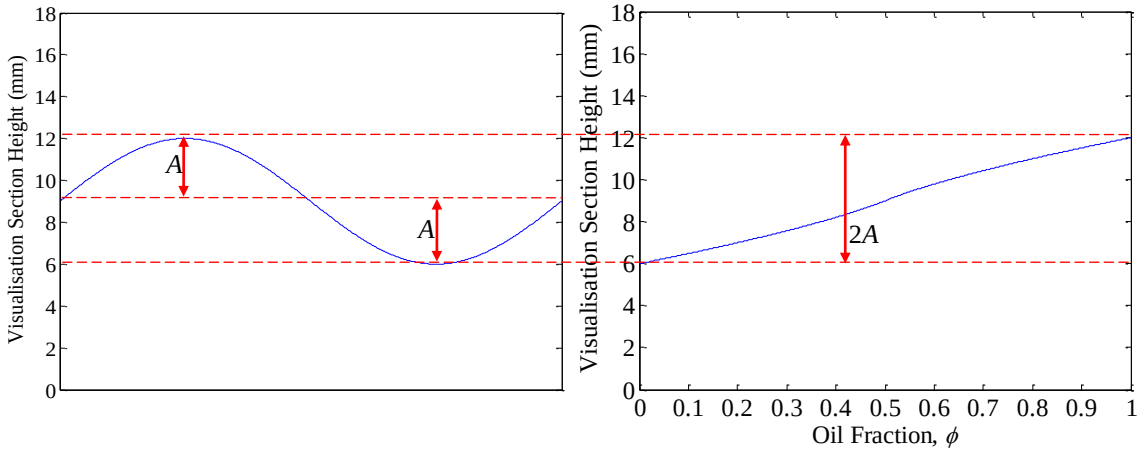

Figure 4-9: (a) Sine wave profile, and; (b) the associated phase distribution profile

Figure 4-5 shows that as the input oil fraction increases the height of the glycerol zone decreases. In addition, one can observe from Figures 4-5 and 4-6 that as the superficial mixture velocity increases the height of the mixed zone increases, i.e., the gradient of the transition between the glycerol zone the oil zone increases; this is more clearly seen in Figure 4-10(a). If one looks beyond the scope of the superficial mixture velocities analysed in this study to those investigated by Soleimani (1999) it can be seen that this trend would be expected to continue all the way to fully dispersed flows in which there the phase fraction is constant along the vertical axis of the channel. From Figure 4-10(b) it can be seen that for a low superficial mixture velocities, the height of the mixed zone has a maximum at an oil input phase fraction of $\varphi_{in} = 0.50$. Furthermore, as the total superficial velocity increases (such as for $U_m = 0.29$ m.s^{-}

[1]) the aforementioned trend continues, though peaks in the mixed zone height are also seen at low and high oil input phase fractions.

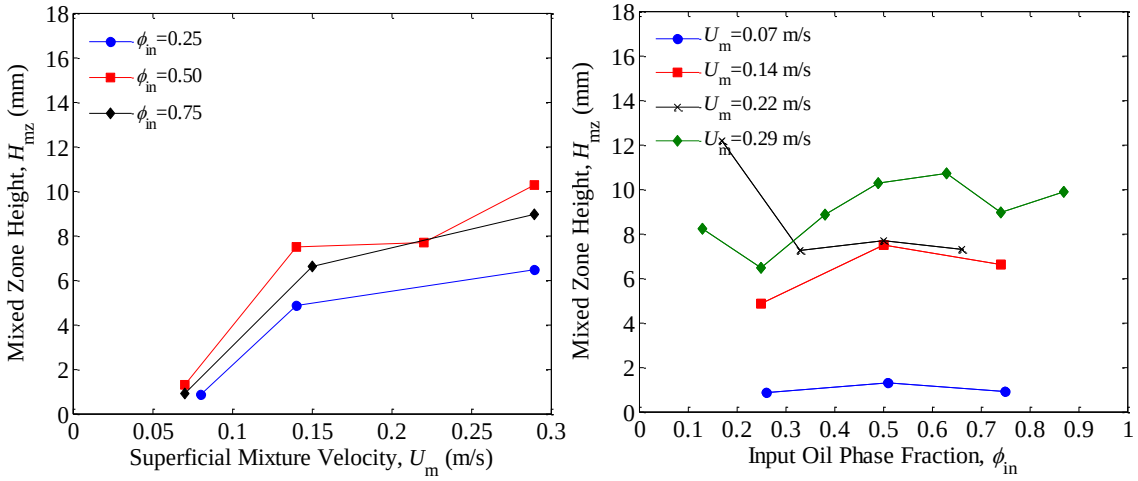

(a) (b)

Figure 4-10: Height of Interface Zone for as a function of (a) superficial mixture velocities U_m for constant input oil fraction φ_{in}; (b) input oil fraction φ_{in} for constant superficial mixture velocities U_m

The presence of droplets and the non-uniform wave characteristics of *dual continuous flow* give rise to more complex features in the vertical phase distribution profiles, such as seen at the points labelled "a" and "b" in Figure 4-5(d), both for a superficial mixture velocity of $U_m = 0.29$ m.s^{-1} and oil input phase fraction of $\varphi_{in} = 0.13$ and $\varphi_{in} = 0.25$, respectively. This "S" shape in the mixed region (see Figure 4-7) can be explained by the presence of an oil droplet layer below the interface. Figures 4-11(a) and 4-11(b) present instantaneous images of the flow for both of these conditions showing that there is an oil-droplet layer below the interface.

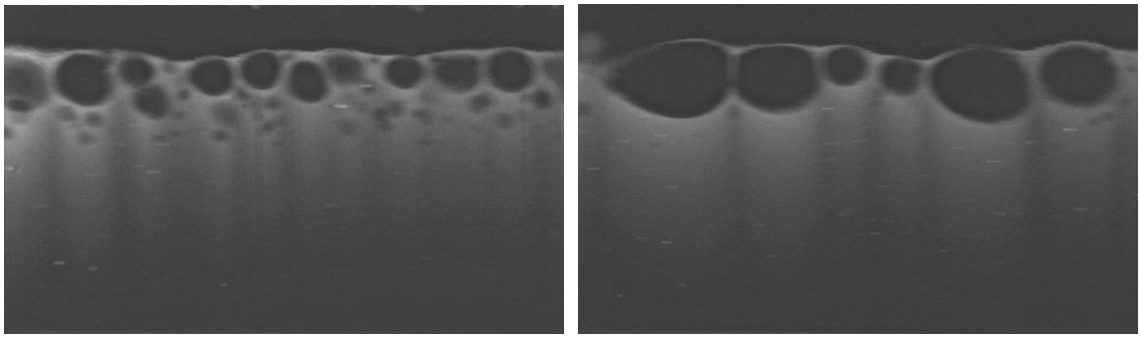

(a) (b)

Figure 4-11: Instantaneous flow images highlight the presence of an oil droplet layer below the interface for $U_m = 0.29$ m.s^{-1} at: (a) $\varphi_{in} = 0.13$, and; (b) $\varphi_{in} = 0.25$

The analysis presented in this section is developed further in Section 4.8 in which the phase distribution profiles are coupled with the respective interface level H measurements (Section 4.6) to determine the phase fraction of the dispersed φ_{disp} phases above and below the interface i.e., the glycerol solution phase fraction entrained in the oil above the interface and the oil entrained in the glycerol solution below the interface. As will be shown in Section 4.8, this allows calculation of the effective viscosity of the two layers for incorporation into models for such flows.

4.5 In-Situ Phase Fraction

An ability to accurately characterise the in-situ phase fractions in two-phase flows is of fundamental importance. It allows the determination of numerous other flow parameters, such as the two-phase density and viscosity which are key requirements for the closure of multiphase models for predicting multiphase flow behaviour, particularly pressure drop and flow pattern transitions, both of which are dependent on the in-situ phase fraction.

One key liquid-liquid flow phenomenon which is dependent on the in-situ phase fraction is phase inversion (see Section 2.3). This phenomenon, i.e., the transition from an oil-in-water dispersion to a water-in-oil dispersion, is associated with a sharp peak in the mixture viscosity (see Figure 2-23), and thus in turn, a sharp peak in the pressure drop. If one considers multiphase flow production lines from oil wells, there can be significant ramifications from operating in this region. The higher viscosity can increase the pumping requirements and furthermore, result in pressure surges that risk exceeding the maximum arrival pressure of the facility the oil lines feed into. Thus with accurate prediction of the in-situ phase fractions one can set and monitor the input conditions so as to ensure they do not encounter the issues associated with phase inversion and continue to operate in a preferred flow regime. The sound prediction of in-situ phase fraction is also a key parameter for predicting heat transfer from flow lines. A comprehensive grasp of the heat dissipation from flow lines is essential as it allows the prediction of the in-situ fluid temperature, which is the controlling parameter in the formation of solid phases such as waxes and hydrates. Knowledge of the fluid temperature in these cases is a key factor in designing systems for the mitigation of solid formation.

This section presents the in-situ phase fraction experimental results and assesses the suitability of various prediction techniques for characterising it. In addition, comparison of the results obtained for in-situ phase fraction $\langle\varphi\rangle_{y,t}$, as a function of the input phase fraction φ_{in}, with results obtained for other systems is evaluated as a means to gain insight in the influence the physical properties of the test fluids.

The results for the in-situ oil phase fraction $\langle\varphi\rangle_{y,t}$ (from Equation 3.5) are shown in Figure 4-12. It can be seen that the in-situ phase fraction $\langle\varphi\rangle_{y,t}$ is lower than the input oil fraction φ_{in} for almost all flow conditions, indicated by the data points in the figure lying below the straight line with unity gradient that passes through the origin (denoted as $S = 1$).

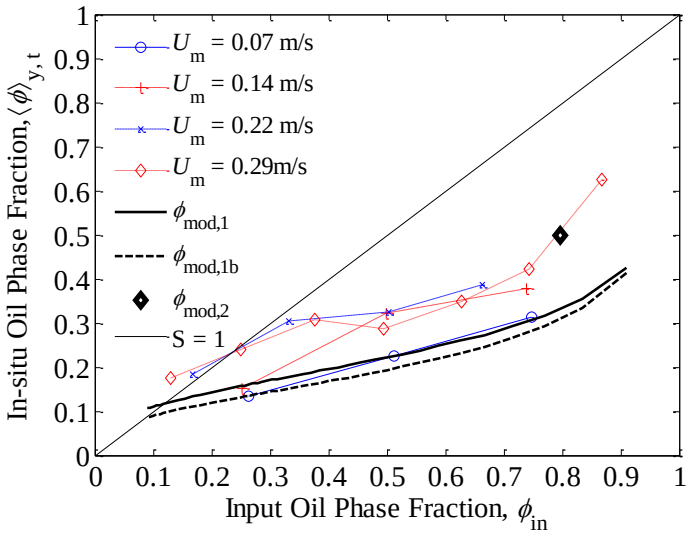

Figure 4-12: In-situ fraction $\langle\varphi\rangle_{y,t}$ as a function of input oil fraction φ_{in} for different superficial mixture velocities U_m

4.5.1 Laminar Drag Model

Firstly, the in-situ phase fraction $\langle\varphi\rangle_{y,t}$ was calculated using a laminar drag model, the details of which are given in Appendix 2. In this model, the two phases are assumed to be flowing in stratified flow and the pressure gradients in the two phases are assumed equal. The pressure gradients for the ith phase may be calculated from the friction factor relationship[1]:

$$f_i = \frac{\Delta p}{\frac{1}{2}\rho_i U_i^2}\frac{D_i}{4L} = \frac{16}{Re_i} \qquad (4.1)$$

1 It should be acknowledged that the recommended form of the Fanning friction factor for flow in a square channel is $f_i = \frac{14.227}{Re_i}$ however, the results obtained for $\varphi_{mod,1}$ are independent of the numerator in Equation 4.1.

where D_i is the equivalent diameter of phase i (taking account of the interfacial area) and $\mathrm{Re}_i = \rho_i U_i D_i / \mu_i$ is the Reynolds number for phase i. Thus there are two equations for the two phases and, after equating pressure drops $\Delta p/L$, Equation 4.1 reduces to a quintic:

$$Xy_1^5 + 4Xy_1^4 + 4Xy_1^3 - 4y_1^2 - 4y_1 - 1 = 0 \qquad (4.2)$$

where:

$$X = \left(\frac{Q_{gs}}{Q_{oil}} . \frac{\mu_{gs}}{\mu_{oil}}\right); \quad \frac{Q_{oil}}{Q_{gs}} = \frac{\varphi_{in}}{1-\varphi_{in}}; \quad Re_i = \frac{\rho_i U_i D_i}{\mu_i}; \quad D_i = \frac{4A_i}{P_i}; \quad y_1 = \frac{Y_{oil}}{Y_{gs}} \qquad (4.3)$$

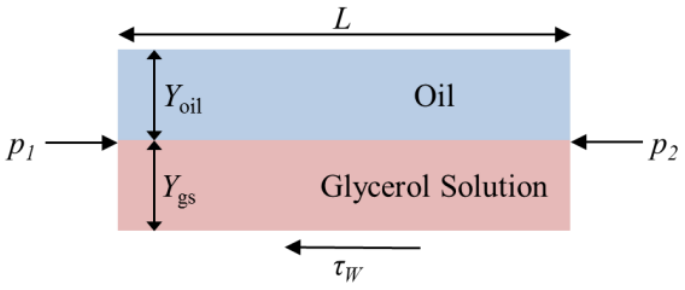

Figure 4-13: Stratified liquid-liquid flow model construction

The height of the interface can be calculated from Equation 4.2 and compared with measured values.

Comparisons of the values of *in situ* phase fraction calculated by the laminar drag model with those measured in the present experiments are shown in Figure 4-12 (here, the laminar drag model is denoted as $\varphi_{mod,1}$); excellent agreement is obtained between the model and the experimental data points relating to the low-velocity stratified flow (U_m =0.07 m.s^{-1}).

In calculating the equivalent diameter of the two flow regions (aqueous and oil), the interfacial contact area was included in the wetted perimeter. A similar model can be derived ($\varphi_{\mathrm{mod,1b}}$) in which the interfacial contact area between the two fluid streams is neglected in terms of its contribution to the equivalent diameter. In this case $D_i = \frac{4Y_{\mathrm{oil}}W}{2Y_{\mathrm{oil}}+W}$, where W is the width of the square channel. In this case Equation 4.2 is modified to the form $Xy_1{}^5 + 6Xy_1{}^4 + 9Xy_1{}^3 - 9y_1{}^2 - 6y_1 - 1 = 0$. The results obtained using this modified formulation are shown in Figure 4-12 by the dashed bold curve; it is clear from Figure 4-12 that the results from the two analyses are almost identical.

Finally, the modelled in-situ oil phase fraction $\langle\varphi\rangle_{y,t}$ presented in Figure 4-6 is defined as:

$$\varphi_{\mathrm{mod,1}} = \langle\varphi\rangle_{y,t} = \frac{Y_{\mathrm{oil}}}{Y_{\mathrm{oil}} + Y_{\mathrm{gs}}} = \frac{y_1}{y_1 + 1} \tag{4.4}$$

4.5.2 Differential Momentum Balance Model

A second form of analysis was also performed, the result from which is denoted by $\varphi_{\mathrm{mod,2}}$ in Figure 4-12. This is based upon the average velocities of each liquid flow in the co-current flow arrangement of two immiscible liquids, derived from a differential momentum balance (Bird et al., 2001). The model assumes that the fluids are flowing sufficiently slowly that no instabilities occur i.e., the interface remains exactly planar. It is applicable to the special case in which the in-situ oil fraction $\langle\varphi\rangle_{y,t} = 0.5$, i.e., when the interface level H is at the midpoint of the pipe ($Y_{\mathrm{oil}} = Y_{\mathrm{gs}} = H = H_{\mathrm{T}}/2$ in Figure 4-13). The input oil fraction φ_{in} that results in this value of in-situ oil fraction (i.e., $\langle\varphi\rangle_{y,t} = 0.5$) is given by:

$$\varphi_{\mathrm{mod},2} = \varphi_{\mathrm{in}} = \frac{y_2}{y_2 + 1} \tag{4.5}$$

where $y_2 = \frac{Q_{\mathrm{oil}}}{Q_{\mathrm{gs}}}$. Now, bearing in mind that $Y_{\mathrm{oil}} = Y_{\mathrm{gs}} = H_{\mathrm{T}}/2$ we obtain:

$$y_2 = \frac{Q_{\mathrm{oil}}}{Q_{\mathrm{gs}}} = \frac{\langle u_x^{\mathrm{oil}} \rangle}{\langle u_x^{\mathrm{gs}} \rangle} \tag{4.6}$$

Hence, $\varphi_{\mathrm{mod},2} = \varphi_{\mathrm{in}}$ can be evaluated from the ratio of the average/bulk velocities of each liquid in the co-current flow, which is derived from differential momentum balances:

$$\langle u_x^{\mathrm{oil}} \rangle = \frac{2}{H_{\mathrm{T}}} \int_0^{H_{\mathrm{T}}/2} u_x^{\mathrm{oil}} dy = \frac{\Delta p H_{\mathrm{T}}^2}{48 \mu_{\mathrm{oil}} L} \left(\frac{7\mu_{\mathrm{oil}} + \mu_{\mathrm{gs}}}{\mu_{\mathrm{gs}} + \mu_{\mathrm{oil}}} \right) \tag{4.7}$$

$$\langle u_x^{\mathrm{gs}} \rangle = \frac{2}{H_{\mathrm{T}}} \int_{-H_{\mathrm{T}}/2}^{0} u_x^{\mathrm{gs}} dy = \frac{\Delta p H_{\mathrm{T}}^2}{48 \mu_{\mathrm{gs}} L} \left(\frac{7\mu_{\mathrm{gs}} + \mu_{\mathrm{oil}}}{\mu_{\mathrm{gs}} + \mu_{\mathrm{oil}}} \right) \tag{4.8}$$

After substituting Equation 4.7 and 4.8 into Equation 4.6 we obtain,

$$y_2 = \frac{\langle u_x^{\mathrm{oil}} \rangle}{\langle u_x^{\mathrm{gs}} \rangle} = \frac{\mu_{\mathrm{gs}}}{\mu_{\mathrm{oil}}} \left(\frac{7\mu_{\mathrm{oil}} + \mu_{\mathrm{gs}}}{7\mu_{\mathrm{gs}} + \mu_{\mathrm{oil}}} \right) \tag{4.9}$$

and finally from Equation 4.5:

$$\varphi_{\mathrm{mod},2} = \frac{m+7}{m+14+m^{-1}} \tag{4.10}$$

where $m = \frac{\mu_{\mathrm{gs}}}{\mu_{\mathrm{oil}}}$ is the ratio of the dynamic viscosities of the two fluids.

Figure 4-12 shows that this prediction is also in good agreement with the measurements, suggesting that the interface level is adjusting in order to satisfy the increased viscous drag caused by the higher viscosity of the glycerol solution. Specifically, this causes the glycerol solution layer at the bottom of the pipe section to thicken with respect to the oil layer on top. For example, see Figure 4-25(a_1) and note the value of $\varphi_{in} = 0.75$.

4.5.3 Homogeneous Flow Model and Slip Ratio

In the homogenous model of two phase flow the central tenet and key assumption is that the slip ratio *S*, i.e. the velocity ratio of the fluids (defined in Equation 4.11) is unity. In what follows an assessment is made of the suitability of a homogenous flow model approach, based on the slip ratio criterion, compared with separated flow models which account for the existence of slip between the phases:

$$S = \frac{u_{oil}}{u_{gs}} \tag{4.11}$$

where u_{oil} and u_{gs} are the average velocities of the oil and glycerol solution. This can be utilised to obtain an expression for the in-situ oil phase fraction $\langle\varphi\rangle_{y,t}$ as a function of the input oil fraction φ_{in}:

$$S = \frac{u_{oil}}{u_{gs}} = \left(\frac{Q_{oil}}{A_{oil}}\right)\Big/\left(\frac{Q_{gs}}{A_{gs}}\right) = \left(\frac{U_{oil}}{\langle\varphi\rangle_{y,t}}\right)\Big/\left(\frac{U_{gs}}{1-\langle\varphi\rangle_{y,t}}\right) = \left(\frac{U_{oil}}{U_{gs}}\right).\left(\frac{1-\langle\varphi\rangle_{y,t}}{\langle\varphi\rangle_{y,t}}\right) \tag{4.12}$$

where:

$$\left(\frac{U_{oil}}{U_{gs}}\right) = \left(\frac{Q_{oil}}{A}\right)\Big/\left(\frac{Q_{gs}}{A}\right) = \left(\frac{Q_{oil}}{Q_{gs}}\right) = \left(\frac{{}^{Q_{oil}}/_{Q_T}}{{}^{(1-Q_{oil})}/_{Q_T}}\right) = \left(\frac{\varphi_{in}}{1-\varphi_{in}}\right) \tag{4.13}$$

Hence the following expression is obtained for the slip ratio:

$$S = \left(\frac{\varphi_{in}}{1-\varphi_{in}}\right).\left(\frac{1-\langle\varphi\rangle_{y,t}}{\langle\varphi\rangle_{y,t}}\right) \tag{4.14}$$

One can see that under homogenous flow conditions, i.e., when $S = 1$, Equation 4.14 reduces to $\varphi_{in} = \langle\varphi\rangle_{y,t}$. The homogenous flow model is denoted by the thin sold line labelled $S = 1$ in Figure 4-12.

It is seen that this approach over-predicts the in-situ phase fraction, with the extent of the over-prediction increasing with an increasing oil input fraction (this will be accounted for and explained to a large extent for in the further analysis below). Hence, a slip ratio of $S = 1$ does not adequately characterise the experimental results contained herein.

In a bid to address the predictive shortcoming of this approach, Figure 4-14 investigates whether a single S value, or alternatively an expression, can be used to characterise these flows.

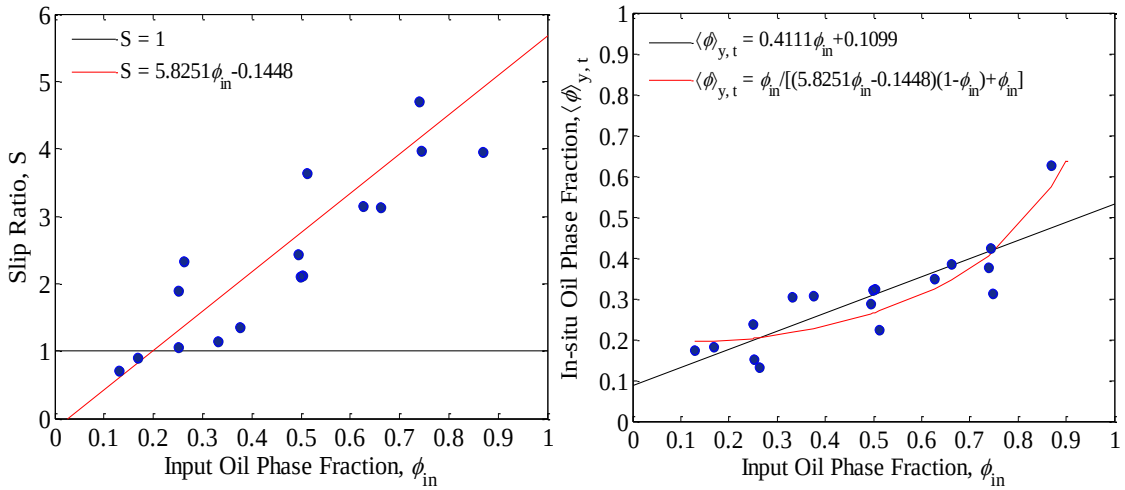

(a) (b)

Figure 4-14: Experimental results and correlations for: (a) slip ratio S as a function of input oil fraction φ_{in}, and: (b) in-situ oil phase fraction $\langle\varphi\rangle_{y,t}$ as a function of input oil fraction φ_{in}

It can be seen in Figure 4-14(a) that the fluids do not have a slip ratio of $S = 1$ except at the low end of input oil phase fractions φ_{in}. This observation gives further confirmation of the inadequacy of the homogeneous flow model to characterise the results presented in this chapter.

From Figure 4-14(a) a "best fit" correlation for the slip ratio is shown, the equation for which is:

$$S = 5.8251\varphi_{in} - 0.1448 \tag{4.15}$$

From Figure 4-14(b) it can be seen that using the above correlation for the slip ratio coupled with Equation 4.14 offers a better correlation between the input oil phase fraction φ_{in} and the in-situ phase fraction $\langle\varphi\rangle_{y,t}$ compared with a simple linear relationship. The plot presented in Figure 4-14(b) (given by the solid blue line) is of the relation:

$$\langle\varphi\rangle_{y,t} = \frac{\varphi_{in}}{(5.8251\varphi_{in} - 0.1448\,)(1 - \varphi_{in}) + \varphi_{in}} \tag{4.16}$$

One significant shortcoming of Figure 4-14(a) and ultimately of Equation 4.16 is that the superficial mixture velocity is not accounted for, and as seen in Figure 4-12, the in-situ phase fraction is a function of this the superficial mixture velocity.

Figure 4-15 examines the effect of the input oil phase fraction φ_{in} on the slip ratio S at constant superficial mixture velocities U_m. The figure includes a comparison with the experimental data acquired by Lovick and Angeli (2004) for an oil-water system.

4.5.4 Model Application and Comparison

From Figure 4-15 it can be seen that for a given oil input phase fraction, as the superficial mixture velocity increases the slip ratio decreases. On inspection of the Lovick and Angeli (2004) data plotted for $U_m = 3.00$ m.s^{-1} the slip ratio is $S \approx 1$. Hence, it can be deduced that as the superficial mixture velocity increases beyond a critical point, the flow can be adequately described via the homogenous flow model. Coupled with the homogenous flow model is the implication that the flow is well mixed and has a turbulent velocity profile (see Figure 5-27(b)), such that the fluid is travelling at approximately the same velocity. This is supported by the fact that at $U_m = 3.00$ m.s^{-1}, Lovick and Angeli (2004) reported the flow as being dispersed. Soleimani (1999) reported a slip ratio of $S \approx 1$ at superficial mixture velocities of $U_m = 2.10$ and 3.00 m.s^{-1}; the flow regime at both these superficial mixture velocities was dispersed flow. However, at a superficial mixture velocity of $U_m = 1.25$ m.s^{-1} the slip ratio was $S > 1$ and the corresponding regime was three-layer flow. Furthermore, Hussain (2004) also reported a decrease in the slip ratio as the superficial mixture velocity increases. This line of inquiry is pursued in Chapter 5 and Chapter 6 in which results obtained for velocity profile by PIV and PVT techniques are also considered.

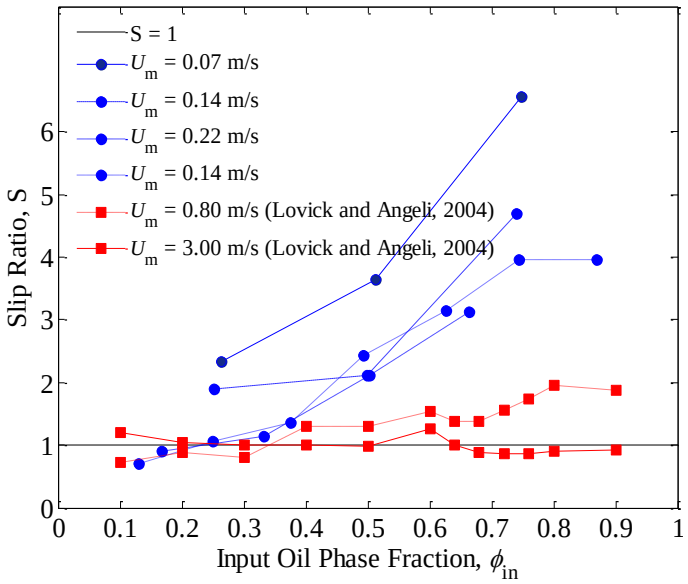

Figure 4-15: Slip ratio S as a function of input oil fraction φ_{in} for different superficial mixture velocities U_m PLIF data is presented in blue and the results from Lovick and Angeli (2004) are presented in red)

Figures 4-16 and 4-17 compare the in-situ phase fraction results of Russell et al. (1959) and Lovick and Angeli (2004) with the present PLIF results and examine the ability of $\varphi_{mod,1}$ to predict their data using the revised form of Equations 4.1 to 4.4 for flow in a circular cross-sectional pipeline, given in Equation 5.6 in Chapter 5. It should be noted that Figure 4-16 does not distinguish between the different constant superficial mixture velocities investigated. However, this distinction is made in Figure 4-17.

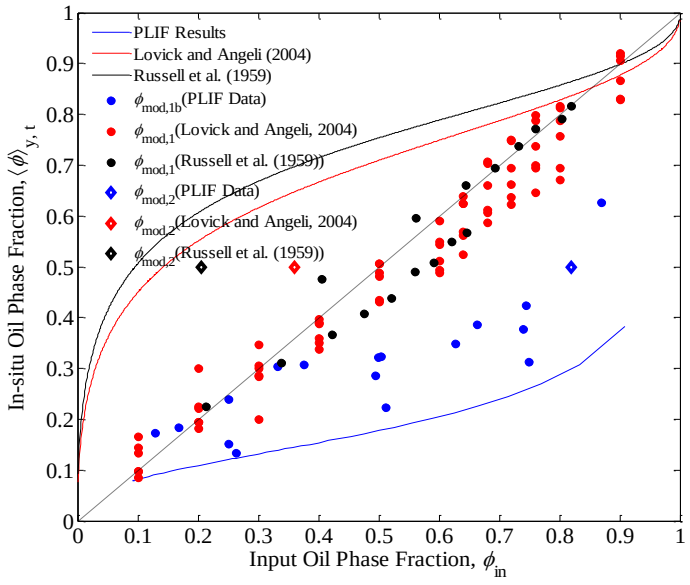

Figure 4-16: In-situ fraction $\langle\varphi\rangle_{y,t}$ as a function of input oil fraction φ_{in} compared with data from Lovick and Angeli (2004) and Russell et al. (1959)

The first notable observation is that the $\varphi_{mod,1}$ predictive curves for the Russell et al. (1959) and Lovick and Angeli (2004) data (red and black lines) occupy the opposite side of the $S = 1$ line (i.e., the $\langle\varphi\rangle_{y,t} > \varphi_{in}$ region) than that occupied by the $\varphi_{mod,1b}$ predictive curve for the present PLIF data (blue line), i.e., $\langle\varphi\rangle_{y,t} < \varphi_{in}$. This can be attributed to the viscosity ratio of the fluids. The laminar drag model predicts that the in-situ oil phase fraction will be less than the input oil phase fraction when the oil viscosity is less than that of the other fluid (in this case, glycerol solution) and the oil density is less than that of the other fluid. Whereas, the laminar drag model predicts that the in-situ oil phase fraction will be greater than the input oil phase fraction when the oil viscosity is greater than that of the other phase and again, has the lower density of the two fluids. This is observed in the experimental results. In the current campaign, $\mu_{oil}/\mu_{aq} \approx 0.04$ whereas for Lovick and Angeli (2004) and Russell et al. (1959), the ratio values were $\mu_{oil}/\mu_{w} \approx 6$ and $\mu_{oil}/\mu_{w} \approx 18$, respectively. It can be seen from Figure 4-16 that the predictive $\varphi_{mod,1}$ curve for Lovick and Angeli (2004) is closer to the $S = 1$ line compared with the predictive curve for Russell et al. (1959) data. The viscosity ratio for the fluids used by

Lovick and Angeli (2004) is closer to unity than those used by Russell et al. (1959). Hence, as $\mu_{oil}/\mu_{aq} \rightarrow 1$, S → 1 and a flow in which $\langle\varphi\rangle_{y,t}$ tends to φ_{in} occurs.

Figure 4-17 presents the data of Lovick and Angeli (2004) and Russell et al. (1959) for a range of constant superficial mixture velocities. It can be seen that the trend observed in Figure 4-14 – that as the superficial mixture velocity increases the in-situ oil phase fraction $\langle\varphi\rangle_{y,t}$ tends towards the input oil phase fraction φ_{in} and hence, towards homogenous flow – is again seen from the data plotted in this form.

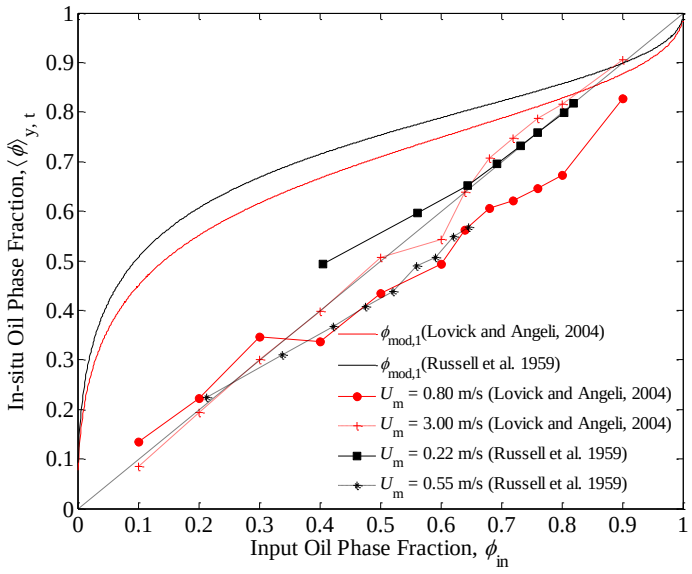

Figure 4-17: In-situ fraction $\langle\varphi\rangle_{y,t}$ as a function of input oil fraction φ_{in} for different superficial mixture velocities U_m for data by Lovick and Angeli (2004) and Russell et al. (1959)

Consideration of Figures 4-12, 4-16 and 4-17 together leads to the observation that at low superficial mixture velocities a laminar drag model provides excellent agreement with the experimental results, and as the superficial mixture velocity increases the flow becomes sufficiently well mixed (i.e., it is in the dispersed flow regime) that $\varphi_{in} = \langle\varphi\rangle_{y,t}$ can be evaluated via the homogenous flow model (i.e. $S = 1$).

These two conditions, i.e., smooth stratified flow and dispersed flow, present the extreme conditions of an envelope in which the in-situ phase fraction can be found. This is presented in Figure 4-18. The complexity arises in predicting the in-situ phase fraction at intermediate flow regimes, i.e., the flow regime termed *dual continuous* flow by Lovick and Angeli (2004) and *three-layer flows* in the current study. Here, both phases are dispersed at various degrees into the continuum of the other. This underpins the need for a modified form of the two-fluid model that accounts for the entrainment of one phase in a continuum of the other in *dual continuous flows*. The information on phase distribution detailed in Section 4.4 can begin to provide an insight into phase entrainment to make these developments.

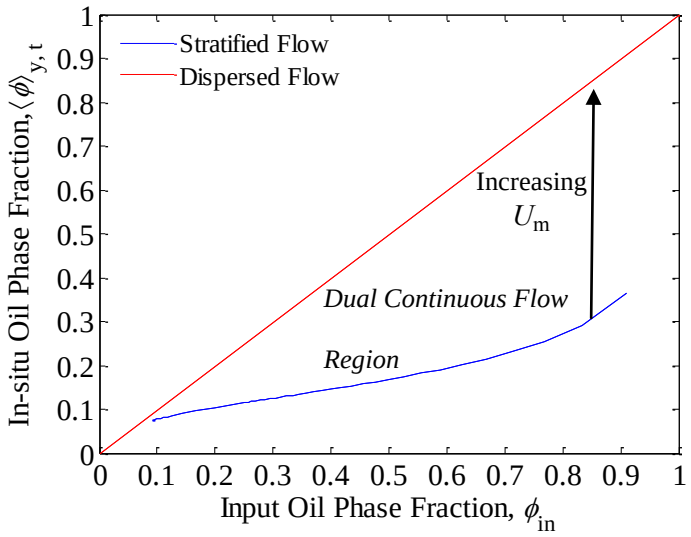

Figure 4-18: In-situ phase fraction envelope

Section 4.8 presents a revised approach for the laminar drag model to account for the entrainment of one phase in a continuum of the other to enable the prediction of the in-situ phase fraction beyond the smooth stratified flow regime.

4.6 Interface Level

This section presents measurements of the position of the liquid-liquid interface analysis made on the PLIF images and compares these measurements with predictions using a modified form of the laminar drag model. The prediction is denoted by $H_{mod,1b}$ and follows the same derivation as Equation 4.4 as detailed in Appendix 2.

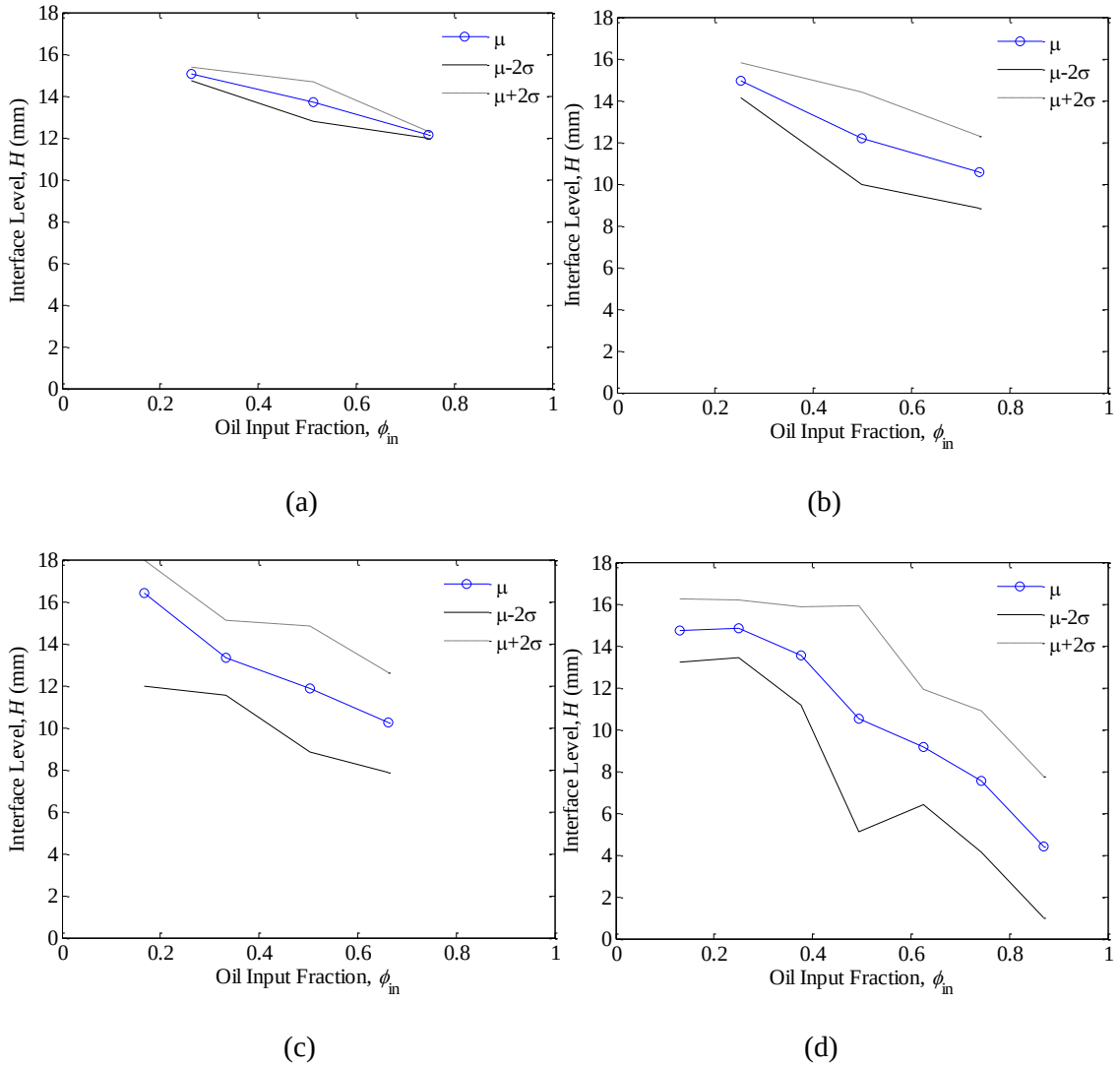

Figure 4-19: The mean (μ) and upper ($\mu + 2\sigma$) and lower ($\mu - 2\sigma$) limits for the interface level H as a function of input oil fraction φ_{in} for superficial mixture velocities U_m of: (a) 0.07 m.s^{-1}, (b) 0.14 m.s^{-1}, (c) 0.21 m.s^{-1}, and (d) 0.29 m.s^{-1}

Figure 4-19 shows the interface level H as a function of input oil fraction φ_{in} for fixed superficial mixture velocities from U_m = 0.07 to 0.29 m.s^{-1}, while Figure 4-20 shows the interface level H as a function of superficial mixture velocities U_m for given oil fractions ranging from φ_{in} = 0.25 to 0.75. The results presented are for the mean values and for the 95% confidence limits of the mean value ± 2σ where σ is the standard deviation.

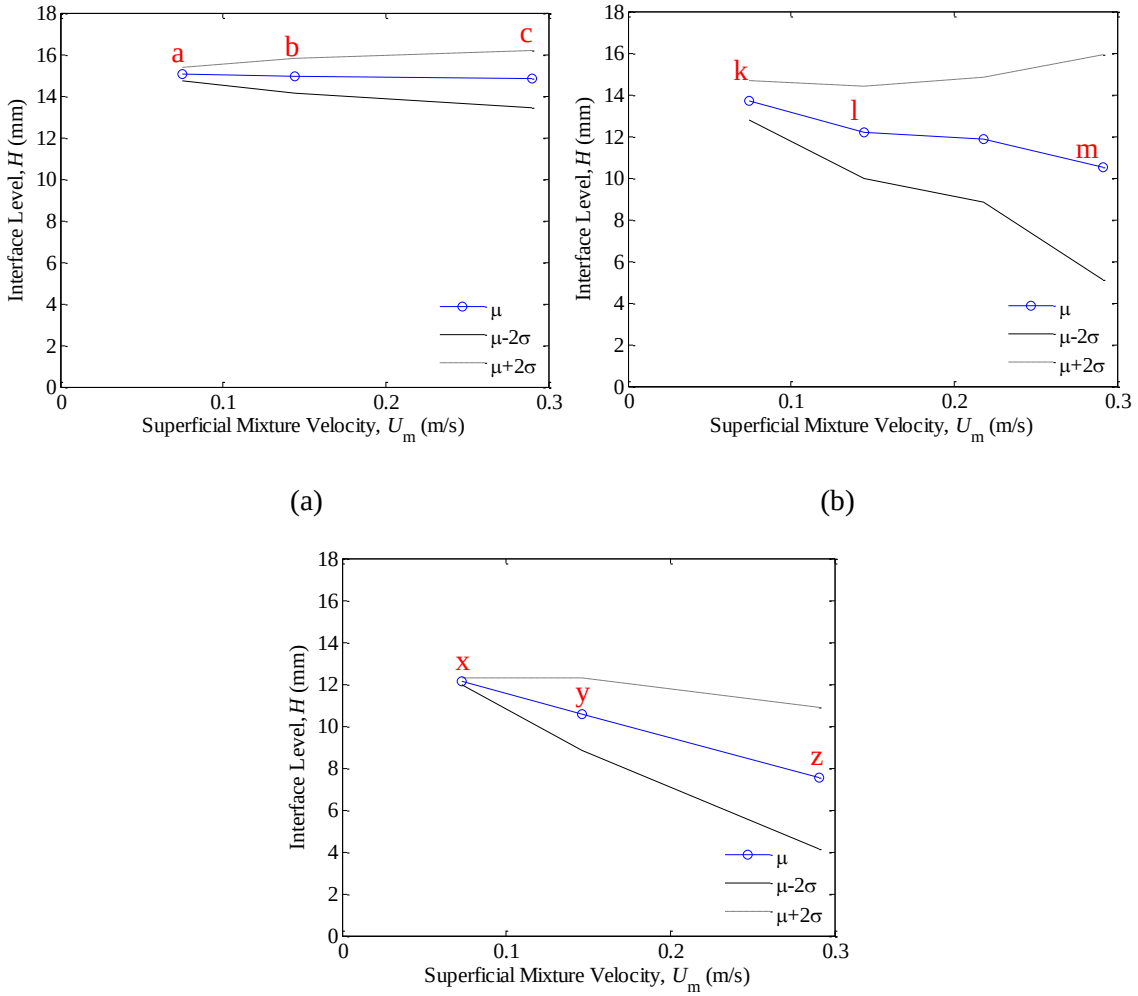

Figure 4-20: The mean (μ) and upper ($\mu + 2\sigma$) and lower ($\mu - 2\sigma$) limits for the interface level H as a function of superficial mixture velocity U_m for input oil fractions φ_{in} of: (a) 0.25, (b) 0.50, and (c) 0.75. Points a, b, c; k, l, m; and x, y, z correspond to the example images and probability histograms in Figures 4-23, 4-24 and 4-25 respectively

These figures reveal that, for a given input oil fraction φ_{in}, the interface level H decreases as the superficial mixture velocity U_m increases. It can also be seen that the rate of decrease in the interface level is greater for higher input oil fractions φ_{in}. Moreover, the extent of the 95% confidence interval ($\mu - 2\sigma \rightarrow \mu + 2\sigma$), which indicates a height range within which the interface level H fluctuates, increases as the superficial mixture velocity U_m increases for a given input oil fraction φ_{in}.

4.6.1 Laminar Drag Model

Figure 4-21 shows that the modified form of the laminar drag model equation (denoted by $H_{mod,1b}$) predicts the lowering of the interface level H as the oil input fraction φ_{in} increases and is in excellent agreement with the experimental data points relating to low-velocity stratified flow ($U_m = 0.07$ m.s^{-1}) in which the flow contains no droplets. However, it fails to capture that the interface level H decreases for a given oil input fraction φ_{in} as the superficial mixture velocity increases. This can be attributed to the fact the model does consider phase break-up and droplet formation.

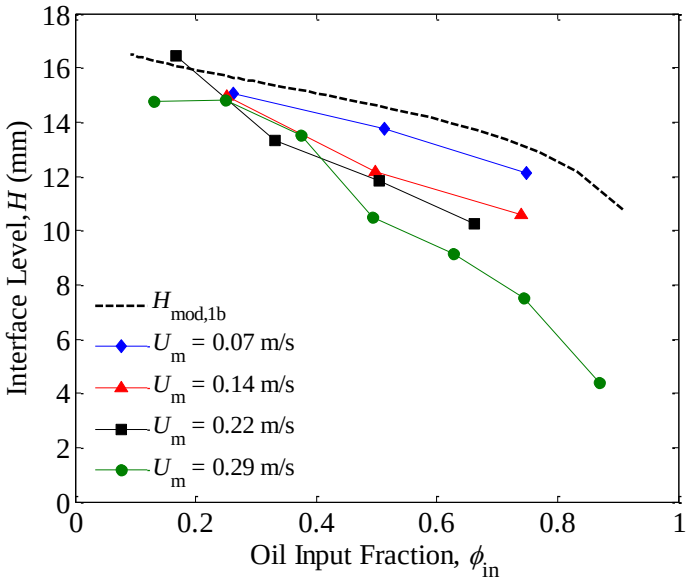

Figure 4-21: Interface Level H as a function of input oil fraction φ_{in} for different superficial mixture velocities U_m

4.6.2 Hall and Hewitt (1993) Predictive Techniques

Hall and Hewitt (1993) presented models for the interface level in gas-liquid and liquid-liquid flows based upon the Taitel and Dukler (1976) 1D two-fluid model for the holdup in stratified gas-liquid flows that assumes a flat gas-liquid interface. Taitel and Dukler (1976) demonstrated that the holdup (and thus, the interface level) for stratified flow is a unique function of the Lockhart and Martinelli (1949) parameter X under the assumption that $\frac{f_G}{f_i} \cong$ constant. For gas-liquid flows, this assumption is extended to $f_G = f_i$ owing to the assumption that the gas is flowing much faster than the liquid. The two-fluid model for stratified oil-water flows presented by Hall and Hewitt (1993) given by:

$$2X_{OW}^2(1-h)^2(2-h) - h^3 = 0 \qquad (4.16)$$

where X_{OW}^2 is the Martinelli parameter given by $X^2 = \frac{\mu_{\mathrm{oil}} u_{\mathrm{oil}}}{\mu_{\mathrm{w}} u_{\mathrm{w}}}$ and h is the dimensionless interface height $h = \frac{H}{H_{\mathrm{T}}}$.

For gas-liquid flow a revised version of Equation 4.16 was presented:

$$(1-h)^3 - \left(\frac{2}{X_{GL}^2}\right) h^2 (1+h) = 0 \qquad (4.17)$$

Predicted interface level curves based on Equations 4.16 and 4.17 are plotted along with the experimental results in Figures 4-22(a) and 4-22(b), respectively. The Hall and Hewitt liquid-liquid flow model over-predicts the observed liquid levels, the over-prediction increasing with increasing superficial velocity and oil input fraction. This over-prediction probably arises because the interface is disturbed (and hence rough) whereas the model assumes a flat interface. Surprisingly, better agreement is observed with the Hall and Hewitt gas-liquid model, but this is probably coincidental.

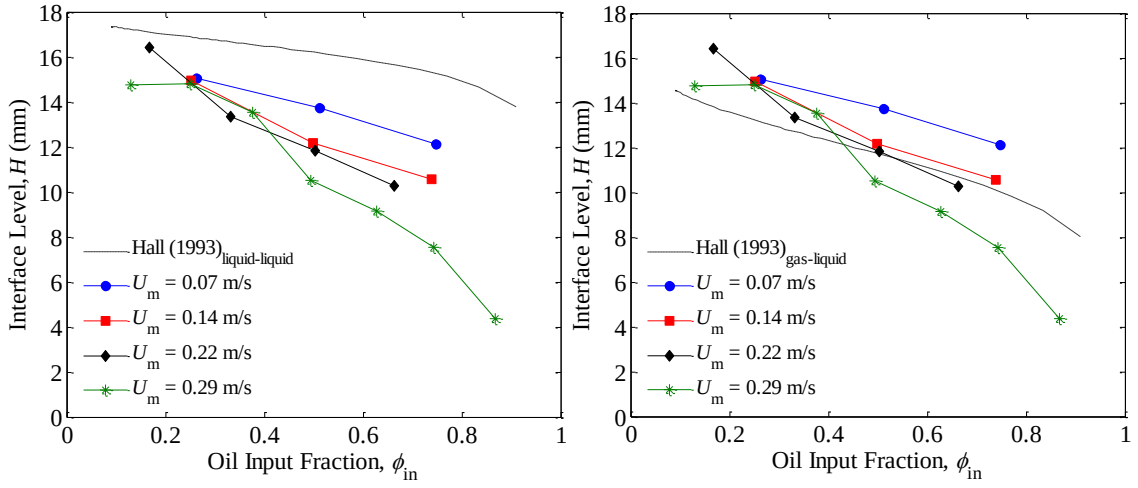

Figure 4-22: Interface Level H as a function of input oil fraction φ_{in} for different superficial mixture velocities U_{m} featuring interface level models presented by Hall and Hewitt (1993) for: (a) stratified liquid-liquid flow, and (b) stratified gas-liquid flow

4.6.3 Probability Histograms

Figures 4-23 to 4-25 present frames and the probability histograms for the points that have been used to construct the mean interface level plots shown in Figures 4-20(a) to 4-20(c), respectively. From inspection of the images ($a_1 \rightarrow c_1$, $k_1 \rightarrow m_1$ and $x_1 \rightarrow z_1$) and the histograms ($a_2 \rightarrow c_2$, $k_2 \rightarrow m_2$ and $x_2 \rightarrow z_2$), one can conclude that the mean interface level μ_H decreases for an increasing superficial mixture velocity U_m while at the same time the interface level fluctuation range widens. We would expect that at a low superficial mixture velocity U_m, when the flow is stratified, that the interface level would be flat and stable H (Shaha, 1999).

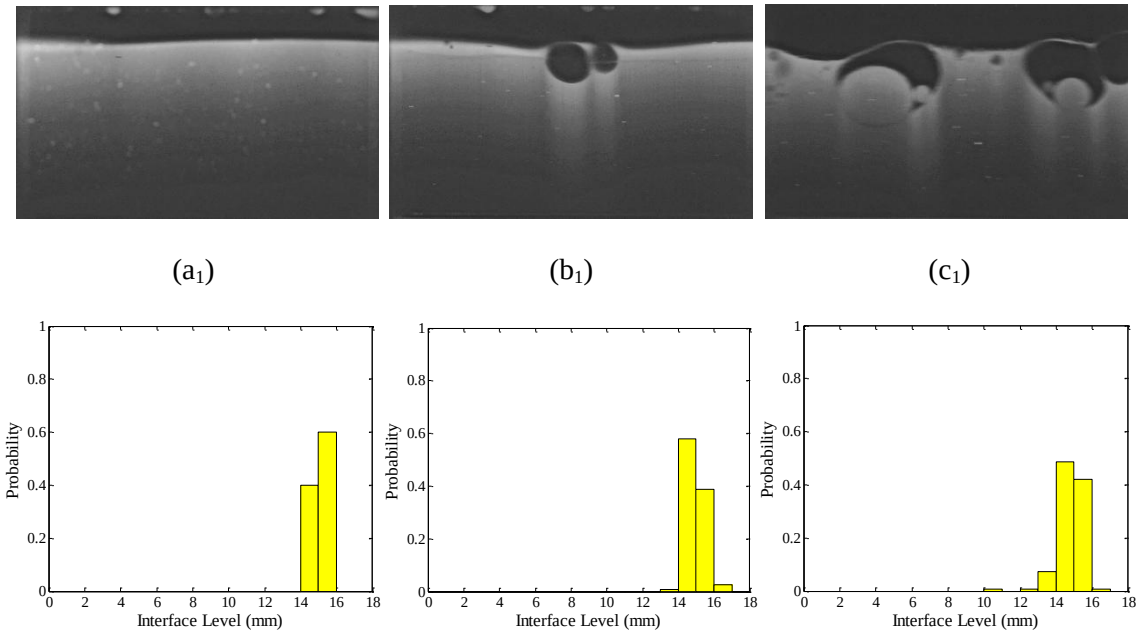

Figure 4-23: Flow images with superficial mixture velocities U_m of: (a_1) 0.07 m.s^{-1}, (b_1) 0.14 m.s^{-1}, (c_1) 0.29 m.s^{-1}, all at an input oil fraction $\varphi_{in} = 0.25$; (a_2), (b_2) and (c_2) show the probability histograms for the same conditions respectively. Data corresponds to Points a, b and c, as labelled in Figure 4-20(a)

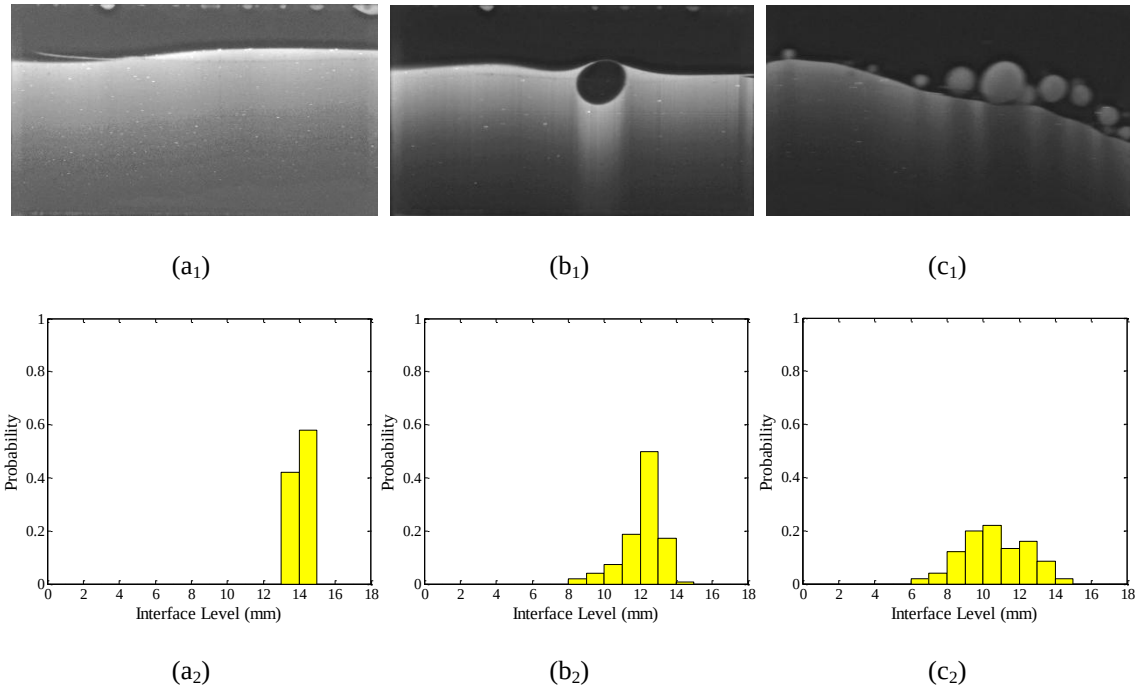

Figure 4-24: Flow images with superficial mixture velocities U_m of: (k_1) 0.07 m.s^{-1}, (l_1) 0.14 m.s^{-1}, (m_1) 0.29 m.s^{-1}, all at an input oil fraction $\varphi_{in} = 0.50$; (k_2), (l_2) and (m_2) show the probability histograms for the same conditions respectively. Data corresponds to Points k, l and m, as labelled in Figure 4.23(b)

From inspection of Figures 4-23 to 4-25 it is seen that at low superficial mixture velocities the interface is found only over a narrow vertical range i.e., as seen in Figure 4-23(a_2), thus fits with the classification of smooth stratified flow. As the superficial mixture velocity increases, it is seen that the range of vertical heights over which it is found widens, with the flow first transitioning into stratified wavy flow, and then, as the superficial mixture velocity continues to increases the flow becomes increasingly disturbed resulting in droplet formation, i.e., the flow regime being *mixed flow* (see Table 4-1). This is coupled with a further widening of the range of interface level heights; see Figures 4-24(c_2) and 4-25(z_2).

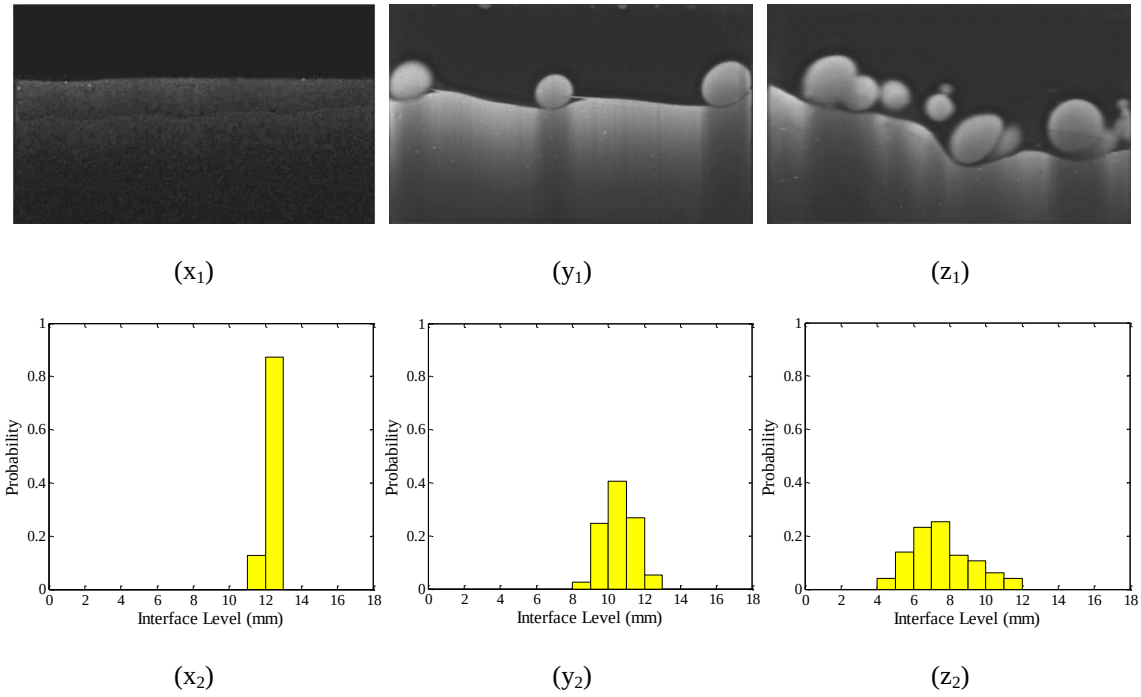

(x_1) (y_1) (z_1)

(x_2) (y_2) (z_2)

Figure 4-25: Flow images with superficial mixture velocities U_m of: (x_1) 0.07 m.s^{-1}, (x_1) 0.14 m.s^{-1}, (x_1) 0.29 m.s^{-1}, all at an input oil fraction $\varphi_{in} = 0.75$; (x_2), (y_2) and (z_2) show the probability histograms for the same conditions respectively. Data corresponds to Points x, y and z, as labelled in Figure 4-20(c)

4.6.4 Interface Depth

Finally, Figure 4-26 below relates the dimensionless interface depth $(1 - h)$ (from the top of the channel, where h is the dimensionless interface height) to the in-situ phase fraction $\langle\varphi\rangle_{y,t}$. It is seen that the dimensionless interface height equates well with the in-situ phase fraction for very low superficial mixture velocities i.e., for stratified flows for which entrainment of one phase in a continuum of the other is not present. However, as the superficial mixture velocity increases the $(1 - h) \cong \langle\varphi\rangle_{y,t}$ relationship breaks down. This can be attributed to entrainment encountered as the superficial mixture velocity is increased, see Figures 4-25(x_1) compared with 4-25(z_1). For lower oil input phase fractions the entrainment is seen to be dominated by oil

droplets below the interface (such as those shown in Figure 4-11); resulting in the depth of the interface from the top of the channel to be lower (i.e., a higher interface level).

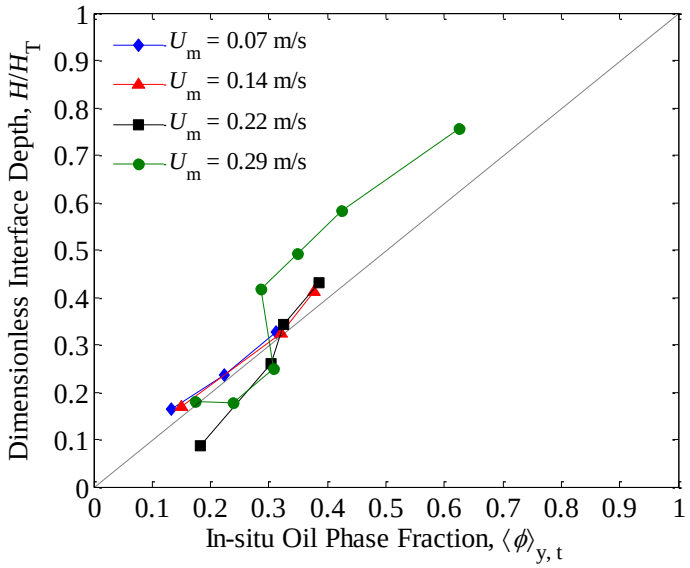

Figure 4-26: Dimensionless interface depth $(1 - h)$ correlated with in-situ phase fraction $\langle \varphi \rangle_{y,t}$

4.7 Droplet Size Distribution

The final form of analysis performed on the PLIF images considers the droplet sizes in the investigated flows. Both oil droplets in glycerol solution and glycerol solution droplets in oil are analysed. The results are shown in Figures 4-27, 4-28 and 4-29 below. Figure 4-27 shows the effects of input oil fraction φ_{in} and superficial mixture velocity U_m on the mean droplet diameters μ_d (defined in Equations 3.8 and 3.9 in Section 3.11). Figures 4-28 and 4-29 present probability histograms for the three flow conditions (with the same input oil fraction of $\varphi_{in} = 0.5$) that have been used to construct Figure 4-27(b).

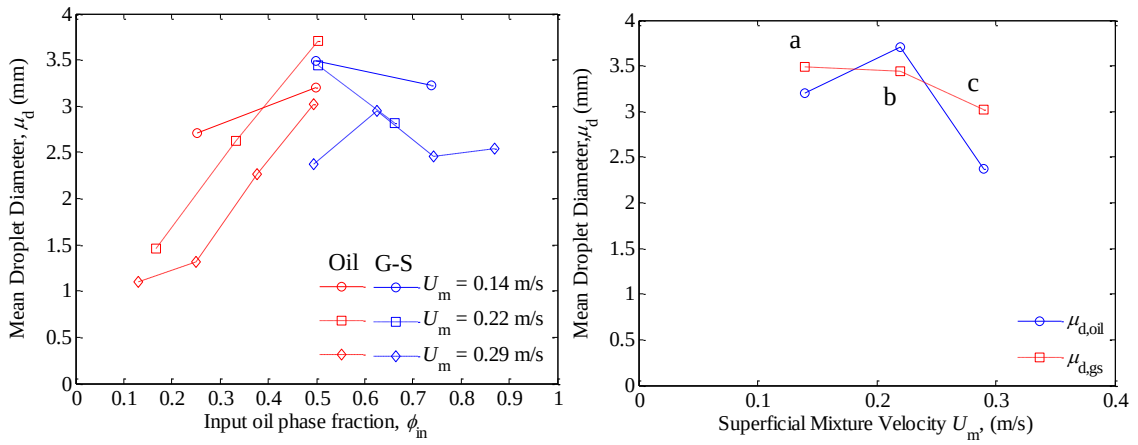

(a) (b)

Figure 4-27: Mean droplet diameter μ_d for: (a) varying input oil fraction φ_{in} and constant superficial mixture velocities U_m = 0.14 m.s^{-1}, 0.22 m.s^{-1} and 0.29 m.s^{-1}, and (b) varying superficial mixture velocity U_m and a constant input oil fraction of φ_{in} = 0.5. Points a, b and c correspond to the probability histograms in Figures 4-28 (for oil) and 4-29 (for glycerol-water). Red symbols represent glycerol-solution droplets and blue symbols for oil droplets

At the lowest tested input oil fraction φ_{in} no glycerol solution-in-oil (w/o) droplets are observed and the droplets are exclusively of oil-in-glycerol solution (o/w). Starting from an input oil fraction φ_{in} = 0.1 – 0.3, Figure 4-27(a) indicates that the average oil droplet diameter $\mu_{d,oil}$ increases monotonically with an increasing input oil fraction φ_{in}. This is the case for all three tested superficial mixture velocities, U_m = 0.14 m.s^{-1}, 0.22 m.s^{-1} and 0.29 m.s^{-1}. When the input oil fraction reaches φ_{in} ~ 0.5, glycerol solution droplets begin to appear in the flow together with the oil droplets, and as the input oil fraction φ_{in} is increased further the number of oil droplets observed in the flow decreases quickly and the flow becomes dominated by glycerol solution droplets. Interestingly, as the input oil fraction φ_{in} is increased in the range $\varphi_{in} > 0.5$ the average oil droplet diameter $\mu_{d,oil}$ tends generally to become smaller. This trend, however, is not as clear for the highest superficial mixture velocity of U_m = 0.29 m.s^{-1} (at least with the investigated envelope of U_m), for which the average oil droplet diameter remains in the range

$\mu_{d,\mathrm{gs}} =$ 2.4 – 2.9 mm (or, $\mu_{d,\mathrm{gs}} \cong$ 2.6 mm to within 10% that is comparable to the experimental uncertainty in this measurements) between $\varphi_{\mathrm{in}} = 0.5$ and $\varphi_{\mathrm{in}} = 0.87$. While noting this exception, if one considers all (both glycerol solution and oil) droplets in the flow it is possible to conclude by considering Figure 4-27(a) that the mean droplet size in the flow increases, reaches a maximum at around $\varphi_{\mathrm{in}} \sim 0.5$ and then decreases again as the input oil fraction φ_{in} is increased. The peak in the mean droplet diameter μ_d occurs in the range $0.5 < \varphi_{\mathrm{in}} < 0.6$. This is consistent with the finding of Pal (1993) who observed a peak in Sauter mean diameter (when measured as a function of water concentration) around the water-in-oil to oil-in-water phase inversion point, though it must be stated that those results were generated in a dispersed flow regime. The peak was found at a water concentration of 30%, which is comparable with the glycerol solution concentration at which the peak occurs in the current study.

Having considered the effect of varying the input oil fraction of φ_{in} at constant superficial mixture velocities U_{m}, Figure 4-27(b) shows results of mean droplet size as a function of superficial mixture velocity U_{m} but for a given (fixed) input oil fraction of $\varphi_{\mathrm{in}} = 0.5$. This value was chosen as it corresponds to conditions in which both glycerol solution and oil droplets exist concurrently in the flow. The mean oil droplet diameter $\mu_{d,\mathrm{oil}}$ increases slightly (by about 15%) and then decreases significantly (by about 36%) as a result of the increase in the superficial mixture velocity U_{m} from 0.14 m.s^{-1} to 0.22 m.s^{-1}, and then to 0.29 m.s^{-1}. At the same time, the mean glycerol solution droplet diameter $\mu_{d,\mathrm{gs}}$ remains approximately constant at low superficial velocities U_{m} from 0.14 m.s^{-1} to 0.22 m.s^{-1}, and then decreases by about 12% at high velocities $U_{\mathrm{m}} = 0.29$ m.s^{-1}. From Figure 4-27(b) and if all droplets in the flow are taken into consideration, it is found that the mean droplet size is small at both low and high superficial mixture velocities U_{m} and is largest at intermediate velocity values, which is in this work is $U_{\mathrm{m}} \cong 0.2$ m.s^{-1}.

4.7.1 Probability Histograms

The above trends can be understood with reference to Figures. 4-28 (for oil-in-glycerol solution droplets) and 4-29 (for glycerol solution-in-oil droplets), which show probability histograms of droplet size, one for each of the data points in Figure 4-27(b).

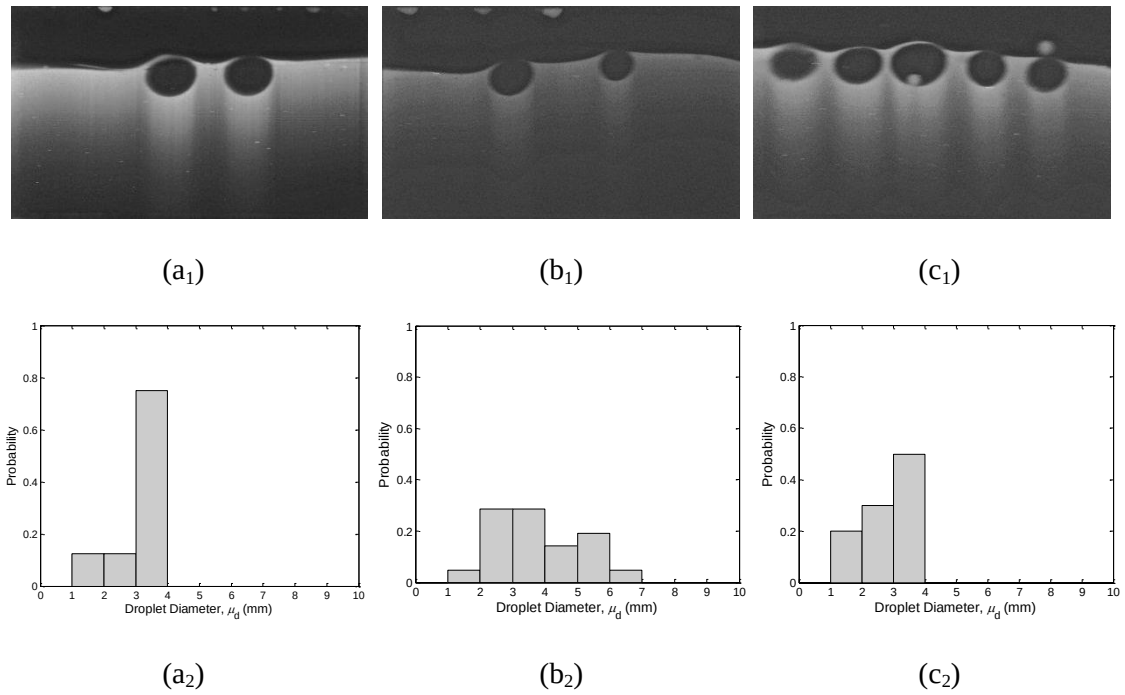

Figure 4-28: Flow images with superficial mixture velocities U_m of: (a_1) 0.07 m.s^{-1}, (b_1) 0.22 m.s^{-1}, (c_1) 0.29 m.s^{-1}, all at an input oil fraction $\varphi_{in} = 0.5$; (a_2), (b_2) and (c_2) show the oil droplet size distribution probability histograms for the same conditions respectively. Data corresponds to Points a, b and c, as labelled in Figure 4-27(b)

The first observation that can be made is that the size distributions are broader for glycerol solution droplets than for oil droplets. In particular, at the lowest superficial mixture velocity of $U_m = 0.07$ m.s^{-1} the oil droplet size histogram is close to a delta function centred at the mean droplet diameter $\mu_{d,oil}$, while at the highest superficial mixture velocity of $U_m = 0.29$ m.s^{-1} the oil droplet size histogram also contains values in a very narrow range around the mean diameter

$\mu_{d,\text{oil}}$. This reveals a strong preference for a certain size of droplet at low and high velocities in the case of oil. At intermediate superficial mixture velocities (i.e., U_m = 0.22 m.s^{-1}) some spreading is apparent, in particular at larger diameters, which explains the slight increase in the mean oil droplet diameter $\mu_{d,\text{oil}}$ shown directly in Figure 4-27(b).

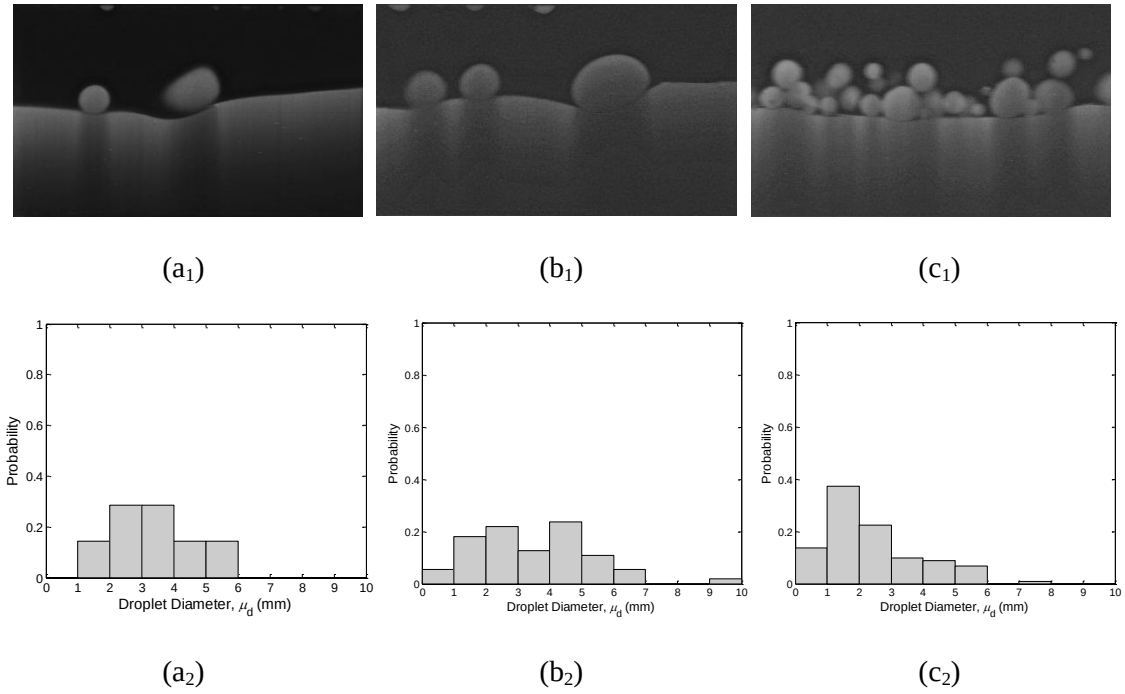

Figure 4-29: Flow images with superficial mixture velocities U_m of: (a_1) 0.07 m.s^{-1}, (b_1) 0.22 m.s^{-1}, (c_1) 0.29 m.s^{-1}, all at an input oil fraction φ_in = 0. 5; (a_2), (b_2) and (c_2) show the glycerol solution droplet size distribution probability histograms for the same conditions respectively. Data corresponds to Points a, b and c, as labelled in Figure 4-27(b)

On the other hand, although glycerol solution droplets are more broadly distributed as stated previously, when the superficial mixture velocity U_m is increased from 0.07 m.s^{-1} to 0.22 m.s^{-1}, the distribution broadens even further and gives rise to a higher probability of having both smaller and larger glycerol solution droplets. Then, at the even higher superficial mixture velocity of U_m = 0.29 m.s^{-1}, the probability of finding larger droplets in the flow decreases, as the probability of finding smaller ones continues to increase. Importantly, this latter observation

concerning the inability of the flow to sustain larger droplets at higher velocities is also evident in the case of oil droplets (compare for example Figures 4-29 (b) and (c)), and leads in both cases to the sharp decrease in the mean diameter of both oil and glycerol solution demonstrated in Figure 4.30(b).

4.8 Predictive Technique Development

This section describes endeavours to develop the laminar drag model presented in Section 4.5 to account for the entrained fluid droplets above and below the interface so as to extend the scope of its application beyond smooth stratified flow to include *dual continuous* flow.

4.8.1 Entrained Phase Fraction

The oil phase fraction above and below the interface level are presented in Figures 4-30 and 4-31. These results have been obtained by coupling the phase distribution profiles (from Section 4.4) for a given experimental run (i.e., a given superficial mixture velocity and oil input fraction combination) with its associated interface level (from Section 4.6). From Figure 4-30(a) it can be seen that the oil phase fraction above the interface decreases as the superficial mixture velocity increases. Conversely, from Figure 4-30(b) it is seen that the oil phase fraction entrained in the glycerol solution phase below the interface level increases as the superficial mixture velocity increase at a given oil input phase fraction. Figure 4-31(a) shows that at low superficial mixture velocities, the oil phase fraction above the interface level is independent of the input oil phase fraction. However, as the superficial mixture velocity increases, the interface declines at a higher rate for higher oil input phase fractions. The converse is seen from Figure 4-31(b). As the superficial mixture velocity increases, the oil phase fraction below the interface increases more quickly for lower oil input phase fractions.

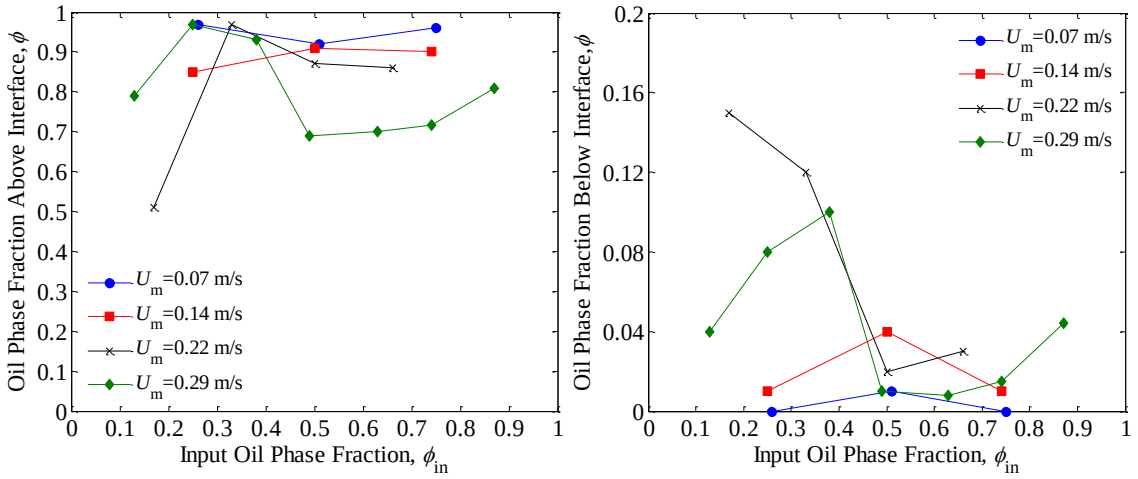

(a) (b)

Figure 4-30: Oil phase fraction as a function of input oil phase fraction φ_{in} for different superficial mixture velocity U_m: (a) above the interface level, and (b) below the interface level

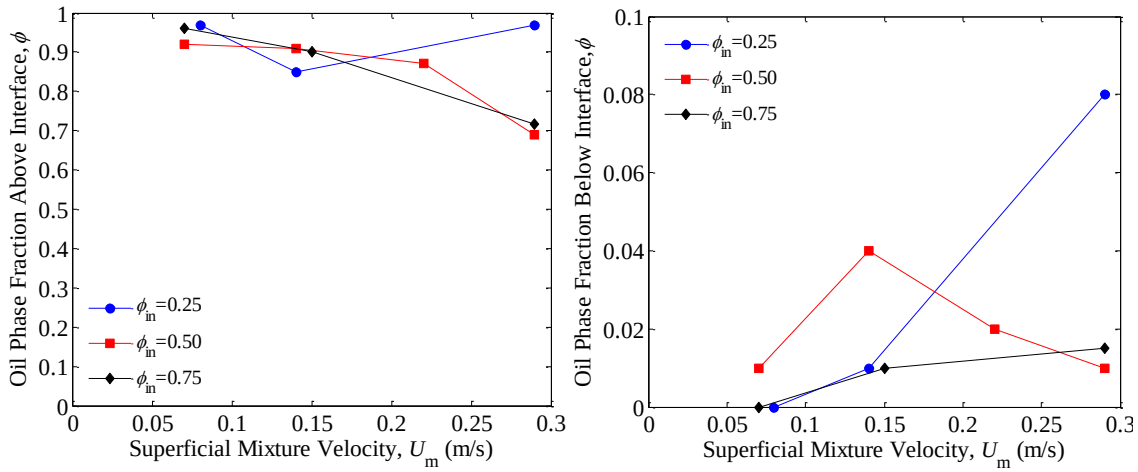

(a) (b)

Figure 4-31: Oil phase fraction as a function of superficial mixture velocity U_m for different input oil phase fraction φ_{in}: (a) above the interface level, and (b) below the interface level

4.8.2 Enhanced Laminar Drag Model

Figure 4-32 presents a revised version of Figure 4-12 in which the fluid viscosity ratio ($^{\mu_{oil}}/_{\mu_{aq}}$) has been amended to account for the glycerol solution droplets dispersed above the interface and the oil droplets dispersed below the interface. This has been done using the results contained in Figure 4-30 and 4-31 of Section 4.8.1. In Figure 4-32, the viscosity ratio has been altered from that of the pure fluids to the viscosity ratio of the flow above the interface to the fluid below the interface ($^{\mu_{above}}/_{\mu_{below}}$). The revised viscosities have been calculated via two means; (1) a linear viscosity interpolation based on the phase fractions, and; (2) the Taylor (1932) viscosity model. These are given in Equation 4.18 and Equation 4.19, respectively.

$$\mu_E = \varphi_{in}.\mu_{oil} - (1 - \varphi_{in}).\mu_{gs} \tag{4.18}$$

$$\mu_R = 1 + 2.5\varphi_{Disp}\left[\frac{K + 0.4}{K + 1}\right] \tag{4.19}$$

Where $\mu_R = \frac{\mu_E}{\mu_{Cont}}$ and $K = \frac{\mu_{Disp}}{\mu_{Cont}}$.

Figure 4-32 presents the experimental PLIF data for constant superficial mixture velocities with three $\varphi_{mod,1b}$ predictive curves included for each; (1) one in which the viscosity ratio is based on that of the individual fluids; (2) another in which the viscosities of the flow above and below the interface (and hence their ratio) have been calculated using a linear viscosity interpolation, and (3) another in which the viscosities of the flow above and below the interface (and hence their ratio) have been calculated using the Taylor (1932) viscosity model.

From inspection of Figure 4-32 it can be seen that accounting for the phase distribution (i.e., the phase fraction of the dispersed phase above and below the interface) coupled with $\varphi_{\text{mod,1b}}$ provided excellent agreement with the experimental data and a marked improved on just using the viscosity ratio of the individual fluids. In essence, the viscosity ratio and the superficial mixture velocity are the fundamental parameters that have to be accounted for in order to adequately predict the in-situ phase fraction. As $\mu_{\text{oil}}/\mu_{\text{aq}} \rightarrow 1$ and the superficial mixture velocities U_{m} increases the in-situ phase fraction tends $\langle\varphi\rangle_{y,t}$ to the input phase fraction φ_{in}.

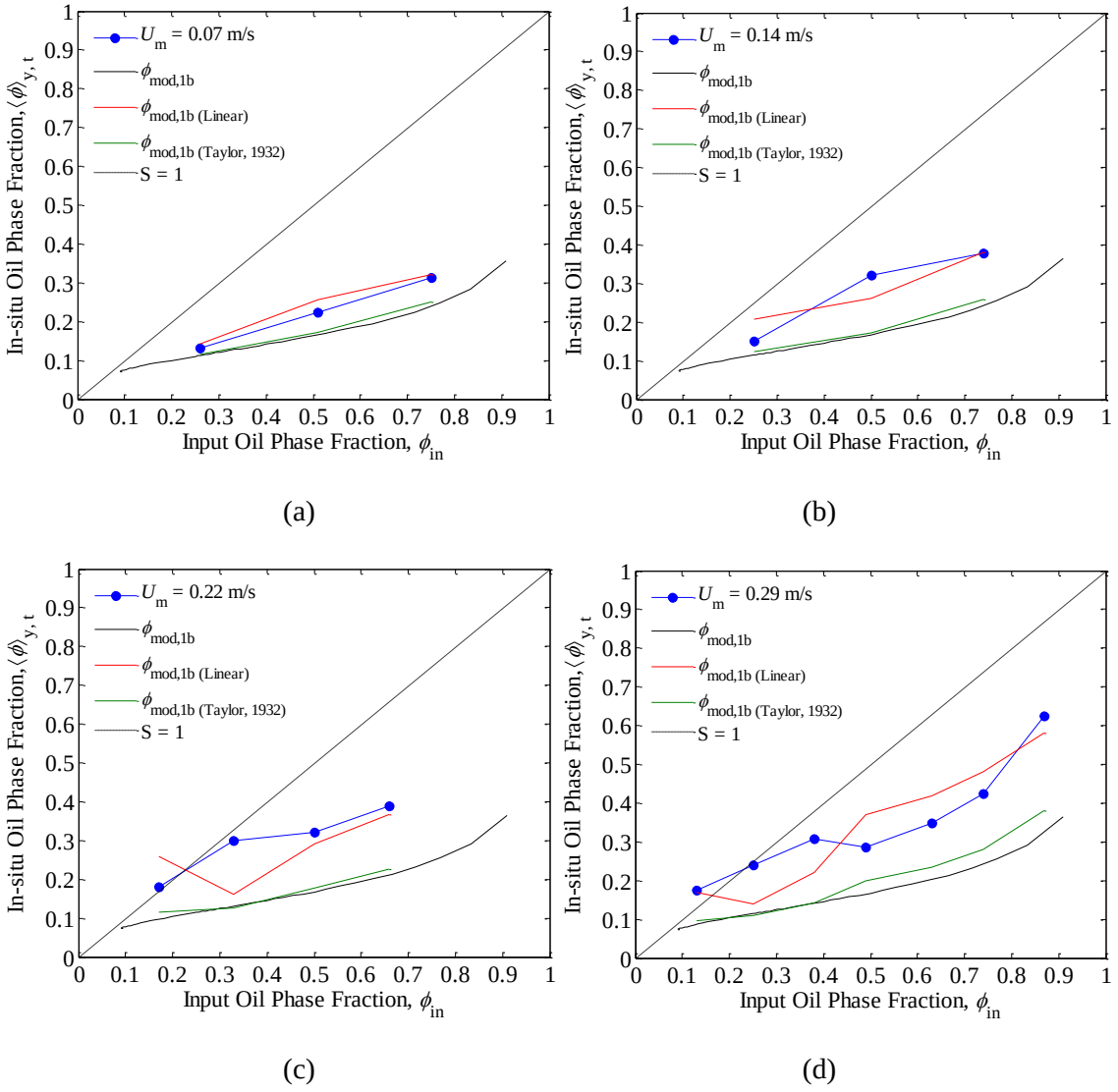

Figure 4-32: In-situ fraction $\langle\varphi\rangle_{y,t}$ as a function of input oil fraction φ_{in} for superficial mixture velocities U_{m}: (a) 0.07 m.s^{-1}; (b) 0.14 m.s^{-1}; (c) 0.21 m.s^{-1}, and; (d) 0.29 m.s^{-1}

It can be seen that the in-situ phase fraction can be accurately predicted as the superficial mixture velocity increases using viscosity ratio values that tend to unit. This can be explained in that as the superficial mixture velocity increases, the flow becomes increasingly turbulent, leading to the entrainment of one phase in a continuum of the other, i.e., oil droplets form below the interface and glycerol solution droplets form above it. Hence, the presence of oil below the interface will lower the viscosity of the flow below the interface and the converse is the case for the glycerol-solution above the interface; they will results in the viscosity of the flow (i.e., the emulsion viscosity) above the interface to increase. Hence, as the degree of mixing above and below the interface increases the results is to bring the viscosities of the flows above and below the interface closer together. The limit of this is when the flow is completely well-mixed (i.e., is in the dispersed flow regime) and there is no interface and the viscosity ratio of the fluid above a given height to that below it is unity. At this point, the in-situ oil phase fraction is equal to the input oil phase fraction.

4.9 Conclusions

A non-intrusive optical visualisation technique, namely planar laser-induced fluorescence (PLIF) has been developed for the use of analysis of co-current liquid-liquid flows involving two immiscible liquids of matched refractive index; in this case discussed in this Chapter, the fluids used were oil and a glycerol-water solution and the channel was square in cross section.. This experimental technique is shown to be a powerful tool that can provide detailed spatiotemporal information of the flow behaviour and hence, a valuable insight into the characteristics of such flows.

The images produced were used qualitatively for the identification of the flow pattern and also quantitatively in estimating the distribution and average of the phase fractions and the droplet size. The technique has proved to be an effective means of capturing the behaviour of

horizontal liquid-liquid flows and has allowed a flow regime map describing this flow behaviour to be generated in a more unequivocal way. Eight distinct flow regimes were observed. These were approximated into four flow types: (1) stratified flow; (2) mixed flow (i.e., a flow with two distinct continuous phase regions with droplets); (3) continuous oil-phase dispersion; and (4) continuous aqueous-phase dispersion.

The investigated flows can be categorised generally as comprising three distinct zones, with a continuous oil phase at the top and a continuous glycerol-water phase at the bottom, separated by a mixed zone. The vertical space covered by the mixed zone increased at higher superficial velocities. The interface level (vertical height from the bottom of the channel) separating the oil and glycerol-water phases decreased when increased input oil fractions were tested, as expected, though it was also found that the measured in-situ oil phase fraction at the measurement plane was considerably lower than the oil phase fraction at the pipe inlet based on the supplied flow rates of oil and glycerol-water. This was explained in terms of the different viscosities of the two liquids and the associated viscous drag in the channel that led to a considerable difference in bulk velocities in the measurement section. At low input oil phase fractions the interface level was not affected by changes to the superficial mixture velocity. However, at higher input oil fractions the interface height decreased as the superficial mixture velocity was increased. Higher superficial mixture velocities also led to increased fluctuations of the interface level and a smaller mean size of droplets in the flow. Glycerol solution droplets were observed predominantly at the lower end of input oil fractions, whereas oil droplets were observed at the higher end. For all tested mixture velocities, the mean droplet size increased initially, reached a maximum and then decreased as the input oil fraction was increased. Further, for a fixed (intermediate) input oil fraction, the mean droplet diameters were largest at intermediate mixture velocities and smallest at high mixture velocities. Of these two observations the more pronounced was the latter.

Having considered the phase fraction and interface information provided by the analysis of the novel spatiotemporal measurements contained herein, the most important lesson learnt is that simplistic modelling approaches, such as the two-fluid model, are unlikely to be capable of representing adequately flows for such complexly mixed fluids. For example, it was reported by Ishii and Mishima (1984) that their conventional one-dimensional two-fluid model exhibited a number of serious shortcomings, which mainly arose due to the inadequate treatment of phase distributions in the domain. The experimental results presented here emphasise the existence of complex mixing patterns encountered in secondary (i.e., aqueous droplet in an oil droplet in a continuous aqueous phase – w/o/w, or oil droplet in an aqueous droplet in a continuous oil phase – o/w/o), and multiple (i.e., o/w/o/w and w/o/w/o, etc.) dispersions, as well as complexities at the interface in liquid-liquid flow. Thus the current investigation underscores the need for these particular flow behaviours to be modelled in order to achieve accurate analytical descriptions of these important flows.

Though interesting and informative results have been obtained with a square cross section duct, it would clearly be closer to industrial practice to use channels of circular cross section. In this latter case, and even with matching of the refractive index of the two fluids and the use of a transparent tube, the wall curvature can lead to significant image distortion. The work presented in Chapter 5 attempts to overcome this disparity by use of a circular cross section visualisation cell and a graticule method to a correct for the image distortion arising from the wall curvature (see Section 3.10.2).

CHAPTER 5

Laser-Induced Fluorescence Studies of Horizontal Liquid-Liquid Flows in a Circular Cross Section Duct

5.1 Introduction

This chapter presents the experimental results obtained using the dedicated circular cross-section visualisation section detailed in Section 3.10.2. The work is a development of that described in Chapter 4 not only in the use of a circular cross section tube (a square cross section tube was used in the work described in Chapter 4) but also in the extension of the laser measurement systems to include (in addition to PLIF) both Particular Image Velocimetry (PIV) and Particule Tracking Velocimetry (PTV). To the best of the author's knowledge, the results described in this Chapter are the first obtained for liquid-liquid systems using simultaneous PLIF, PIV and PTV. The use of a circular cross section tube is more representative of industrial pipeline systems but is optically more challenging. The provision of detailed data in the circular pipe section has been made feasible by using an image correction technique involving the use of a graticule (printed target) detailed in Sections 3.11.1. The enhanced measurement capability, and specifically the use of PIV and PTV enabled the detailed diagnostic inspection of the co-current liquid-liquid flow velocity profiles.

The analysis methodology performed on the experimental data, and the associated results presented in this chapter, are similar to those used to characterise the flows presented in Chapter 4. However, herein the quantitative analysis is extended to include results for the interface wave velocity $\langle U_{\text{int}} \rangle_t$ and the velocity profiles in the flow $\langle U_x \rangle_{y,t}$. A qualitative analysis of the results, including images of the flow regimes observed and a flow regime map constructed from the flow regime classifications, is presented first in Section 5.3. Following this, the subsequent sections present the results from the quantitative analyses of the flow images as follows: (1) vertical phase distribution profiles (Section 5.4); (2) in-situ phase fractions (Section 5.5); (3) interface level data (Section 5.6); (4) droplet size distribution results (Section 5.7); (5) interface wave velocity results (Section 5.8), and; (6) velocity profiles (Section 5.9). Finally, conclusions from this part of work are presented in Section 5.10.

In the work described in this Chapter, the flow was initiated by injecting the oil phase at the top of the pipe and the (heavier) aqueous (glycerol solution) phase at the bottom of the tube (see Figure 3.5). Thus, in the experiments described in this Chapter, the two liquid phases started in an orientation which is the natural one. A further series of experiments was carried out in which the injection was inverted (oil phase at the bottom and aqueous on top). This series of measurements is described in Chapter 6.

5.2 Experimental Operation

The experiments described in this Chapter were conducted by employing a similar procedure to that outlined in Section 4.2. However, in the experiments described in this Chapter, an Olympus i-SPEED 3 high speed camera (see Section 3.4.1) was used rather than the Phantom V710 Monochromatic System used for the experiments described in Chapter 4. The use of the circular cross-section visualisation cell involved the use of a graticule to calibrate for the image distortion arising for the refractive index disparities. Though the refractive index of the fluids is

closely matched, there are differences between the refractive index of the fluids and the borosilicate glass circular tube visualisation test section. Though the distortion effects are minimised by placing the borosilicate glass visualisation section inside a square acrylic resin (Perspex^{TM}) box filled with a fluid of the same refractive index (i.e., Exxsol D80) there is still a need for correction of the image to get reliable quantitative information. The procedure for using the graticule calibration piece is detailed in Section 3.11.1.

The investigated flow conditions are defined via the same two independent parameters as used in Chapter 4, namely: (1) the superficial mixture velocity U_m and; (2) the inlet volumetric phase fraction of oil in the pipe φ_{in}. These parameters (defined in Section 4.2) were varied independently in 48 runs and kept constant for the duration of each run. The investigated experimental conditions spanned a range of U_m from 0.11 to 0.84 m.s^{-1}. In addition, φ_{in} was varied between 0.1 and 0.9. The matrix of experimental conditions is largely the same as that in Chapter 4.

The analysis presented in this chapter is focussed in the lower U_m range (0.10 to 0.42 m.s^{-1}); the aim has been to capture the flow regime transition from stratified to *dual continuous* flow, with the aim of enhancing understanding of the flow characteristics in the regime region between stratified and dispersed flow.

5.3 Flow Phenomena and Regime Map

Eight distinct flow regimes have been observed in the current PLIF study. These have been identified using the same classification system as used in Chapter 4. Instantaneous images of each of the flow regimes are presented in Figure 5-1. Once again, the flows can be grouped into four more general flow regimes, namely: (1) stratified flow; (2) mixed flow, which is characterised by two distinct continuous phase regions with droplets in each; (3) two-layer flow,

which comprised of a dispersed region and a continuous, unmixed region; and (4) dispersed flows. These are the same as those identified in Chapter 4; the generalised grouping is presented in Table 4-1.

A flow regime map relating the flow classifications to the input oil fraction φ_{in} and the superficial mixture velocity U_m is presented in Figure 5-2. From the flow regime map (Figure 5-2) it can be seen that the stratified flow regime is observed up to a superficial mixture velocity of $U_m = 0.34$ m.s^{-1}; this being 0.27 m.s^{-1} higher than the highest superficial mixture velocity (i.e., $U_m = 0.07$ m.s^{-1}) at which the stratified regime was observed for the square cross-section visualisation section (see Figure 4-2). However, above a superficial mixture velocity of $U_m = 0.17$ m.s^{-1} stratified flow is only observed at low oil input phase fractions $\varphi_{in} < 0.4$.

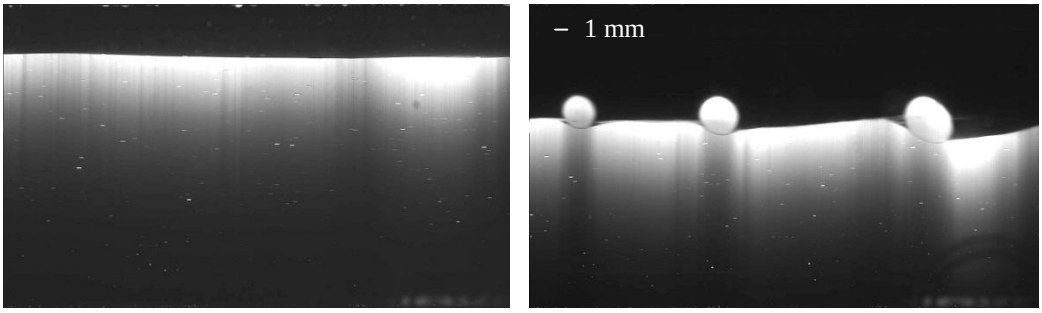

(a) Stratified flow

(b) Stratified flow with droplets

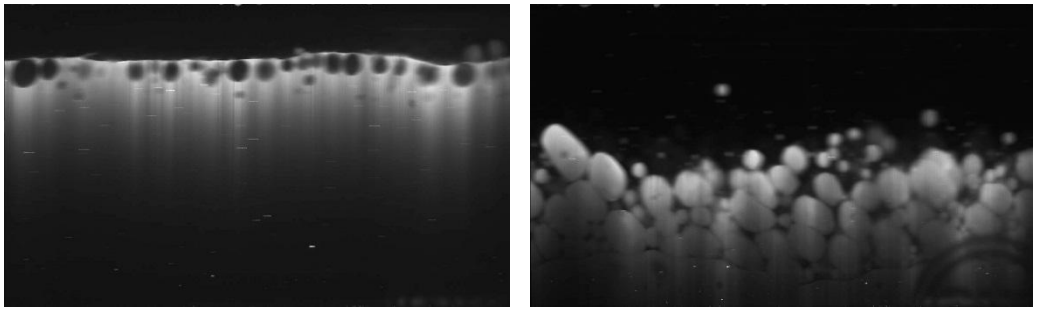

(c) Oil droplet layer

(d) Glycerol solution droplet layer

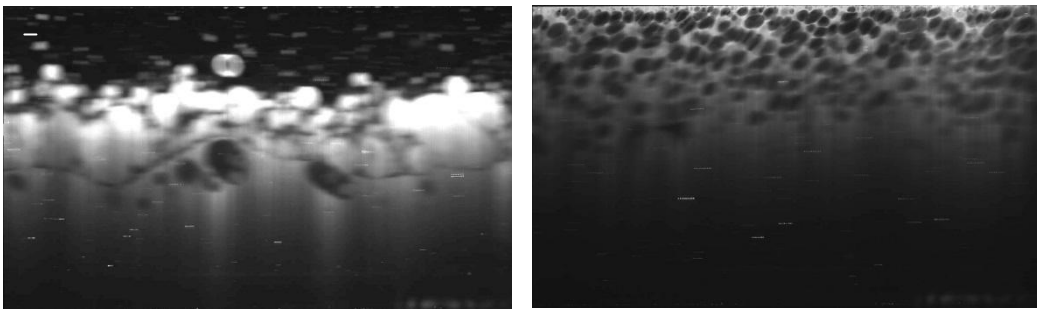

(e) Three layer flow

(f) Oil dispersion over glycerol solution

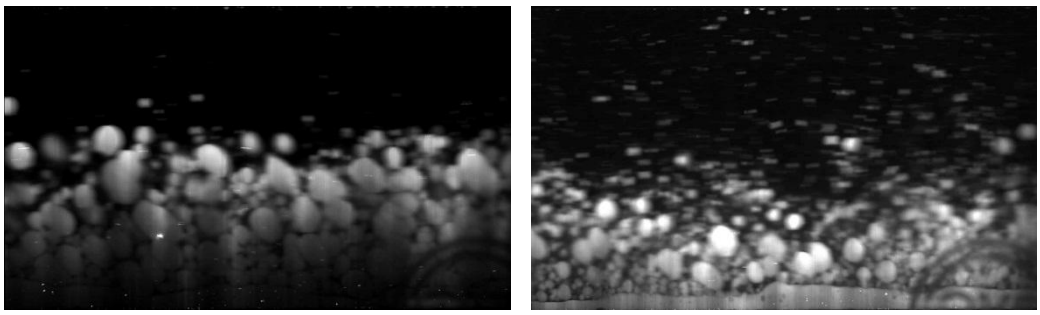

(g) Oil flow over glycerol solution dispersion with glycerol solution film

(h) Glycerol solution dispersion with glycerol solution film

Figure 5-1: Images of the 8 distinct flow regimes observed in the circular cross section experimental campaign

Above a superficial mixture velocity of $U_m = 0.34$ m.s^{-1} droplets are found at all oil input phase fraction and the flow is different forms of stratified flow with droplet i.e., above $U_m = 0.34$ m.s^{-1} the flow has transitioned to *dual continuous* flow for all oil input phase fractions. As the superficial mixture velocity increases, the range of oil input phase fractions covered by *dual continuous* flow diminishes and dispersed flows being to form at the oil input phase fraction extremes i.e., very low (near zero) and very high (near unity) oil input phase fractions.

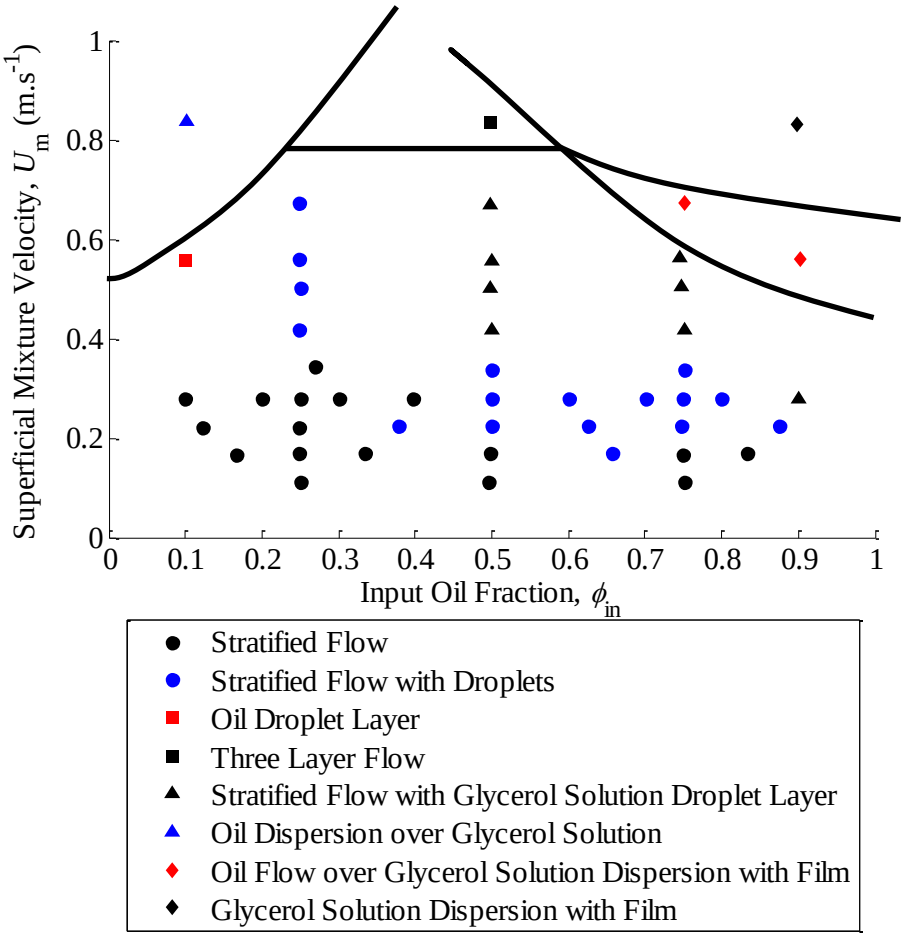

Figure 5-2: Flow regime map

At a superficial mixture velocity of $U_m = 0.84$ m.s^{-1} the flow changes to *three-layer* flow at an oil input phase fraction of $\varphi_{in} = 0.5$ and to dispersed flows at higher oil input phase fractions. Oil dispersions begin to form at an oil input phase fraction of $\varphi_{in} = 0.1$ and glycerol solution dispersions begin to form at an oil input phase fraction of $\varphi_{in} = 0.9$. Compared with the flow

regime map constructed from the results obtained for the PLIF campaign using the square cross-section visualisation cell (see Figure 4-2), the flow regime transitions occur at higher superficial mixture velocities for the circular tube case. For all the oil input phase fractions investigated, *dual continuous* flow was not seen for superficial mixture velocity below $U_m = 0.34$ m.s^{-1} whereas, this transition occurred at a superficial mixture velocity of $U_m = 0.07$ m.s^{-1i} in the case of the square cross-section duct.

Furthermore, dispersions were observed at a superficial mixture velocity of $U_m \approx 0.6$ m.s^{-1} when using the square cross-section duct, whereas the transition to dispersions is first seen at a superficial mixture velocity of $U_m \approx 0.8$ m.s^{-1} in the circular cross section duct. One possible explanation for these differences might be the extra turbulent mixing caused at the transition from the circular cross section duct to the square cross section duct in the experiments described in Chapter 4 (though every effort had been made to make this transition a smooth one).

As was the case with the PLIF study presented in Chapter 4, the flow regimes are in good general agreement with those from previous studies (Soleimani, 1999; Lovick and Angeli, 2003; Hussain, 2004), yet some flow regimes identified by previous researchers were not observed in the present study. Neither, oil-slugs-in-water (Charles et al., 1961; Hasson et al., 1970) nor annular flows (Russell et al., 1959; Charles et al., 1961; Hasson et al., 1970 and Arirachakaran et al., 1989) were observed in the current study. This absence of annular flows is consistent with the observations of Angeli (1995), Nädler and Mewes (1995), Soleimani (1999) and Hussain (2004). The absence of annular flows might be attributed to the fact that the oil phase used in investigations where annular flow was not observed (including the present experiments) was not dense and viscous enough to sustain an oil core.

The regime transitions observed with the circular pipe section relate much more closely to the transitions observed by Soleimani (1999) than the experimental study presented in Chapter 4,

which was performed using a square cross-section duct. *Three-layer* flow has been identified in the present campaign, however its onset was not seen until much higher superficial mixture velocities when compared with the flow regime map presented in Chapter 4 (see Figure 4-2) i.e., at $U_m \approx 0.8$ m.s^{-1} for the circular duct compared to $U_m \approx 0.4$ m.s^{-1} for the square duct. The present circular duct data align much more closely with the transition to three layer flow observed by Soleimani (1999), ($U_m \approx 1$ m.s^{-1}) and Hussain (2004), ($U_m \approx 0.8$ m.s^{-1}). Hussain (2004) reported stratified-wavy flow with droplets at superficial mixture velocities up to $U_m \approx 3$ m.s^{-1}; this is much higher than the limit found in the current study, in which stratified-wavy flow with droplets was only observed up to superficial mixture velocities up to $U_m \approx 0.67$ m.s^{-1}. However, the current value more closely relates to the limit reported by Soleimani (1999), which was a superficial mixture velocity of $U_m \approx 0.7$ m.s^{-1}.

5.4 Vertical Phase Distribution Profiles

This section presents the vertical phase distribution profiles of the circular section liquid-liquid flows. The method employed to calculate the vertical oil phase fraction profiles $\bar{\varphi}(y)$ (defined in Equation 3.3) is detailed in Section 3.11.2. Figure 5-3 shows vertical phase profiles $\bar{\varphi}(y)$ for superficial mixture velocities U_m in the range 0.11 to 0.42 m.s^{-1} at selected input oil fractions φ_{in} of: (a) 0.25, (b) 0.50 and (c) 0.75. Figure 5-4 shows vertical oil phase fraction profiles $\bar{\varphi}(y)$ for the full range oil fractions φ_{in} and with selected superficial mixture velocities U_m of: (a) 0.11 m.s^{-1}; (b) 0.17 m.s^{-1}; (c) 0.22 m.s^{-1}; (d) 0.28 m.s^{-1}; (e) 0.34 m.s^{-1} and; (f) 0.42 m.s^{-1}.

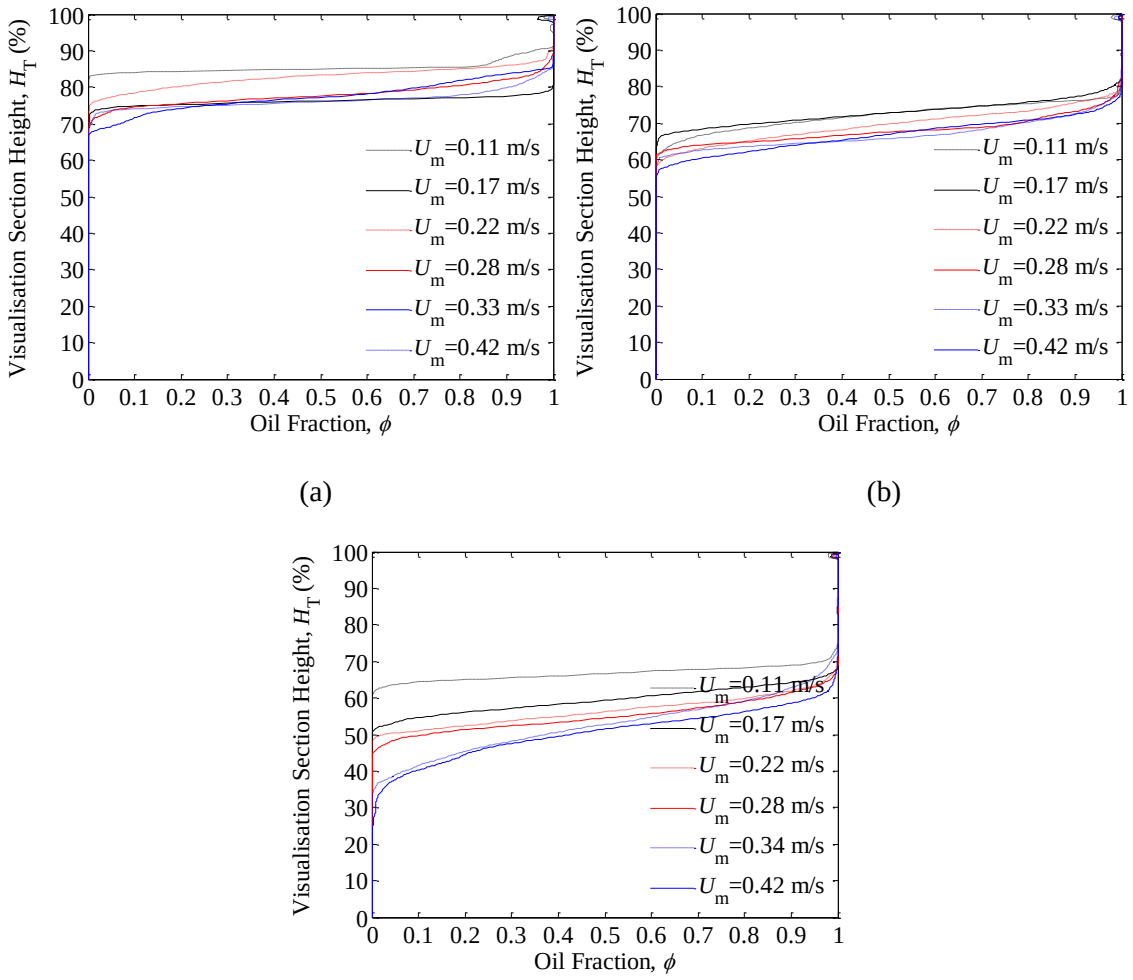

Figure 5-3: Vertical oil phase fraction profiles $\bar{\varphi}(y)$ for different superficial mixture velocities U_m at an input oil fraction φ_{in} of: (a) 0.25; (b) 0.50, and; (c) 0.75

From inspection of Figures 5-3 and 5-4 it can been seen that the flows show similar vertical distribution characteristics to those observed in the experimental study for square cross section ducts presented in Chapter 4. Specifically, that the flow has three distinct regimes: (1) an oil region at the top of the pipe; (2) a glycerol solution region at the bottom of the pipe and; (3) a mixed region separating them. This zone characterisation is illustrated in Figure 4-7 of Chapter 4.

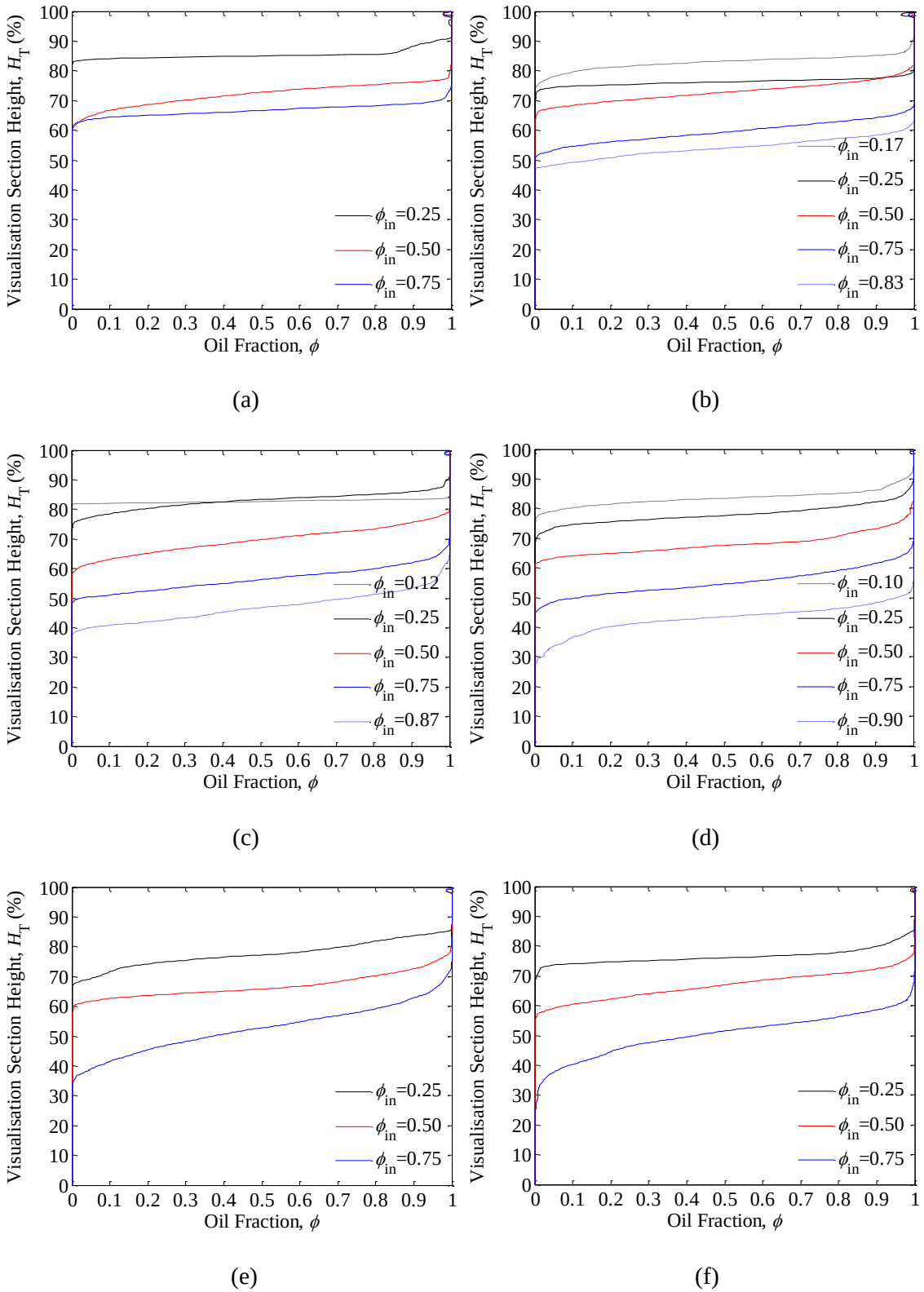

Figure 5-4: Vertical oil phase fraction profiles $\bar{\varphi}(y)$ at different input oil fractions φ_{in} for a superficial mixture velocity U_m of: (a) 0.11 m.s^{-1}; (b) 0.17 m.s^{-1}; (c) 0.22 m.s^{-1}; (d) 0.28 m.s^{-1}; (e) 0.34 m.s^{-1}, and; (f) 0.42 m.s^{-1}

For stratified flows (such as for the U_m = 0.22 m.s^{-1} and φ_{in} = 0.12 case, presented in Figure 5-4(c)) the mixed region covers a narrow vertical band. Figure 5-5 presents instantaneous flow images for the flow under these conditions to demonstrate the flow is stratified. As the oil input fraction increases for a given superficial mixture velocity, two observations are made: (1) the height of the glycerol solution at the bottom of the pipe decreases, and; (2) the vertical range covered by the mixed region increases i.e., the gradient of the transition from the glycerol solution region to the oil region increases (see Section 5.4.1). From inspection of Figure 5-3 it is seen that the gradient of the transition from the glycerol solution region to the oil region (i.e., the height of the mixed region) also increases as the superficial mixture velocity increases for a given oil input fraction. The three aforementioned findings concur with the findings presented in Chapter 4. As discussed in Chapter 4 (Section 4.3), Soleimani (1999) and Hussain (2004) presented phase distribution profiles but for higher superficial mixture velocities ($U_m \approx$ 2-3 m.s^{-1}) than analysed in the current study. Their results indicate that the gradient of the transition from the aqueous phase (glycerol solution in the present study) region to the oil region increases until there is a constant oil phase fraction all along the vertical profile of the pipe.

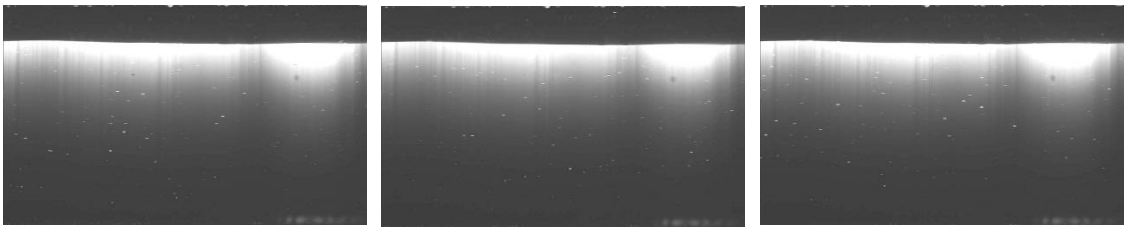

(a) (b) (c)

Figure 5-5: Instantaneous flow images for an oil input phase fraction $\varphi_{in} = 0.12$ and superficial mixture velocity $U_m = 0.22$ m.s^{-1} at: (a) $t =$ 0 s; (b) $t =$ 1 s, and; $t =$ 2 s

5.4.1 Mixed Zone Height

Analysis of the results shown in Figures 5-3 and 5-4 reveals that the height of the mixed zone increases with an increasing superficial mixture velocity and an increasing oil input phase fraction (though this trend is difficult to discern by superficial visual inspection). Figure 5-6 presents the height of the mixed zone as a function of the independent variables i.e., the superficial mixture velocity and the input oil phase fraction.

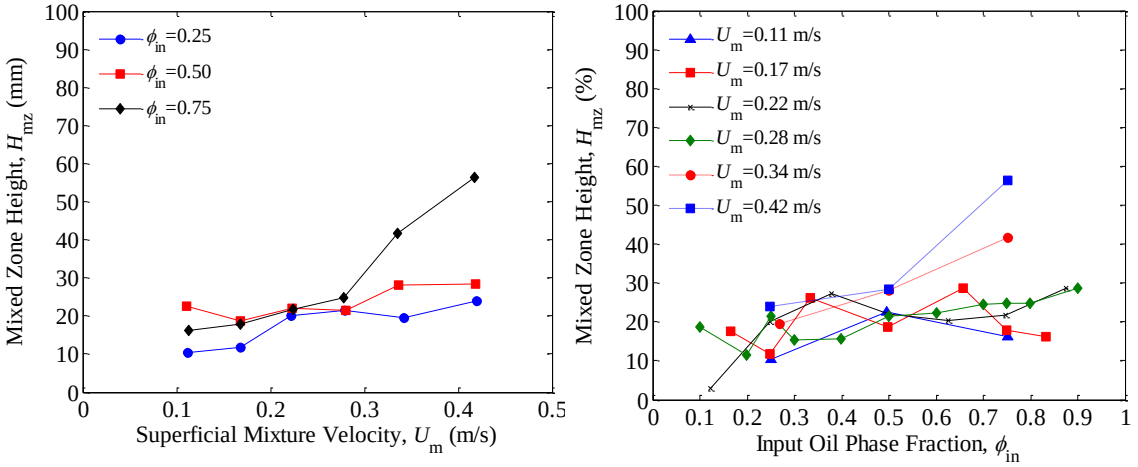

(a) (b)

Figure 5-6: Height of Interface Zone for as a function of (a) superficial mixture velocities U_m for constant input oil fraction φ_{in}; (b) input oil fraction φ_{in} for constant superficial mixture velocities U_m

From Figure 5-6(a) it can be seen that as the superficial mixture velocity increases, the height of the mixed zone increases (i.e., the gradient of the transition between the glycerol zone the oil zone becomes shallower) for a given oil input phase fraction. Further, from Figure 5-6(b) it can be seen that for low superficial mixture velocities (U_m = 0.11 m.s^{-1}) the height of the mixed zone has a maximum at an oil input phase fraction of $\varphi_{in} = 0.50$. As the superficial mixture velocity is increased, it is seen that the height of the mixed zone increases monotonically with

oil input phase fraction. The rate of the increase in the height of the mixed zone with oil input phase fraction is higher at higher superficial mixture velocities. Clearly, these observations reveal the effects of higher turbulence levels (at the higher superficial mixture velocities)in promoting mixing of the two initially separated flows, thus promoting a diffuse 'mixed zone' in between the two liquid phases.

5.5 In-Situ Phase Fraction

This section presents the results for in-situ oil phase fraction $\langle\varphi\rangle_{y,t}$. The in-situ oil phase fractions have been calculated using the phase distribution profiles coupled with a numerical integration technique to account for the curvature of the visualisation cell wall. For a given image, the phase fraction is calculated via the integral;

$$\langle\varphi\rangle_y(t) = \int_{y=0}^{y=H_T} \frac{1}{A}\varphi(y,t)\,dy \qquad (5.1)$$

For a given run (i.e., a fixed combination of U_m and φ_{in}) the average in-situ oil fraction, $\langle\varphi\rangle_{y,t}$ is calculated using Equation 3.5, in which, $\langle\varphi\rangle_y(t)$ is$\langle\varphi\rangle_{y_i}$.

Figure 5-7 shows that the in-situ oil fraction $\langle\varphi\rangle_{y,t}$ is lower than the input oil fraction φ_{in} for almost all flow conditions (as was the case for the square cross section duct – see Chapter 4, Figure 4-12). This is indicated by the data points being below the $S = 1$ (homogeneous flow model) line in Figure 5-6. Two different approaches were taken to estimate the in-situ oil phase fraction as a function of the input oil phase fraction. These are presented in Figure 5-7 as $\varphi_{mod,1}$ and $\varphi_{mod,2}$; their derivations are explained below in Sections 5.5.1 and 5.5.2, and have been calculated using the same basis as $\varphi_{mod,1b}$ and $\varphi_{mod,2}$ as that used in Figure 4-12.

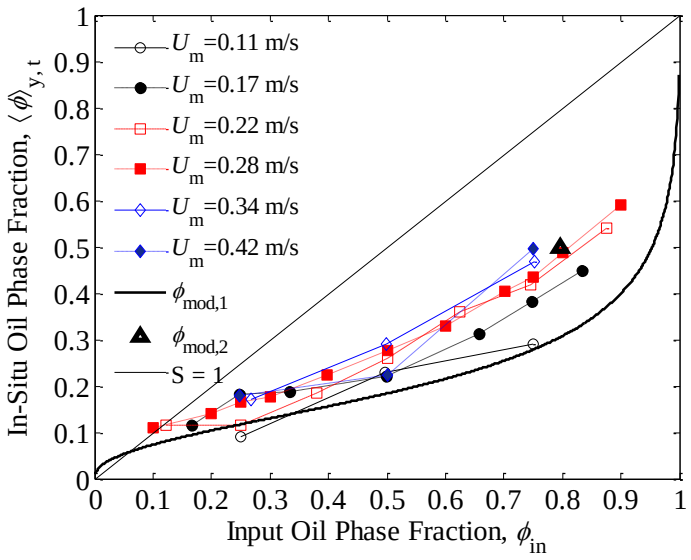

Figure 5-7: In-situ fraction $\langle\varphi\rangle_{y,t}$ as a function of input oil fraction φ_{in} for different superficial mixture velocities U_m

5.5.1 Laminar Drag Model

The "laminar drag model" for prediction of the in-situ phase fraction was developed by equating the frictional pressure drop in a two layer flow, i.e., by considering an equilibrium between viscous drag due to laminar flow and pressure drop in the pipe. This model is denoted by $\varphi_{mod,1}$ in Figure 5-7. It has been derived using the same basis as $\varphi_{mod,1b}$ in Chapter 4.

There is very good agreement between $\varphi_{mod,1}$ and the experimental results, particularly at lower input oil fractions (typically, $0.1<\varphi_{in}<0.5$) and lower superficial mixture velocities. The derivation of $\varphi_{mod,1}$ is outlined below. Firstly, the dimensionless pressure is related to the Reynolds number through a Fanning friction factor f:

$$f_i = \frac{\Delta p}{\frac{1}{2}\rho_i U_i^2}\frac{D_i}{4L} = \frac{16}{Re_i} \qquad (5.2)$$

Once written for each phase 'i' and after equating pressure drops $\Delta p/L$, Equation 5.2 reduces to:

$$\left(\frac{\mu_{\text{oil}}}{\mu_{\text{gs}}}\right).\left(\frac{\varphi_{\text{in}}}{1-\varphi_{\text{in}}}\right).F = 1 \tag{5.3}$$

where:

$$F \equiv f(\theta) = \left[\frac{\theta - sin\theta}{2\pi - sin\theta}\right].\left[\frac{2\pi - \theta}{\theta}\right]^2 \tag{5.4}$$

and;

$$\frac{Q_{\text{oil}}}{Q_{\text{gs}}} = \frac{\varphi_{\text{in}}}{1-\varphi_{\text{in}}}; \qquad Re_i = \frac{\rho_i U_i D_i}{\mu_i}; \qquad D_i = \frac{4A_i}{P_i} \tag{5.5}$$

Here, P_i is defined as the periphery of each layer in contact with the wall; a summary, the parameters used to construct Equations 5.2 to 5.5 are defined in Figure 5-8 below.

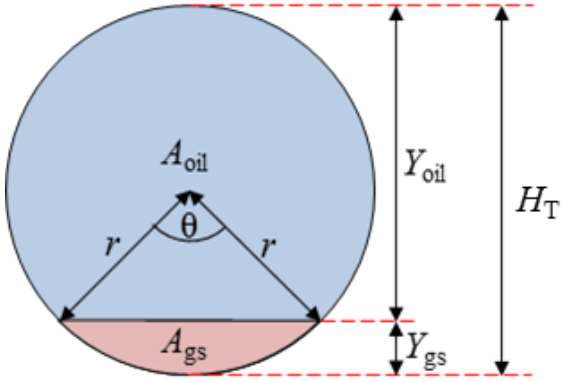

Figure 5-8: Stratified liquid-liquid flow model construction

Finally, the modelled in-situ oil phase fraction $\langle\varphi\rangle_{y,t}$ presented in Figure 5-7 is defined as:

$$\varphi_{\mathrm{mod},1} = \langle\varphi\rangle_{y,t} = \frac{A_{\mathrm{oil}}}{A_{\mathrm{oil}} + A_{\mathrm{gs}}} = 1 - \frac{(\theta - sin\theta)}{2\pi} \tag{5.6}$$

In Equations 5.2 to 5.6 θ is in radians. It should be noted that the contact area between the fluids has not been included in the calculation of $\varphi_{\mathrm{mod},1}$.

5.5.2 Differential Momentum Balance Model

The second means of comparison, denoted by $\varphi_{\mathrm{mod},2}$ in Figure 5-7 has been calculated using the exact same methodology as $\varphi_{\mathrm{mod},2}$ presented in Figure 4-12; it is derived from a differential momentum balance (Bird et al., 2001) and is applicable to the special case in which the in-situ oil fraction $\langle\varphi\rangle_{y,t} = 0.5$ and when the interface level H is at the midpoint of the pipe, i.e., $Y_{\mathrm{oil}} = Y_{\mathrm{gs}} = H = H_{\mathrm{T}}/2$ in Figure 5-8. This form of prediction is also in excellent agreement with the experimental results. Therefore, the same conclusions can be drawn as were made for the study using a square cross-section visualisation cell, presented in Chapter 4. Specifically, that the interface level is adjusting in order to satisfy the increased viscous drag caused by the higher viscosity of the glycerol solution.

5.5.3 Homogeneous Flow Model and Slip Ratio

This section assesses the suitability of using the homogenous flow model to characterise liquid-liquid flows, i.e. the velocity ratio of the fluids (defined in Equation 4.11) is unity. The homogeneous flow model is compared with the separated flow model which accounts for the existence of slip between the phases. The homogenous flow model is denoted by the thin sold line labelled $S = 1$ in Figure 5-7.

As was the case with the results presented in Chapter 4 (see Figure 4-12), it is seen from Figure 5-7 that the homogenous flow model over-predicts the in-situ phase fraction. Again, the extent of the over-prediction increases with an increasing oil input fraction. In a bid to address the predictive shortcoming of adopting a homogenous flow model, Figure 5-9 investigates whether a single S value or expression, can be used to characterise these flows.

From Figure 5-9(a) it is evident that the use of the homogenous flow model (i.e., $S = 1$) gives a very poor characterisation of the flows of the current experimental campaign, albeit except at the lowest input oil phase fractions investigated. The findings are the same as those of Chapter 4 (see Figure 4-14) and hence give further validation of the inadequacy of the homogeneous flow model to characterise the result for the flow matrix investigated (which are roughly the same for Chapters 4 and 5).

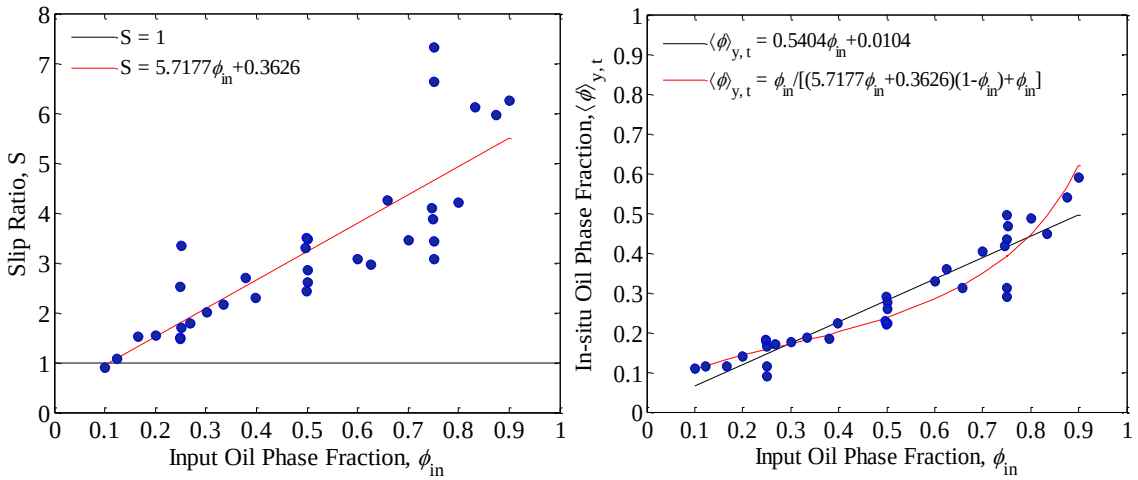

(a) (b)

Figure 5-9: Experimental results and correlations for: (a) slip ratio S as a function of input oil fraction φ_{in}, and: (b) in-situ oil phase fraction $\langle\varphi\rangle_{y,t}$ as a function of input oil fraction φ_{in}

From Figure 5-9(a) a "best fit" correlation for the slip ratio is shown, the equation for which is:

$$S = 5.7177\varphi_{\text{in}} + 0.3626 \tag{5.7}$$

This is rather similar to the "best fit" correlation for the slip ratio for the experimental results of Chapter 4. To highlight the similarity, the in-situ phase fraction that can be calculated from the slip ratio correlations (Equations 5.7 and 4.15) i.e., Equations 4.16 and 5.8, are shown together in Figure 5-10. The correlation for in-situ phase fraction derived from Equation 5.7 and Equation 4.14 (Equation 5.8 below) is seen to have excellent agreement with the experimental data and is (again) an improvement on using a linear expression to relate the input oil phase fraction to the in-situ phase fraction.

$$\langle\varphi\rangle_{y,t} = \frac{\varphi_{\text{in}}}{(5.7177\varphi_{\text{in}} + 0.3626)(1-\varphi_{\text{in}}) + \varphi_{\text{in}}} \tag{5.8}$$

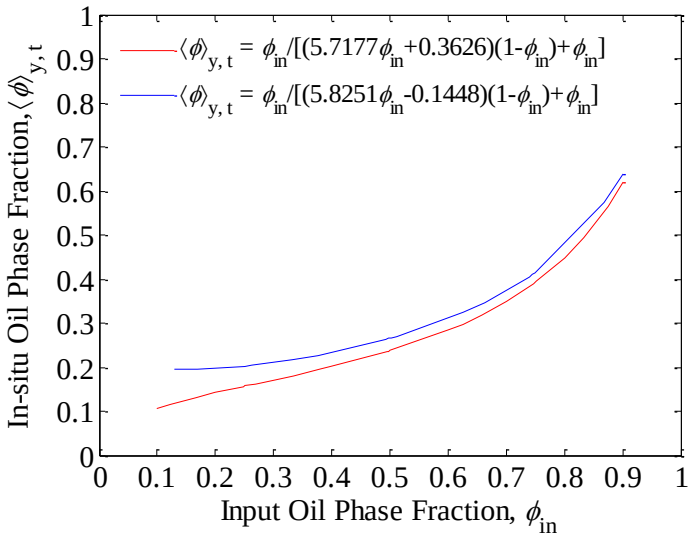

Figure 5-10: Comparison of the correlations for in-situ oil phase fraction $\langle\varphi\rangle_{y,t}$ as a function of input oil fraction φ_{in} for the square cross-section visualisation cell PLIF results (Equation 4.16) shown in blue and the circular cross-section visualisation cell PLIF results (Equation 5.8) shown in red

Due to the fact that the superficial mixture velocity is not accounted for in Figure 5-9, Figure 5-11 examines the effect of the input oil phase fraction φ_{in} on the slip ratio S at constant superficial mixture velocities U_m and includes a comparison with experimental data acquired by Lovick and Angeli (2004) for an oil-water system.

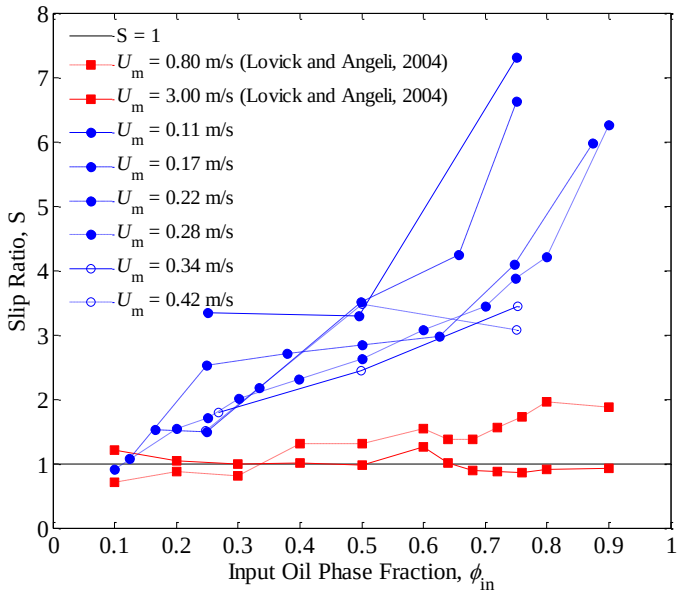

Figure 5-11: Slip ratio S as a function of input oil fraction φ_{in} for different superficial mixture velocities U_m PLIF data is presented in blue and the results from Lovick and Angeli (2004) are presented in red)

The same conclusions can be drawn from Figure 5-11 as from Figure 4-15 in Chapter 4. Specifically, that for a given oil input phase fraction, as the superficial mixture velocity increases the slip ratio decreases. For the reasons outlined in Section 4.5.3, it can again be deduced that as the superficial mixture velocity increases beyond a critical point, the flow is sufficiently well mixed (i.e., dispersed) that it can be can be adequately described via the homogenous flow model. In Section 5.9 the slip ratio is linked to the velocity profile (and the associated flow regime) as a means to verify the conditions under which a homogenous flow model suitably describes the flows.

5.5.4 Model Application and Comparison

Figure 5-12 compares the PLIF in-situ phase fraction results with the experimental results of Lovick and Angeli (2004) and Russell et al. (1959) and with the predictions from the laminar drag model $\varphi_{\mathrm{mod},1}$ (Equation 5.6). The same conclusions can be drawn from Figure 5-12 as from Figures 4-16 and 4-17 in Chapter 4, namely that at low superficial mixture velocities the laminar drag model provides excellent agreement with the experimental results. However, as the superficial mixture velocity increases, mixing in the flow increases leading to the entrainment of one liquid as drops into a continuum of the other; when such entrainment occurs, the laminar drag model breaks down.

However, for sufficiently high superficial mixture velocities (see the Lovick and Angeli, 2004 data for $U_{\mathrm{m}} = 3.00$ m.s^{-1}) the flow becomes sufficiently well mixed (i.e., it is in the dispersed flow regime) that it can be adequately characterised by the homogeneous flow model, i.e., $S = 1$ hence $\langle\varphi\rangle_{y,t} = \varphi_{\mathrm{in}}$.

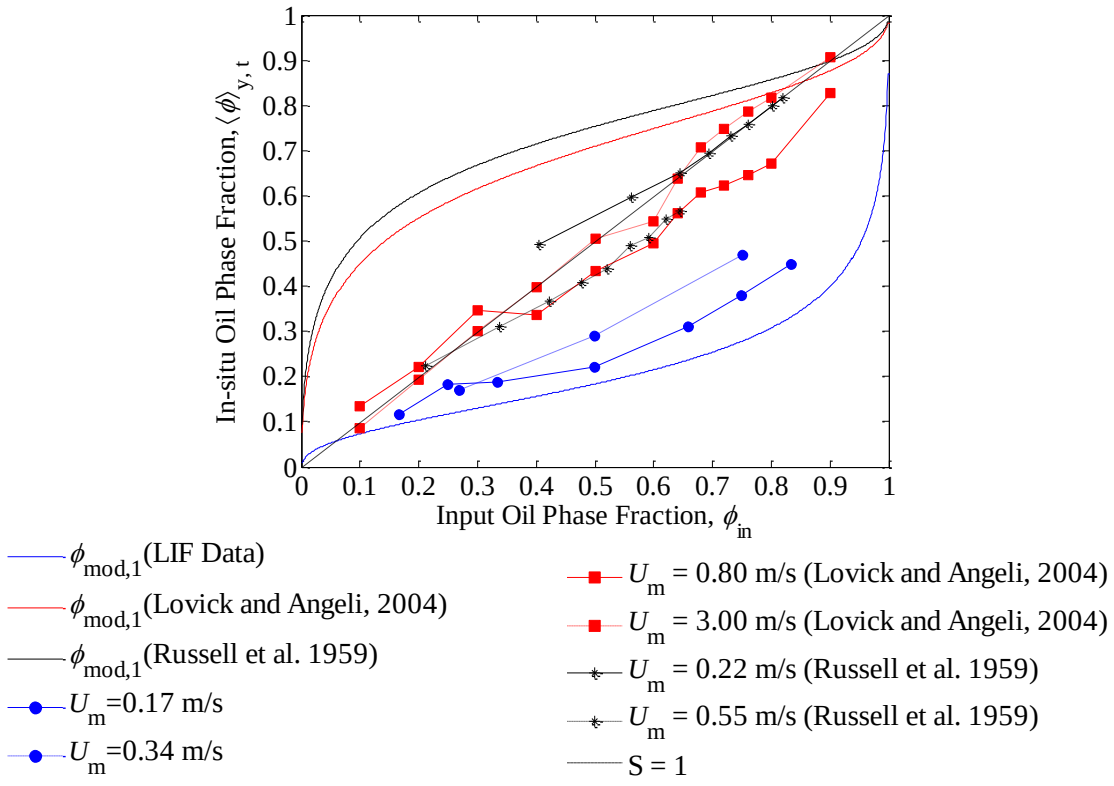

Figure 5-12: In-situ fraction $\langle\varphi\rangle_{y,t}$ as a function of input oil fraction φ_{in} for different superficial mixture velocities U_m compared with data from Lovick and Angeli (2004) and Russell et al. (1959)

As mentioned in Section 4.5, the difficulty arises when trying to predict the in-situ phase fraction between these two boundaries (stratified and dispersed flows), i.e., for *dual continuous* flows. However, as was demonstrated in Chapter 4, good agreement with the laminar drag model can be obtained for dual continuous flow when effective viscosities are calculated for the fluid mixtures below and above the interface. It will be demonstrated in Section 5.8 that very good agreement is yielded when using an amended form of the laminar drag model in which the entrainment of one fluid in a continuum of the other is accounted for to enable the viscosities of the flow above and below the interface to be deduced from the values for the single fluids. As this has been demonstrated to work in Chapter 4, the undertaking has not been repeated herein, however, the principle is demonstrated pictorially by means of an envelope plot in Figure 5-13.

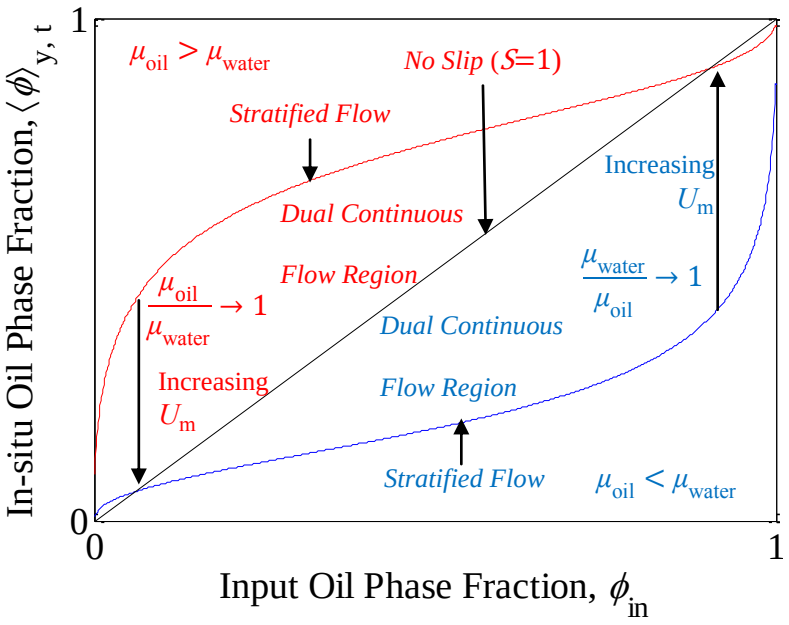

Figure 5-13: In-situ phase fraction envelope

5.6 Interface Level

This Section presents the experimental data for interface level in stratified flows obtained from analysis of the PLIF images, and also presents comparisons between the data and two alternative prediction approaches. Figure 5-14 presents the results of the interface level H as a function of input oil fraction φ_{in} for fixed superficial mixture velocities from U_m = 0.11 to 0.28 m.s^{-1}.

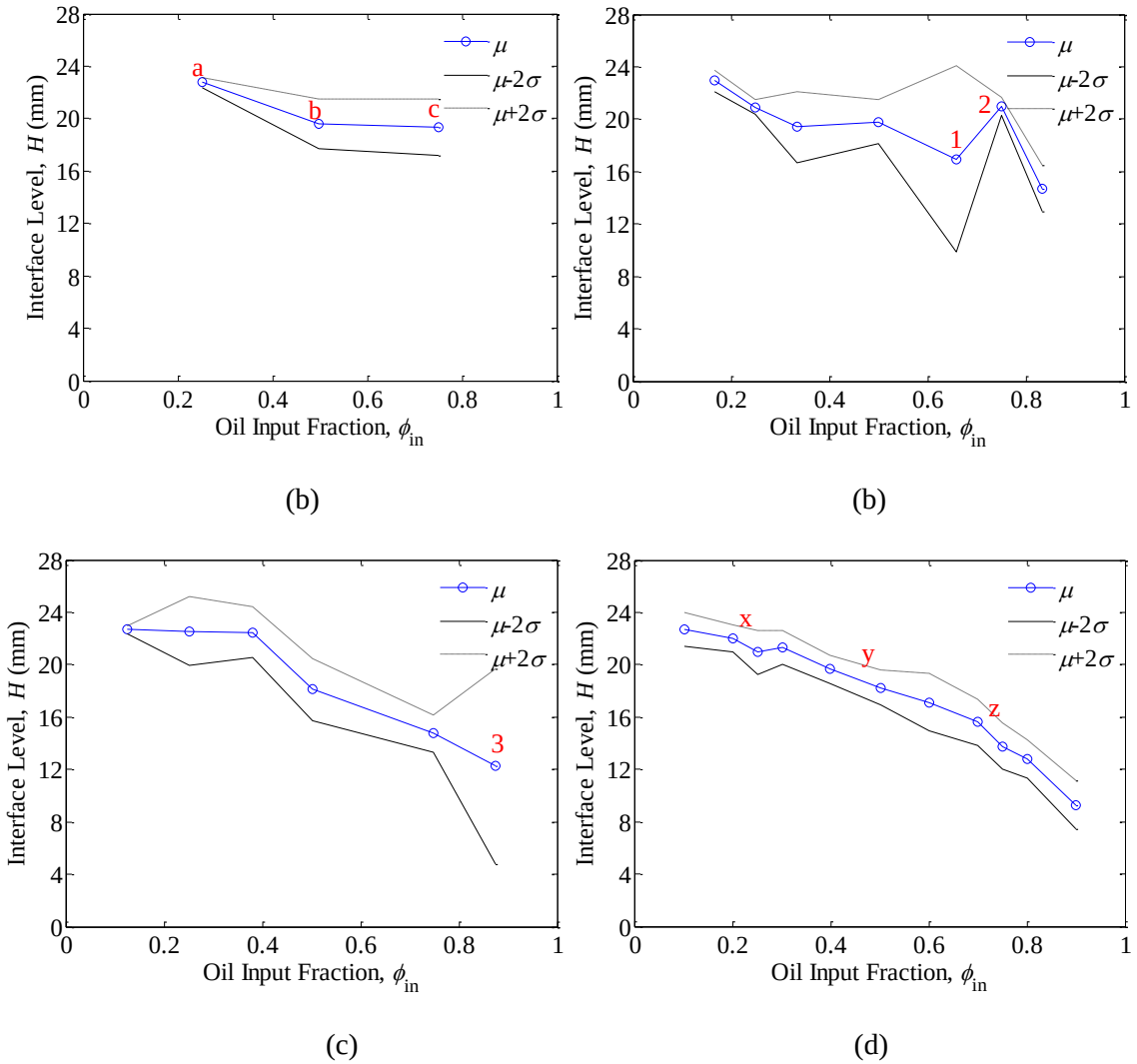

Figure 5-14: The mean (μ) and upper ($\mu + 2\sigma$) and lower (μ a2σ) limits for the interface level H as a function of input oil fraction φ_{in} for superficial mixture velocities U_m of: (a) 0.11 m.s^{-1}; (b) 0.17 m.s^{-1}; (c) 0.22 m.s^{-1}, and (d) 0.28 m.s^{-1}

The results reveal that, for a given superficial mixture velocity U_m, the interface level decreases as the oil input fraction increases. This trend is seen to be more prominent for higher superficial mixture velocities. Figure 5-14 shows the interface level H as a function of superficial mixture velocity U_m for a given oil input fraction ranging from $\varphi_{in} = 0.25$ to 0.75.

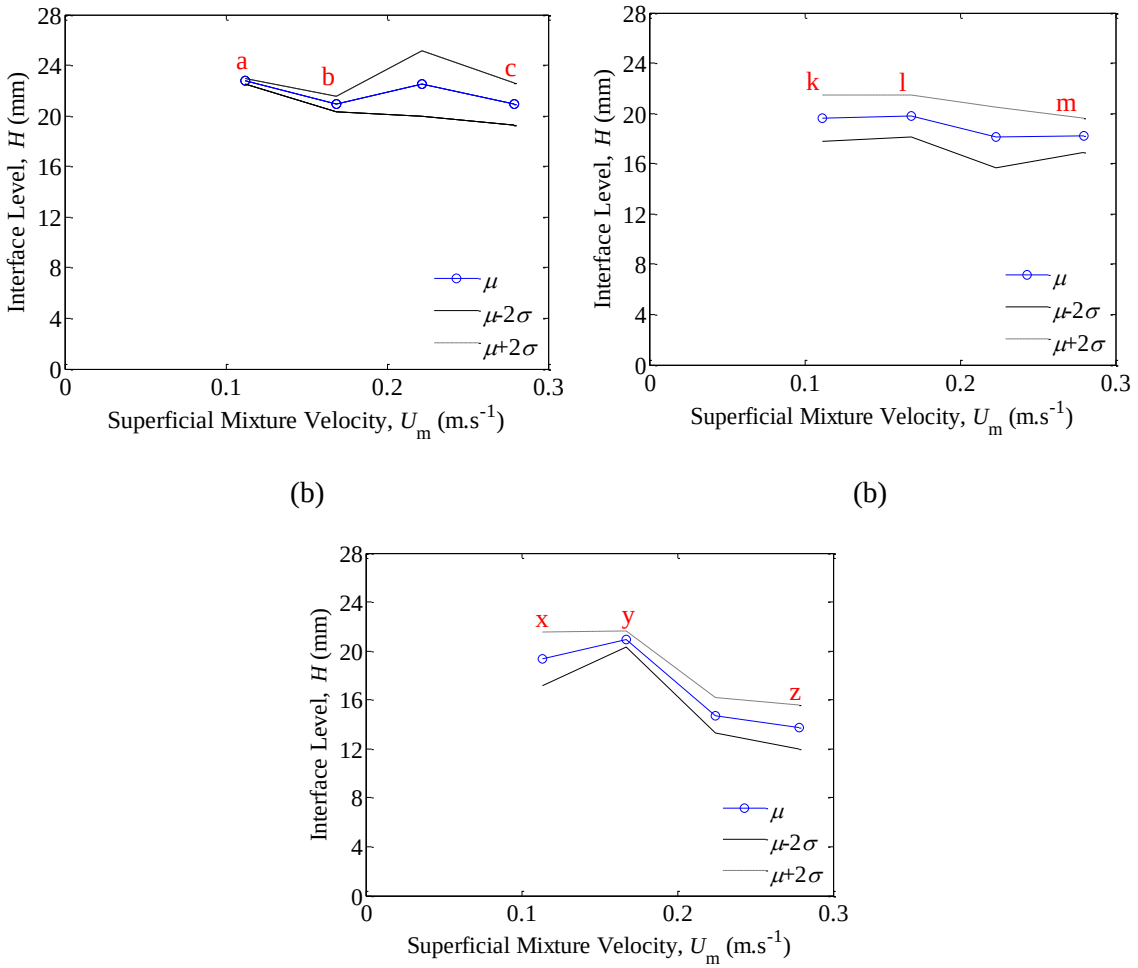

Figure 5-15: The mean (μ) and upper ($\mu + 2\sigma$) and lower (μ a2σ) limits for the interface level H as a function of superficial mixture velocity U_m for input oil fractions φ_{in} of: (a) 0.25, (b) 0.50, and (c) 0.75. Points a, b, c; k, l, m; and x, y, z correspond to the example images and probability histograms in Figures 5-16, 5-17 and 5-18 respectively

Inspection of Figure 5-15 reveals that as the superficial mixture velocity U_m increases, the mean interface level decreases for a given oil input fraction φ_{in}. From comparison of Figures 5-15(a) to 5-15(c) it is seen that as the oil input oil fraction φ_{in} increases, the rate at which the interface level decreases for an increasing superficial mixture velocity U_m increases. These trends are seen more clearly in Figures 5-21 and 5-22.

5.6.1 Probability Histograms

Figures 5-16 and 5-17 present instantaneous images and interface level probability histograms for the points that have been used to construct the mean interface level plots shown in Figures 5-14(a) and 5-14(d), respectively. From inspection of the instantaneous images ($a_1 \rightarrow c_1$ and $x_1 \rightarrow z_1$) and the histograms ($a_2 \rightarrow c_2$ and $x_2 \rightarrow z_2$), one can easily see that the mean interface level μ_H decreases with an increasing oil input oil fractions φ_{in} for a given superficial mixture velocity U_m. From comparison of Figures 5-14(a) → 5-14(d) it is seen that the rate of decrease in interface level increases as the superficial mixture velocity U_m is increased. The results shown in Figure 5-14 indicate no discernable trend in the extent of the distribution spread, i.e., the 95% confidence interval ($\mu - 2\sigma \rightarrow \mu + 2\sigma$). However, with the exception of three points which have been numbered 1 → 3 and shown in Figures 5-14(b) and 5-14(c), the 95% confidence interval is approximately constant for a given superficial mixture velocity U_m.

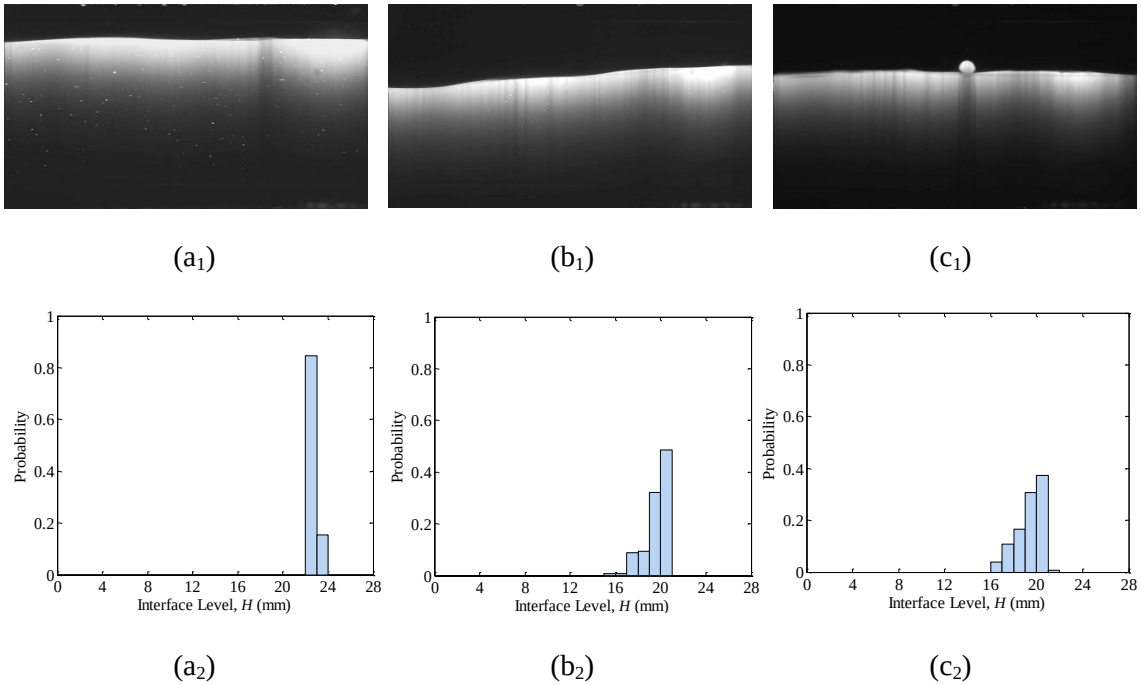

Figure 5-16: Flow images with input oil fraction φ_{in} of (a_1) 0.25, (b_1) 0.50, (c_1) 0.75, all at a superficial mixture velocities U_m = 0.11 m.s^{-1}; (a_2), (b_2) and (c_2) show the probability histograms for the same conditions respectively. Data corresponds to Points a, b and c, as labelled in Figure 5-14(a)

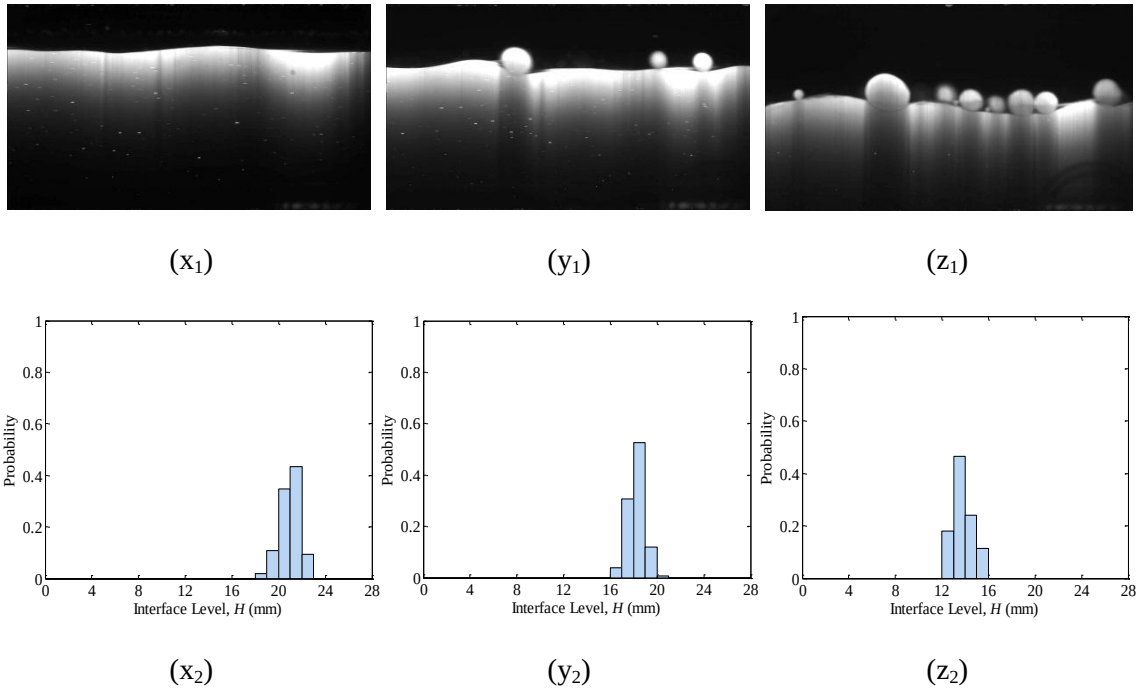

Figure 5-17: Flow images with input oil fraction φ_{in} of (x_1) 0.25 m.s^{-1}, (y_1) 0.50, (z_1) 0.75, all at a superficial mixture velocities U_m = 0.28 m.s^{-1}; (x_2), (y_2) and (z_2) show the probability histograms for the same conditions respectively. Data corresponds to Points a, b and c, as labelled in Figure 5-14(d)

Figures 5-16 to 5-18 present frames and the probability histograms for the points that have been used to construct the mean interface level plots shown in Figures 5-15(a) to 5-15(c), respectively. From inspection of the images ($a_1 \rightarrow c_1$, $k_1 \rightarrow m_1$ and $x_1 \rightarrow z_1$) and the histograms ($a_2 \rightarrow c_2$, $k_2 \rightarrow m_2$ and $x_2 \rightarrow z_2$), one can conclude that the mean interface level μ_H decreases for an increasing superficial mixture velocity U_m while at the same time the interface level fluctuation range widens. We would expect that at a low superficial mixture velocity U_m, when the flow is stratified, that the interface level would be flat and stable H (Shaha, 1999).

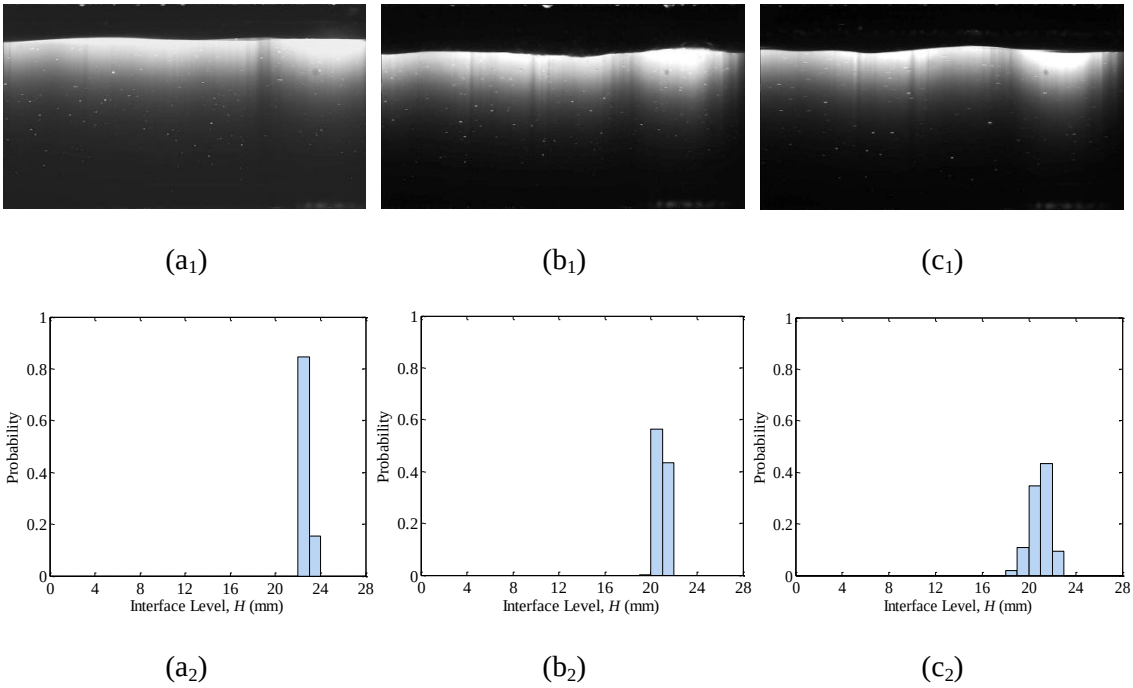

Figure 5-18: Flow images with superficial mixture velocities U_m of: (a_1) 0.11 m.s^{-1}, (b_1) 0.17 m.s^{-1}, (c_1) 0.28 m.s^{-1}, all at an input oil fraction $\varphi_{in} = 0.25$; (a_2), (b_2) and (c_2) show the probability histograms for the same conditions respectively. Data corresponds to Points a, b and c, as labelled in Figure 5-14(a)

From inspection of Figures 5-16 to 5-20 it can be seen that at lower superficial mixture velocities the interface level is found to cover only a narrow range of vertical heights (see Figures 5-16(a_2) and 5-18(a_2)) consistent with a smooth stratified flow. The height of the mixed zone is seen to increase at the transition to dual continuous flow; see Figures 5-17(z_2) and 5-20(z_2).

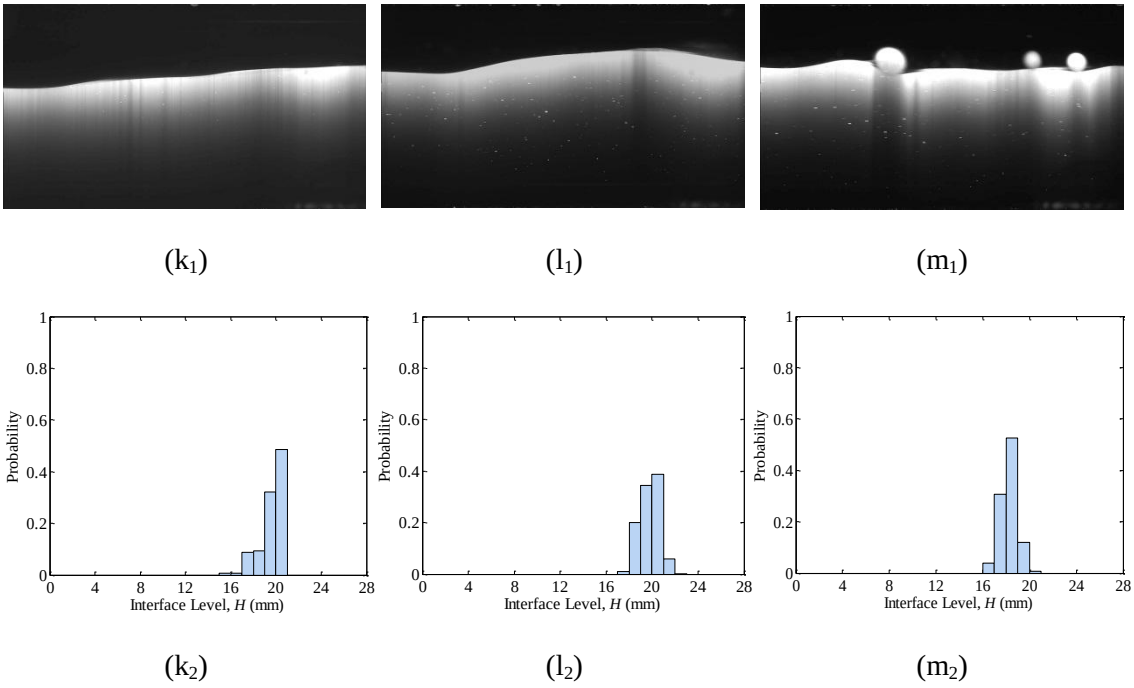

Figure 5-19: Flow images with superficial mixture velocities U_m of: (k_1) 0.11 m.s^{-1}, (l_1) 0.17 m.s^{-1}, (m_1) 0.28 m.s^{-1}, all at an input oil fraction $\varphi_{in} = 0.50$; (k_2), (l_2) and (m_2) show the probability histograms for the same conditions respectively. Data corresponds to Points k, l and m, as labelled in Figure 5-14(b)

The widening of the interface height range with increasing superficial mixture velocity is a manifestation of the corresponding increase of the amplitude of the waves on the interface and is probably linked to the onset and increase of turbulence in the flow as the superficial mixture velocity increases. Increased turbulence can lead to droplet formation and the entrainment of one phase in a continuum of another which can further widen the range of interface level heights.

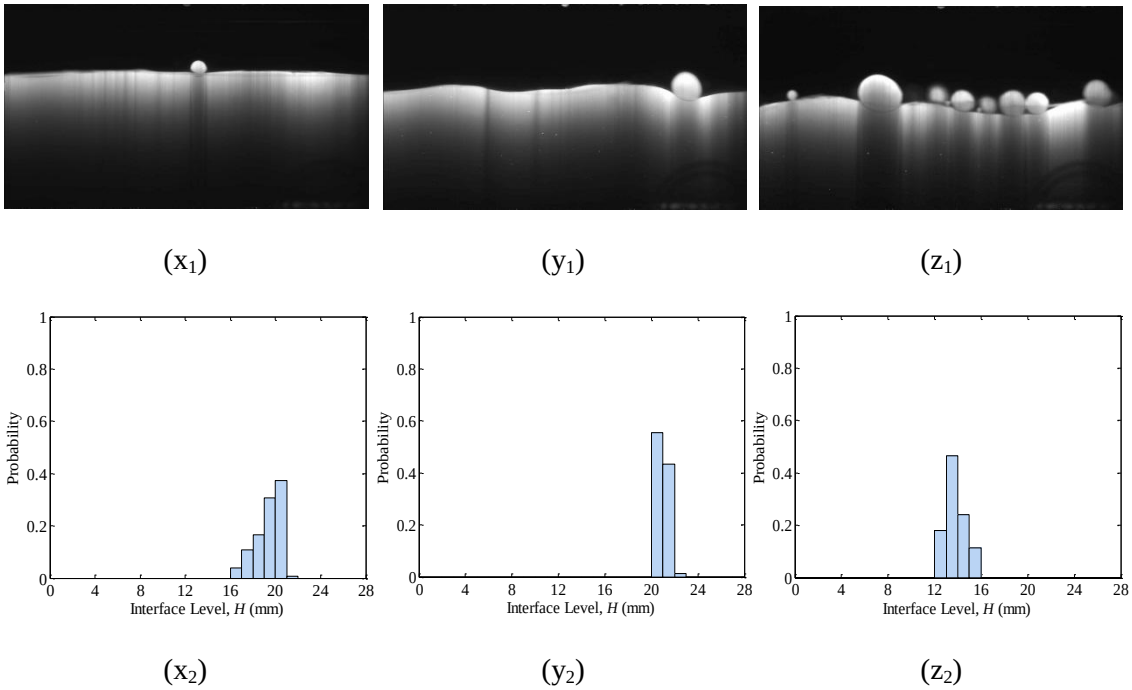

Figure 5-20: Flow images with superficial mixture velocities U_m of: (x_1) 0.11 m.s^{-1}, (x_1) 0.17 m.s^{-1}, (x_1) 0.28 m.s^{-1}, all at an input oil fraction $\varphi_{in} = 0.75$; (x_2), (y_2) and (z_2) show the probability histograms for the same conditions respectively. Data corresponds to Points x, y and z, as labelled in Figure 5-14(c)

5.6.2 Laminar Drag Model

Figure 5-21 shows that the modified form of the laminar drag model (Equation 5.6), denoted by $H_{mod,1}$ predicts the lowering of the interface level H as the oil input fraction φ_{in} increases and is in very good agreement with the experimental data points relating to low-velocity stratified flows ($U_m = 0.11$ to 0.17 m.s^{-1}) in which the flow contains no droplets. It was discussed in Chapter 4 that due to the fact that the laminar drag model does not account for phase break-up and droplet formation the model fails to capture that the interface level decreases for a given oil input phase fraction as the superficial mixture velocity increases.

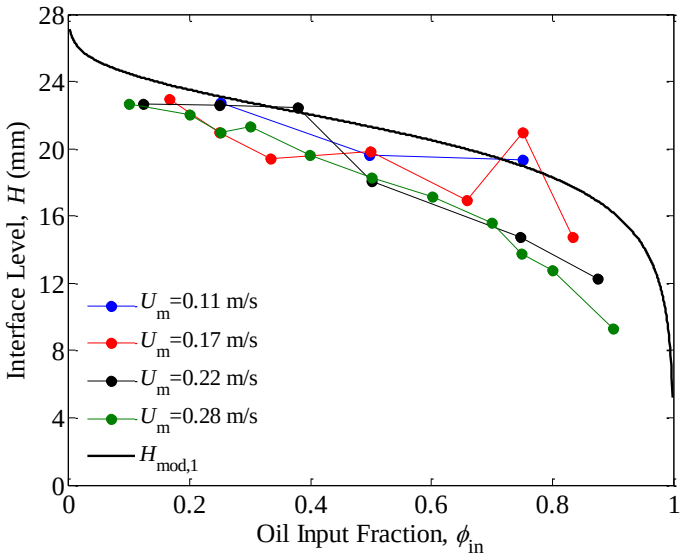

Figure 5-21: Interface Level H as a function of input oil fraction φ_{in} for different superficial mixture velocities U_m

5.6.3 Predictive Technique of Hall and Hewitt (1993)

Figure 5-22 compares the experimental results for interface level with predictions from the stratified flow models presented by Hall and Hewitt (1993). The Hall and Hewitt model for liquid-liquid flows generally over-predicts the data. However, the liquids in the present study are such that the oil phase is less dense than the aqueous phase, but also less viscous. This is similar to the case of a gas-liquid flow and the Hall and Hewitt model for this case is compared with the present data in Figure 5-22(a).

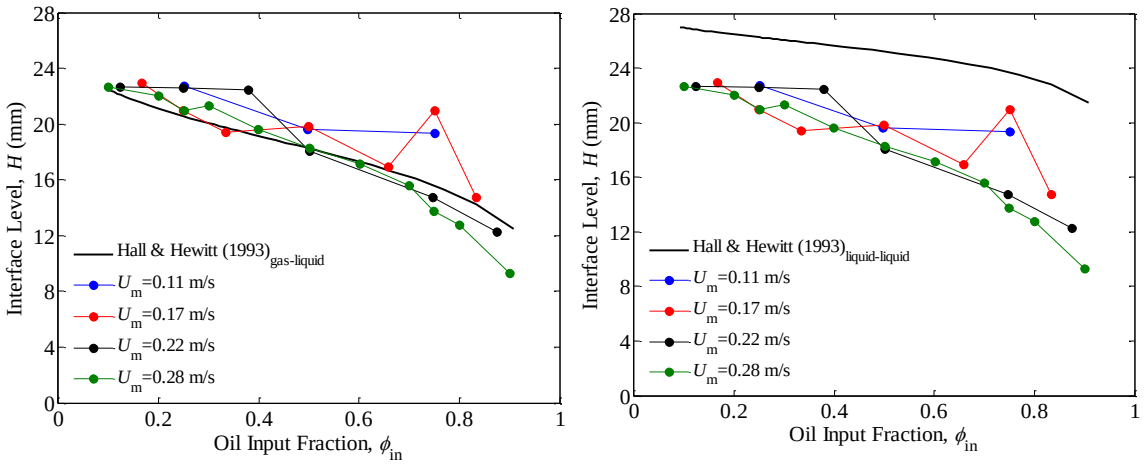

(a) (b)

Figure 5-22: Interface Level H as a function of input oil fraction φ_{in} for different superficial mixture velocities U_m featuring interface level models presented by Hall and Hewitt (1993) for: (a) stratified liquid-liquid flow, and (b) stratified gas-liquid flow

It is seen that both predictive techniques capture the lowering of the interface level with an increasing oil input phase fraction. However, the liquid-liquid model over-predicts the interface level for all flowing conditions investigated; the difference increases with an increasing oil input phase fraction for a given superficial mixture velocity. The model for gas-liquid systems shows excellent agreement with the present experimental data.

The breakdown in the ability of the Hall and Hewitt (1993) liquid-liquid model to accurately predict the interface level as the superficial mixture velocity increases can be attributed to the model assuming a flat interface between the two liquids. However, and particularly at higher mixture velocities, the interface is not flat and is covered with waves. The Hall and Hewitt gas liquid flow model takes account of such waves by assigning an enhanced interfacial friction.

5.7 Droplet Size Distribution

This section presents the results for droplet size which have been obtained from the analysis of the PLIF images for the circular tube case. As explained in Chapter 3 and above, these images were first corrected (using the graticule method) for the distortion caused by the circular channel wall. Here, the results presented are for glycerol solution droplets –in – oil. As a consequence of, either: the absence, or; the lack of abundance of oil – droplets – in – glycerol solution in these experiments, it was not possible to obtain a sufficient sample size to study the characteristics of oil droplets entrained in the aqueous (glycerol solution) phase. The results glycerol solution droplets – in – oil are presented in Figures 5-23 to 5-25 below. Figure 5-23 shows the effects of: (a) oil input fraction φ_{in}, and; (b) superficial mixture velocity U_m on the mean glycerol solution droplet diameters $\mu_{d,gs}$ (defined in Equations 3.8 and 3.9 in Section 3.11.5). Figures 5-24 and 5-25 present instantaneous images ($a_1 \rightarrow c_1$ and $x_1 \rightarrow z_1$) and probability histograms ($a_2 \rightarrow c_2$ and $x_2 \rightarrow z_2$) for the points labelled a → c and x → z in Figure 5-23.

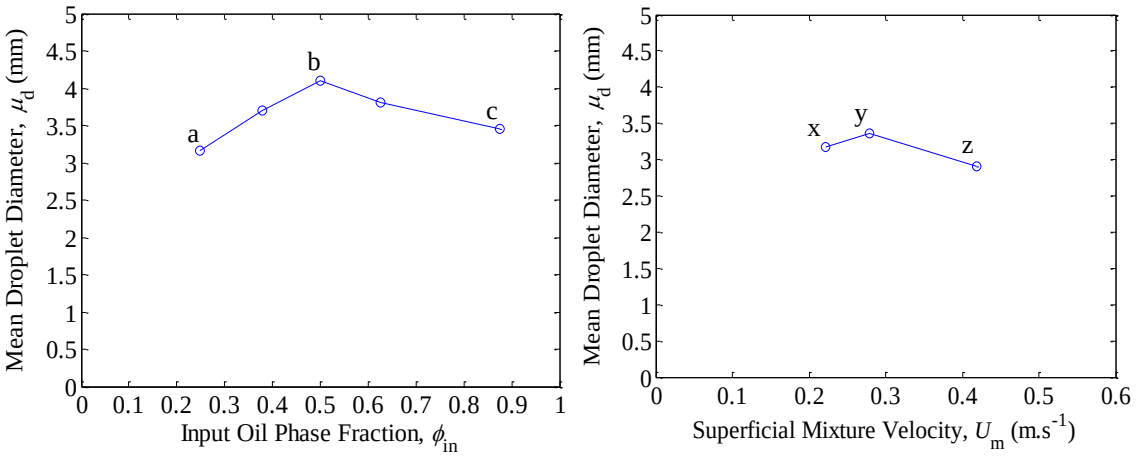

(a) (b)

Figure 5-23: Mean glycerol solution droplet diameter $\mu_{d,gs}$ for: (a) varying input oil fraction φ_{in} and constant superficial mixture velocities $U_m = 0.22$ m.s^{-1}, and; (b) varying superficial mixture velocity U_m and a constant input oil fraction of $\varphi_{in} = 0.25$. Points a, b and c correspond to the instantaneous images $a_1 \rightarrow c_1$ and probability histograms $a_2 \rightarrow c_2$ in Figure 5-24. Points x, y and z correspond to the instantaneous images $x_1 \rightarrow z_1$ and probability histograms $x_2 \rightarrow z_2$ in Figure 5-25

Figure 5-23(a) indicates that for a fixed superficial mixture velocity U_m, the average glycerol solution droplet diameter $\mu_{d,gs}$ increases at a constant rate with an increasing oil input fraction up to $\varphi_{in} = 0.5$. However, as the oil input fraction φ_{in} is increased further, the average glycerol solution droplet diameter decreases monotonically, i.e., the mean droplet diameter is shown to peak at an oil input fraction of $\varphi_{in} = 0.5$ with a value of $\mu_{d,gs} = 4.1$ mm, at a superficial mixture velocity of $U_m = 0.22$ m.s^{-1}. As was seen with the PLIF study presented in Chapter 4, this result is consistent with the fining of Pal (1993) who observed a peak in the droplet size at the phase inversion point, $\varphi_{in,water} = 0.3$. This is also consistent with the findings of Liu (2005) who also observed a maximum in the droplet size at the phase inversion point.

Figure 5-23(b) shows results for mean glycerol solution droplet size as a function of superficial mixture velocity U_m for a given (fixed) input oil fraction of $\varphi_{in} = 0.25$. The mean glycerol solution droplet diameter $\mu_{d,gs}$ increases slightly (by about 6%) and then decreases (by about 14%) as a result of the increase in the superficial mixture velocity U_m from 0.22 m.s^{-1} to 0.28 m.s^{-1}, and then to 0.42 m.s^{-1}.

5.7.1 Probability Histograms

Figures 5-24 and 5-25 show probability histograms of glycerol solution droplet size and instantaneous images for the points a → c and x → z in Figure 5-23(a) and 5-23(b), respectively. From Figure 5-24 it can be seen that as the oil input fraction is increased for a given superficial mixture velocity (in this case, $U_m = 0.22$ m.s^{-1}) the glycerol solution droplets occupy the same diameter range though the distribution becomes more uniform with increasing oil input fraction. Figure 5-25(x_2) shows that, at a low superficial mixture velocity of $U_m = 0.22$ m.s^{-1}, there is a clear preference for droplets of a certain size. The preference for this size is maintained as the superficial mixture velocity is increased (firstly to $U_m = 0.28$ m.s^{-1}and then on to $U_m = 0.42$ m.s^{-1}), however, the probability for smaller droplets decreases as the superficial mixture velocity is increased.

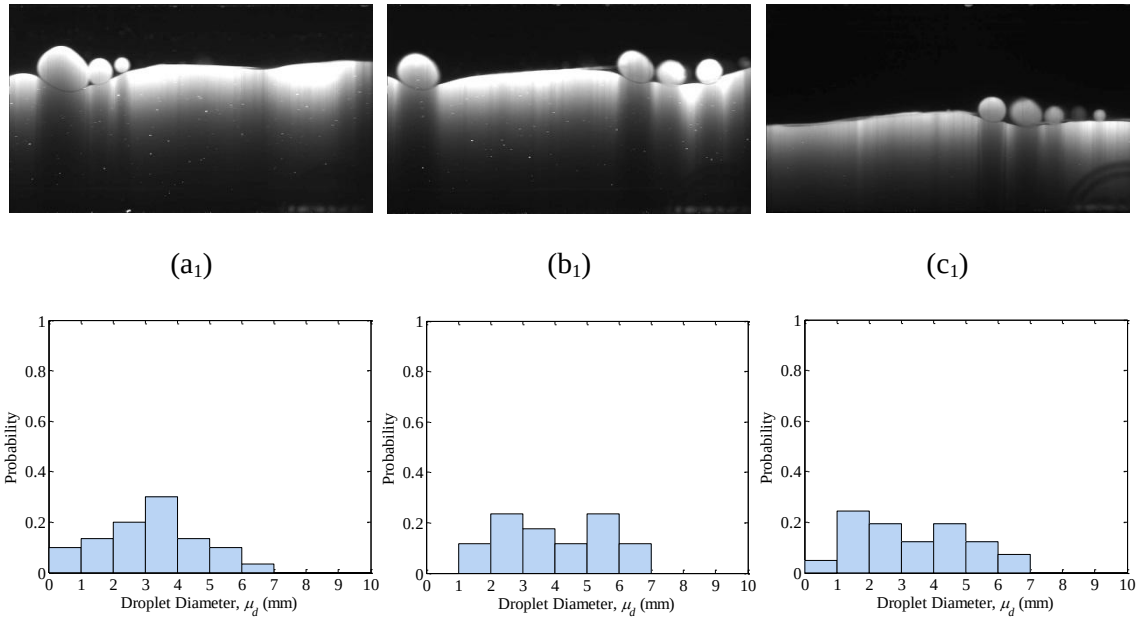

Figure 5-24: Flow images with a superficial mixture velocity U_m = 0.22 m.s^{-1} at oil input fractions φ_{in} of: (a_1) 0.25, (b_1) 0.50 and, (c_1) 0.87; (a_2), (b_2) and (c_2) show the glycerol solution droplet size distribution probability histograms for the same conditions respectively. Data corresponds to Points a, b and c, as labelled in Figure 5-23(a)

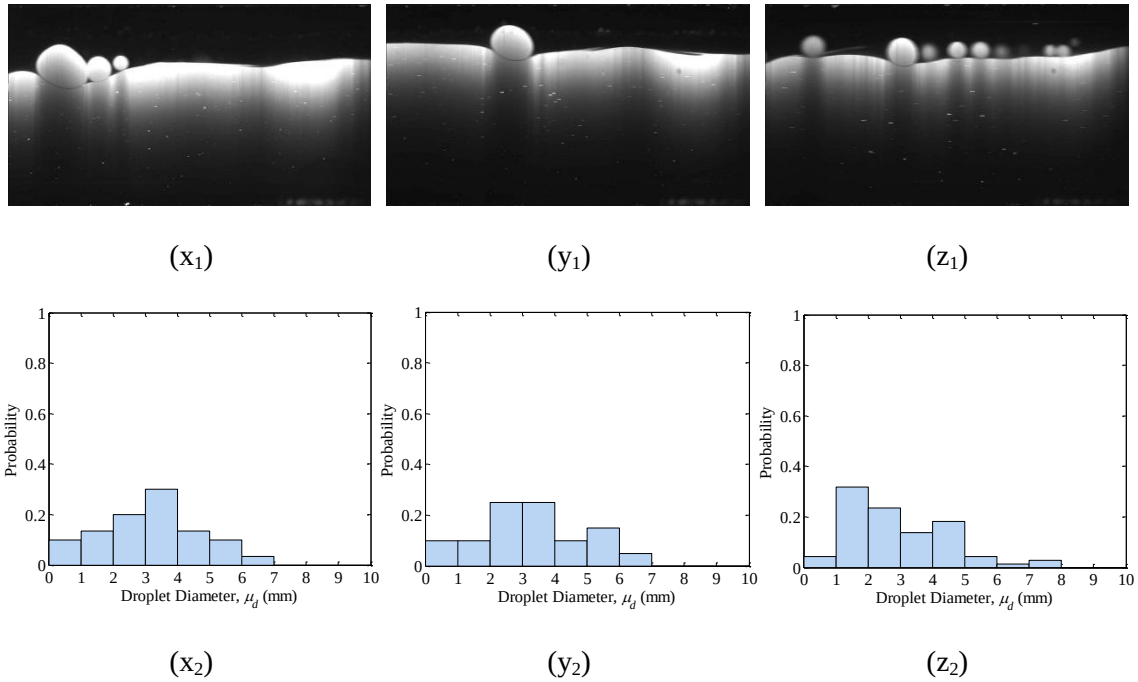

Figure 5-25: Flow images with an oil input fraction fractions φ_{in} = 0.25 at superficial mixture velocities U_m of (x_1) 0.22, (y_1) 0.28 and, (z_1) 0.42; (x_2), (y_2) and (z_2) show the glycerol solution droplet size distribution probability histograms for the same conditions respectively. Data corresponds to Points x, y and z, as labelled in Figure 5-23(b)

5.8 Interfacial Wave Velocity

The interfacial wave velocity $\langle U_{int} \rangle_t$ has been determined from the PLIF images; the procedure adopted is detailed in Section 3.11.6. Though an extensive analysis was performed, investigating the relationship of the interface wave velocity with: (1) superficial mixture velocity U_m; (2) the superficial velocity of the individual phases U_{oil} and U_{gs}; (3) oil input fraction φ_{in}; (3) the velocity at the interface, and; (4) the interface level, However, this endeavour has not provided a clear quantitative insight into the factors which govern interfacial velocity. Here, the results are presented in Table 5-1 for reference. We can see that the wave velocity is within the range 0-0.5 m.s^{-1}, and is typically of the same order as the superficial mixture velocities in the background flow.

Table 5-1: Interface wave velocity $\langle U_{\text{int}} \rangle_t$ results

Superficial Mixture Velocity, U_{m} (m.s^{-1})	**Oil Input Fraction, φ_{in}**	**Interface Wave Velocity $\langle U_{\text{int}} \rangle_t$**	
		Mean (m.s^{-1})	**Standard Deviation (m.s^{-1})**
0.11	0.25	0.00	0.00
	0.50	0.01	0.00
	0.75	0.22	0.09
0.17	0.25	0.14	0.08
	0.33	0.39	0.13
	0.50	0.40	0.18
	0.66	0.14	0.09
	0.75	0.39	0.17
0.22	0.12	0.00	0.00
	0.25	0.37	0.12
	0.50	0.41	0.13
	0.63	0.40	0.11
	0.75	0.24	0.07
	0.87	0.28	0.06
0.28	0.10	0.47	0.26
	0.20	0.44	0.17
	0.25	0.41	0.14
	0.40	0.48	0.16
	0.50	0.52	0.13
	0.60	0.53	0.10
	0.70	0.53	0.10
	0.75	0.49	0.11
	0.80	0.45	0.09
	0.90	0.38	0.08

5.9 Velocity Profiles

This section presents velocity profile results that have been generated using the PTV and PIV techniques detailed in Section 3.11.7. The velocity profile results are presented first as a function of superficial mixture velocity for a constant oil input fractions and then, subsequently, as a function of flow regime. Finally, the relationship between velocity U_H at the interface and the interface level H is examined.

Figure 5-26 shows velocity profiles for superficial mixture velocities in the range $U_m = 0.11$ to 0.42 m.s^{-1} at oil input fractions φ_{in} of (a) 0.25; (b) 0.50, and; (c) 0.75. For a given run (i.e., a fixed superficial mixture velocity U_m and fixed oil input fraction φ_{in}) the velocity profile has been divided by the superficial mixture velocity of that run, i.e., it has been normalised. From inspection of Figure 5-26 it can be seen that once normalised, the velocity profiles for a given oil input fraction φ_{in} collapse to a 'generic' profile that is largely independent of the superficial mixture velocity (though with some exceptions). However, there is a region that retains dependence to the superficial mixture velocity, namely the interface region, (which is labelled as the mixed zone in Figure 4-7 of Chapter 4). This dependence can be attributed to the transition through the different flow regimes that are encountered as the superficial mixture velocity is increased.

Though the velocity of the two phases must be close to being the same at the interface, there may be thin boundary layers in the interface region in either or both phases in which the velocity may change significantly. These changes may manifest themselves as an apparent step change in velocity from one phase to the other as the interface region is traversed. The "step-change" at the interface is seen to be most prominent for the lowest superficial mixture velocities investigated, U_m = 0.11 to 0.22 m.s^{-1}. As first discussed in Section 5.5.3 (see in particular, Figure 5-11), the Slip Ratio S between the two liquid phases is highest for these

conditions. From Figure 5-11 it is also seen that the Slip Ratio increases with input oil phase fraction. Comparing Figures 5-26(a) and 5-26(b), the "step-change" at the interface is seen to increase with oil input phase fraction. Ultimately, if there is sufficient shear (i.e., a sufficient velocity difference) across the interface, this will give rise to the Kelvin-Helmhotlz instability which can cause waves at the common interface and the onset of a transition to other flow regimes, first *dual continuous* flow and ultimately *dispersed* flow which have their own characteristic velocity profiles, as discussed in Section 5.9.1.

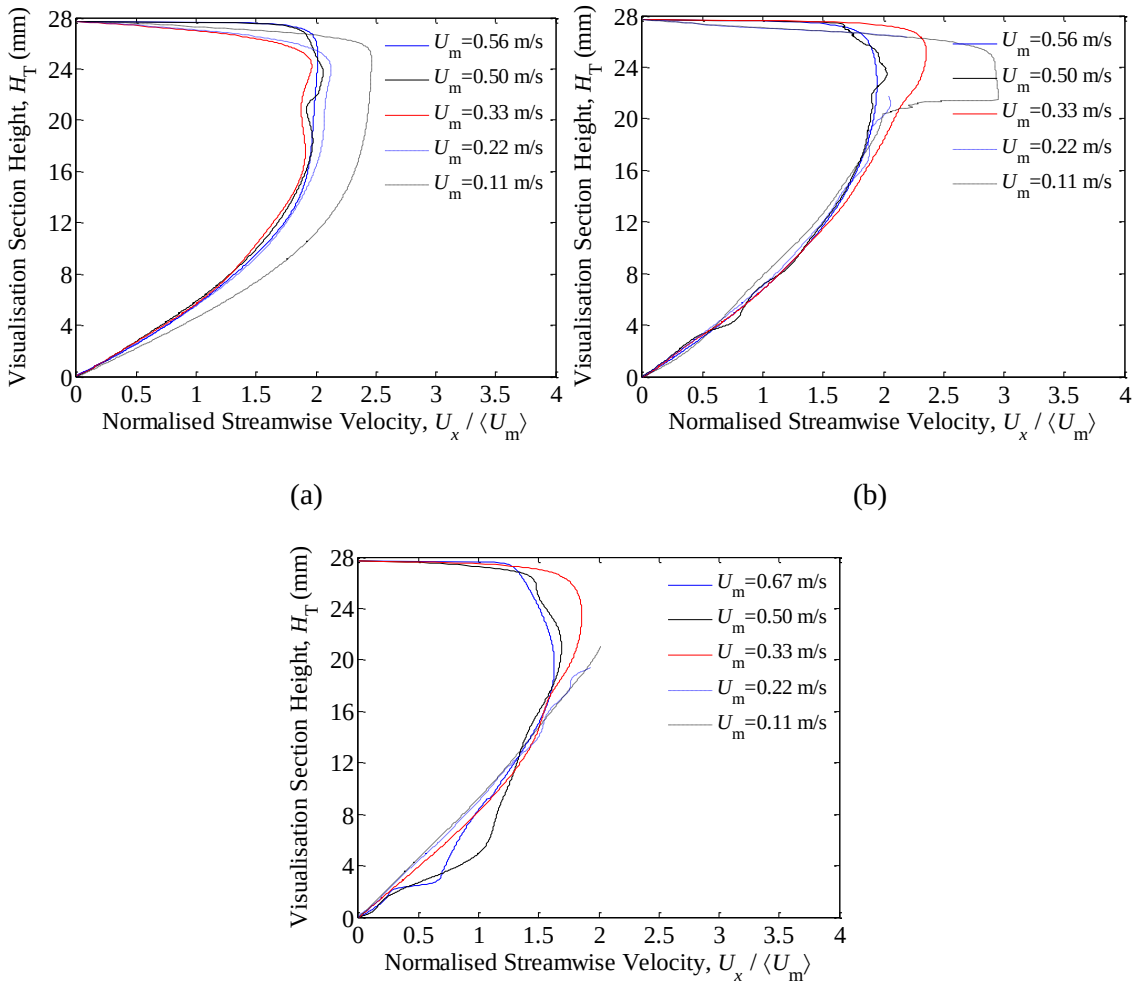

Figure 5-26: Normalised velocity profiles $U_x/\langle U_m \rangle$ for different superficial mixture velocities U_m at an input oil fraction φ_{in} of: (a) 0.25; (b) 0.50, and; (c) 0.75

5.9.1 Flow Regime Analysis

In the present experiments, there was a considerable difference in viscosity between the oil and aqueous phases, with the (lower) aqueous phase having a much higher viscosity. This can give rise to laminar flow in the aqueous phase co-existing with turbulent flow in the oil phase. Such a change in the nature of the flow from the lower to the upper region would be expected to give rise to characteristic changes in the nature of the velocity profile. This change in the nature of the velocity distribution between laminar and turbulent flow is illustrated by considering the simpler case of single phase flows in a tube as shown in Figure 5-27.

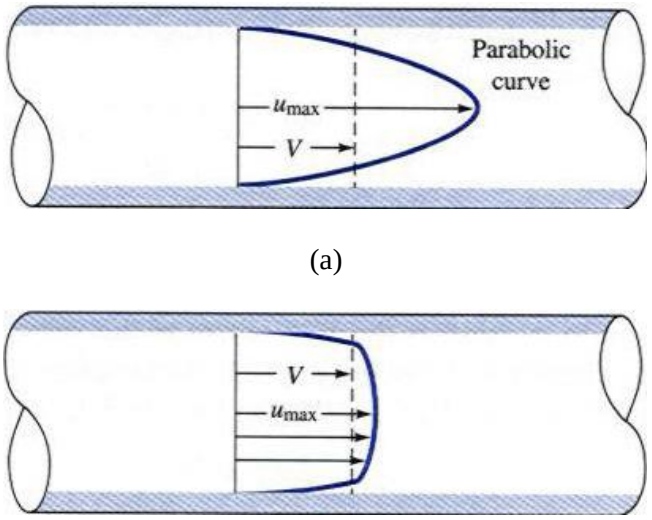

Figure 5-27: Velocity profiles for: (a) laminar flow, and; (b) turbulent flow, taken from Sellens (2008)

Figure 5-28 presents normalised velocity profiles ($a_1 \rightarrow a_3$) and corresponding instantaneous images ($b_1 \rightarrow b_3$) for two stratified flow cases, with the following input conditions: (1) $U_m = 0.17$ m.s^{-1} and $\varphi_{in} = 0.17$, and; (2) $U_m = 0.28$ m.s^{-1} and $\varphi_{in} = 0.38$. Inspection of the velocity profiles ($a_1 \rightarrow a_2$) in relation to the flow images ($b_1 \rightarrow b_2$) shows that, from the bottom of the test section, the velocity profile follows a parabolic curve up to the interface,

characteristic of a velocity profile for laminar flow (see Figure 5-27(a)). For U_m =0.28 m.s^{-1} (Figure 5-28 (2)) the velocity profile in the upper region is clearly of a turbulent type. For U_m = 0.17m.s^{-1} there is a step change in velocity in the interface region and, above this region, the velocity profile in the oil phase seems to be more characteristic of a laminar than a turbulent flow.

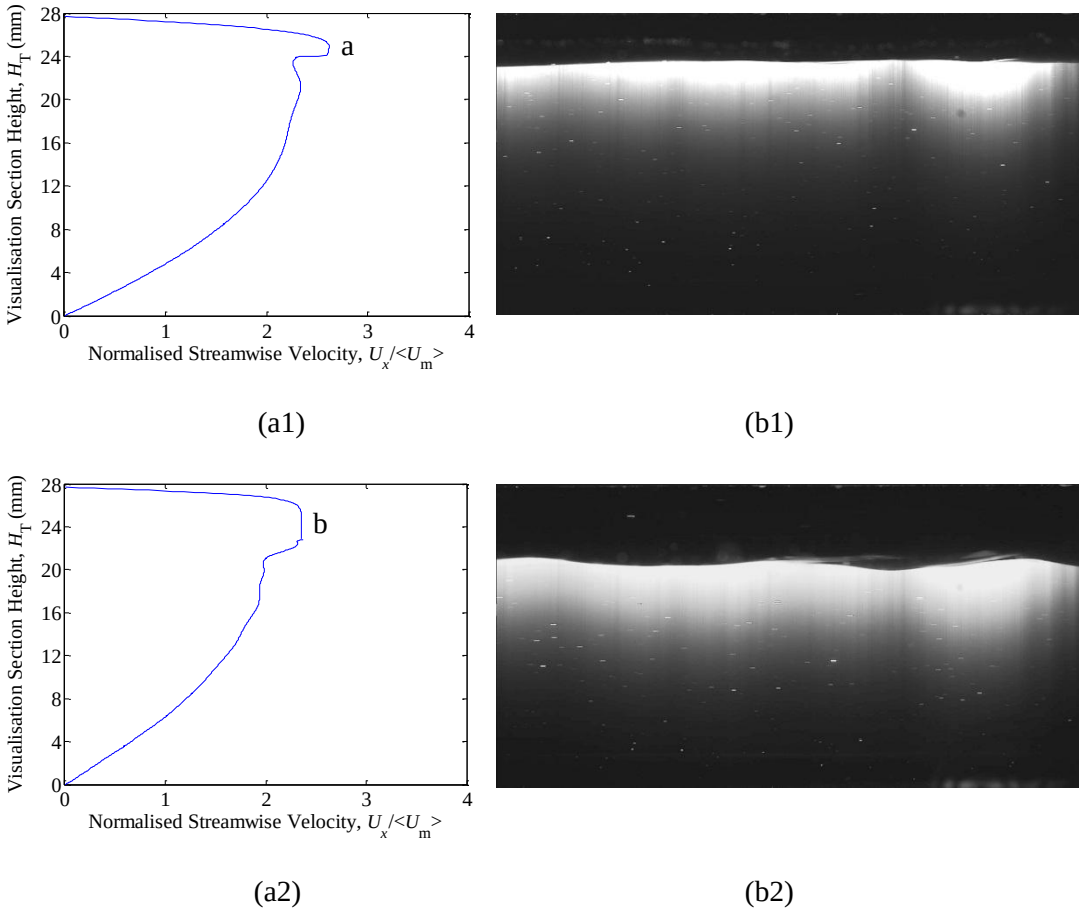

Figure 5-28: Velocity profiles ($a_1 \rightarrow a_2$) and instantaneous images ($b_1 \rightarrow b_2$) for: (1) U_m = 0.17 m.s^{-1} and φ_{in} = 0.17, and; (2) U_m = 0.28 m.s^{-1} and φ_{in} = 0.38

The results shown in Figure 5-28 are consistent with the Reynolds numbers of the individual phases which can be calculated using a combination of the volumetric flow-rates (Q_i) of the individual phases coupled with the respective in-situ phase fractions, such that,

$$\mathrm{Re}_i = \frac{\rho_i . U_i . D_i}{\mu_i}, \tag{5.7}$$

where,

$$U_i = \frac{Q_i}{\langle \varphi \rangle_{y,t} . \pi . \left({D_i^2}/{4} \right)}, \tag{5.8}$$

and,

$$\langle \varphi \rangle_{y,t} . A = A_i = \pi . \left(\frac{D_i}{2} \right)^2, \tag{5.9}$$

where A is the total cross-sectional area of the pipe and A_i is the cross-sectional area occupied by phase *i*.

It is found that for the results shown in Figure 5-28 (1) both liquids have a Reynolds number in the laminar range (Re < 2000), Re_{oil} = 943 and Re_{gs} = 60, i.e., the flow is dominated by viscous forces rather than inertial forces and hence both the Reynolds number and velocity profile for each of the phases indicates that away from the interface both liquids are travelling as laminar flow. Performing the same analysis for the case shown in Figure 5-28(2) indicates that the glycerol solution is still travelling as laminar flow (Re_{gs} = 55); this is supported by the shape of the velocity profile for the glycerol solution in Figure 5-28(a_2). However, the Reynolds number for the oil phase is no longer in the laminar region (Re_{oil} = 3414). This is in line with the shape of the velocity profile of the oil phase in Figure 5-28(a_2), which is steeper closer to the pipe wall and so more characteristic of a turbulent flow. It should be emphasised that the results presented in Figure 5-28 and the associated calculations of the Reynolds numbers of the individual phases were for runs in which the two phases remain separated and there are no droplets present, i.e., for stratified flow only.

Figure 5-29 presents a velocity profile and an instantaneous flow image for the case of a stratified flow with droplets; the stratified flow regime changes into the stratified flow with droplets as the superficial velocity is increased. On comparison with the velocity profiles presented for stratified flow (see Figure 5-28), the step-change (arising due to a shear layer) is no longer observed and the profile follows a much smoother transition due to the mixing at the interface of the two fluids.

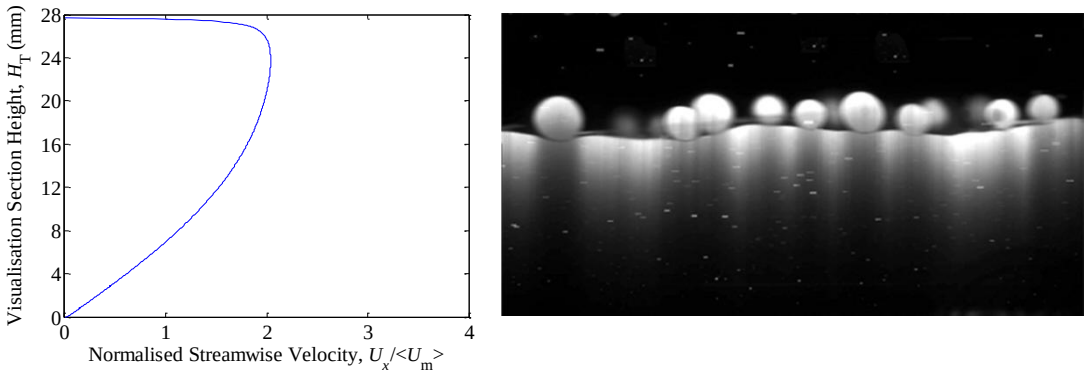

(a) (b)

Figure 5-29: Velocity profile (a) and instantaneous flow image (b) for stratified flow with droplets at U_m = 0.42 m.s^{-1} and φ_{in} = 0.50

It can be seen that the flow profile within the glycerol solution phase (i.e., up to $H \approx 8$ mm) is parabolic, which, on comparison with Figure 5-28(a) indicates that the glycerol solution is travelling as laminar flow. Above the mixing zone the same observation is made with respect to the oil phase, indicating it is also laminar flow.

Figure 5-30 presents a velocity profile and an instantaneous flow image for at U_m = 0.84 m.s^{-1} and φ_{in} = 0.50. Here the flow regime is *three-layer flow*. Three distinct regions to the profile are identifiable, these being: (1) a single phase glycerol-solution region (i.e., up to $H \approx 16$ mm), (2) a highly dispersed region (i.e., from $H \approx 8$ mm up to $H \approx 24$ mm), and (3) a single phase oil

region up to the top of the channel. From the shape of the velocity profile it is deduced that all three regions are turbulent.

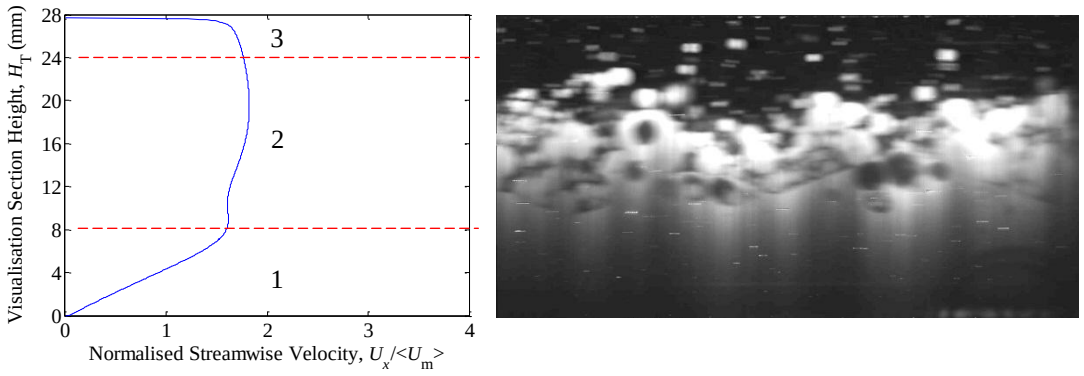

(a) (b)

Figure 5-30: Velocity profile (a) and instantaneous flow image (b) for three-layer flow with droplets at U_m = 0.84 m.s^{-1} and φ_{in} = 0.50

Figure 5-31 presents velocity profiles and instantaneous flow images for (1) U_m = 0.67 m.s^{-1} and φ_{in} = 0.75, and; (2) U_m = 0.56 m.s^{-1} and φ_{in} = 0.75, respectively. In both cases, there is a thin layer (up to $H \approx 2$ mm) of glycerol-solution on the pipe wall. Above $H \approx 2$ mm there is a second layer arising from the flow of a glycerol-solution droplet region above the glycerol-solution film, travelling at a different velocity to that of the film.

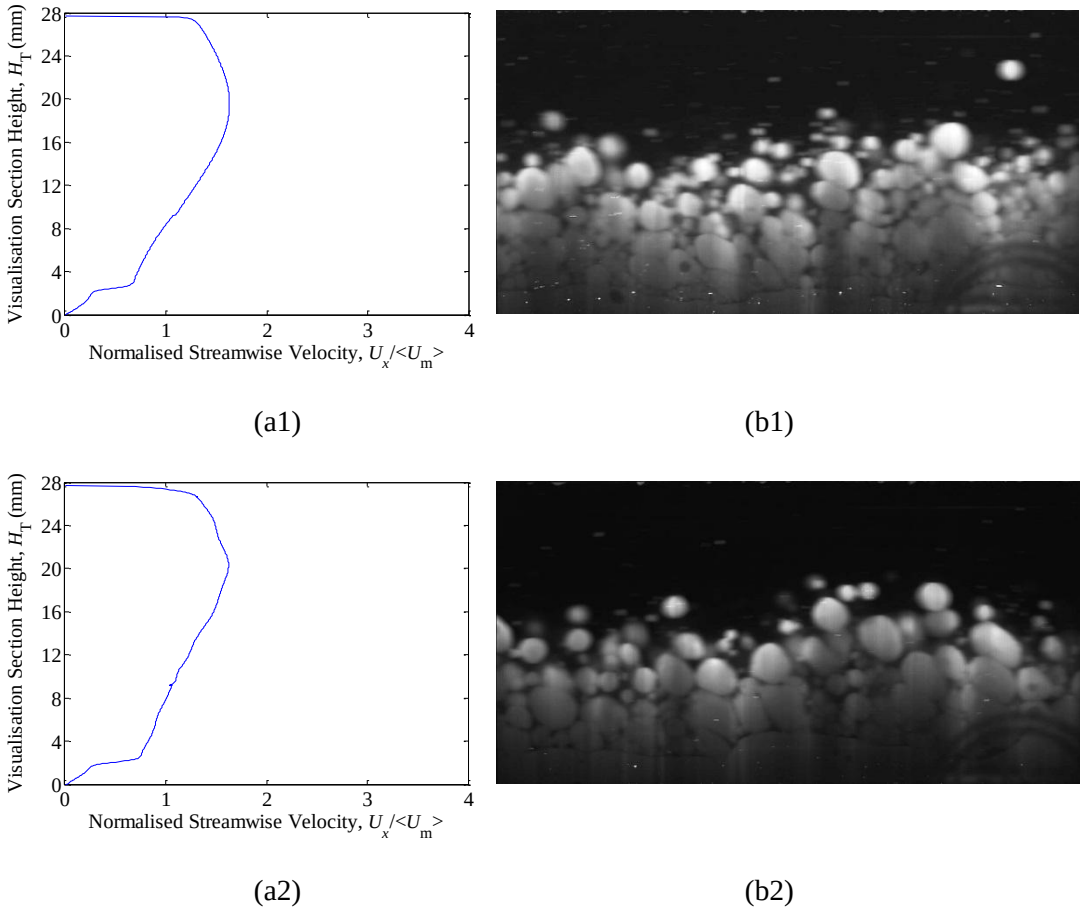

Figure 5-31: Velocity profiles ($a_1 \rightarrow a_2$) and instantaneous images ($b_1 \rightarrow b_2$) for: (1) U_m = 0.67 m.s^{-1} and φ_{in} = 0.75, and; (2) U_m = 0.56 m.s^{-1} and φ_{in} = 0.75

Figure 5-32 presents normalised velocity profiles ($a_1 \rightarrow a_2$) and instantaneous images ($b_1 \rightarrow b_2$) for dispersed flows. Figure 5-32 (1) (U_m = 0.84 m.s^{-1} and φ_{in} = 0.25) shows results for a dispersion of oil droplets in glycerol solution and Figure 5-32 (2) (U_m = 0.83 m.s^{-1} and φ_{in} = 0.90) shows results for a dispersion of glycerol solution droplets in oil. Inspection of the velocity profile in Figure 5-32(a1) in relation to the instantaneous flow image shown in Figure 5-32(b1) shows that the step changes in the velocity profile observed at $H \approx 24$ mm and $H \approx 20$ mm are due to discrete layers of oil droplets flowing at different velocities.

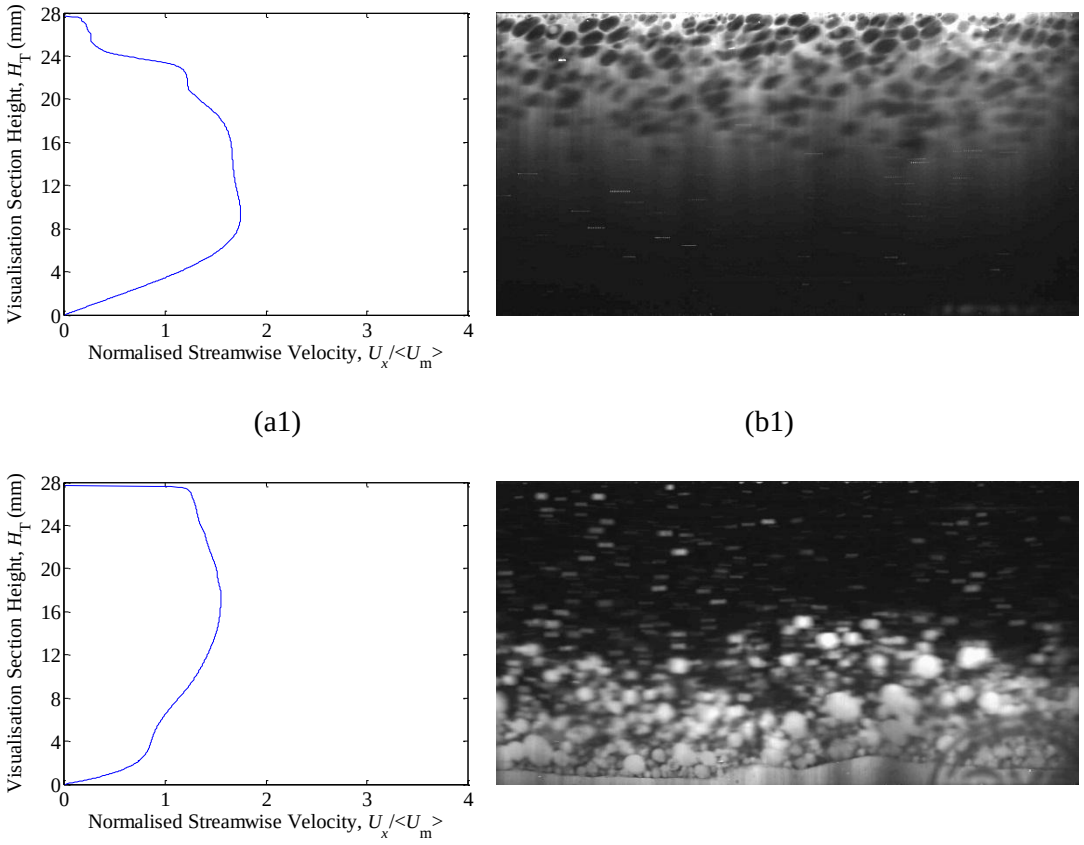

Figure 5-32: Velocity profiles ($a_1 \rightarrow a_2$) and instantaneous images ($b_1 \rightarrow b_2$) for dispersed flows, at: (1) U_m = 0.84 m.s^{-1} and φ_{in} = 0.25, and; (2) U_m = 0.83 m.s^{-1} and φ_{in} = 0.90

Finally, Figure 5-33 presents interface level H values as a function normalised interface level velocity ($U_x/\langle U_m \rangle$). From inspection of the figure it is evident that once normalised, the velocity at the interface increases with an increase in the interface level.

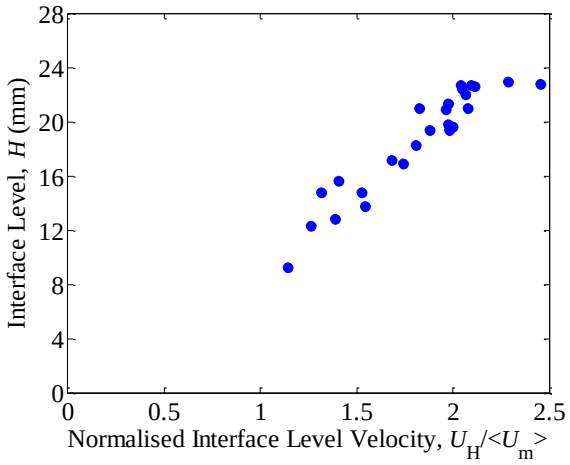

Figure 5-33: Interface level H as a function normalised interface level velocity ($U_x/\langle U_{\mathrm{m}}\rangle$)

A more sophisticated analysis of stratified laminar liquid-liquid flow is presented by Ng (2002). This analysis takes account of interfacial tension and contact angle at the triple interface. The analysis can be used to examine critically the assumption of a flat interface implicit in the data reduction process described above and also gives information on the two-dimensional velocity profiles in such flows. A detailed description of the Ng (2002) analysis is given in Chapter 6 together with an assessment of its implications in the present work.

5.10 Conclusions

A novel, non-intrusive, spatiotemporally resolved optical (laser) measurement technique, incorporating laser-induced fluorescence with both particle image velocimetry (PIV) and particle tracking velocimetry (PTV), was developed and then used to measure co-current liquid-liquid flows in a circular pipe section. The current experimental campaign is a development of the study presented in Chapter 4 but it makes use of a test section with a geometry more representative of industrial pipeline systems (i.e., with a circular cross-section). This has been achieved through the use of an optical calibration technique to correct for the image distortion arising from the curvature refraction through the imaging line-of-sight through the test section wall material and into the inspected flows. As was the case in Chapter 4, the experimental

technique is again shown to be a powerful tool that can provide detailed spatiotemporal information of the flowing behaviour. Characterisation of the flows has been developed herein to include both phase information and velocity profiles.

The findings of the current study in terms of flow regimes are comparable to those of Chapter 4. Eight distinct flow regimes have again been observed. These have been grouped into the following four flow types: (1) stratified flow; (2) mixed flow (i.e., a flow with two distinct continuous phase regions with droplets); (3) continuous oil-phase dispersion; and (4) continuous aqueous-phase dispersion.

As was the case in Chapter 4, the flow is again seen to be comprised of three distinct zones, with a continuous oil phase at the top and a continuous glycerol-water phase at the bottom, separated by a mixed zone. The vertical space covered by the mixed zone increased at higher superficial velocities.

The laminar drag model (tailored for a circular cross-section pipeline) is again shown to give excellent agreement with experimental in-situ phase fraction and interface level results. The gas-liquid interface level predictive technique presented by Hall and Hewitt (1993) is shown to have excellent agreement with the current experimental results.

The velocity profile results give insights into the nature of the flow (laminar or turbulent) in various regions of the cross section and at various flow conditions.

Though the current Chapter presents a detailed account of the behaviour of co-current liquid-liquid flows, there is little discussion is made about the instability mechanisms that are driving flow regime transition and development of the flow. The work described in Chapter 6 develops

the current study by using a different inlet orientation to investigate the effects different instability mechanisms (particularly, the Rayleigh-Taylor instability) have on the flow.

CHAPTER 6

Investigation of the Effects of the Inlet Configuration on Horizontal Initially Stratified Liquid-Liquid Flows

6.1 Introduction

In Chapter 5, studies of liquid-liquid flows are reported in which the flow was visualised using PLIF and the velocity profiles measured using PTV and PIV. In those measurements, the visualisation cell was placed L_E = 6.20 m (such that L_E/D = 244) from the inlet of the horizontal 25.4 mm internal diameter test section. In the work described in Chapter 5, the heavier (aqueous glycerol solution) phase was injected at the bottom of the channel and the lighter oil (Exxsol D80) phase was injected at the top of the channel. In the experimental work described in the present Chapter, the experiments were repeated with the aqueous phase injected at the top of the channel and the oil phase at the bottom, i.e. in the opposite orientation to that in which they would naturally separate. The objectives in this further study were as follows:

(1) To determine whether the flow had become fully developed at the measurement point. If the results for these two extreme injection scenarios were similar, then it could reasonably be argued that fully-developed flow had been achieved.

(2) To investigate whether the additional instabilities might arise as a result of the change in injection strategy giving rise to different flow structures (flow patterns). Specifically, in the case of the aqueous phase being injected above the oil phase, Rayleigh-Taylor instability may occur, giving rise to a phase breakup mechanism whose effects may persist from the inlet to the measurement section.

Though the main focus of this Chapter is on the presentation of this new set of experimental results, several additional features have also been addressed which include:

(1) Considering the effects of interfacial instabilities on flow patterns. A background discussion on this topic is given in what follows below in Section 6.1.

(2) The effects of contact angle and interfacial tension have been evaluated on the basis of the analysis of Ng (2002). This work is presented in Section 6.8.2.

The development of the flow from (initially) stratified flow to the more complex flow regimes (i.e., *dual continuous* and *dispersed* flows) can arise due to increased flow complexity and enhanced mixing that is associated with turbulence.

Turbulence arises at higher flow velocities (i.e. higher liquid flow rates), from nonlinear inertial effects (described by the Reynolds number) that cannot get damped out (or, dissipated) by viscous (momentum) diffusion. It is no surprise that the regimes maps presented in Chapters 4 and 5 showed stratified flows at lower superficial mixture velocities, and increasing phenomenological flow complexity at higher velocities.

However, the flow complexity can also be augmented by the following instability mechanisms:

1. **Kelvin–Helmholtz (KH) instability**

   If small amplitude waves are present at the interface in a stratified flow, the pressure above the waves changes in a manner which is out of phase with wave height. This causes a suction force on the wave peaks. If this suction force is sufficient to overcome

the influences of gravity and surface tension, then the waves can grow leading to the Kelvin-Helmholtz instability.

2. **Rayleigh–Taylor (RT) instability**

   This instability mechanism is relevant to flows where a dense fluid is situated above a lighter fluid with gravity acting, and again, involves the instability of the interface between two liquid layers. In this case the heavier liquid will sinks under gravity into the lighter liquid which is displaced, and the lighter liquid flows upwards and has a fingering nature with bubbles of the lighter liquid rising into the denser liquid above, and spikes of the heavier liquid descending into the lighter liquid below.

Either of these mechanisms can give rise to mixing of the stratified layers.

The onset of the aforementioned instabilities can be predicted by means of several dimensionless numbers that can characterise liquid-liquid flows. Those pertinent to the current analysis are detailed below.

The ***Richardson*** number (*Ri*) expresses the ratio of potential to kinetic energy:

$$Ri = \frac{gh}{U^2}, \tag{6.1}$$

where h is a representative vertical lengthscale and U a representative velocity.

For a flow with a varying distribution of density and velocity (though with the lighter fluid layers over the heavier ones), the onset of the Kelvin-Helmholtz (KH) instability is given by a suitably-defined *Ri* number. Typically the layer is unstable for $Ri < 0.25$. The *Ri* number values

for the matrix of experimental conditions for the high-speed PLIF-PTIV campaigns of Chapter 5 and in the present chapter are:

Ri$=gh/U^2 = 0.05/0.3^2 - 0.05/0.07^2 = 0.5 - 10$ with h~0.005m and $U_m = 0.07 - 0.3$ m.s^{-1}

Ri$=gh/U^2 = 0.1/0.3^2 - 0.1/0.07^2 = 1 - 20$ with h~0.01m and $U_m = 0.07 - 0.3$ m.s^{-1}

Ri$=gh/U^2 = 0.05/0.5^2 = 0.3$ with h~0.005 m and $U_m = 0.4$ m.s^{-1}

Ri$=gh/U^2 = 0.1/0.6^2 = 0.3$ with h~0.01 m and $U_m = 0.6$ m.s^{-1}

We can see that for the range of superficial velocities used, the Richardson number is typically greater than 0.25, and we would not expect the KH instability mode to occur, though at the higher velocity ratios between the two phases (i.e., highest and lowest inlet phase fractions) it would begin to play a role.

The ***Atwood*** number (A) is a ratio of buoyancy to gravity and is employed in the study of hydrodynamic instabilities in density stratified flows. It is written as a ratio of the density difference between the two liquids to the sum of the same densities,

$$A = (\rho_1 - \rho_2)/(\rho_1 + \rho_2), \qquad (6.2)$$

where the subscript "1" denotes the heavier and "2" the lighter fluid.

In Rayleigh-Taylor (RT) instability, the vertical penetration distance y (this is actually denoted as z in Figure 6-1(a)) of the fluid interface into the two phases (or equivalently, the outer edges of the "mixing zone") is a function of the timescale $\tau = Agt^2$, where t is the time, such that an asymptotic scaling law $y = \alpha\tau$ is obeyed.

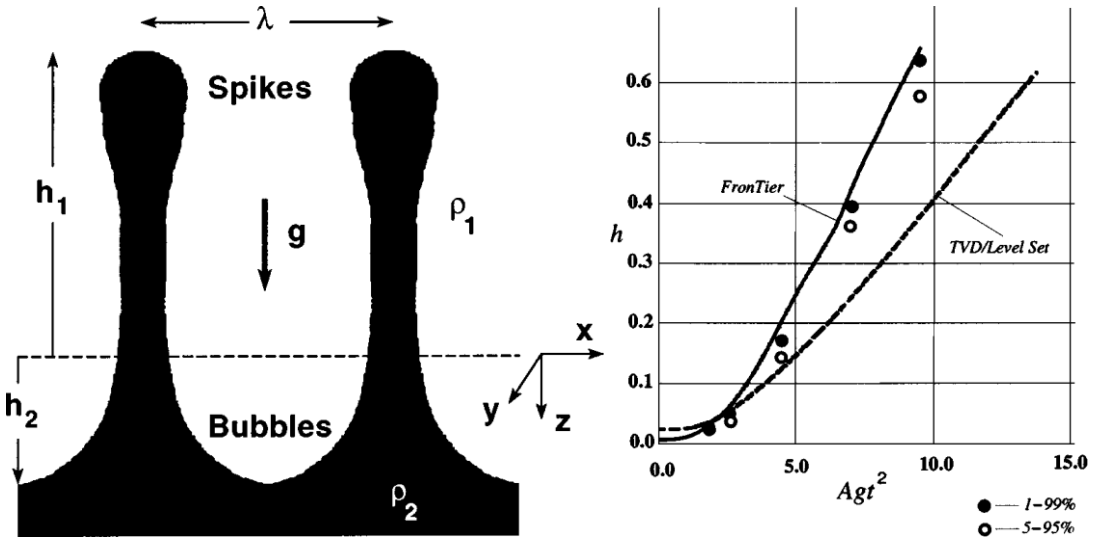

(a) (b)

Figure 6-1: (a) Definitions from Dimonte and Schneider (2000), and; (b) Simulations from Glimm et al., (2000)

Dimonte and Schneider (2000) investigated the turbulent RT instability over an extensive range of density ratios (R, where $R = \rho_2/\rho_1$) $1.3 < R < 50$ [$0.15 < A < 0.96$, where $A = (R-1)/(R+1)$] using a linear electric motor, backlit photography and LIF to diagnose the mixing layer in the flow. For a constant acceleration, the bubble (Glimm et al., 2001) and spike (Dimonte and Schneider, 2000) amplitudes were found to increase as:

$$h_i = \alpha_i A g t^2, \qquad (6.3)$$

with $a_2 \sim 0.05 \pm 0.005$ and $a_1 \sim a_2 R^{Da}$ with $Da \sim 0.33 \pm 0.05$. Here: $R = 1.5$ and $A = 0.2$, $a_1 \sim 0.05 \times 1.5^{0.33} = 0.057$ and $a_2 \sim 0.05$.

Assuming the bubbles and spikes are from a RT instability in the liquid–liquid flows under investigation, the time for the bubbles to move to the bottom of the pipe in the present experiments is [calculated from Equation 6.3] $t_2 = (D/\alpha_2 A g)^{1/2} = 0.45$ s; and the time needed

for the spikes to reach to the top of the pipe is $t_1 = (D/\alpha_1 Ag)^{1/2} = 0.42$ s. The distance travelled by the bulk flow during this advection time is 0.07 to 0.3 m.s^{-1} × 0.45 s = 0.03 to 0.14 m. This is at least 44 times less the 6.20 m distance from the inlet to the visualisation section. Certainly it is expected that there is enough time for the bubbles and spikes to extend all the way across the liquid height and the fluid to mix in the vertical direction due to the RT instability. Even at the highest investigated velocity of $U_m = 1.46$ m.s^{-1}, the distance travelled is 1.46 m.s^{-1} × 0.45 s = 0.66 m, an order of magnitude shorter than the 6.2 m development length.

As mentioned previously, the ***Reynolds*** number measures the ratio of inertial to viscous forces:

$$Re = \frac{\rho U D}{\mu}. \qquad (6.4)$$

When the viscous forces dominate, the flow is characterised by smooth laminar flow (i.e., *stratified* flow). On the other hand, when the inertial forces dominate the viscous forces, the flow becomes turbulent leading to instabilities such as eddies, vortices and waves (at the interface). The values of *Re* for the current experimental conditions are given in Table 6-1.

Table 6-1: Reynolds numbers for the current experimental matrix

U_m (m/s)	Re (Oil)	Re (G-S)
0.07	240	20
0.3	1,040	80
1	3,480	260
1.46	5,080	370

N.B.: Typically Re < 2,000 – 3,000 should be a laminar flow, with little "mixing", such that a flow should remain mainly stratified in the absence of the RT instability.

Considering the above, there are two main mechanisms for "mixing" in the liquid-liquid flows studied in the work described in this thesis:

1. High Reynolds numbers (hence inertial forces dominated flow) leading to turbulence. This is observed in the velocity profiles shown in Figure 5-28(a_2) in which it is seen that the oil layer is turbulent (detected from the oil profile shape and the Reynolds number of the oil phase, $Re_{\mathrm{oil}} = 3414$) whereas the glycerol solution layer is laminar ($Re_{\mathrm{gs}} = 55$) and has a and parabolic velocity profile for the phase. For these independent variable conditions (U_{m} = 0.28 m.s^{-1} and φ_{in} = 0.38) the onset of waves at the interface are observed and the transition from stratified flow to stratified wavy flow is triggered by the transition of the oil phase to the turbulent Reynolds number region.
2. RT instability in the inverted flow (the inverted inlet orientation is explained in Section 6.2), which is the motivation behind the experiments presented in the present chapter.

Recall also that, from the above calculated *Ri* values and considering the KH instability onset threshold ($Ri < 0.25$), we can say that this instability is not usually an issue at the flows discussed here, but could begin to play a role at the extreme inlet phase fractions and at higher superficial mixture velocities, where the shear between the two liquid-liquid flow layer is at its greatest.

Considering the independent variable matrix and the inlet configuration, there are, between Chapter 5 and the experimental results presented herein, four different flow instability scenarios, these are listed in Table 6-2 below.

Table 6-2: Flow instability scenarios

Scenario Number	Reynolds number (Re)	RT instability
1	Laminar	Stable
2	Turbulent	Stable
3	Laminar	Unstable
4	Turbulent	Unstable

N.B.: Scenario 1 and 2 relate to the PLIF campaign in Chapter 5, scenarios 3 and 4 relate to the current (Chapter 6) PLIF campaign.

So, in synopsis, for the PLIF and PIV/PTV study presented in Chapter 5, flow regime transition is dominated by high Reynolds numbers leading to turbulence. The current chapter develops the work presented in Chapter 5 by investigating the influence that different instability mechanisms have on flow regime transition from initially stratified flow. This is done by introducing the test fluids into the test section such that the denser fluid (glycerol solution) is on top of the less dense fluid (Exxsol D80 oil) with the aim on imposing a RT instability mode.

6.2 Experimental Operation

The experimental campaign was carried out using the same operational procedure as that outlined in Section 5.2 i.e., with a circular cross-section visualisation cell (see Section 3.10.2) and an Olympus i-SPEED 3 high speed camera (see Section 3.4.1). However, the inlet orientation is "inverted" with respect to that in Chapter 5 as to induce a RT instability in the flow, i.e., the glycerol-solution is introduced to the test section above the oil; the denser liquid is introduced to the test section above the less dense liquid. A photograph of inlet to the test section is shown in Figure 3.5 and the two inlet configurations are illustrated in Figure 6-1.

The experimental matrix is similar to that used for PLIF and PIV/PTV studies presented in Chapter 5. A campaign 48 runs was performed that were each defined by the same independent variables used to classify the runs in Chapter 4 and Chapter 5 i.e., the superficial mixture velocity U_{m} and the inlet volumetric phase fraction of the oil φ_{in}. The experimental runs spanned a range of superficial mixture velocity from $U_{\mathrm{m}} = 0.11$ to 0.84 m.s^{-1} and φ_{in} was varied from 0.1 to 0.9. The quantitative analysis focused on the superficial mixture velocity range U_{m} = 0.11 to 0.42 m.s^{-1} to capture the development of stratified flow to dual continuous flow to enhance the understanding of the mechanism driving this flow regime transition.

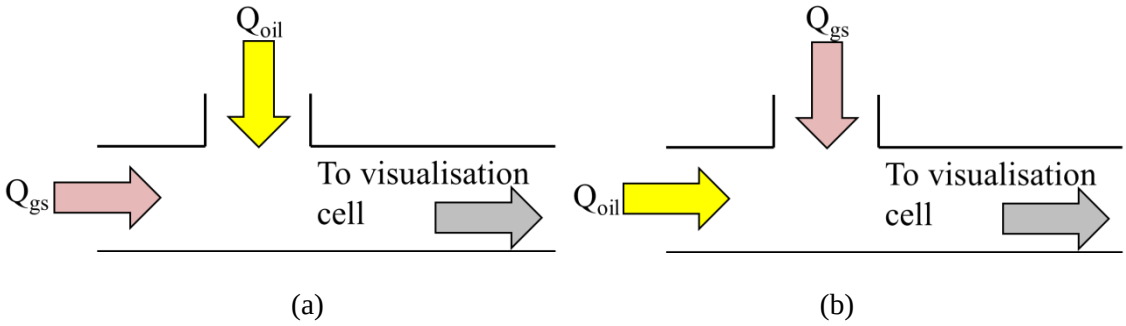

Figure 6-2: Inlet orientation for (a) the "normal" configuration as used in Chapter 5, and; (b) the "inverted" inlet configuration as used in the current (Chapter 6) PLIF study.

6.3 Flow Phenomenology and Regime Map

Applying the flow regime classification system defined in Chapter 4, only 6 of the 8 flow regimes observed in the PLIF campaigns of Chapters 4 and 5 have been observed in the current campaign. The two regimes absent from the current experimental campaign are: (1) three layer flow, and; (2) glycerol solution dispersion with a glycerol solution film. However, 8 (not 6) instantaneous flow images are presented in Figure 6-3 to convey the 6 different flow regimes observed. This is because within the scope of the classification methodology adopted in Chapters 4 and 5 there was a relatively broad range in the number of droplets presented in both:

(1) the *oil droplet layer flow* regime, see Figure 6-3(c) and 6-3(e), and; (2) the glycerol solution droplet layer regime, see Figures 6-3(d) and 6-3(f).

A flow regime map relating the flow regime classifications to the independent variables, the superficial mixture velocity U_{m} and the inlet volumetric phase fraction of oil in the pipe φ_{in} is presented in Figure 6-4. The flow regime map is again in good agreement with those presented by previous researchers (Soleimani, 1999; Lovick and Angeli, 2003; Hussain, 2004). However, on comparison with the flow regime map presented in Chapter 5 (see Figure 5-2) it can be seen that the *stratified flow with droplets* flow regime is seen at both lower superficial mixture velocities ($U_{\mathrm{m}} = 0.17$ m.s^{-1} opposed to $U_{\mathrm{m}} = 0.22$ m.s^{-1}) and lower oil input fractions in the current campaign (see Figure 6-2). It is found that the onset of the flow regime characterised *stratified flow with a glycerol solution droplet layer* occurs at the same superficial mixture velocity (i.e., $U_{\mathrm{m}} = 0.42$ m.s^{-1}) in both the results described in Chapter 5 (aqueous phase injected at bottom of tube) and in the study reported in the current chapter (aqueous phase injected at the top of the tube).

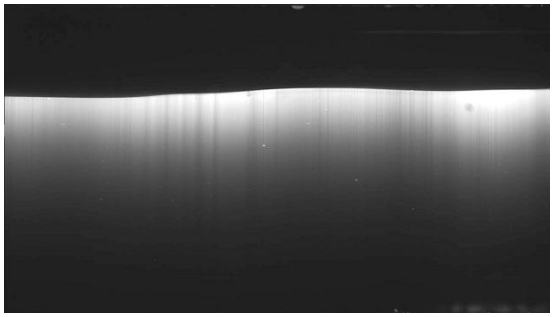

(a) Stratified flow

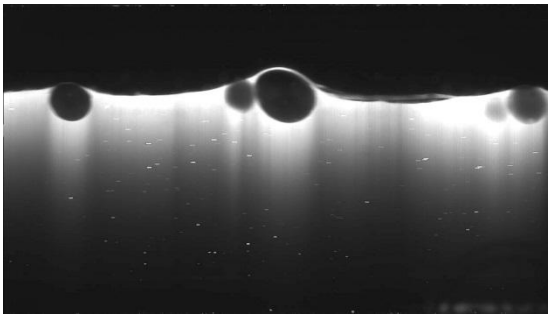

(b) Stratified flow with droplets

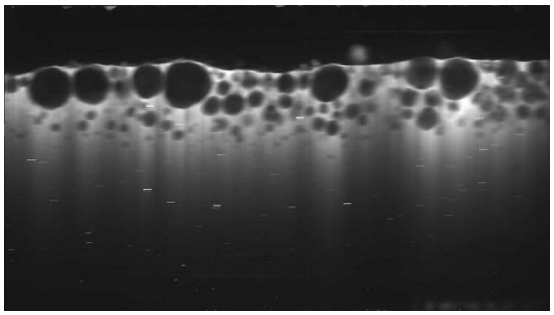

(c) Oil droplet layer

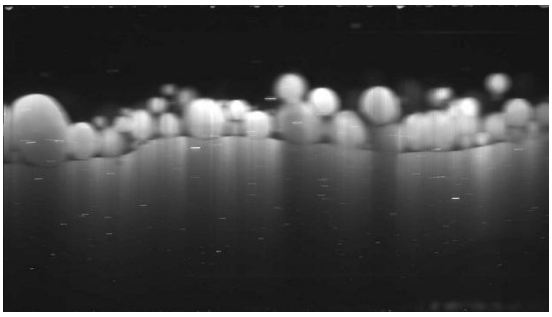

(d) Glycerol solution droplet layer

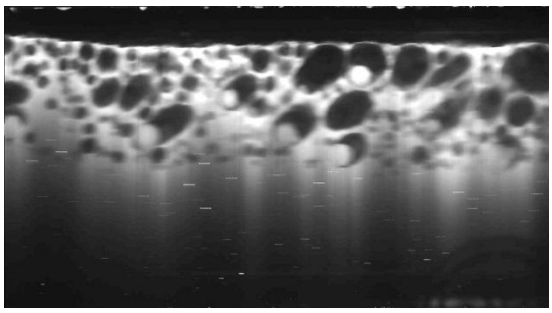

(c) Oil droplet layer

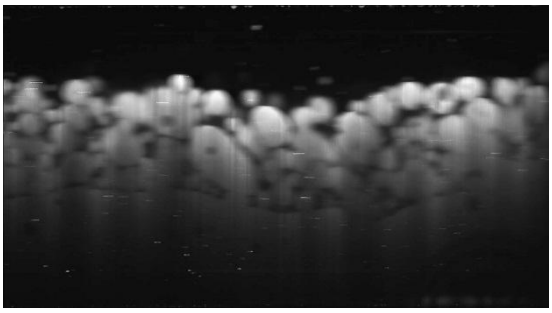

(d) Glycerol solution droplet layer

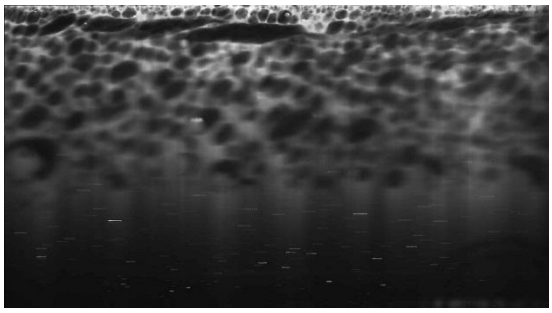

(e) Oil dispersion over glycerol solution

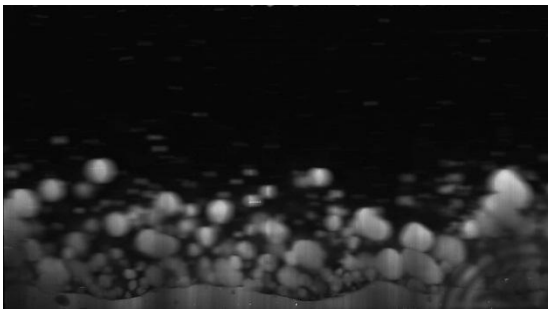

(f) Oil flow over glycerol solution dispersion with glycerol solution film

Figure 6-3: Images of the 8 distinct flow regimes observed in the circular cross experimental campaign with an "inverted" inlet configuration

On visual inspection of Figure 6-4, in comparison with Figure 5-2 in Chapter 5, it can be seen that the flow regime maps are largely comparable. The major difference between the flow regime maps presented in Chapters 5 and 6 is that oil droplets are a considerably more prevalent in Figure 6-4 (in Chapter 6) than they are in Figure 5-2 (in Chapter 5). In particular, the oil droplet layer flow regime is seen across a much broader range of conditions (U_m = 0.28 - 0.55 m.s^{-1}) in Figure 6-4 as opposed to just at U_m = 0.55 m.s^{-1} in Figure 5-2.

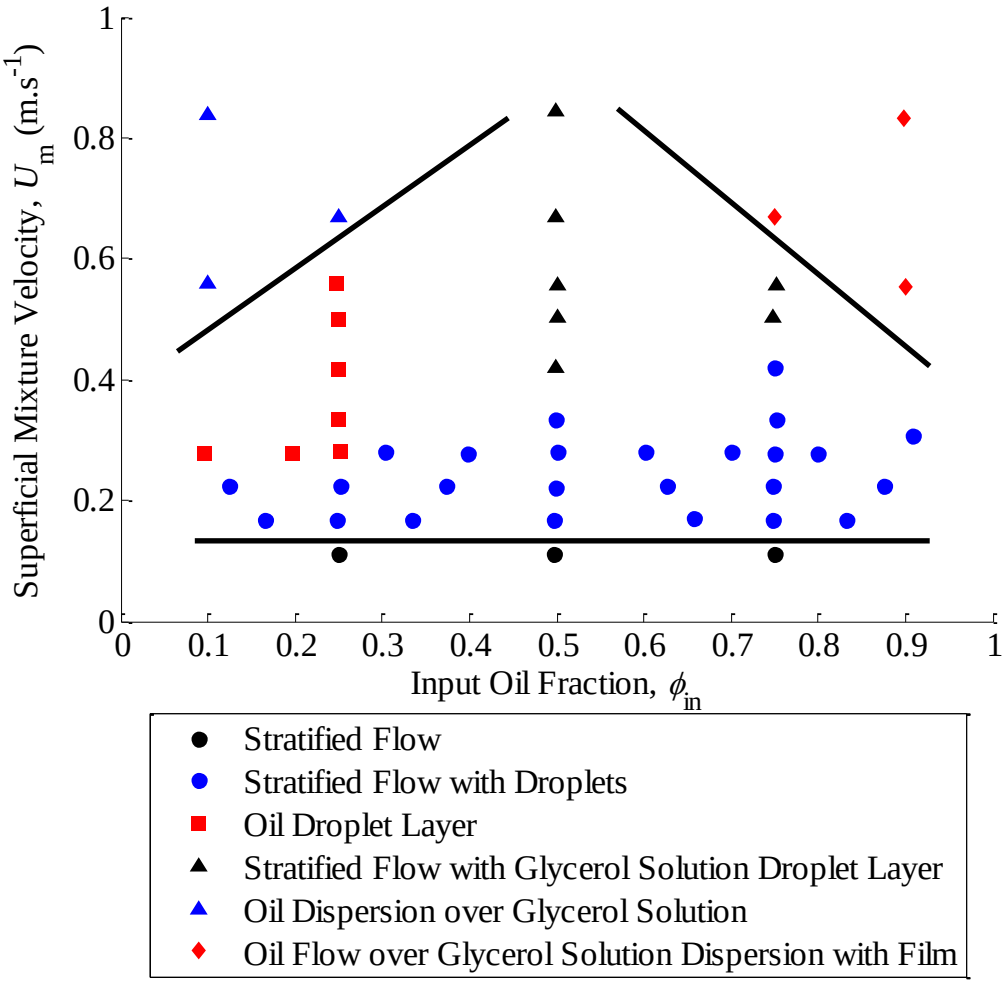

Figure 6-4: Flow regime map

From the RT instability preliminary analysis in Section 6-1, based on Equation 6.3, and considering the time that should elapse from the flow entering the test section to reach the

visualisation cell, it was calculated that sufficient time should have elapsed for the flow not to be affected by the inlet configuration. However, from the experimental results it can be concluded that the flow is still displaying characteristics different to those observed in the work described in Chapter 5, and these differences must be due to the "inverted" inlet configuration (see Figure 6-3(b) compared to Figure 5-1(b)).

When the flow regime maps presented in Figures 5-2 and 6-4 are compared in terms of the *dual continuous* flow regime classification the flow regime maps become much more closely aligned. However, the tranisition to *dual continuous* flow for the "normal" inlet configuration (Figure 6-2(a)) is seen to occur at a superficial mixture velocity of $U_{\mathrm{m}} = 0.22$ m.s^{-1} at oil inlet phase fractions $\varphi_{\mathrm{in}} > 0.4$ and $U_{\mathrm{m}} \approx 0.40$ m.s^{-1} for $\varphi_{\mathrm{in}} < 0.4$, whereas for the "inverted" (Figure 6-2(b)) inlet configuration the transition to dual continuous flow occurs at the much lower superficial mixture velocity of $U_{\mathrm{m}} = 0.17$ m.s^{-1} for all oil input phase fractions investigated. It is also seen that there is a higher occurrence of oil droplets below the interface when the flows are "inverted" at the inlet. This is evident from Figure 6-7 in which instantaneous images of the flow for the "normal" and the "inverted" inlet configurations are shown for the same independent variable values. Hence it is clear that the flow is still exhibiting characteristics resulting from the inlet configuration. The predominant difference between the flows at low oil input phase fraction ($\varphi_{\mathrm{in}} < 0.4$) in Figure 5-2 and 6-4 is the existence of an oil droplet layer below the interface and, to a lesser degree, a lack of glycerol-water droplets above it. These differences are discussed later in this chapter.

6.4 Vertical Phase Distribution Profiles

This section presents the vertical phase distribution results for the "inverted" inlet configuration (see Figure 6-2(b)). Figure 6-5 shows vertical phase distribution profiles $\bar{\varphi}(y)$ for superficial

mixture velocities in the range U_m = 0.11 to 0.42 m.s^{-1} at selected input oil fractions φ_{in} of: (a) 0.25; (b) 0.50, and; (c) 0.75. It corresponds to Figure 5-3 of Chapter 5 albeit with the different inlet configuration to the test section and, has been calculated using the same technique i.e., that given in Section 3.11.2. Figure 6-6 shows vertical phase distribution profiles $\bar{\varphi}(y)$ for a range of input oil fractions φ_{in} for superficial mixture velocities U_m of: (a) 0.11 m.s^{-1}; (b) 0.17 m.s^{-1}; (c) 0.22 m.s^{-1}; (d) 0.28 m.s^{-1}; (e) 0.34 m.s^{-1} and; (f) 0.42 m.s^{-1}; This relates to Figure 5-4 of Chapter 5.

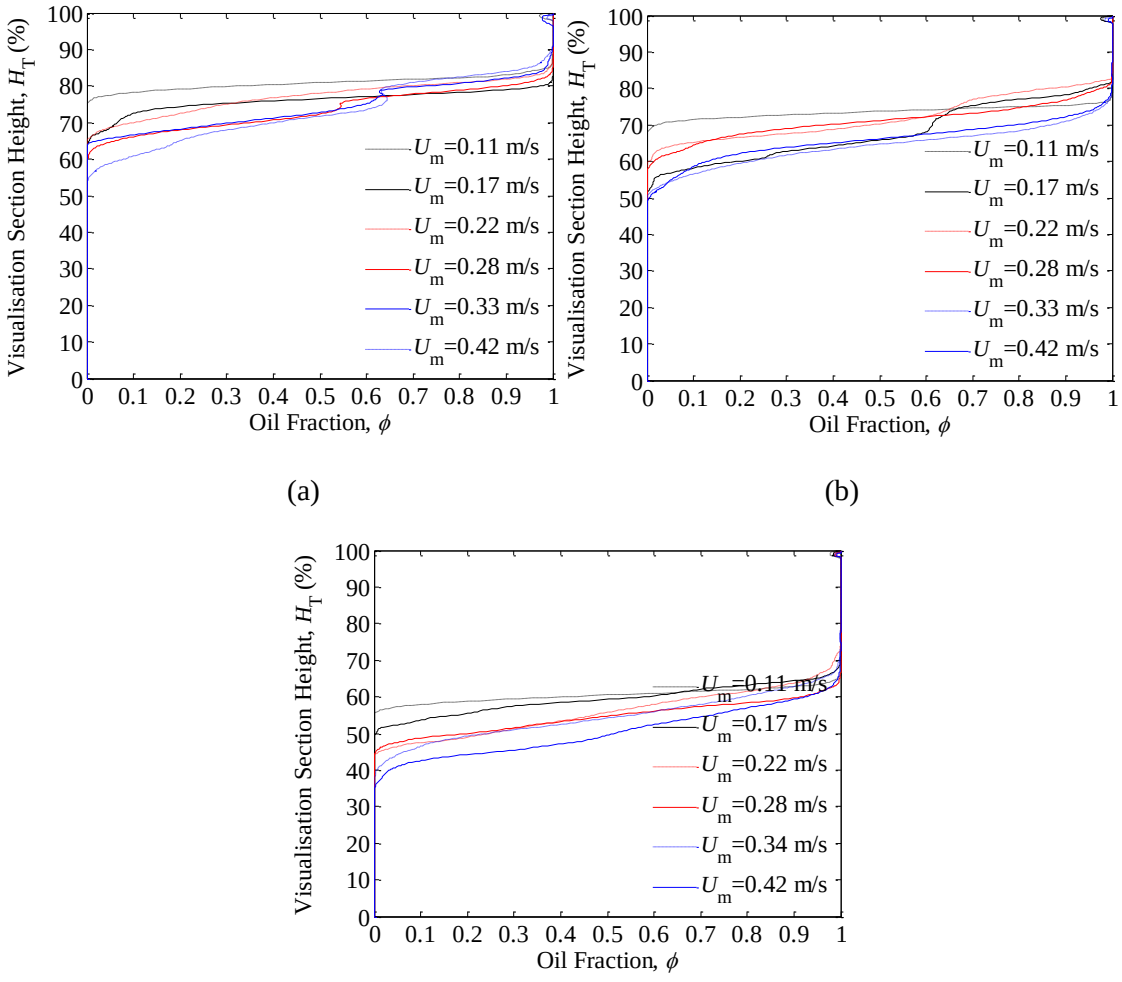

Figure 6-5: Vertical oil phase fraction profiles $\bar{\varphi}(y)$ for different superficial mixture velocities U_m at an input oil fraction φ_{in} of: (a) 0.25, (b) 0.50, and (c) 0.75

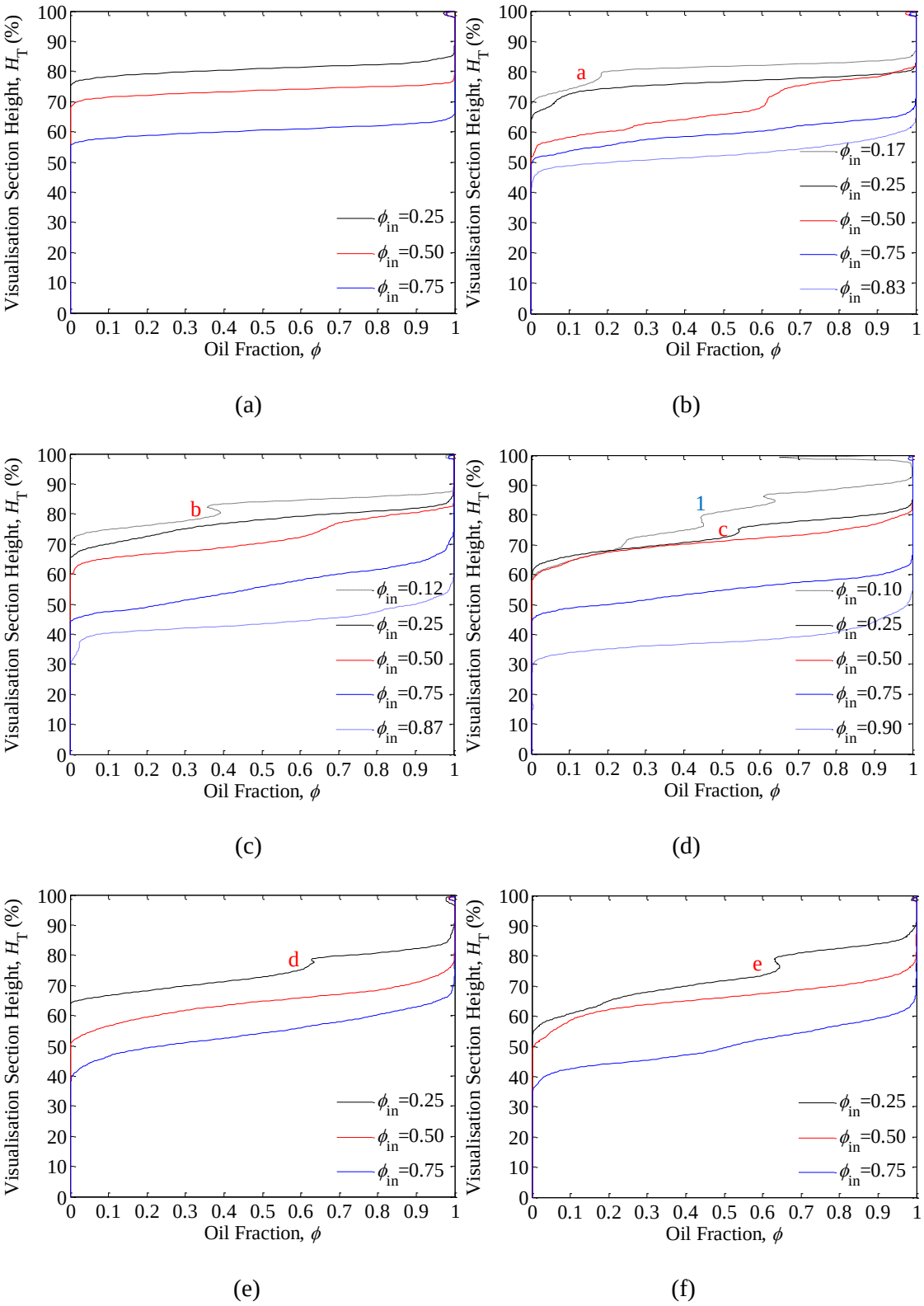

Figure 6-6: Vertical oil phase fraction profiles $\bar{\varphi}(y)$ at different input oil fractions φ_{in} for a superficial mixture velocity U_m of: (a) 0.11 m.s^{-1}, (b) 0.17 m.s^{-1}, (c) 0.22 m.s^{-1}, (d) 0.28 m.s^{-1}, (c) 0.33 m.s^{-1}, (d) 0.42 m.s^{-1}

Figure 6-6 shows vertical phase distribution profiles $\bar{\varphi}(y)$ for a range of input oil fractions φ_{in} for superficial mixture velocities U_m of: (a) 0.11 m.s^{-1}; (b) 0.17 m.s^{-1}; (c) 0.22 m.s^{-1}; (d) 0.28 m.s^{-1}; (e) 0.34 m.s^{-1} and; (f) 0.42 m.s^{-1}. This relates to Figure 5-4 of Chapter 5.

Once again, the flow is seen to adhere to the zone characterisation first presented in Chapter 4 and illustrated in Figure 4-7, i.e., there are three distinct regions to the flow: (1) an oil region; (2) a glycerol solution region, and; (3) a mixed region separating them. The dynamics of the mixed region parallel the findings of Chapters 4 and 5. Specifically, the mixed region covers a very narrow vertical band for stratified flows and increases for a given superficial mixture velocity; as oil input fraction is increased the height of the mixed band increases. In addition, the height of the glycerol solution layer at the bottom of the pipe decreases under the aforementioned conditions. The vertical height covered by the mixed region is also seen to increase as the superficial mixture velocity (for a given oil input fraction) increases.

However, on further inspection it is seen that the phase distribution profiles for several of the runs (i.e., independent variable combinations) feature "kinks" in the mixed zone (labelled a → e in Figure 6-6). These are found exclusively at low oil input phase fractions, predominantly at $\varphi_{in} = 0.1$ to 0.25. On visual inspection of these instantaneous flow images (see Figure 6-7) it is observed that the kinks can be attributed to an oil droplet layer below the interface.

Figure 6-7 also features instantaneous images of the flow for the same independent variables but for the "normal" inlet configuration from Chapter 5 (left hand side, i.e., those denoted by an "a"). From comparing the "inverted" inlet condition results (right-hand side, i.e., those denoted by a "b") with the "normal" inlet condition results (left hand side), it is concluded that the inlet configuration does have an effect on the flow regime at the distance far downstream of the inlet (L/D = 244) at which the PLIF-PTIV measurements were taken.

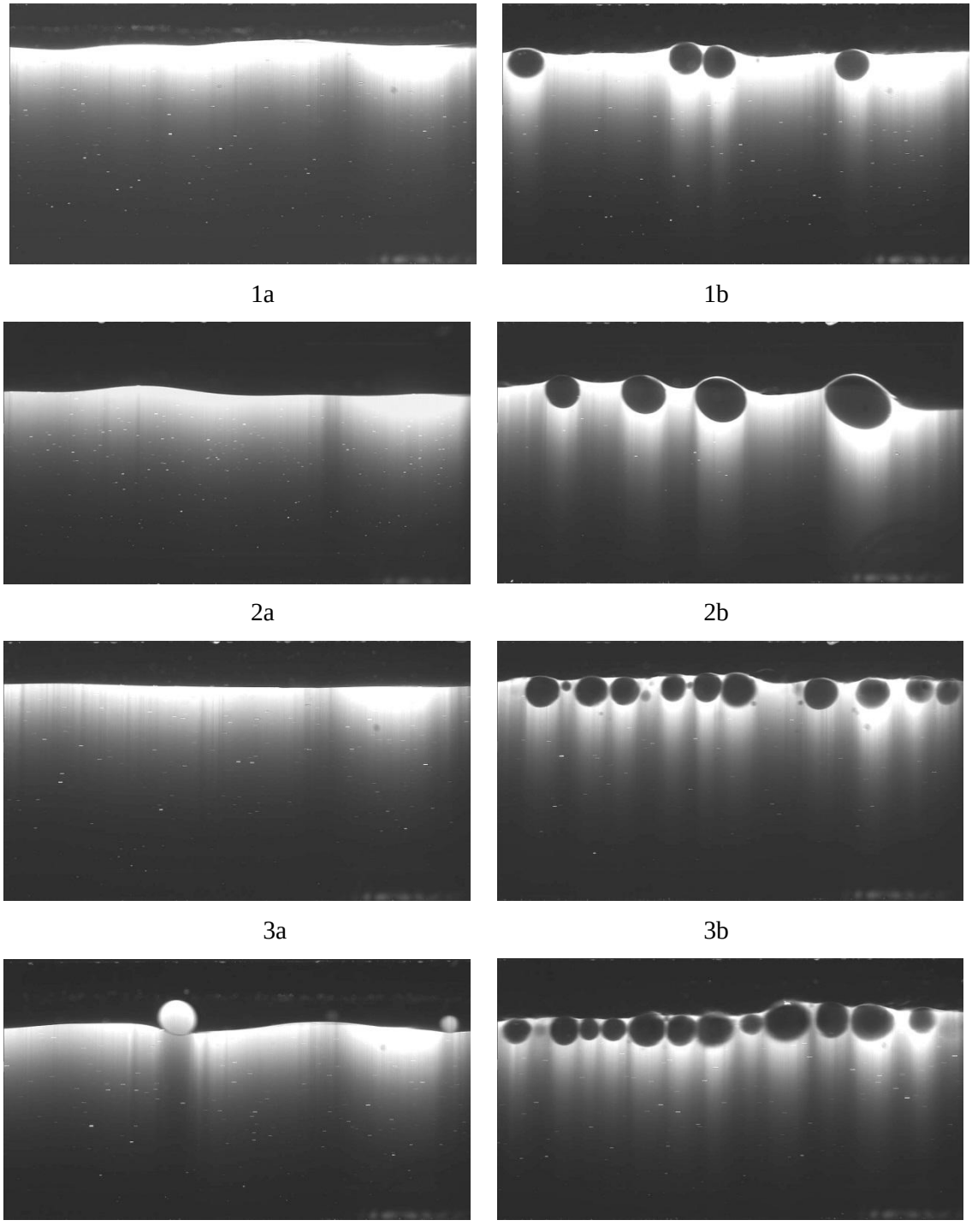

Figure 6-7: Instantaneous flow images for: (1) $U_{\mathrm{m}} = 0.17$ m.s^{-1} for $\varphi_{\mathrm{in}} = 0.17$; (2); $U_{\mathrm{m}} = 0.22$ m.s^{-1} for $\varphi_{\mathrm{in}} = 0.12$; (3) $U_{\mathrm{m}} = 0.28$ m.s^{-1} for $\varphi_{\mathrm{in}} = 0.25$, and; (4) $U_{\mathrm{m}} = 0.33$ m.s^{-1} for $\varphi_{\mathrm{in}} = 0.25$; "a" refers to the "normal" inlet configuration and "b" to the "inverted" inlet configuration.

A more complex mixed-zone profile is seen for the conditions $U_{\mathrm{m}} = 0.28$ m.s^{-1} for $\varphi_{\mathrm{in}} = 0.1$ (labelled "1" in Figure 6-6(d)). An instantaneous image of the flow for these conditions is presented in Figure 6-8(b); this is presented alongside an instantaneous image of the flow for the same independent variable values but taken for the "normal" inlet configuration (see Figure 6-8(a)). Analysis of the profile labelled "1" from Figure 6-6(d) in relation to Figure 6-8(b) (in actual fact, the following remark is based upon observation of the video of the aforementioned flowing conditions) reveals that there are three distinct regions to the oil dispersion in the flow. These are: (i) a layer of small oil droplets at the top of the pipe, below which there is (ii) a layer of fast moving long oil droplets, and below which (iii) is another layer of oil droplets albeit the same size as those at the top of the channel. On comparison with Figure 6-8(a) it is seen that the flow is significantly different. This can be attributed to the inlet configuration inducing a RT instability hence more mixing in the flow. As calculated in Section 6.1, enough time has elapsed for the droplets to reach the top of the channel, which is what is observed in Figure 6-8(b). However, these risen oil droplets have not coalesced to form a continuous oil region at the top of the channel. The reasons for this result are discussed below.

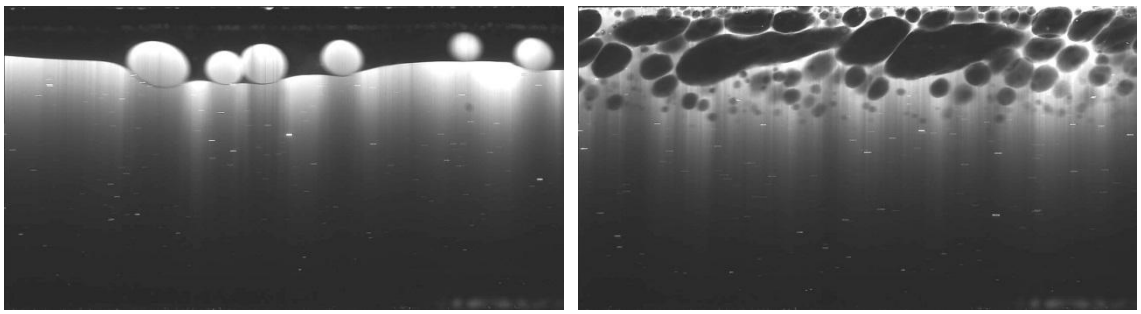

(a) (b)

Figure 6-8: Instantaneous flow images for a superficial mixture velocity $U_{\mathrm{m}} = 0.28$ m.s^{-1} and an oil input phase fraction $\varphi_{\mathrm{in}} = 0.1$ for: (a) the "normal" inlet configuration, and; (b) the "inverted" inlet configuration

The coalescence of two droplets of one phase (in this case, oil) in a continuum of another phase (in this case, glycerol solution) is governed by the dynamics of the intervening film. Essentially, for coalescence to occur, the film has to drain away under the pressure created by the two droplets coming together until the film is sufficiently thin locally for intermolecular effects to come into operation to rupture it. However, this drainage, and ultimately coalescence, is retarded by the viscosity of the film (and also any surfactants present that can rigidify the interface). In this case, the glycerol solution film has a significantly higher viscosity than the oil phase and hence results in the drainage process being slower, retarding the coalescence process.

It is possible to estimate the time take for the film to drain based on the viscosity of the continuous phase. This offers one possible explanation why oil droplets are more readily seen than glycerol solution droplets; should glycerol solution droplets form, the oil film drainage time necessary for their coalescence may be much lower than the glycerol solution film drainage time for the coalescence of two oil droplets. Furthermore, one would expect the "inverted" inlet configuration to results in smaller oil droplets than the "normal" inlet configuration (whether this is in fact the case will be examined in Section 6.7) and droplet size will also have a role to play in the coalescence of the two oil droplets.

This reasoning presents a possible explanation of the difference in flow regimes arising from the two different inlet orientations and that if a "fully developed" flow regime does exist for a given set of independent variables (superficial mixture velocity and input oil phase fraction) the time necessary for its formation (for the "inverted" inlet case in particular) cannot be solely based on the droplet and spike settling times but must also account for the conditions necessary for the droplets to coalesce. In other words, the droplet coalescence dynamics may persist far downstream of the inlet, giving rise to (possibly) very different flow regimes. It also emphasises the need to consider the inlet conditions when comparing results from modelling predictions to actual liquid-liquid flows.

6.4.1 Mixed Zone Height

Figure 6-9 presents the height of the mixed zone as a function of: (a) superficial mixture velocity, and; (b) input oil phase fraction. On comparison with Figure 5-6 (i.e., the equivalent results for the "normal" inlet configuration) it is seen that for a given superficial mixture velocity, the mixed zone height remains relatively stable for an increasing oil input phase fraction for the "inverted" inlet, as opposed to exhibiting an increase with an increasing oil input phase fraction as was observed with the "normal" inlet configuration. Secondly, on further comparison, it is seen that the mixed zone height is larger for the "inverted" inlet configuration.

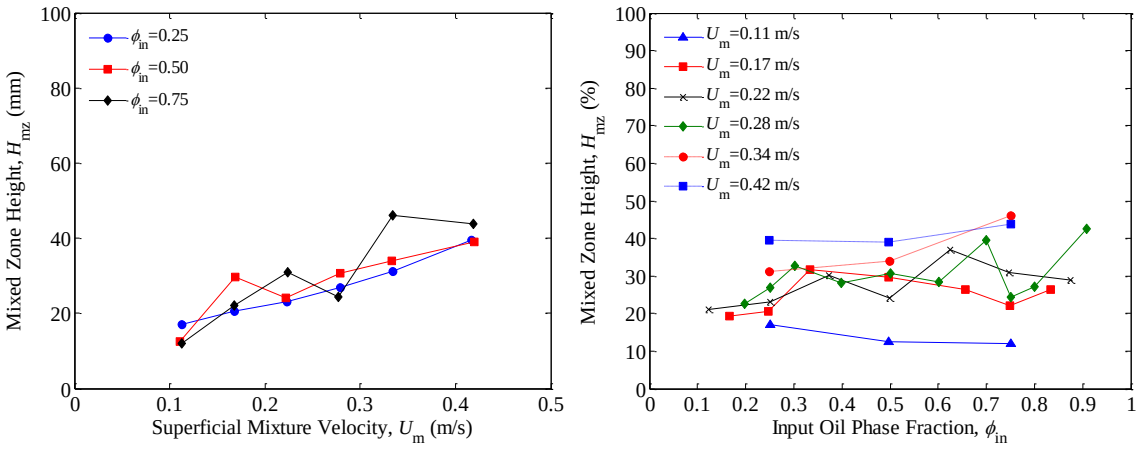

(a) (b)

Figure 6-9: Height of Interface Zone for as a function of (a) superficial mixture velocities U_m for constant input oil fraction φ_{in}; (b) input oil fraction φ_{in} for constant superficial mixture velocities U_m

6.5 In-Situ Phase Fraction

This section presents the results for in-situ oil phase fraction $\langle\varphi\rangle_{y,t}$ for the "inverted" inlet configuration to the test section inlet (Figure 6-2(b)). To recap, the in-situ oil phase fractions

were calculated by using the phase distribution profiles coupled with a numerical integration technique to account for the curvature of the visualisation cell wall; see Equations 5.1 and 3.5.

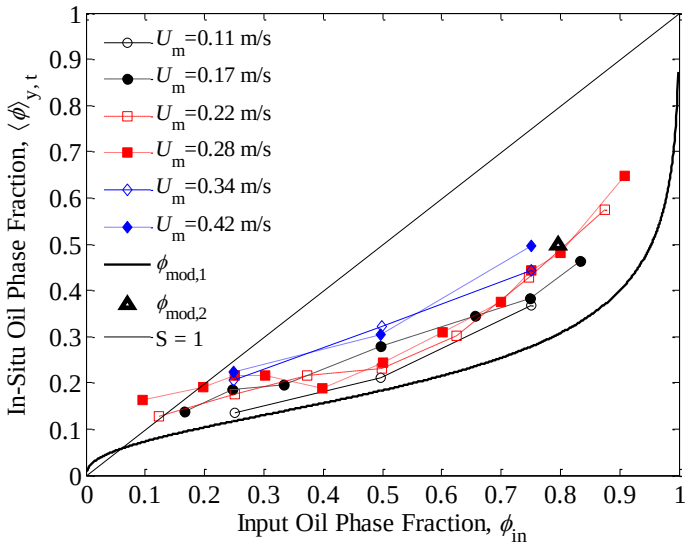

Figure 6-10: In-situ fraction $\langle\varphi\rangle_{y,t}$ as a function of input oil fraction φ_{in} for different superficial mixture velocities U_{m}

The results concur with the findings in Chapters 4 and 5 (see Figure 4-12 and 5-7, respectively); specifically, from Figure 6-10 it can be seen that the in-situ oil fraction $\langle\varphi\rangle_{y,t}$ is lower than the input oil fraction φ_{in} for almost all flow conditions; indicated by the data points being below the $S = 1$ (homogeneous flow model) line in Figure 6-10.

Two different, but in both cases simple, approaches have been taken to estimate (i.e., model) the in-situ oil phase fraction as a function of the input oil phase fraction. These are presented in Figure 6-10 as $\varphi_{\text{mod},1}$ and $\varphi_{\text{mod},2}$; their derivations are explained below and have been calculated using the same basis as $\varphi_{\text{mod},1b}$ and $\varphi_{\text{mod},2}$ in Figure 4-12.

6.5.1 Laminar Drag Model

This form of analysis is based on considering an equilibrium between the viscous drag due to laminar flow and pressure drop in the pipe. The derivation is presented in Appendix 2 but owing to the circular geometry, features the revisions presented in Section 5.5.1.

The laminar drag model, as with the results in Chapters 4 and 5, shows very good agreement with the low superficial mixture velocity experimental results. Although, better agreement is seen at like-for-like flowing conditions (i.e., input oil fraction φ_{in} and superficial mixture velocity velocities U_m values) for the "normal" inlet configuration, shown in Figure 5-7. This can be attributed to the imposed RT instability (due to the "inverted" inlet configuration) that gives rise to increased turbulence and in turn more mixing (e.g., the oil droplet layer seen in Figure 6-7) which moves the flow away from stratified flow (for which the laminar drag model is derived) and towards *dual continuous* flow for which, it is seen in Chapter 4, that the predictive ability of the model deteriorates; unless the viscosities of the flowing material above and below the interface are amended to account for the entrained flow.

6.5.2 Differential Momentum Balance Model

This predictive technique is denoted by $\varphi_{mod,2}$ and is based upon a differential momentum balance, see Section 4.5.2 for the derivation. This is again in excellent agreement with the experimental results. Hence, the same conclusion can be made i.e., that the interface level is adjusting in order to satisfy the increased viscous drag caused by the higher viscosity of the glycerol solution.

6.5.3 Homogeneous Flow Model and Slip Ratio

This section investigates the slip ratio S of the flows and in turn the suitability of using a homogeneous flow model ($S = 1$) to characterise the flows. Figure 6-11 investigates whether a single value or expression for the slip ratio can be used to characterise the flows.

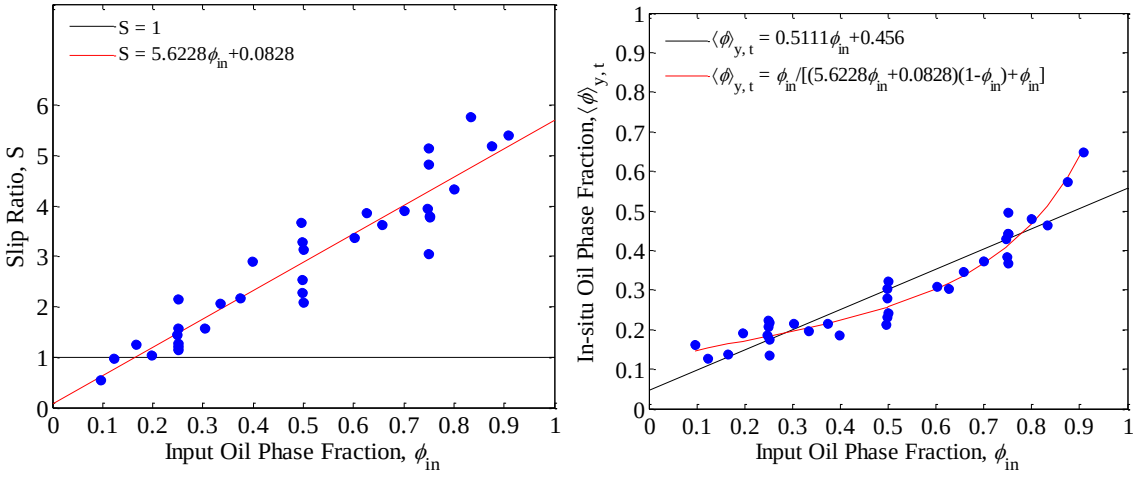

(a) (b)

Figure 6-11: Experimental results and correlations for: (a) slip ratio S as a function of input oil fraction φ_{in}, and: (b) in-situ oil phase fraction $\langle\varphi\rangle_{y,t}$ as a function of input oil fraction φ_{in}

The findings are synonymous with those of Chapters 4 and 5, specifically, that a homogenous flow model gives a very poor characterisation of the current flow matrix. This can again be accounted for in terms of the flow regime. As established upon comparison with experimental data by Lovick and Angeli (2004), a homogeneous flow model only beings to characterise the flow well when the superficial mixture velocity (and hence also Reynolds number) is sufficiently high to lead to turbulence, with its associated broadband flow structures (eddies and vortices) acting to mix the flow to the extent that the flow changes to dispersed flow.

The slip ratio results are extremely similar to the correlations for the in-situ phase fraction results in Chapters 4 and 5. The correlation for the current results is given in Equation 6.5.

$$S = 5.6228\varphi_{\text{in}} + 0.0828 \tag{6.5}$$

A correlation for the in-situ phase fraction based on Equations 6.5 and 4.14 is given in Equation 6.6 below:

$$\langle\varphi\rangle_{y,t} = \frac{\varphi_{\text{in}}}{(5.6228\varphi_{\text{in}} + 0.0828)(1 - \varphi_{\text{in}}) + \varphi_{\text{in}}} \tag{6.6}$$

This is plotted along with the correlations for the results in Chapters 4 and 5 (Equations 4.16 and 5.8, respectively) in Figure 6-13; more below.

Figure 6-12 compares the experimental results slip ratio from all three experimental campaigns. Figure 6-12(a) indicates that the results are broadly similar. This leads to the conclusion that the flows, at least with regards to the slip ratio, are dominated by the same flow and mixing processes, e.g., turbulent transport.

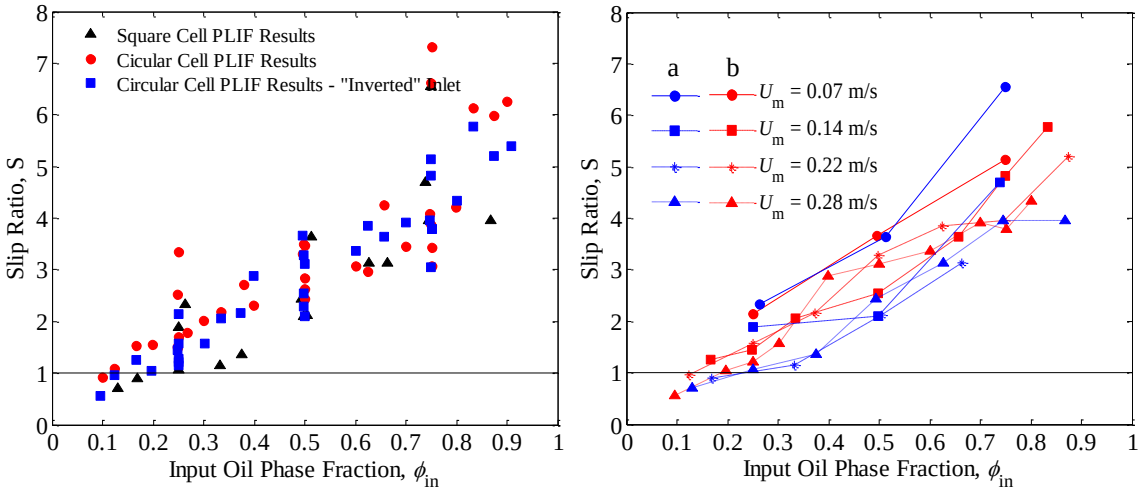

(a) (b)

Figure 6-12: (a) Slip ratio S as a function of input oil fraction φ_{in} for all three PLIF experimental campaigns, and; (b) Slip ratio S as a function of input oil fraction φ_{in} for different superficial mixture velocities U_m, where "a" denotes the "normal" inlet configuration and "b" the "inverted" inlet configuration

Figure 6-12(b) explores the relative trends between the two circular cross-section campaigns for constant superficial mixture velocities U_m , from which two observations are made: (1) that as the superficial mixture velocity increases, the slip ratio tends towards unity, and; (2) the results are largely independent of the inlet orientation. Figure 6-12(b) also shows that there is an exception to the earlier conclusion concerning the similarity of the slip ratio across the flow campaigns; the "normal" inlet flows at medium inlet fractions (φ_{in} ~ 0.3-0.7) and velocities (U_m = 0.14 - 0.28 m.s^{-1}) typically experience lower slip ratios than their "inverted" counterparts. Clearly a secondary mechanism must be responsible for this, not accounted for by U_m (or *Re*).

Figure 6-13 indicates that there is a characteristic in-situ phase fraction curve for the current system, based upon the test fluids and the independent variables (superficial mixture velocity and input oil phase fraction). Hence, it can be deduced that after the entrance length

(L/D = 244) to the visualisation cells, the in-situ phase fraction is independent of the inlet orientation and the test section geometry.

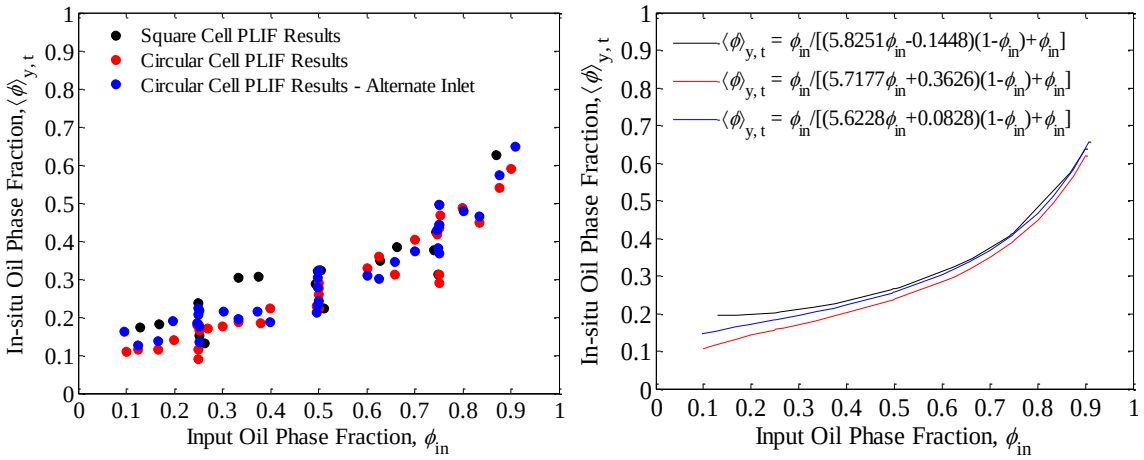

(a) (b)

Figure 6-13: (a) In-situ phase fraction experimental results, and; (b) In-situ phase fraction correlations for the square cross-section visualisation section (black) and the circular cross section visualisation section with the "normal" inlet configuration (red) and "inverted" inlet configuration (blue)

6.6 Interface Level

The results of the interface level analysis that has been performed on the "inverted" inlet PLIF-PTIV images are presented in this section. The section is also concerned with the suitability of two simple estimation approaches in predicting the interface level in stratified flows.

Figure 6-14 presents the results of the interface level H as a function of input oil fraction φ_{in} for fixed superficial mixture velocities from U_m = 0.11 to 0.28 m.s^{-1}. Figure 6-15 presents the same results of the interface level H, but as a function of the corresponding superficial mixture velocity U_m.

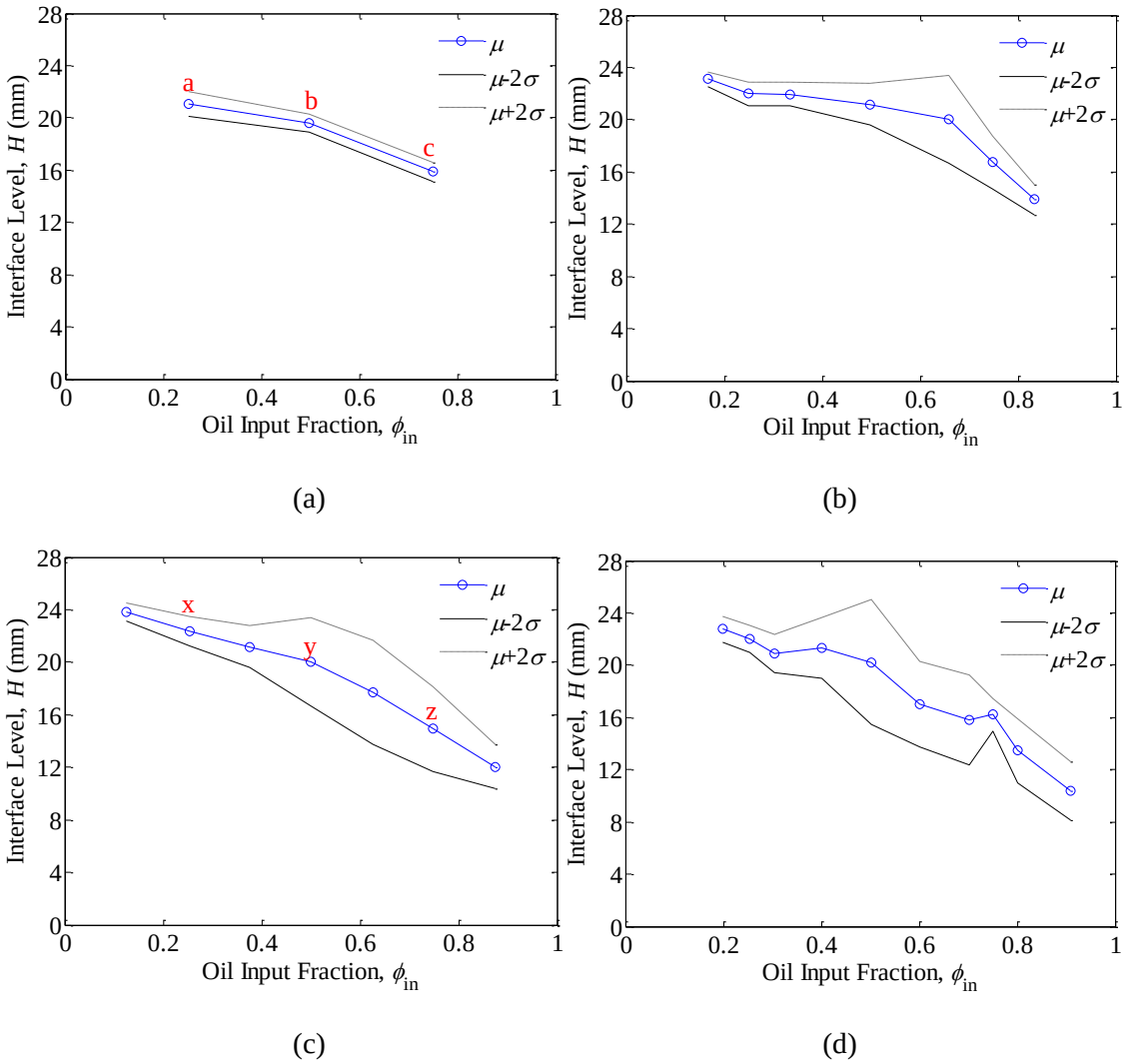

Figure 6-14: The mean (μ) and upper ($\mu + 2\sigma$) and lower ($\mu - 2\sigma$) limits for the interface level H as a function of input oil fraction φ_{in} for superficial mixture velocities U_m of: (a) 0.11 m.s^{-1}, (b) 0.17 m.s^{-1}, (c) 0.22 m.s^{-1}, and (d) 0.28 m.s^{-1}

Two trends are observed from Figures 6-14 and 6-15. Firstly, that for a given superficial mixture velocity, as the oil input phase fraction increases, the interface level reduces. The second observation is that as the superficial mixture velocity increases, the fluctuation of the interface level heights also increases; this is seen most prominently in Figure 6-15(b) and is pursued in Section 6.6.1.

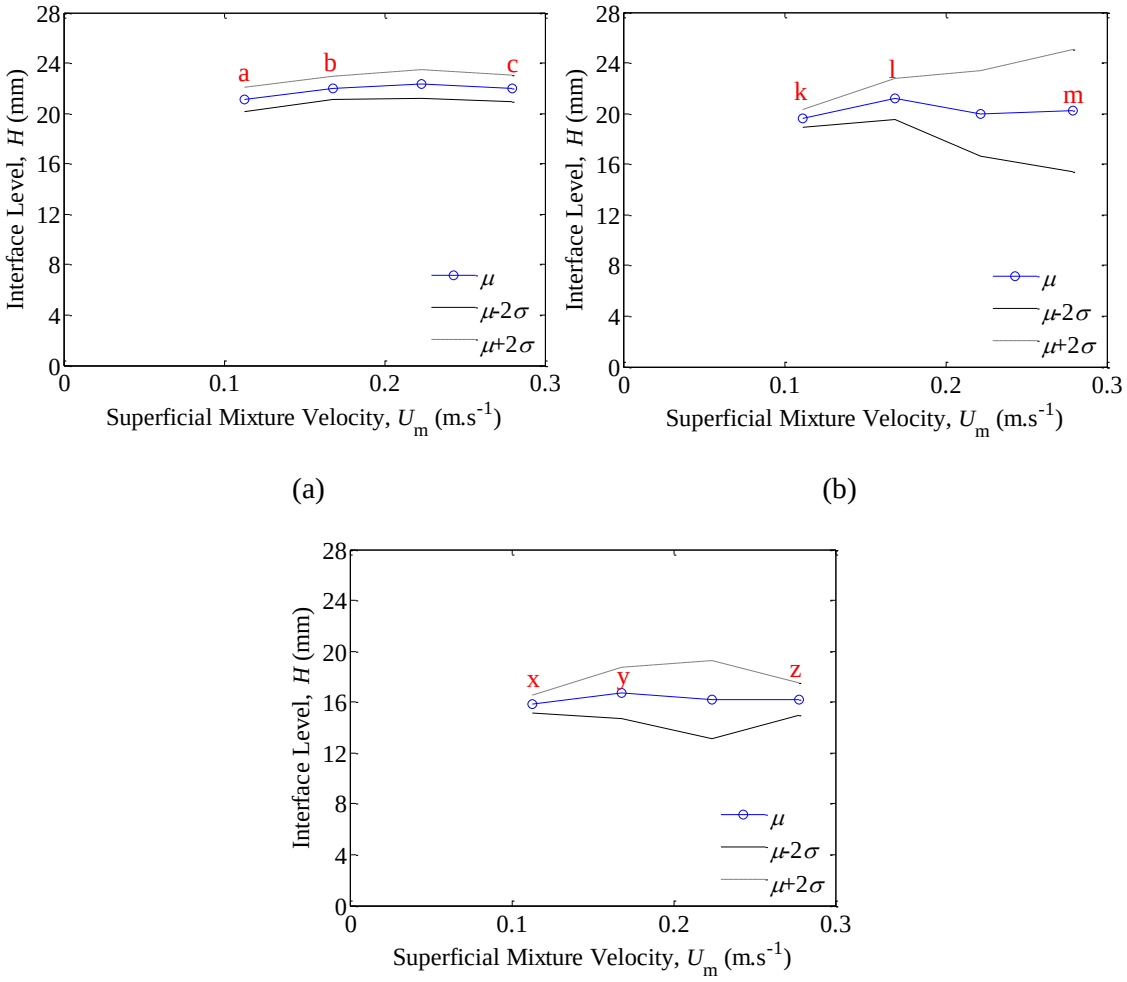

Figure 6-15: The mean (μ) and upper ($\mu + 2\sigma$) and lower ($\mu - 2\sigma$) limits for the interface level H as a function of superficial mixture velocity U_m for input oil fractions φ_{in} of: (a) 0.25, (b) 0.50, and (c) 0.75. Points a, b, c; k, l, m; and x, y, z correspond to the example images and probability histograms in Figures 4.12, 4.13 and 4.14 respectively.

The widening of the upper (μ - 2σ) and lower ($\mu + 2\sigma$) interface level limits (for the 95% confidence interval) with an increasing superficial mixture velocity can be attributed to turbulence. As the superficial mixture velocity increases, the Reynolds number increases, which, when sufficiently high will lead to turbulence which can present as waves at the common interface which can grow in amplitude with superficial mixture velocity. This trend

can intensify when the superficial mixture velocity passes another threshold, Ri <0.25, giving rise a KH instability at the common interface, which will manifest as waves at this interface, thus widening the 95% confidence interval for the interface level height further.

6.6.1 Interface Level Probability Distributions

Figures 6-16 and 6-17 present instantaneous images and corresponding interface level probability histograms for the points that have been used to construct the mean interface level plots shown in Figures 6-14(a) and 6-14(c), respectively.

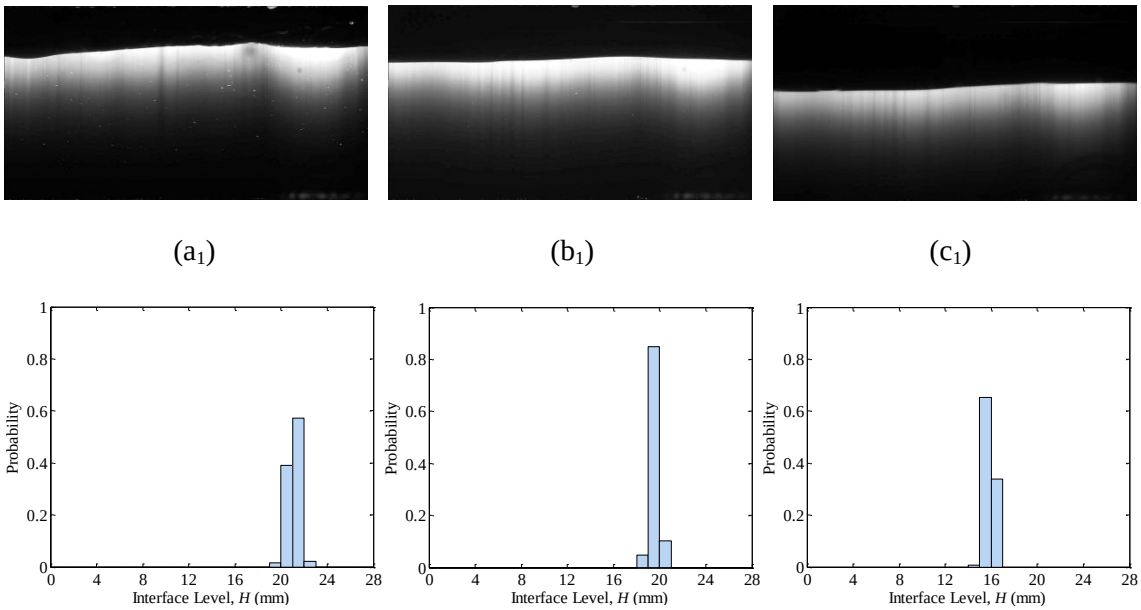

(a_1) (b_1) (c_1)

(a_2) (b_2) (c_2)

Figure 6-16: Flow images with input oil fraction φ_{in} of (a_1) 0.25, (b_1) 0.50, (c_1) 0.75, all at a superficial mixture velocities U_m = 0.11 m.s^{-1}; (a_2), (b_2) and (c_2) show the probability histograms for the same conditions respectively. Data corresponds to Points a, b and c, as labelled in Figure 6-14(a)

From inspection of the instantaneous images ($a_1 \rightarrow c_1$ and $x_1 \rightarrow z_1$) and the histograms ($a_2 \rightarrow c_2$ and $x_2 \rightarrow z_2$), one can readily see that the mean interface level μ_H decreases gradually with an increasing oil input oil fraction φ_{in} for a given superficial mixture velocity U_m. For the histograms presented in Figure 6-16, the superficial mixture velocity is $U_m = 0.11$ m.s^{-1}. From Table 6-1 it is seen that for a superficial mixture velocity of this order, both phases have a Reynolds number that corresponds to laminar flow. As a result, the influence of the transport (mixing) associated with turbulent fluctuations at the common interface will be absent, and only very low amplitude waves are to be expected and in turn, for the interface level to cover only a very narrow range of heights. This is what is seen in the results in Figure 6-16.

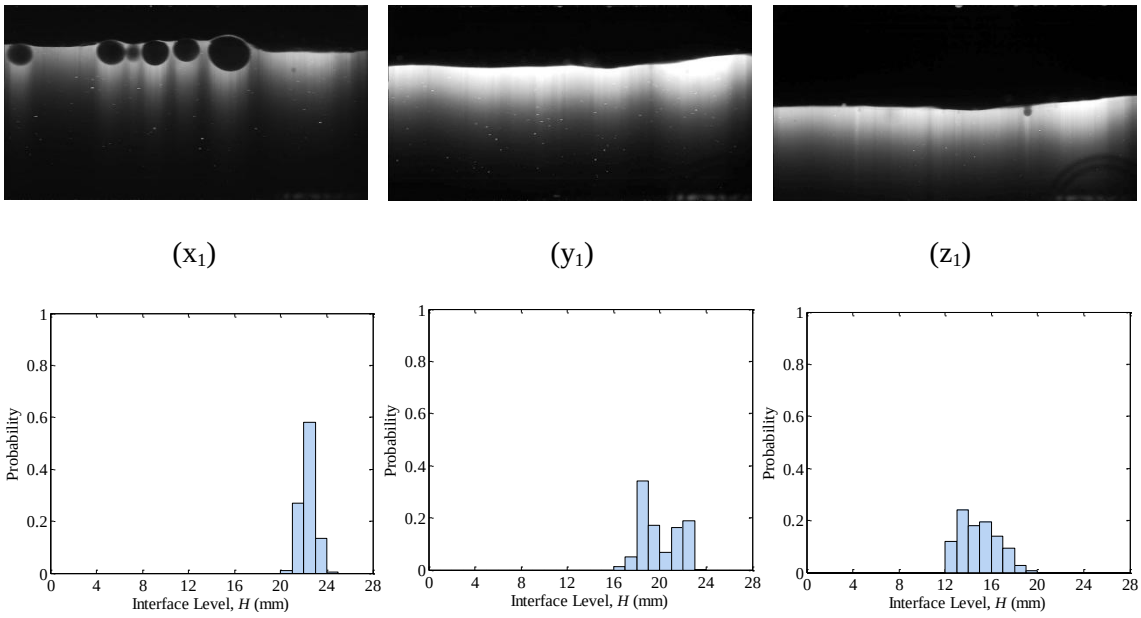

(x_1) (y_1) (z_1)

(x_2) (y_2) (z_2)

Figure 6-17: Flow images with input oil fraction φ_{in} of (x_1) 0.25, (y_1) 0.50, (z_1) 0.75, all at a superficial mixture velocities U_m = 0.17 m.s^{-1}; (x_2), (y_2) and (z_2) show the probability histograms for the same conditions respectively. Data corresponds to Points x, y and z, as labelled in Figure 6-14(c)

For the histograms presented in Figure 6-17, the superficial mixture velocity is $U_m = 0.22$ m.s^{-1}, thus, the flow cases in Figure 6-17 have higher Reynolds numbers than those in Figure 6-16. As a result, the influence of turbulent disturbances at the interface will be greater and, in turn, waves of greater amplitude are expected in Figure 6-17; albeit still relatively low amplitude waves owing to the Reynolds numbers still being low. On comparison with Figure 6-16, it is observed that the interface level probability distributions presented in Figure 6-17 are associated with a larger spread (higher standard deviation), as expected.

Proceeding further, Figures 6-18 to 6-20 present instantaneous images and interface level probability histograms for the points that have been used to construct the mean interface level plots shown in Figures 6-15(a) to 6-15(c), respectively.

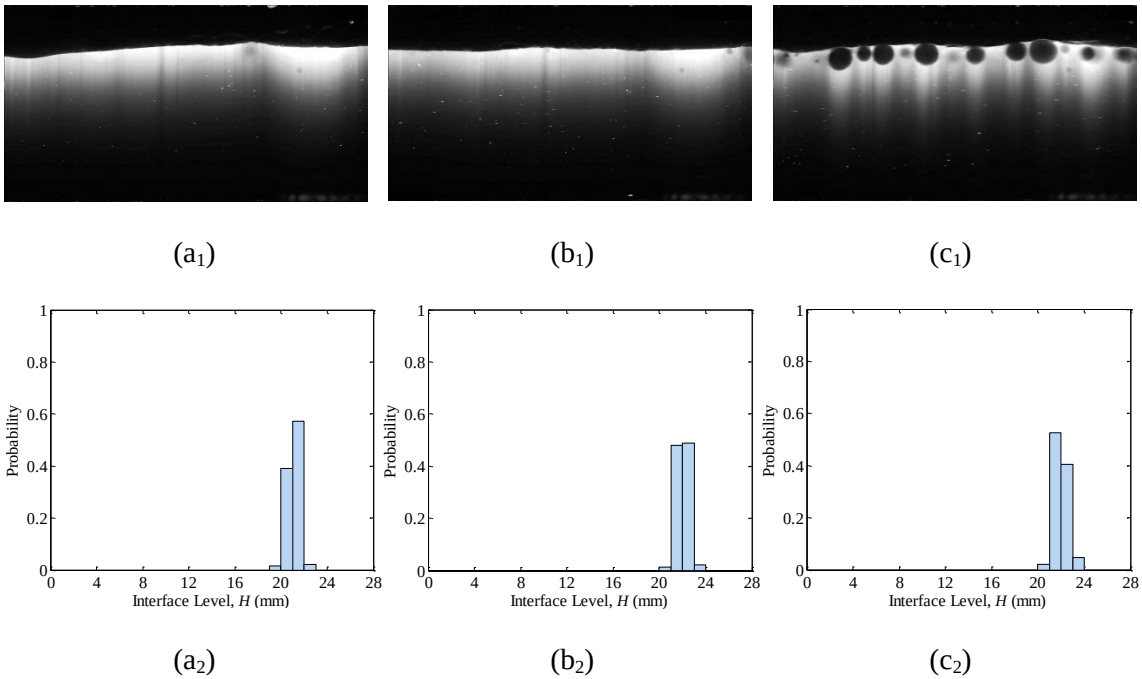

Figure 6-18: Flow images with superficial mixture velocities U_m of: (a_1) 0.11 m.s^{-1}, (b_1) 0.17 m.s^{-1}, (c_1) 0.28 m.s^{-1}, all at an input oil fraction $\varphi_{in} = 0.25$; (a_2), (b_2) and (c_2) show the probability histograms for the same conditions respectively. Data corresponds to Points a, b and c, as labelled in Figure 6-15(a)

From the instantaneous images ($a_1 \rightarrow c_1$ and $x_1 \rightarrow z_1$) and the histograms ($a_2 \rightarrow c_2$ and $x_2 \rightarrow z_2$), two key observations are made. Firstly, that as the superficial mixture velocity increases for a constant oil input phase fraction, the mean interface level remains roughly constant; this is more obviously noticeable in Figure 6-15. The second key observation is aligned with the findings of Figures 6-16 and 6-17; that as the superficial mixture velocity increases the probability distribution for the interface level heights widens. Further to this, these trends are seen to be most prominent for intermediate input oil phase fractions ($\varphi_{in} = 0.5$).

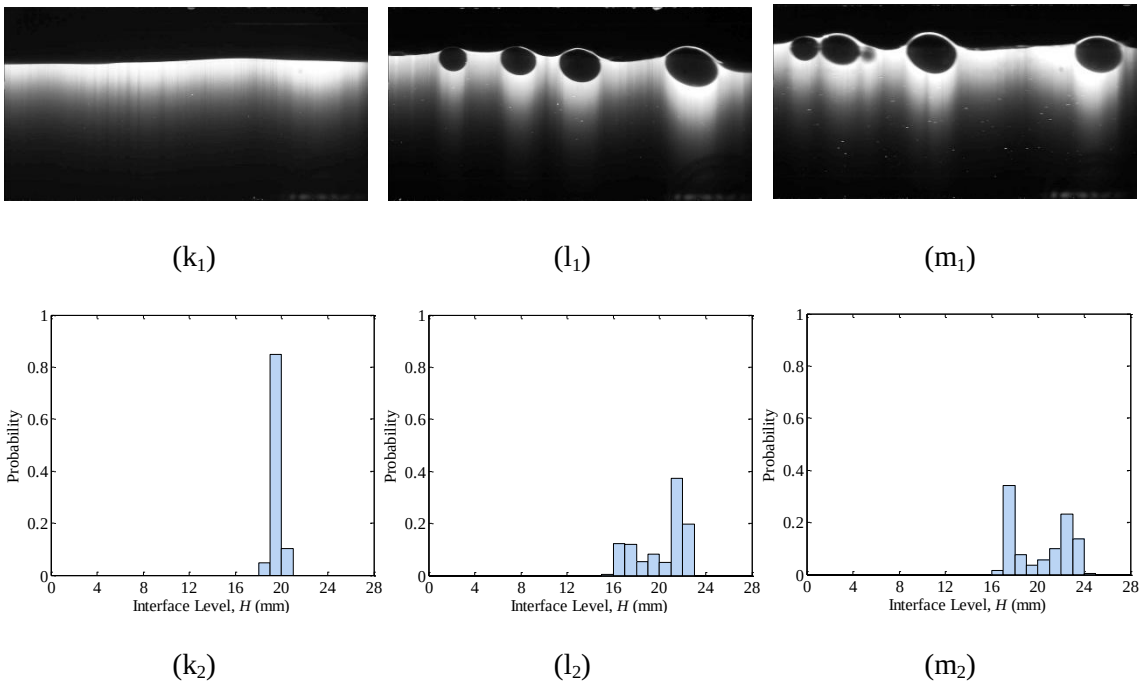

Figure 6-19: Flow images with superficial mixture velocities U_m of: (k_1) 0.11 m.s^{-1}, (l_1) 0.17 m.s^{-1}, (m_1) 0.28 m.s^{-1}, all at an input oil fraction $\varphi_{in} = 0.50$; (k_2), (l_2) and (m_2) show the probability histograms for the same conditions respectively. Data corresponds to Points k, l and m, as labelled in Figure 6-15(b)

The interface level probability distribution results for low superficial mixture velocities and low input oil phase fractions are found to be highly comparable for both inlet configurations investigated; compare Figures 5-18 and 6-18. However, a disparity between the results for the

two different inlet orientations develops as the superficial mixture velocity increases for intermediate input oil phase fraction ($\varphi_{in} = 0.5$). This can be attributed to the fact that under these conditions, oil droplets below in the interface are more readily found when using the "inverted" inlet orientation which gives rise to further fluctuations in the interface level.

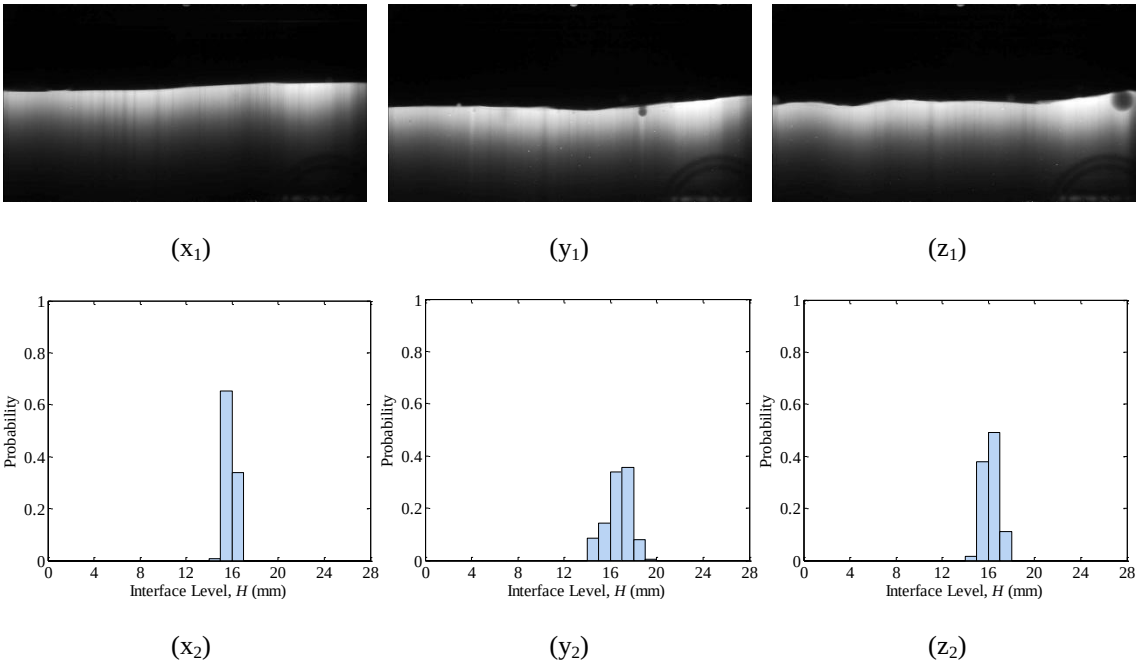

Figure 6-20: Flow images with superficial mixture velocities U_m of: (x_1) 0.11 m.s^{-1}, (x_1) 0.17 m.s^{-1}, (x_1) 0.29 m.s^{-1}, all at an input oil fraction $\varphi_{in} = 0.75$; (x_2), (y_2) and (z_2) show the probability histograms for the same conditions respectively. Data corresponds to Points x, y and z, as labelled in Figure 6-15(c)

On further comparison of Figures 5-18 to 5-20 with Figures 6-18 to 6-20 it is seen that the mean interface level height is largely the same, regardless of the inlet configuration which just widens the probability distribution when it is set to impose a RT instability (i.e., is "inverted).

6.6.2 Laminar Drag Model

Figure 6-21 presents predicted values of interface level obtained from the laminar drag model (Equation 5.6), denoted by $H_{mod,1}$, along with interface level experimental results for the "inverted" inlet configuration PLIF-PTIV runs.

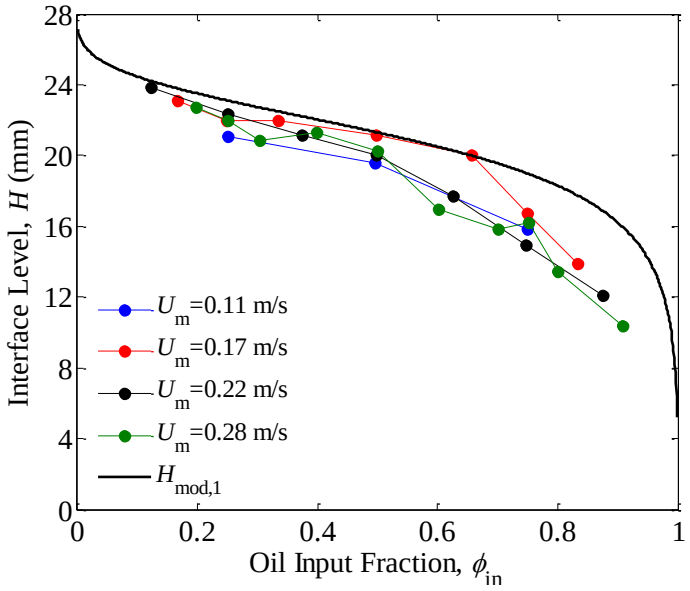

Figure 6-21: Interface Level H as a function of input oil fraction φ_{in} for different superficial mixture velocities U_m

The laminar drag model gives excellent agreement with the experimental results, especially for the $U_m = 0.17$ m.s^{-1} flow case; more so than for the same conditions when using the "normal" inlet orientation. It should be noted that from $U_m = 0.11$ to 0.17 m.s^{-1} the interface level is seen to rise with the increased superficial mixture velocity for a given input oil phase fraction. However, the interface level then lowers progressively from $U_m = 0.17$ to 0.28 m.s^{-1}, again for a given oil input phase fraction. This observation can be attributed to the oil droplet layer that is present below the interface for the superficial mixture velocities $U_m \geq 0.17$ m.s^{-1} (arising from the "inverted" inlet orientation), which results in the raising of the interface level in the

experiments with $U_m = 0.11$ and 0.17 m.s^{-1}. Hence, the fact that the laminar drag model appears to capture the interface level well at $U_m = 0.17$ m.s^{-1} is coincidental. It is the presence of this oil droplet layer that gives the indication that the laminar drag model better predicts the current results compared with those in Chapter 5 (see Figure 5-21). Nevertheless, on inspection of the experimental results for stratified flow ($U_m = 0.11$ m.s^{-1}) for each of the inlet orientations with the predictions of $H_{mod,1}$, it can be concluded that that laminar drag model is in very good agreement with the experimental results, irrespective of the inlet orientation.

6.6.3 Hall and Hewitt (1993) Predictive Technique

The experimental results generated with the "inverted" inlet arrangement are presented in Figure 6-22 along with interface level predictive models by Hall and Hewitt (1993) for gas-liquid flows (Figure 6-22(a)) and, liquid-liquid flow (in Figure 6-22(b)).

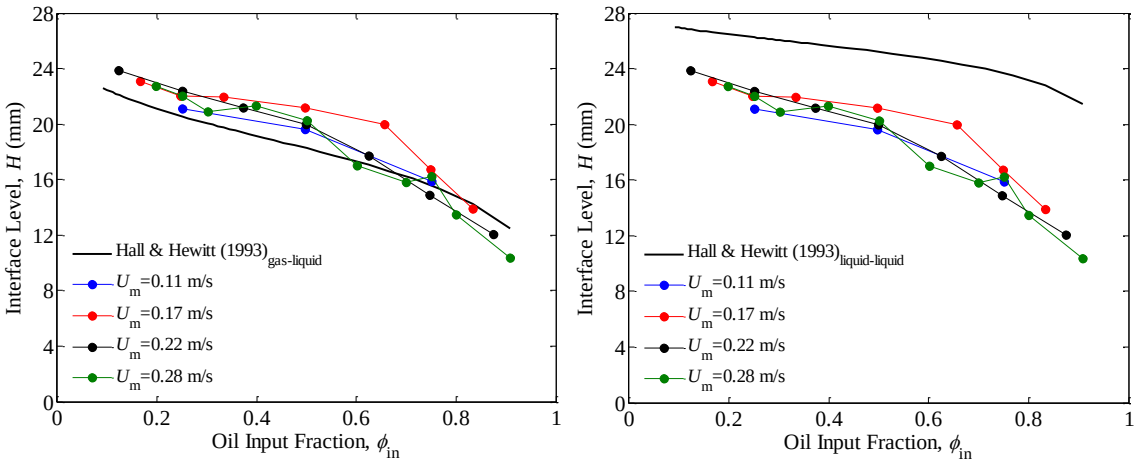

(a) (b)

Figure 6-22: Interface Level H as a function of input oil fraction φ_{in} for different superficial mixture velocities U_m featuring interface level models presented by Hall and Hewitt (1993) for: (a) stratified gas-liquid flow, and; (b) stratified liquid-liquid flow

Both predictive techniques capture the lowering of the interface level with an increasing oil input phase fraction, although, as seen in Figure 6-22(b), the liquid-liquid model over-predicts the interface level, with the extent of the over-prediction being more significant as the input oil phase fraction increases. One possible explanation for this is that the Hall and Hewitt (1993) models assume a flat interface between the two flowing fluids, whereas we know that as the superficial mixture velocity increases the interface moves away from being flat (this is seen in the widening of the interface level probability histograms with an increasing superficial mixture velocity that was reported in Section 6.6.1). Thus, the flow is no longer representative of the case on which the model is based.

6.7 Droplet Size Distribution

This section presents the droplet size analysis that has been performed on the PLIF- images from the "inverted" runs. The results contained herein are limited to the mean droplet diameters $\mu_{d,\mathrm{gs}}$ for both phases as a function of input oil phase fraction φ_{in} at a superficial mixture velocity of $U_{\mathrm{m}} = 0.28$ m.s^{-1}. The results are shown in Figure 6-23.

Results at other superficial mixture velocities or, as a function of superficial mixture velocity at constant input oil phase fractions are not presented since there were insufficient data points to create these plots. On comparing Figure 6-23 with the corresponding Figure 5-23 generated from data in the normal inlet configuration, it can be stated that the behaviour of the mean droplet size is much more erratic for the "inverted" inlet condition. The typical mean droplet size is in the range from about 1.5 mm to a maximum of about 4.5 mm (this is 25% of the height of the pipe).

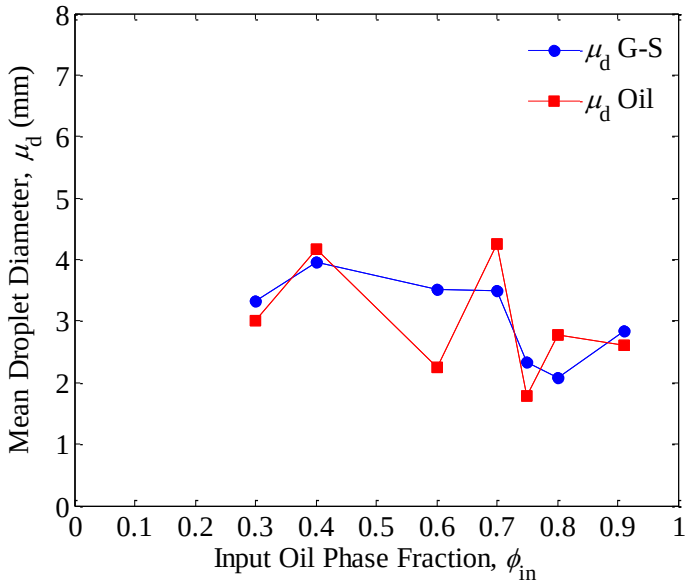

Figure 6-23: Mean droplet diameter μ_d as a function of input oil phase fraction φ_{in} and a constant superficial mixture velocity of $U_m = 0.28$ m.s^{-1}, for glycerol solution droplets (blue circles) and oil droplets (red squares)

6.8 Velocity Profiles

This section presents velocity profile results that have been generated using the technique detailed in Section 3.11.7 on the PLIF images acquired when using the "inverted" inlet orientation. Figure 6-24 shows velocity profiles for normalised superficial mixture velocities (i.e., the velocity profile has been divided by the superficial mixture velocity of that run) in the range $U_m = 0.11$ to 0.84 m.s^{-1} at oil input fractions φ_{in} of (a) 0.25; (b) 0.50, and; (c) 0.75.

Referring to Figure 6-24, and in line with what was observed in Section 5.9, once normalised, the velocity profiles for a fixed oil input fraction φ_{in} collapse to a 'generic' profile. Out of the three selected input oil fractions φ_{in}, the case with the greatest deviations from this generic profile is the case with the lowest φ_{in} (= 0.25).

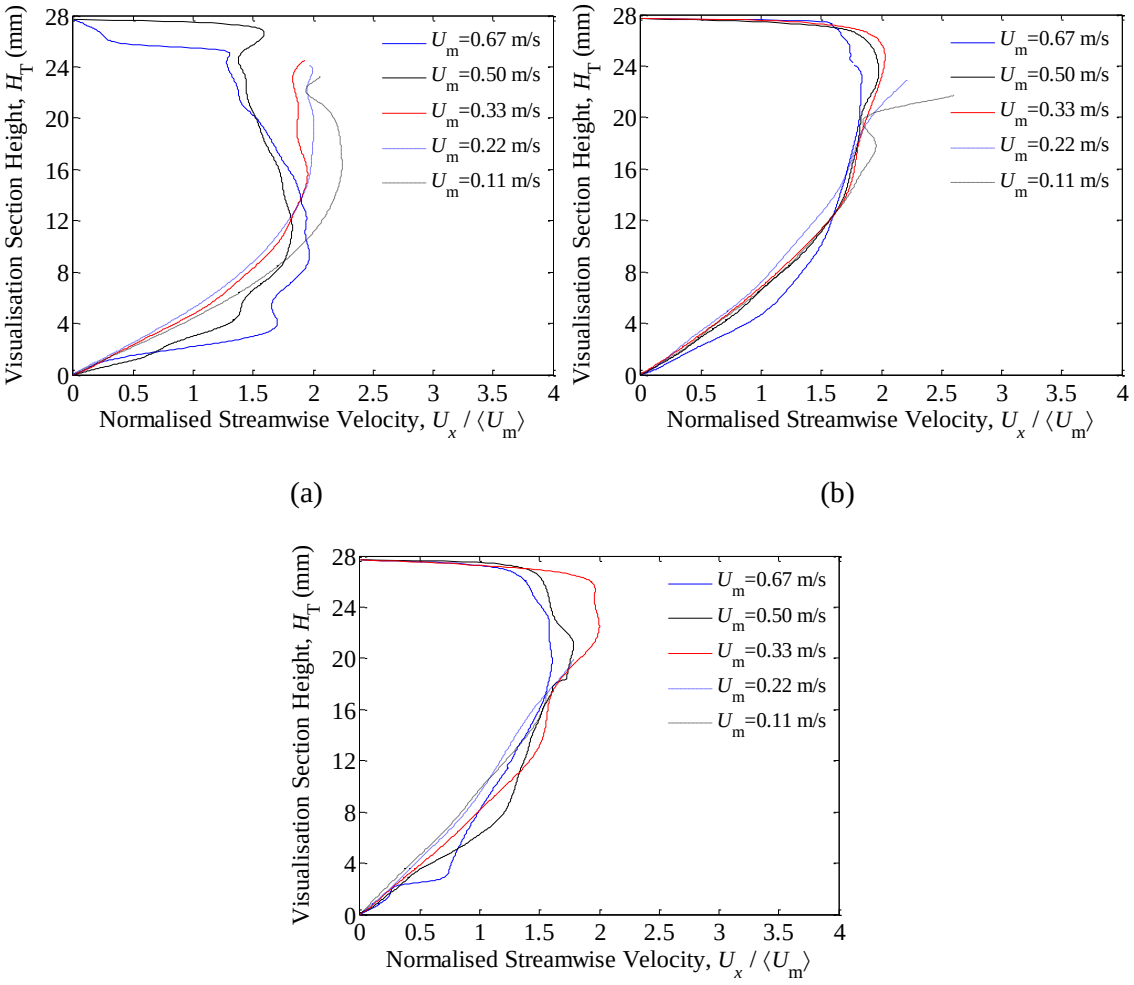

Figure 6-24: Normalised velocity profiles $U_x/\langle U_m \rangle$ for different superficial mixture velocities U_m at an input oil fraction φ_{in} of: (a) 0.25; (b) 0.50, and; (c) 0.75

In more detail, the interface region is seen to retain a dependence on the superficial mixture velocity, with the "step change" observed in Figure 5.9 also present in the results for the inverted inlet configuration. In the "normal" inlet orientation flows in Chapter 5 this step change was attributed to a velocity difference between the two liquids either side of the interface – there is slippage (i.e., a non-unity slip ratio) across the interface – with the trends aligning with those found for the slip ratio. The shear layer is seen to increase with input oil

phase fraction; the absence of the shear layer from the $\varphi_{in} = 0.75$ cases can be attributed to our limited ability to capture the velocity profile above the interface level for these runs.

The "normal" inlet orientation flows in Chapter 5 exhibited flow transitions (and associated velocity profiles) that were well accounted for by the change in the superficial mixture velocity (Reynolds number and transition to turbulence) and, if there was sufficient shear across the interface (typically expected at the extreme inlet phase fractions close to zero or unity), the added effect of a Kelvin-Helmholtz instability. However, in the current study there is an additional instability mechanism at play that can influence the flow regime and thus the velocity profiles, namely, the Rayleigh-Taylor instability. As discussed previously in the chapter and illustrated in Figures 6-7 and 6-8, this can results in the entrainment of oil droplets below the interface for some flow cases. However, the velocity profiles for like-for-like independent variable combinations are highly comparable for the two inlet orientations.

6.8.1 Flow Regime Analysis

This section presents pairs of velocity profiles along with instantaneous PLIF images of the flow from the same run. The intention is explain the emerging velocity profiles by means of the interactions between the two phases, i.e., the flow regime. The findings are in complete concurrence with those established in Section 5.9.1.

Figure 6-25 presents a velocity profile and an instantaneous image for stratified flow, and although the velocity profile only extends up to the interface, it can be seen that the results are in complete agreement with those seen in Figure 5-28 for the "normal" inlet orientation. From Table 6-1 it is seen that both phases have Reynolds numbers in the laminar flow region and

thus, the parabolic velocity profile [which is a characteristic of laminar flow, see Figure 5-27(a)] of the glycerol solution flow is expected.

A "step" is seen in the velocity profile at a height of approximately 20 mm, which is a shear layer arising from the bulk velocity difference of the two phases. Based on the run conditions, namely the input oil phase fraction (φ_{in} = 0.50) and the in-situ oil phase fraction ($\langle\varphi\rangle_{y,t}$ = 0.21) and Equation 4.14, it can be calculated that the flow has a non-unity slip ratio (in this case, S = 3.8), and thus (from Equation 4.11) it is seen that the oil velocity is larger than the glycerol solution velocity. Owing to this, a shear layer and thus a shift to the right in the velocity profile above the interface is expected.

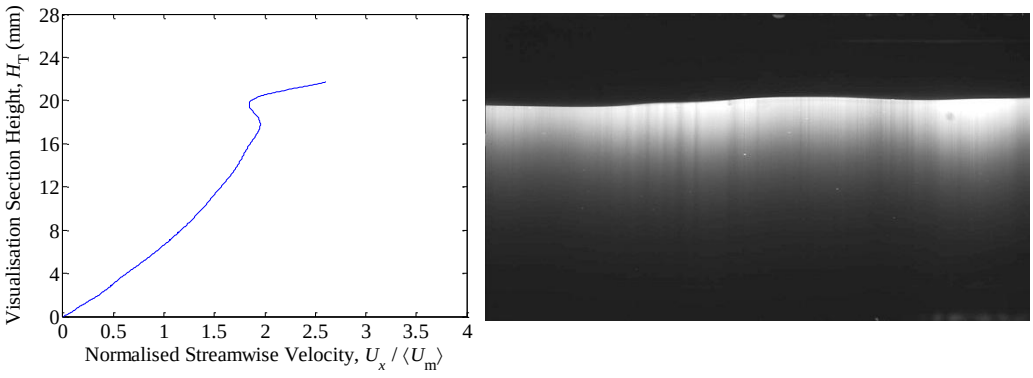

(a) (b)

Figure 6-25: Velocity profiles (a) and instantaneous images (b) for a superficial mixture velocity of U_m = 0.11 m.s^{-1} and an input oil phase fraction φ_{in} = 0.50

For the flow regimes that can collectively be termed *dual continuous* flow, the "step" (shear layer) at the interface is absent and the profile over the mixed region becomes flatter, i.e., the flow regime develops from a parabolic velocity profile that is characteristic of laminar flows to a flatter one indicative of turbulent flows. This would be expected since for the flow to develop a mixed region, flow mixing arising from some form of instability or fluctuations will need to occur. As previously discussed (and although a Rayleigh-Taylor instability has been imposed

on the flow in the current study) the main driver for mixing in the experimental conditions covered in the work done with both inlet configurations is related to the broadband turbulent fluctuations (and enhanced transport) which can cause mixing of the flow and thus the formation of droplets in one phase in a continuum of the other. These fluctuations are produced from nonlinear inertial forces in the flow and can be described by the Reynolds number (owing to increased superficial mixture velocities), which passes a transitional threshold value. Here a flow with a turbulent velocity profile (see, Figure 5-27(b)) is expected.

Figure 6-26 presents a velocity profile and an instantaneous image for the *glycerol solution droplet layer* flow regime (i.e., *dual continuous* flow). From Table 6-1 it can be seen that the Reynolds number of the oil phase for the experimental run presented in Figure 6-28 is in the turbulent region.

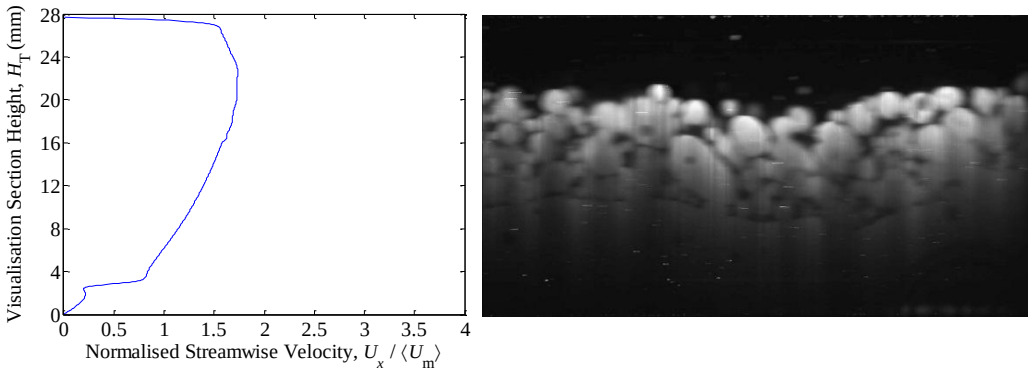

(a) (b)

Figure 6-26: Velocity profiles (a) and instantaneous images (b) for a superficial mixture velocity of U_m = 0.84 m.s^{-1} and an input oil phase fraction φ_{in} = 0.50

At even higher superficial mixture velocities (relative to the flow case presented in Figure 6-26) the turbulence intensity (magnitude of the fluctuations in the flow) increases leading to further mixing of the phases. In addition, high levels of shear at the interface, at high or low inlet phase fractions, can lead to the onset of the Kelvin-Helmholtz instability mechanism and in turn,

further mixing. Ultimately, these different mechanisms for mixing the flow will lead to the transition to *dispersed* flow which are characterised by turbulent velocity profiles over the dispersed region; see Figure 6-27.

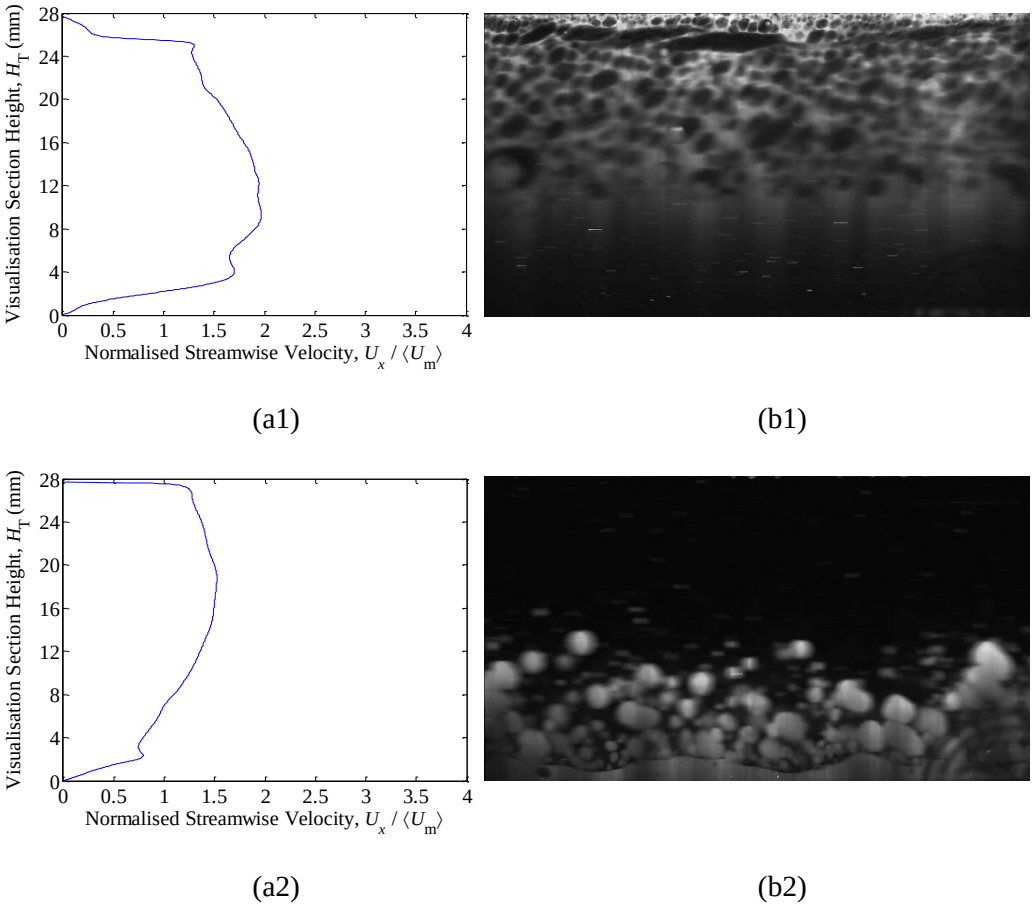

Figure 6-27: Velocity profiles ($a_1 \rightarrow a_2$) and instantaneous images ($b_1 \rightarrow b_2$) for: (1) U_m = 0.84 m.s^{-1} and φ_{in} = 0.10, and; (2) U_m = 0. 83 m.s^{-1} and φ_{in} = 0.90

6.8.2 Contact Angle Analysis

It is important to note that the presented in-situ oil phase fraction and velocity profiles were taken at the centreline of the visualisation section, owing to the planar nature of the optical diagnostic techniques that has been applied. A key assumption that has been employed, particularly for the in-situ phase fraction estimations from the resulting data, is that the flows

have a flat interface; this ignores the effects of surface tension and the contact angle at the pipe wall (see Figure 6-28) which is a reasonable assumption when the density difference between the two fluids is large, Ng (2002). Curvature at the interface can become significant for systems with a density ratio near unity, small diameter pipelines and large interfacial tension. Hence the appropriateness of this assumption to the current PLIF studies needs to be investigated.

The interface between two fluids can be characterised by some key parameters, one of which is the Bond number (Bo) which is a ratio of the gravitational forces to the inertial forces; as the Bond number increases the common interface tends towards a flat surface. The expression for the Bond number is given in Equation 6.7 below,

$$\mathrm{Bo} = \frac{\Delta\rho . g . r^2 . \cos\alpha}{\gamma_{\mathrm{AB}}}, \tag{6.7}$$

where $\Delta\rho$ is the density difference between the phases; g is the acceleration due to gravity; r is the radius of the pipe; α is the inclination of the pipeline, for the current system $\alpha = 0^{\circ}$ (see Figure 6-28(b)), and; γ_{AB} is the interfacial tension.

Prior to evaluating the Bond number for the current system it should be noted that the interface will be a flat surface if Equation 6.8 is satisfied:

$$\varepsilon = 1 - \langle\varphi\rangle_{y,t,} = \frac{\theta - \cos\theta \sin\theta}{\pi}, \tag{6.8}$$

where θ is the contact angle, see Figure 6-28(a).

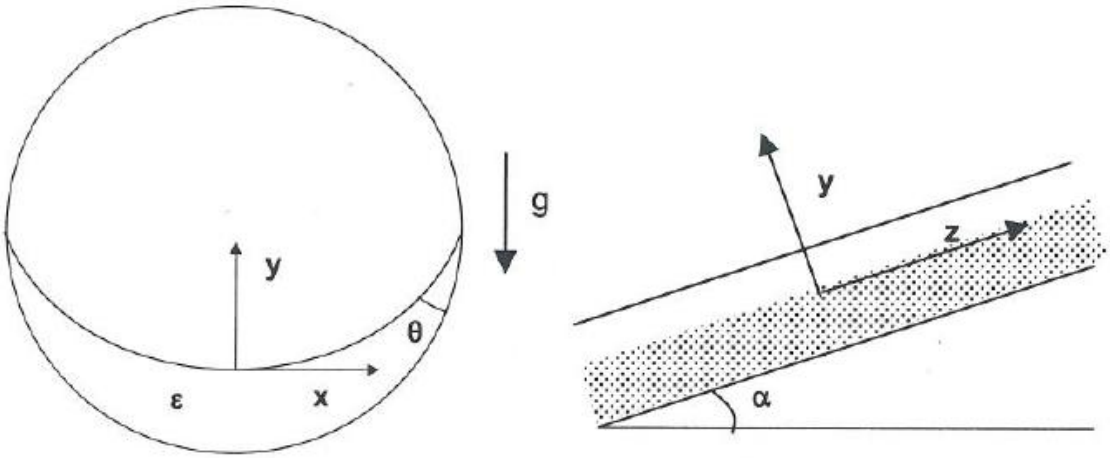

(a) (b)

Figure 6-28: The geometry and coordinates of the flow systems, showing: (a) axial, and; (b) side views, Ng (2002)

The contact angle for the two test fluids has been measured using the following technique. By filling a box constructed of the same material as the test section with Exxsol D80 and inserting a droplet of the glycerol-solution into the oil. Then allowing enough time for the droplet to settle; three hours was allowed for this. Then a camera was used to take an image of the settled droplet, as shown in Figure 6-29, and the contact angles at either side of the droplet were then measured using imageJ. This was then repeated 10 times. Using this technique, the contact angle was found to be $\theta = 51.3^{\circ}$ with a standard deviation of $\sigma = 3.3^{\circ}$.

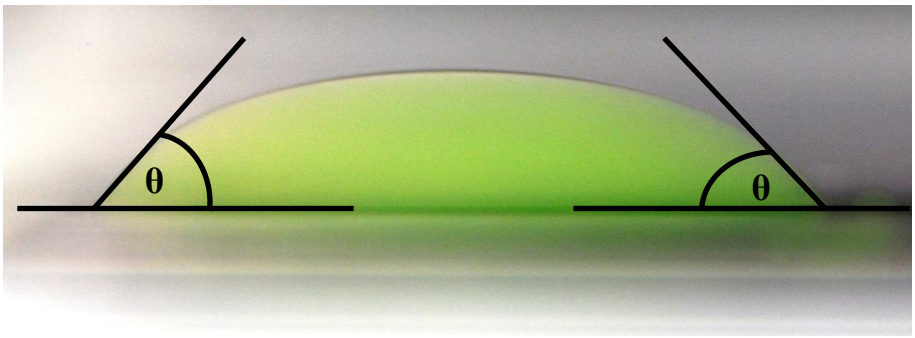

Figure 6-29: Contact angle measurement technique

Now, applying this value to Equation 6.6, it is found that $\varepsilon = 0.28$. This implies that when the glycerol solution hold-up is $\varepsilon = 0.28$ (i.e., the in-situ oil phase fraction $\langle\varphi\rangle_{y,t,} = 0.72$) the interface will be a flat surface. However, for holdup values less than this, $\varepsilon < 0.28$ (i.e., in-situ oil phase fraction $\langle\varphi\rangle_{y,t,} > 0.72$) the interface is expected to be concave and conversely, for holdup values less than this, $\varepsilon > 0.28$ (i.e., in-situ oil phase fraction $\langle\varphi\rangle_{y,t,} < 0.72$) the interface is expected to be convex. From reviewing the in-situ phase fraction results (see Figures 5-7 and 6-10) it is seen that a glycerol solution hold-up value of $\varepsilon = 0.28$ (i.e., the in-situ oil phase fraction $\langle\varphi\rangle_{y,t,} = 0.72$) was not encounter in either of the PLIF campaigns involving the circular cross section visualisation cell (all recorded hold-up values were higher). However, based upon the prediction from $\varphi_{\text{mod},1}$ for stratified flow, a glycerol solution hold-up value of $\varepsilon = 0.28$ is obtained for an input oil phase fraction of $\varphi_{\text{in}} \approx 0.95$. Now, considering that all measured glycerol solution hold-up value are lower than the value yielded from Equation 6.6, it is expected that the liquid-liquid interface for stratified flow will be convex. Therefore, it is necessary to calculate the Bond number to assistance in the evaluation of the interface curvature; from Equation it is found to be Bo $\approx$ 250.

Ng (2002) presented predictions for the shape of the interface which can be compared with the current liquid-liquid system using the calculated Bond number (Bo $\approx$ 250) and the contact angle ($\theta = 51.3^{\circ}$). Figure 6-30 presents the predictions from Ng (2002) for the shape of the interface based upon a Bond number of Bo $= 250$ and different contact angles (note that the results pretaining to a contact angle of $\theta = 0.9\pi$ radians (51.6°) are shown in Figure 6-33(b)).

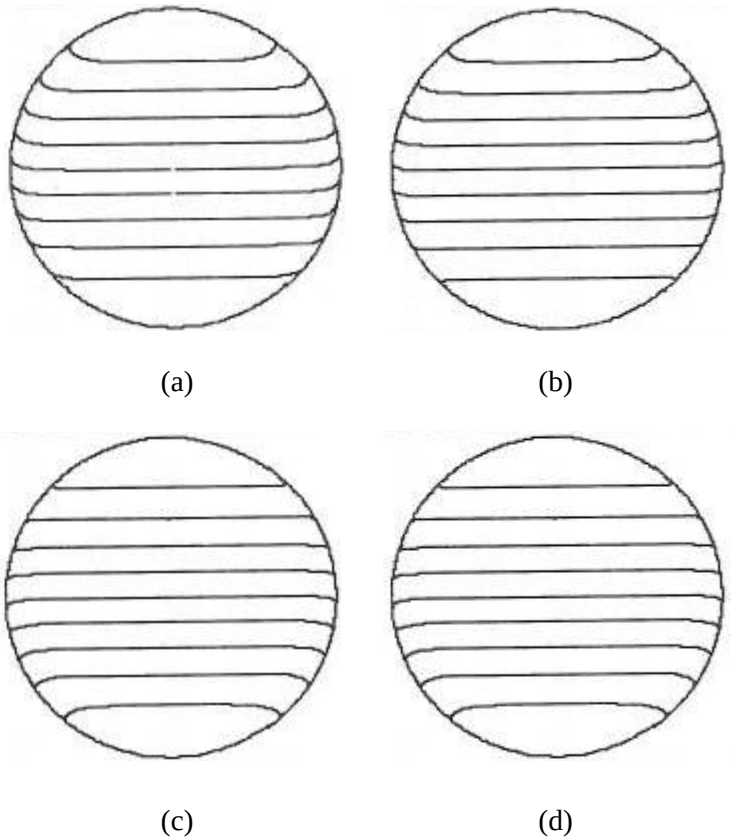

Figure 6-30: Interface shapes for a Bond number Bo = 250 and contact angles: (a) $\theta = 0.1\pi$; (b) $\theta = 0.3\pi$; (c) $\theta = 0.5\pi$, and; (d) $\theta = 0.7\pi$, all for $\varepsilon = 0.1, 0.2, \ldots, 0.9$ computational results by Ng (2002)

From Figure 6-30 it is seen that the interface shape for stratified flow is flat apart from the immediate vicinity of the pipe wall and that for the Bond number (Bo ≈ 250) of the current system, the interface shape is flat irrespective of the contact angle, apart from the region near the fluid boundary with the pipe wall. This is an important finding, as it validates the in-situ phase fraction results which were calculated from the phase distribution profiles using a numerical integration technique *assumed a flat surface at the interface*.

One limitation of the current work is that the velocity profiles are measured only at the centreline of the pipeline, again owing to the planar nature of the optical diagnostic techniques that we have used. Although modelled for different system parameters than for the current

system, the three-dimensional results generated by Ng (2002) can give an insight into the overall shape of the velocity profile of the flow.

Figure 6-31 presents interface level H values as a function normalised interface level velocity ($U_x/\langle U_\mathrm{m}\rangle$). The trend observed is the same as that seen in Chapter 5 (see Figure 5-33). Specifically, that once normalised, the velocity at the interface increases with an increase in the interface level.

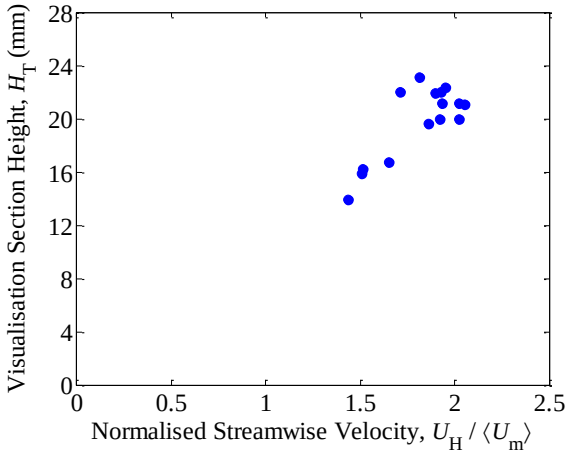

Figure 6-31: Interface level H as a function normalised interface level velocity ($U_\mathrm{H}/\langle U_\mathrm{m}\rangle$).

Ng (2002) presented dimensionless flowrate values as a function of hold-up (i.e., the dimensionless interface level). The modelled results Ng (2002) obtained are based on a contact angle of $\alpha = \pi/3$ ($\approx 51.6^\circ$) are shown in Figure 6-32. From Figure 6-32 it is seen that the dimensionless flowrate increases with interface level. Furthermore, when the Bond number is sufficiently high (Bo $\geq$ 25), the dimensionless flowrate (as a function of hold-up) results tend towards the same profile; for the current system, the value is Bo $\approx$ 250. Now, although this is higher than the Bond number Ng (2002) used to generate the velocity profile results in Figure 6-33, one can infer that because the Bond number Ng (2002) used to generate the results was sufficiently high (Bo $=$ 50), the results are applicable to the current system. From Figure 6-33 it

is seen that dimensionless interfacial velocity (at the centreline) increases with hold-up (i.e., increases with interface level). Thus the simulated results by Ng (2002) concur with the current experimental findings. As the Bond number of the current system is large it can be concluded – on comparison with results presented by Ng (2002) – that at the interface, the maximum interfacial velocity covers a broad range, extending across most of the width of the pipeline.

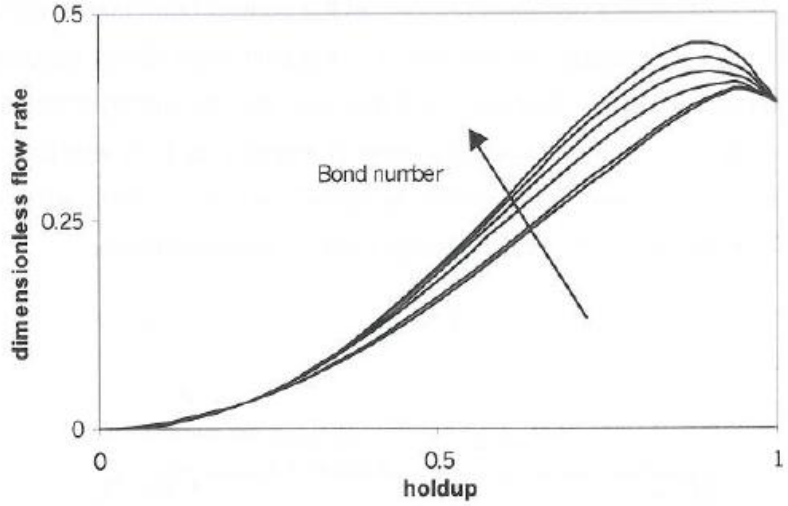

Figure 6-32: Variation of the dimensionless flow rate with hold-up and Bond number, Bo = 0.1, 1, 10, 25, 50 and 100 with a contact angle $\alpha = \pi/3$, taken from Ng (2002)

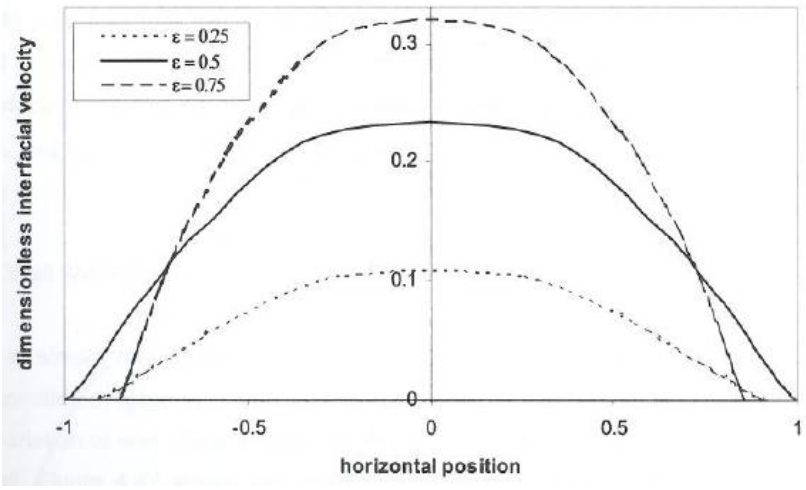

Figure 6-33: Variation of the dimensionless interfacial velocity profile for hold-up values $\varepsilon = 0.25$, 0.5 and 0.75 (Bo = 50 and $\alpha = \pi/3$), taken from Ng (2002)

Ng (2002) presented directly images of three-dimensional velocity profiles. Two of these are shown in Figure 6-34 below; considering these profiles coupled with the shape behaviour of the profile with Bond number, contact angle and viscosity ratio (where $\mathrm{m} = \mu_A/\mu_B$ where A is the less dense phase) a feel for the three-dimensional profile type can start to be made.

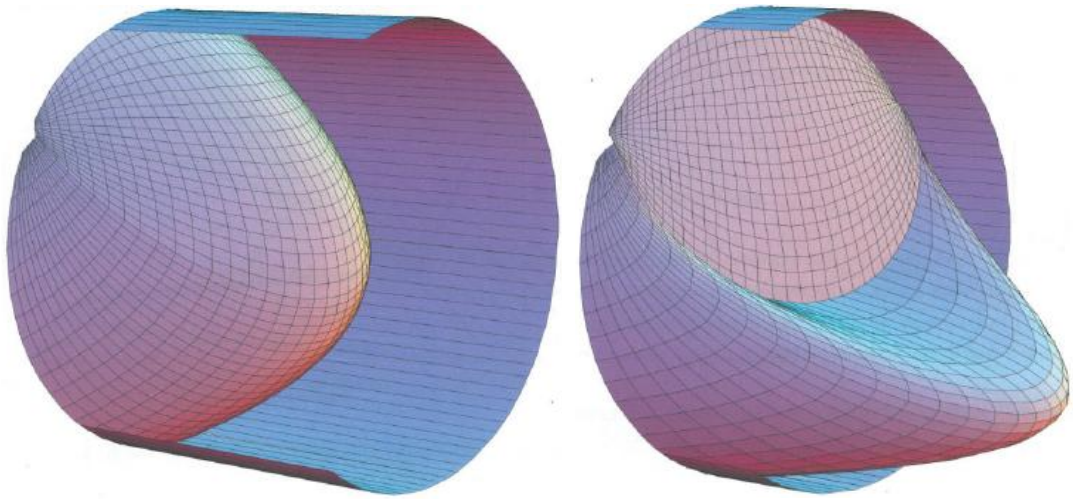

(a) (b)

Figure 6-34: Velocity profile across the pipe cross section for a hold-up of $\varepsilon = 0.3$, contact angle of $\theta = \pi/3$ and a Bond number of $\mathrm{Bo} = 10$ for: (a) $\mathrm{m} = 1.6$, and; (b) $\mathrm{m} = 45$ where $\mathrm{m} = \mu_A/\mu_B$ where A is the less dense phase, Ng (2002)

Firstly, for the profiles shown in Figure 6-34 the Bond number is $\mathrm{Bo} = 10$ whereas the value for the current system is significantly higher ($Bo \approx 250$). So, based on Figure 6-30 the system will have a flatter interface that the convex one featured in Figure 6-34(b). The fact that the contact angle is very similar is less important than the Bond number, as seen Figure 6-30. Comparing Figures 6-34(a) and 6-34(b) on the basis of their different m values it is seen that extend of the shear layer at the interface increases as the m moves away from unity.

One major difference between the current system and the results generated by Ng (2002) is that in the current system the less dense phase (Exxsol D80) is also the less viscose phase hence

$m < 1$; the value is $m \approx 0.03$. Therefore, the "step" in the velocity profile will be above the interface (as seen in Figure 6-25). In essence, the three-dimensional velocity profile for laminar flow of the two liquids used in the current experimental study will be comparable to Figure 6-34(b) yet rotated 180° with a flat interface with a maximum velocity at the interface extending across a great width of the channel.

6.9 Conclusions

An advanced optical diagnostic technique capable of the high-speed spatiotemporal measurement of liquid phase (with PLIF) and flow velocity distribution (with PTV and PIV) has been applied to acquire measurements of horizontal, initially stratified liquid-liquid flows. In the present chapter results are provided from an experimental campaign that goes beyond the study presented in Chapter 5, by investigating the influence of injecting the heavier (aqueous) phase at the top of the tube rather than at the bottom (as was the case in the experiments described in Chapter 5). This change introduces the possibility of phase breakup near the inlet by the Rayleigh-Taylor instability. The effects of this instability near the inlet may persist along the tube and influence the observed flow behaviour.

The findings of the current study, in terms of flow regimes and their characteristics, are comparable *though not identical* to those of Chapter 5. An increased propensity for oil droplets below the interface has been observed, and only six of the eight flow regimes identified in Chapter 5 were observed in the study with the aqueous phase being injected at the top of the pipe. The regimes not observed in this case were (1) three-layer flow, and; (2) glycerol solution dispersion with a glycerol solution film. However, if the flow regime maps of Chapter 5 and the current chapter are evaluated on the more general basis of transition to *dual continuous* flow, then the two flow regime maps are very similar.

From the flow regime map it is seen that for flows in which roughly equal volumetric flowrates (i.e., $\varphi_{\mathrm{in}} \approx 0.5$) of the two-liquids are injected into the pipeline, the velocity for transition from stratified flow to other flow regimes (i.e., *dual continuous* and in turn, dispersed flow) is higher than for input oil phase fractions that approach the limits (i.e., $\varphi_{\mathrm{in}} = 0$ and 1). This is expected because at $\varphi_{\mathrm{in}} \approx 0.5$ flow regime transition is governed by turbulence (i.e., related to Reynolds number).

The same velocity profile behaviour has been found in the current study as were found in Chapter 5. In addition, in the current Chapter the work has been extended to analyse the horizontal interface shape that separates the two phases, which has been found to be relatively flat. This validates the methodology for calculating the in-situ phase fraction, the central tenet of which was that the assumption that the interface was flat across the pipe cross-section.

CHAPTER 7

Conclusions and Suggestions for Future Work

7.1 Conclusions

The following main conclusions have been drawn from the work described in this thesis:

(1) For what is believed to be the first time, a combination of Planar Laser Induced Fluorescence (PLIF), Particle Tracking Velocimetry (PTV) and Particle Image Velocimetry (PIV) has been used in the study of horizontal liquid-liquid flows. The experiments have been facilitated by the refurbishment of an existing Imperial College liquid-liquid flow facility (TOWER) and the development and use of a liquid/liquid combination (aqueous glycerol solution and Exxol^{TM}) in which the refractive indices of the two fluids have been precisely matched.

(2) The initial experiments were conducted using a square cross section duct which avoided the image distortion caused by the (transparent) walls if a circular cross section duct is used. In the later experiments, where circular cross section pipes were employed, it was found possible to correct the received images for this distortion by photographing a

graticule placed at the centre of the channel and using a computer image processing system to generate undistorted images.

(3) The PLIF images gave a clear indication of the distribution of the phases at the channel centre line and the images (and particularly the movie sequences of images) could be used qualitatively in obtaining information about the flow patterns occurring. New insights were obtained about the nature of the flow patterns as a result of this process. The PLIF images could also be used *quantitatively* in generating data on phase distribution, in-situ phase fraction, interface level and drop size distribution. Extensive information on all these quantities (and comparison of the measurements with previous information and models) is presented in this thesis.

(4) In the circular tube experiments, two methods of injection of the phases were used. In the first (see Chapter 5), the heavier (glycerol solution) phase was injected in its natural location at the bottom of the channel. In the second case (see Chapter 6), the heavier phase was injected at the top of the channel. In this case, breakup of the liquid at the injector would be expected to occur as a result of Raleigh-Taylor instability. Even with the considerable distance between the injection point and the measurement location (6.20 m, such that $L/D = 244$) some differences are still observed between the flows resulting from the two injection strategies.

(5) Extensive data on velocity profiles were obtained using PTV and PIV. Examination of these profiles indicated major differences between the two phases. In the lower (aqueous glycerol solution) phase, the profile usually showed the curved shape characteristic of laminar flow. In the upper (Exxol^{TM} D80) phase, the velocity profile often showed the flattened form characteristic of turbulent flow.

(6) Extensive work was carried out on modelling of the flows. Much of the data fitted well with a simple laminar-laminar stratified flow model (see Appendix 2). Comparisons were also made with the stratified flow models of Hall and Hewitt (1993) and revealed that the gas-liquid form of their model fitted the present data well (see Chapters 5 and 6). The laminar-laminar and Hall and Hewitt (1993) models are based on the assumption of a flat interface. The validity of this assumption was investigated (see Chapter 6) by considering the model of Ng (2002). In this latter model, account is taken of wetting angle at the triple interface and of interfacial tension. To aid this investigation, measurements were made of the wetting angle. It was concluded that the assumption of a flat interface was a reasonable approximation in modelling the present tests.

7.2 Suggestions for Future Work

The technology developed in the work described here can clearly be a basis for extensive further investigations. Specific suggestions for the extension of the work are as follows:

(1) In the experiments described here, a fluorescent dyestuff was added to the aqueous phase to allow clear identification of that phase in the PLIF studies. The dyestuff used was Eosin Y. Though separate measurements indicated that this dyestuff had a negligible effect on interfacial tension (and was therefore unlikely to be significantly surface active), the dyestuff did significantly absorb the laser light sheet and produced "shadows" on the images reflecting this partial absorption process. It is suggested, therefore, that a search for a more optimal dyestuff be undertaken.

(2) It is strongly suggested that an investigation should be performed to identify a series of refractive index matched test fluid pairs that can be employed in the TOWER facility, so that the influence of the physical properties of the test fluids on flow development can be investigated. Further to this, PLIF campaigns in which surfactants are added to the flow should be performed to enhance understanding of how their presence effects the flowing behaviour, particular the flow regimes and velocity profiles.

(3) The refractive indices of the test fluids are functions of temperature. If a heat exchanger were inserted into the TOWER facility prior to the test section inlet it would allow the flow inlet temperature to be maintained at a value for which the refractive indices of the two test fluids are most closely matched, hence minimising the distortion to the PLIF images arising due to the disparity in the refractive indices of the test fluids caused by the temperature fluctuations.

(4) Fitting the TOWER facility with pressure transducers would allow the simultaneous recording of pressure drop with PLIF and PTV/PIV measurements. The availability of pressure gradient measurements would allow a much broader scope of analysis to be undertaken.

(5) There is a need for better prediction methods for flow regime transitions in liquid-liquid flows. The development of such methods might lean on what has been done in gas-liquid flow. A detailed investigation of the phase inversion phenomenon (which is accompanied with a characteristic spike in pressure drop) could be carried out with the aid of PLIF and PIV/PTV images and measurements.

(6) In light of the differences in the flow regimes arising from the different inlet orientations, the current work could be progressed by investigating the flow at different

axial positions downstream of the test section inlet to develop the understanding of the progression to fully developed flow. This could be further developed by investigating the influence of mixing elements at the inlet to the test section upon reaching fully developed flow.

(7) For the PLIF studies presented in Chapters 4 to 6, the test section was horizontal; the influence of different inclinations on the flow is an area of significant practical importance and this area could be pursued with the methods developed in the present study.

(8) The channel wall material can have a significant influence on liquid-liquid flows (as was shown in the work of Angeli and Hewitt, 2000a). In the present work, the test section upstream of the measurement section was made of stainless steel. It would be instructive to study any changes which might occur with different pipe materials, such as acrylic resin.

(9) Though the focus in the present work has been on pipeline flows (and there is scope for much further work in this area as discussed above) the PLIF and PTV/PIV system developed in the current work could be utilised to investigate other forms of liquid-liquid systems, such as stirred vessels.

(10) In the present work, the PTV and PIV methods have been used primarily to measure mean velocity fields. However, there is no reason why this technology could not be extended to the investigation of *fluctuating* velocities including fluctuations arising from interfacial wave action and turbulence and such an extension is strongly recommended.

References

Angeli, P. (1996). Liquid-liquid dispersed flows in horizontal pipes. Department of Chemical Engineering and Chemical Technology, Imperial College London. **PhD Thesis**.

Angeli, P. and G. F. Hewitt (2000a). "Flow structure in horizontal oil-water flow." International Journal of Multiphase Flow **26**(7): 1117-1140.

Angeli, P. and Hewitt, G. F., (2000b). Flow structure in horizontal oil-water flow. Int. J. Multiph. Flow **26** (7), 1117-1140.

Angeli, P. and G. F. Hewitt (2000). "Drop size distributions in horizontal oil-water dispersed flows." Chemical Engineering Science **55**(16): 3133-3143.

Aomari, N., R. Gaudu, F. Cabioc'h and A. Omari (1999). "Rheology of water in crude oil emulsions." Colloids and Surfaces A: Physicochemical and Engineering Aspects **139**(1):13-20

Arashmid, M. and G. V. Jeffreys (1980). "Analysis of the phase inversion characteristics of liquid-liquid dispersions." AlChemE Journal **26**(1).

Arirachakaran, S., K. D. Oglesby, M. S. Malinowsky, O. Shoham and J. P. Brill (1989). "An analysis of oil/water phenomena in horizontal pipes." SPE Productions Operations Symp. (SPE 18836).

Barbosa, J. R., Govan, A. H. and Hewitt, G. F. (2001). Visualisation and modelling studies of churn flow in a vertical pipe. Int. J. Multiph. Flow 27 (12), 2105-2127.

Barnes, H. A. (1994) "Rheology of emulsions – a review." Colloids and Surfaces A: Physicochemical and Engineering Aspects **91**:89-95

Bell, J. M., Y. D. Chin, A. Kvaerner and S. Hanrahan (2005). State of the art of ultra deepwater production technologies. 2005 Offshore Technology Conference (2^{nd} – 5^{th} May 2005), Houston, Texas, U.S.A. (OTC 17615)

Bingham, E. C. (1916) "An Investigation of the Laws of Plastic Flow." U.S. Bureau of Standards Bulletin, **13**: 309-353

Bird, R. B., W. E. Stewart and E. N. Lightfoot (2001) "Transport Phenomena." John Wiley and Sons, New York.

Brauner, N. (2001). "The prediction of dispersed flows boundaries in liquid-liquid and gas-liquid systems." International Journal of Multiphase Flow **27**(5): 885-910.

Brauner, N. and A. Ullmann (2002). "Modeling of phase inversion phenomenon in two-phase pipe flows." International Journal of Multiphase Flow **28**(7): 1177-1204.

Brinkman, H. C. (1952). "The viscosity of concentrated suspensions and solutions." Journal of Chemical Physics **20**: 571.

Brooks, B. W. and H. N. Richmond (1994). "Phase inversion in non-ionic surfactant-oil-water systems--III. The effect of the oil-phase viscosity on catastrophic inversion and the

relationship between the drop sizes present before and after catastrophic inversion." Chemical Engineering Science **49**(11): 1843-1853.

Charles, M. E., G. W. Govier and G. W. Hodgson (1961). "The horizontal pipeline flow of equal density oil-water mixtures." Canadian J. Chem. Eng., **39**(1): 27-36.

Charles, M. E. and Lilleleht, L. U., 1966. Correlation of pressure gradients for the stratified laminar-turbulent pipeline flow of two immiscible liquids. Can. J. Chem. Eng. **44** (1), 47-49.

Chen, J., 2003. Study on oil-water two phase pipe flow. **Ph.D**. thesis, University of Petroleum, Beijing.

Chong, J. S., E. B. Christiansen, A. D. Baer (1971) "Rheology of concentrated suspensions." J. Appl. Poly. Sci. 15:2007-2021

Clayton, W. (1935). The theory of emulsion and their technical treatment. I. P. Blakiston's Son and Company. Philadephia.

Coulaloglou, C. A. and Tavlarides, L. L., 1976. Drop size distribution and coalescence frequencies of liquid-liquid dispersions in flow vessels. AIChE J. 22 (2), 289-297.

Decarre, S. and J. Fabre (1997). "Phase inversion prediction study." Journal of L' Institute Francais du Prtrole **Vol. 52**: pp. 415-424.

Dimonte, G. and M. Schneider (2000) “Density Ratio Dependence of Rayleigh–Taylor Mixing for Sustained and Impulsive Acceleration Histories.” Physics of Fluids **12**:304–32

Du, H., Fuh, R. A., Li, J ., Corkan, A. and Lindsey, J. S., 1998. PhotochemCAD: A computer-aided design and research tool in photochemistry. Photochem. Photobiol. **68** (2), 141-142.

Efthimiadu, I. and I. P. T. Moore (1994). "Phase inversion of liquid-liquid dispersions produced between parallel shearing plates." Chemical Engineering Science **49**(9): 1439-1449.

Eilers, H. (1943). “Die viskositat-konzentrationsabhangigkeit kolloider systeme in organischen losungsmitteln.” Kolloid-Z **102**(2): 154-169

Einstein, A. (1906). “Theory of Brownian movement.” Ann. Phys., German **19:**289-306

Falco, J. W., R. D. Walker and D. O. Shah (1974). "Effects of phase-volume ratio and phase inversion on viscosity of microemulsions and liquid crystals." A.I.ChE Journal **20**(3):510-514.

Farah, M. A., R. C. Oliveira, J. N. Caldas, K. Rajagopal (2005) “Viscosity of water-in-oil emulsions: Variation with temperature and water volume fraction.” Journal of Petroleum Science and Engineering, **48**(3–4):169-184

Glimm, J., J. W. Grove, X. L. Li, W. Oh and D. H. Sharp (2001) “A Critical Analysis of Rayleigh–Taylor Growth Rates”. Journal of Computational Physics **169**:652–677

Guzhov, A. I., A. D. Grishin, V. F. Medredev and O. P. Medredeva (1973). "Emulsion Formation During the Flow of Two Liquids in a Pipe." Neft Khoz **8**: 58-61 (in Russian).

Hall, A. R. W. (1992). Multiphase flow of oil-water-gas in horizontal pipes. Department of Chemical Engineering & Chemical Technology London, Imperial College of Science, Technology & Medicine, University of London. **PhD Thesis**.

Hall, A. R. W. and Hewitt, G. F (1993). "Application of two-fluid analysis to laminar stratified oil-water flows." International Journal of Multiphase Flow **19**(4): 711-717.

Hasson, D., U. Mann and A. Nir (1970). "Annular flow of two immiscible liquids." Canadian J. Chem. Eng. **Vol. 48**: pp. 514-520.

Hatschek, E. (1928) "Viscosity of liquids." Bell, London

Hewitt, G. F., Jayanti, S., and Hope, C. B., 1990. Structure of thin liquid films in gas-liquid horizontal flow. Int. J. Multiph. Flow **16**(6), 951-957.

Hinze, J. (1955). "Fundamentals of the hydrodynamic mechanism of splitting in dispersion processes." AIChE J. **Vol. 1**(No. 3):289-295.

Hughmark, G. A. (1962). "Pressure drop in horizontal and vertical co-current gas-liquid flow." IEC Fund. **2**:315.

Hughmark, G. A. (1971). "Drop breakup in turbulent pipe flow." AIChE J. **Vol. 4**: pp. 1000.

Hussain, S. A. (2004). Experimental and computational studies of liquid-liquid dispersed flows. Department of Chemical Engineering and Chemical Technology, Imperial College London. **PhD Thesis**.

Ioannou, K., O. J. Nydal and P. Angeli (2005). "Phase inversion in dispersed liquid-liquid flows." Experimental Thermal and Fluid Science **29**(3): 331-339.

Ishii, M. and Mishima, K., 1984. Two-fluid model and hydrodynamic constitutive relations. Nucl. Eng. Des. **82**(2-3), 107-126.

Joseph, D. D., M. Renardy, M. and Y. Renardy (1984). "Instability of the flow of two immiscible liquids with different viscosities in a pipe." J. Fluid Mech., **141**: 309-317.

Kashid, M. N. and D. W. Agar (2007) "Hydrodynamics of liquid–liquid slug flow capillary microreactor: Flow regimes, slug size and pressure drop." Chem. Eng. J. **131** (1-3), 1-13.

Kolmogorov, A. N. (1949). "On the breaking of drops in turbulent flow." Doklady Akad, Nauk. **66**: 825-828.

Krieger, I.M. and T. J. Dougherty (1959). "A mechanism for non-Newtonian flow in suspensions of rigid spheres". Trans. Soc. Rheol. **3**, 137-152

Kubie, J. and G. C. Gardner (1977) "Drop sizes and drop dispersion in straight horizontal tubes and in helical coils." Chem. Eng. Sci. **Vol. 32**: 195-202.

Kurban, A.P.A. (1997) Stratified Liquid-liquid Flow, Ph.D Thesis, Imperial College, University of London, UK.

Laflin, G. C. and K. D. Oglesby (1976). An Experimental Study On The Effects Of Flow Rate, Water Fraction And Gas-Liquid Ratio On Air-Oil-Water Flow In Horizontal Pipes, University of Tulsa. **B. S. Thesis**.

Lang, P., Auracher, H., (1996). Heat transfer to nonmiscible liquid-liquid mixtures flowing in a vertical tube, Experimental Thermal and Fluid Science, 12: 364-372.

Liu, L. (2005). Optical and computational studies of liquid-liquid flows. Chemical Engineering and Chemical Technology, Imperial College London. **PhD Thesis**.

Lovick, J (2003) Horizontal, Oil-Water Flows in the Dual Continuous Flow Regime, University College London. **PhD Thesis**.

Lovick, J. and P. Angeli (2004). "Experimental studies on the dual continuous flow pattern in oil-water flows." International Journal of Multiphase Flow **30**(2): 139-157.

Luhning, R. W. and H. Sawistowski (1971). Phase inversion in stirred liquid-liquid systems. Proc. Int. Solvent Extr. Conf. . The Hague, Society of Chemicial Industry, London**:** 873-887.

MacLean, D. L. (1973). A theoretical analysis of bicomponent flow and the problem of the interface shape, Trans. Soc. Rheology, **17**: 385-399

Malinowsky, M. (1975). An experimental study of oil-water and air-oil-water flowing mixtures in horizontal pipes, The University of Tulsa. **M.S. Thesis**.

Markides, C. N. and E. Mastorakos (2006) "Measurements of scalar dissipation in a turbulent plume with planar laser-induced fluorescence of acetone." Chem. Eng. Sci. **61**(9), 2835-2842.

Martinez, A. E., S. Arirachakaran, O. Shoham and J. P. Brill (1988). "Prediction of Dispersion Viscosity of Oil/Water Mixture Flow in Horizontal Pipes." Society of Petroleum Engineers Paper (SPE 18221).

McClarey, M. J. and G. A. Mansouri (1978). "Factors Affecting the Phase Inversion of Dispersed Immiscible Liquid-liquid Mixtures." AIChemE Journal, Symposium Series **74**(173): 134-139.

Mooney, M. (1951). The viscosity of a concentrated suspension of spherical particles. Journal of Colloid and Interface Science, **6:**162–170.

Nädler, M. and D. Mewes (1995) "Effects of the liquid viscosity on the phase distributions in horizontal gas-liquid slug flow." International Journal of Multiphase Flow **21**(2), 253-266.

Nädler, M. and D. Mewes (1997). "Flow induced emulsification in the flow of two immiscible liquids in horizontal pipes." International Journal of Multiphase Flow **23**(1): 55-68.

Ng, T. S. (2002). Interfacial structure of stratified pipe flow, Chemical Engineering and Chemical Technology, Imperial College London. **PhD Thesis**.

Oglesby, K. D. (1979). An experimental study on the effects of oil viscosity mixture velocity and water fraction on horizontal oil-water flow, University of Tulsa, USA. **MSc. Thesis**.

Pal, R. (1993). "Pipeline Flow of Unstable and Surfactant-Stabilized Emulsions." Aiche Journal **39**(11): 1754.

Pal, R. and Rhodes, E (1989) "Emulsion Flow in Pipelines." Int. J. Multiphase Flow, Vol 15, No 6, pp. 1011-1017.

Pal, R., (2000). "Viscosity concentration equation for emulsions of nearly spherical drops." J. Colloid Interface Sci. **231**:168– 175.

Phan-Thien, N. and Pham, D.C. (1997). "Differential multiphase models for poly-dispersed suspensions and particulate solids." J. Non-Newton. Fluid Mech. 72:305–318.

Richardson, E. G., 1933. U¨ ber die Viskosita¨t Emulsionen. Kolloid-Z. 65:32.

Ronningsen, H. P. (1995) "Correlations for predicting Viscosity of W/O Emulsions based on North Sea Crude Oils." Proc. SPE Int. Symp. Oil Field Chem., Houston, Texas, 1995.

Roscoe, R. (1952) "The viscosity of suspensions of rigid spheres" British Journal of Applied Physics. **3**(8) 267-269

Russell, T. W. F. and Charles, M. E., 1959. The effect of the less viscous liquid in the laminar flow of two immiscible liquids. Can. J. Chem. Eng. 37 (1), 18-24.

Russell, T. W. F., G. W. Hodgson and G. W. Govier (1959) "Horizontal pipeline flow of mixtures of oil and water." Can. J. Chem. Eng. **37**(1), 9-17.

Sajjadi, S., M. Zerfa and B. W. Brooks (2002) "Dynamic behaviour of drops in oil/water/oil dispersions." Chem. Eng. Sci. 57 (4), 663-675.

Selker, A. H. and J. Selicher, C. A. (1965). "Factors affecting which phase will disperse when immiscible liquids are stirred together." Canadian J. Chem. Eng. **43**: 298-301.

Sellens, R. (2008) "Power law profiles in pipes." Faculty of Engineering and Applied Science, Queen's University < http://me.queensu.ca/People/Sellens/PowerLaw.html>

Shaha, J., 1999. Phase interactions in transient stratified flow. **PhD** thesis, Imperial College London, London.

Simmons, M. J. H and Azzopardi, B. J. (2001) "Drop size distributions in dispersed liquid-liquid pipe flow." Int. J. Multiph. Flow **27**(5), 843-859.

Soleimani, A. (1999). Phase Distribution and associated phenomena in oil-water flows in horizontal tubes. Department of Chemical Engineering and Chemical Technology. London, Imperial College, University of London. **PhD** thesis

Sotgia, G. and P. Tartarini (2001). Experimental and theoretical investigation on pressure drop reductions in oil-water flows. Proceedings of ICMF-2001 (4th International Conference of Mulitphase Flow)

Taylor, G.I. (1932). "The viscosity of a fluid containing small drops of another liquid." Proc. R. Soc., A **138**, 41–48.

Taitel, Y. and A. E. Dukler (1976). "A model for predicting flow regime transitions in horizontal and near horizontal gas-liquid flow." AIChE Journal **22**(1): 47-55.

Tidhar, M., J. C. Merchuk, A. N. Sembira and D. Wolf (1986). "Characteristics of a Motionless Mixer for Dispersion of Immiscible Fluids - II. Phase Inversion of Liquid-Liquid Systems." Chem. Eng. Sci. **41**(3): 457-462.

Tobin, T. and Ramkrishna, D. (1992) " Coalescence of charged droplets in agitated liquid-liquid dispersions." AIChE J. **38** (8), 1199-1205.

Tokeshi, A., Minagawa, T., Uchiyama, K., Hibara, A., Sato, K., Hisamoto, H. and Kitamori, T., (2002) "Continuous-flow chemical processing on a microchip by combining microunit operations and a multiphase flow network." Anal. Chem. **74**(7):1565-1571.

Trallero, J. L. (1995). Oil-water flow pattern in horizontal pipes. Department of Petroleum Engineering, University of Tulsa, USA.

Tsouris, C. and J. Dong (2000). "Effects of electric fields on phase inversion of liquid-liquid dispersions." Chemical Engineering Science **55**(17): 3571-3574.

Vand, V. (1948) ColbMChem**.** J. Phys. **52:**277.

Wallis, G. B. (1969). One dimensional two-phase flow. New York, McGraw-Hill.

Ward, J. P. and Knudsen, J. G., 1967. Turbulent flow of unstable liquid-liquid dispersions: drop sizes and velocity distributions. AIChE J. 13 (2), 356-365.

Wegmann, A. and von Rohr, P. R., 2006. Two phase liquid-liquid flows in pipes of small diameters. Int. J. Multiph. Flow 32 (8), 1017-1028.

Xu, X. X. (2007). "Study on oil water two-phase flow in horizontal pipelines." Journal of Petroleum Science and Engineering **59**(1-2): 43-58.

Yeh, G. C., F. H. Haynie and R. A. Moses (1964). "Phase-Volume Relationship at the Point of Phase Inversion in Liquid Dispersions." AlChemE Journal **10**(2): 260-265

Yeo, L. Y., O. K. Matar, E. S. Perez de Ortiz and G. F. Hewitt (2002). "A simple predictive tool for modelling phase inversion in liquid-liquid dispersions." Chemical Engineering Science **57**(6): 1069-1072.

APPENDIX 1:

Start-Up and Shut-Down Procedure

The TOWER rig is a complex facility. It is important to operate it in an efficient and safe manner. Thus, for the benefit of future users, it has been considered useful to place on record here a summary of the start-up and shut-down procedures.

Start-Up Procedure

1. Check all valves are closed
2. Ensure that the aqueous phase (water or, in the present work aqueous glycerol solution) and oil tanks are at least ¾ full. If not, open valve CV5 and/or CV6 respectively and add water and/or oil until tanks reach desired level, then fully close both valves
3. Fully open the valves before (BV5 & BV2) and the valves after (BV6 & BV7) the pumps
4. Fully open control valves CV1 and CV3, and partially open CV2 and CV4
5. If running the aqueous phase at low flow, fully open valve BV10. If running the aqueous phase at high flow, fully open valve BV11
6. If running oil at low flow, fully open valve BV12. If running oil at high flow, fully open valve BV13
7. To introduce water flow to the top of the inlet, open valves BV15 and BV19. To introduce water flow to the bottom of the inlet, open valves BV14 and BV18
8. To introduce oil flow to the top of the inlet, open valves BV17 and BV19. To introduce oil flow to the bottom of the inlet, open valve BV16 and BV18. Ensure that the phases are always introduced at opposing orientations.

9. Open valve BV21

10. Open CV5 and CV6

11. Switch on pumps M1 and M2

12. Bleed pressure transducer tappings upstream and downstream to remove any trapped air.

13. Increase aqueous phase flowrate by opening CV2 whilst simultaneously closing valve CV1. Increase oil flowrate by opening CV4 whilst simultaneously closing valve CV3. Adjust each to desired levels

Shut-Down Procedure:

1. Turn off pumps M1 and M2

2. Close valves CV5 and CV6

3. Close valve BV21

4. Shut all valves in the mixing section (BV15-BV19)

5. Close all valves flow meter valves (BV10-BV13)

6. Fully close valves CV4, CV3, CV2 and CV1

7. Close BV5 and BV6, BV2 and BV7

APPENDIX 2

Derivation of Laminar Drag Model

Equation 4.2 has been derived by first considering the frictional pressure drop Δp experienced by each of the two test fluids over a pipe length L:

$$\Delta p_i = \frac{1}{2}\rho_i U_i^2 \, f_i \frac{4L}{D_i}, \tag{A1}$$

$$\Delta p_{\text{oil}} = \frac{1}{2}\rho_{\text{oil}} U_{\text{oil}}^2 \, f_{\text{oil}} \frac{4L}{D_{\text{oil}}}, \tag{A2}$$

$$\Delta p_{\text{gs}} = \frac{1}{2}\rho_{\text{gs}} U_{\text{gs}}^2 \, f_{\text{gs}} \frac{4L}{D_{\text{gs}}}, \tag{A3}$$

where the subscript ‘oil’ denotes the oil flow and the subscript ‘gs’ that of the glycerol solution. The hydraulic diameter D is,

$$D_i = \frac{4A_i}{P_i}, \tag{A4}$$

with A_i and P_i the cross-sectional area and the wetted perimeter of fluid ‘i’ respectively. Also, f_i denotes the Fanning friction factor of fluid ‘i’ that for laminar flow is given as,

$$f_i = \frac{16}{Re_i}, \tag{A5}$$

and, Re_i is the Reynolds number associated with the flow of fluid 'i', which in turn is defined as,

$$Re_i = \frac{\rho_i U_i D_i}{\mu_i} . \tag{A6}$$

Equating the pressure drops for each liquid flow in our arrangement gives,

$$\Delta p_i = \Delta p_{\text{oil}} = \Delta p_{\text{gs}} . \tag{A7}$$

Now, substituting the laminar relation for the Fanning friction factor from Eq. A5 into the frictional pressure drop equation for each liquid, i.e., Eq. A2 for oil and Eq. A3 for the glycerol solution, and dividing the oil pressure drop by that of the glycerol solution, i.e., Eq. A2/Eq. A3, gives,

$$\frac{\rho_{\text{oil}}}{\rho_{\text{gs}}} \left(\frac{U_{\text{oil}}}{U_{\text{gs}}}\right)^2 \frac{Re_{\text{gs}}}{Re_{\text{oil}}} \frac{D_{\text{gs}}}{D_{\text{oil}}} = 1 . \tag{A8}$$

After substituting the Reynolds number definition (Eq. A6) for each liquid flow into Eq. A8 we obtain,

$$\frac{U_{\text{oil}}}{U_{\text{gs}}} \frac{\mu_{\text{oil}}}{\mu_{\text{gs}}} \left(\frac{D_{\text{gs}}}{D_{\text{oil}}}\right)^2 = 1 . \tag{A9}$$

Returning to the hydraulic diameters of the two fluid flows from Eq. A4, we can also write,

$$D_{\text{oil}} = 2 \frac{Y_{\text{oil}} W}{Y_{\text{oil}} + W} , \tag{A10}$$

$$D_{\mathrm{gs}} = 2\frac{Y_{\mathrm{gs}}W}{Y_{\mathrm{gs}}+W}\,. \tag{A11}$$

where Y_i is the (absolute) time-averaged depth of liquid 'i' and W is the width of the square channel, such that,

$$W = Y_{\mathrm{oil}} + Y_{\mathrm{gs}}\,. \tag{A12}$$

Note that, in Equation A11, the *wetted perimeter* for each phase is taken as the sum of the perimeter of the phase in contact with the wall of the channel *plus* the interfacial perimeter.

Dividing through the expressions for the two hydraulic diameters (Eqs. A10 and 11), we have,

$$\frac{D_{\mathrm{oil}}}{D_{\mathrm{gs}}} = \frac{Y_{\mathrm{oil}}}{Y_{\mathrm{gs}}}\frac{(Y_{\mathrm{gs}}+W)}{(Y_{\mathrm{oil}}+W)}\,. \tag{A13}$$

Now we define a dimensionless liquid flow depth,

$$y_1 = \frac{Y_{\mathrm{oil}}}{Y_{\mathrm{gs}}}\,, \tag{A14}$$

and substitute this into Eq. A13 to obtain,

$$\frac{D_{\mathrm{gs}}}{D_{\mathrm{oil}}} = \frac{1}{y_1}\frac{(2y_1+1)}{(y_1+2)}\,. \tag{A15}$$

The substitution of the hydraulic diameter ratio $D_{\mathrm{gs}}/D_{\mathrm{oil}}$ from Eq. A15 into the expression for the pressure drop ratio $\Delta p_{\mathrm{oil}}/\Delta p_{\mathrm{gs}}$, Eq. A9, gives,

$$\frac{U_{\text{oil}}}{U_{\text{gs}}}\frac{\mu_{\text{oil}}}{\mu_{\text{gs}}}\left(\frac{1}{y_1}\frac{2y_1+1}{y_1+2}\right)^2 = 1\,. \tag{A16}$$

Finally, performing a mass balance gives:

$$\frac{Y_{\text{oil}}}{Y_{\text{gs}}}\frac{U_{\text{oil}}}{U_{\text{gs}}} = \frac{Q_{\text{oil}}}{Q_{\text{gs}}} \Rightarrow \frac{U_{\text{oil}}}{U_{\text{gs}}} = \frac{1}{y_1}\frac{Q_{\text{oil}}}{Q_{\text{gs}}}\,. \tag{A17}$$

Substituting the superficial velocity ratio $U_{\text{oil}}/U_{\text{gs}}$ from Eq. A17 into the pressure drop ratio $\Delta p_{\text{oil}}/\Delta p_{\text{gs}}$, Eq. A16 gives:

$$\frac{1}{y_1}\frac{Q_{\text{oil}}}{Q_{\text{gs}}}\frac{\mu_{\text{oil}}}{\mu_{\text{gs}}}\left(\frac{1}{y_1}\frac{2y_1+1}{y_1+2}\right)^2 = 1\,, \tag{A18}$$

$$\Rightarrow \frac{4y_1^2+4y_1+1}{y_1^5+4y_1^4+4y_1^3} = \frac{Q_{\text{gs}}}{Q_{\text{oil}}}\frac{\mu_{\text{gs}}}{\mu_{\text{oil}}} = X\,, \tag{A19}$$

in which, parameter X has been defined as being equal to the multiple of the ratios of the volumetric flow rates and dynamic viscosities of the glycerol solution to the oil flows. Therefore, we obtain Eq. 4.2 as,

$$X{y_1}^5 + 4X{y_1}^4 + 4X{y_1}^3 - 4{y_1}^2 - 4y_1 - 1 = 0\,. \tag{A20}$$

“Stay hungry. Stay foolish."

The Whole Earth Catolog